# EXPERIMENTAL INVESTIGATION ON AXISYMMETRIC TURBULENT WAKES WITH ZERO MOMENTUM DEFECT

Thesis by

Hiroshi Higuchi

In Partial Fulfillment of the Requirements

for the Degree of

Doctor of Philosophy

California Institute of Technology

Pasadena, California

1977

(Submitted July 19, 1976)

ACKNOWLEDGEMENTS

The author wishes to thank Professor Toshi Kubota for his guidance and encouragement throughout the research.

He would like to express his gratitude to Dr. James Kendall of the Jet Propulsion Laboratory for making his wind tunnel, mini-computer and subroutine programs available for the present investigation.

Gratitude is also due Dr. Donald Collins for the stimulating discussions and for his help on the flow visualization, and due Prof. Anatol Roshko for his encouragement and valuable discussions.

Prior to the present investigation Dr. Vijay Kulkarny obtained a far-wake expansion solution to the momentumless wake with constant eddy viscosity model, and the discussion with him is appreciated.

The author acknowledges the technical assistance offered by the staffs of the machine shop and the hypersonic group at GALCIT and by the staffs of the Physics Section at JPL.

The manuscript was proofread by Mrs. Karen Cheetham, and was typed by Mrs. Virginia Conner.

Some of the figures were traced by the author himself and should be distinguished from nicer ones by Mrs. Betty Wood or busier ones by the computer.

Last, but not least, the author wishes to take this opportunity to thank his parents for their patience, understanding and tacit yet warm encouragement from miles away.

# ABSTRACT

An experimental investigation of a turbulent axisymmetric wake with zero momentum defect was carried out. The experiment was conducted in a low speed wind tunnel with a circular tube mounted parallel to the stream. A controlled amount of air was injected into the stream at the end of the model to cancel the drag produced by the turbulent boundary layer on the model. The measurements on the mean flow and the fluctuation quantities were carried up to 90 diameters downstream. By adjusting the strength of the injection, the behavior of the pure wake, the co-flowing jet and the matched injection were examined, and the self-similar properties both in the mean velocity and the turbulent intensity were found to exist in these cases. Rapid decays of the centerline velocity and the maximum turbulent intensity were observed in the matched injection case. The effect of the initial condition was studied by artificially thickening the boundary layer on the model, and it was observed that the wake relaxes into the final decay law sooner. The unmatched cases, both strong and weak injections, were also investigated; the strong injection case was found to relax into the self-similar weak jet profile and the weaker injection case was observed to approach to the similar wake profile.

Flow visualization was conducted on the plane of symmetry and the entrainment process by the engulfing large eddies was visualized in the pure wake and in the co-flowing jet. A lack of large rotations was observed in the matched injection case and the lack of production of turbulent energy was attributed to the faster decay of the flow properties.

# TABLE OF CONTENTS

Table of Contents (Cont'd)

Table of Contents (Cont'd)

List of Figures

List of Figures (Cont'd)

List of Figures (Cont'd)

List of Figures (Cont'd)

List of Figures (Cont'd)

List of Figures (Cont'd)

# CHAPTER I

# INTRODUCTION

During the past few decades, a large number of experiments have been conducted on wakes, jets, and mixing layers in order to study the turbulent free shear layers. Among the axisymmetric free shear flows, the turbulent wakes have been investigated since Hall and Hislop's experiment on the wake of a circular body (Hall and Hislop, 1938). Recent measurements include the wake of a sphere by Uberoi and Freymuth (1970), the wake of a circular disk (Carmody 1964, Oswald and Kibens 1971) and the wake of a spheroid by Chevray (1968). The axisymmetric turbulent jet has also received many experimental investigations since the early experiment of Kuethe (1935), including the recent extensive measurement by Wygnanski and Fiedler (1969).

In addition to the submerged jets, the axisymmetric jet with a co-flowing secondary stream have received a fair amount of investigations with the applications toward the combustion and jet pumps. The earliest experiment was reported by Viktorin (1941) and more recent investigations include a work by Fejer et al. (1967) covering the various jet velocity to secondary stream velocity ratios. These experiments on the co-flowing jet were conducted with tapered nozzle geometry to eliminate the boundary layer outside the nozzle wall. Questions on the turbulent flows in these conventional free shear layers have not yet been exhausted and await further investigation. A somewhat extensive bibliography on these free shear flows is found in a report by Harsha (1971).

However, it was not until recently that people became interested in the cases where both jet and wake are present. It is well known that, at large distance from the source or the body, the flow is characterized by the momentum flux of the jet or the drag acting on the body. Therefore, among the mixed wakes with an interaction between jet and wake, of particular interest is the case in which the strength of the jet is adjusted to cancel exactly the drag of the body, thus producing a zero momentum defect in the wake. This situation can be found in the wake behind self-propelled bodies, for example behind submarines or torpedoes.

A few investigations have been carried out previously. Naudascher and his students (Ridjanovic 1963, Wang 1965, Naudascher 1965) were the first to investigate this type of flow experimentally. They placed a circular disk and injected a jet on the axis to match the momentum. Exit velocity of the jet was $U_j \cong 3.64\ U_\infty$, and the diameter ratio between the disk and the jet was 4.12. Reynolds number based on the disk diameter was 55,000. This measurement of the mean velocity extends up to 25 diameters and the measurement of the fluctuation quantities extends to $X/D = 130$. The self-preserving nature was observed both in mean flow and the fluctuation quantities.

Another group, Ginevskii et al. (1966, 1972), similarly measured a momentumless wake produced by a circular ring and the jet on the axis inside the free jet. The velocity ratio between the free stream and the jet was $U_J/U_\infty = 3.85$. Their mean flow and correlation measurements extend up to 40 diameters downstream.

More recent investigations are somewhat applied in their nature. Gran (1973) investigated the turbulent wake of a propeller-driven slender body. He eliminated the possible disturbance due to the model support by using the vertical wind tunnel and suspending the model from above. Reynolds number based on the model diameter was 63,000. The swirl velocity produced by a propeller rotating at 67,000 rpm was of the same order of magnitude as the axial velocity difference. His measurements extend to $X/D = 15 \sim 20$, but unfortunately the wake was not axially symmetric.

Schetz and his co-workers (1975), Swanson et al. (1974), Chieng et al. (1974) conducted experiments at a higher Reynolds number, $Re_D = 618,000$. One of the models was a propeller-driven slender body which was similar to Gran's but had a larger propeller, rotating at about 12,000 rpm. The initial mean velocity profile has an annular jet off the centerline and the velocity defect near the edge. At the last two stations ($X/D = 20, 40$) the velocity profile relaxes into a nearly Gaussian profile with velocity defect in the wake. Schetz et al. also tested a jet-driven slender body. The afterbody had a center-body with an annular jet. Exit velocity of the jet was about 1.14 times the free stream velocity due to the large jet diameter in comparison to other jet driven bodies. The initial mean velocity profile exhibited two wake regions, one from the center body and another from the boundary layer of the main body. At the

last three stations, from X/D = 10 to X/D = 40, the velocity profile relaxes into a profile with the excess velocity near the centerline and the velocity defect toward the edge as seen in Naudascher's result.

Some other investigations in water are reported to be underway including the stratification effect. However, the results are not available in the open literature.

In order to summarize the data currently available, the axial variation of the maximum velocity differences measured in the aforementioned experiments are plotted in Fig. 1. It should be mentioned, however, that the maximum velocity was literally taken even when the velocity profile lacked the self-preserving nature in certain cases. Naudascher's results seem to exhibit an asymptotic behavior. Ginevskii et al.'s data of axial length scale are normalized by the jet diameter since the ring diameter is not mentioned in their papers. With the drag coefficient of the ring estimated from Naudascher's experiment, the ring diameter was estimated from the given jet velocity ratio to be about 4.4 times the jet diameter. When this is taken for a normalization, their data points fall among other data groups. Slow relaxation to the final decay in Schetz et al.'s data is due to the complex initial condition. Their results on the propeller driven body show a different trend and appear to be approaching a line $x^{-2/3}$. The line with a slope of $x^{-4/5}$ is the result of the constant eddy viscosity model and will be discussed shortly. Similar plotting was made to compare

the maximum turbulence level, but no unified view can be achieved on the turbulence decay law. In short, some of the data available suffered from too complex initial conditions and the most data available do not extend far enough from the body to conclude the asymptotic behavior of the wake. The results by Naudascher will be compared with the present results.

On the analytical side, Birkhoff and Zarantonello reported the dimensional analysis of a momentumless wake (Birkhoff and Zarantonello, 1957). Also a similar argument is presented by Tennekes and Lumley (1972). Here a more inclusive analysis was carried out and is given in the appendix. As is discussed in the appendix, for the pure wake or jet, the exponent for the centerline velocity decay rate and the spreading rate are determined from the condition of constant momentum flux in the flow

$$\text{Axisymmetric Wake} \quad \Delta u_{\mathcal{L}} \sim x^{-2/3}, \; r_o \sim x^{1/3}$$
$$\text{Axisymmetric Jet} \quad \Delta u_{\mathcal{L}} \sim x^{-1}, \; r_o \sim x,$$

while these exponents become indeterminate for zero momentum wake. When the viscosity coefficient is constant across the flow as in laminar flows or in the constant eddy-viscosity model for turbulent flow, the constancy of moment of momentum equation can be integrated to render a needed condition. (When the mixing length theory is applied, the wake had to be numerically integrated and the exponents were obtained in order to satisfy the boundary conditions.) The constant eddy viscosity hypothesis gives $\Delta u_{\mathcal{L}} \sim x^{-4/5}$, $r_o \sim x^{-1/5}$. The former result is included in Fig. 1. The calculation with Prandtl's hypothesis and the mixing length theory show a very poor agreement with the existing experimental data.

The asymptotic expansion for the laminar wake and the turbulent wake with the Prandtl's hypothesis on eddy viscosity were obtained and the results indicate that, when there is a non-zero momentum term, the lower order term representing the pure wake or the jets will eventually mask the zero momentum term at large distances downstream. This mixed wake is discussed in Tennekes and Lumley but their Gram-Charlier expansion does not agree with the present one. The reason is that they expanded only the mean velocity terms while they assumed the single wake spreading rate and the single eddy viscosity term, both of which should also be expanded. The analysis is presented in Appendix A-1.

Other types of turbulent models have been applied previously. Prandtl-Kolomogoroff's model $\varepsilon \sim \sqrt{q^2}\,\Lambda$ was applied by Gran (1973). The result showed fairly good agreement with his result but not with Naudascher's. Bradshaw's turbulent kinetic energy model $\tau \sim a\,\overline{q^2}$ was applied by Swanson, Schetz et al. using their data as the initial condition for numerical integrations. Agreements are fairly good if not excellent. Finally, second-order closure model by Donaldson was applied to the Naudascher's experiment (Lewellen et al. 1973). Centerline velocity decay was predicted considerably slower than the experimental results.

Most recently Finson (1975), noting the reduction of turbulent energy production in momentumless wakes, deleted the production term from the energy equation while retaining it in the shear stress equation. Taking the constants from the experiments on homogeneous grid turbulence, he obtained a decay law close to the Naudascher's

experimental results.

The above being the current knowledge on the problem, the following questions have not been answered:

(1) Does momentumless wake behave in a singular manner? What is the behavior of the wake if the jet or the propulsion is not quite matched with the drag, either a little too strong or a little too weak?

(2) What is the asymptotic behavior of a momentumless wake? Why does the simple modeling of turbulence, such as the eddy viscosity model or the mixing length theory apparently fail completely while it describes fairly well the turbulent shear flow such as jets or wakes?

In order to answer these questions, the experimental investigation was proposed. (The second point above was touched by Finson's analysis, but an experimental verification was still desired.)

Objectives of the present investigation are stated as follows:

(1) To cover the far wake region as well as the proximity of the body in order to examine if the self-preserving wake exists and check the asymptotic behavior.

(2) To make the model and the initial conditions as simple and well-defined as possible.

(3) To study the effect of the initial condition. Since the data with disk as a turbulence generator are available, other configurations should be tried.

(4) To investigate the behavior of the wake for the slightly unmatched conditions in addition to the matched condition, i.e. zero momentum wake.

(5) To compare with the pure wake and the jet flow in order to obtain a more unified view of turbulent shear flow in general.

# CHAPTER II

# EXPERIMENTAL SETUP

## 2.1. Wind Tunnel

The present investigation on a far wake requires a sufficiently long test section with uniform free stream velocity and a low turbulence level. Also, it was necessary to support the model and to deliver the propulsive momentum, in the present case, a jet, into the model without leaving undesirable disturbances in the flow. With these considerations, a low turbulence subsonic wind tunnel at JPL was chosen. The tunnel is of the open return circuit type and has an easily accessible settling chamber. The setup is shown in Fig. 2.

The fan upstream is driven by a 25 HP AC induction motor through a magnetic clutch, and the speed of the fan is controlled by the amount of the slippage determined by the main magnetic field and the induced eddy-current field. The fan has variable pitch blades which are set to achieve maximum velocity without causing stall.

Driven air goes through two layers of 10 mesh screens in the flow straightener section and ten layers of 40 mesh screens in the diffuser section and in the settling chamber to achieve a low turbulence level in the test section. Immediately downstream of the vertical strut, which is used to supply air into the base of the model, another fine mesh screen is placed to minimize the disturbance. Measurements on the free stream turbulence level and on the effect of the vertical strut are discussed in section 3.4.

The settling chamber has a cross section of 6' x 6' and provides a 9-to-1 contraction ratio with respect to the test section. In

addition to the screens, the settling chamber has an acoustically treated section with folded fiberglass sheets to suppress the fan noise propagating into the test section designed for experiments on acoustics.

The test section measures 2' x 2' in the cross section and 10' in length. The front panel is made of Plexiglas for optical observation, and the bottom wall is hinged at the upstream end and is adjustable to compensate the boundary layer growth on the walls to achieve a constant pressure. A major part of the experiment is done under the condition of the fully engaged magnetic clutch which gives a steady nominal freestream velocity of 16.2 m/sec.

The room was air conditioned and enough warmup time is allowed after starting the tunnel to attain stationary conditions. The ambient temperature and pressure are monitored with accuracy of 0.1$^{o}$C and 0.2 mb respectively throughout the experiment. The variation of ambient temperature during the experiments was less than 1$^{o}$C.

A traverse mechanism fabricated for the present experiment slides on a rail on top of the test section. It can be positioned continuously over the entire range of the axial stations. The vertical arm of the traverse protrudes through the $\frac{1}{2}$" wide slit on the top wall along the rail. Vertical motion is provided by a variable speed 1/60 HP DC motor through a threaded rod. The horizontal arm of the traverse is attached at the bottom of the vertical arm. A miniature DC motor drives a pulley and cable mechanism housed in the horizontal arm to traverse a probe holder. Friction of the horizontal motion was minimized with the use of linear bearings. The probes are mounted far enough upstream to eliminate interference with the traverse

mechanism yet without permitting vibration of the probe. The vertical and horizontal positions are calibrated and read by the outputs from the potentiometers with 0.1% linearity which gives the reading of transverse positions within 0.005" accuracy.

2.2. Models

A model simulating a self-propelled body is made of a 1" dia. thin wall (.028") aluminum tubing supported from the settling section. The model tube is 48 1/8" long, a 12" length of which is in the test section. The model slips into a $4\frac{1}{2}$" long tapered section. Four .006" diameter music wires are attached to the tapered section from the contraction section walls and are used to adjust the orientation of the model. One pair of these wires is placed with forward inclination and the other pair with backward inclination to take up the axial force on the model. Upstream of this transition section is a 1.5" dia., .035" wall aluminum tube with 44" length. This tube is screwed into a base element which sandwiches a 36x40 mesh screen for its support. Supply air comes into this base element from the bottom and top of the wind tunnel through a $\frac{1}{2}$" tubing with airfoil section fairing around it.

In order to produce a turbulent boundary layer on the model, the boundary layer is tripped by placing a 3/32" wall O-ring at 31" from the downstream end of the tube model. With freestream velocity 16.2 m/sec, the Reynolds number based on tube diameter is 27,300. Figure 3 shows a definition sketch of the smooth wall case and gives the nomenclature used in the present investigation.

The last part of the model tube slides out and can be replaced by a rough wall model. The rough wall model is made of the same

1" tube with a roughness element slid onto it. The roughness element was machined from a solid aluminum rod to form 25 axi-symmetric square elements, each of which measures 3/32" both in height and width and is placed at 3/8" intervals. (See Fig. 4).

The boundary layer profiles on the smooth wall and the rough wall models are discussed in Chapter IV.

2.3. Air Supply System

A controlled amount of air is injected at the end of the model parallel to the freestream to balance the drag of the body. House air with a supply pressure of approximately 95 psig is introduced into the air supply control system described in Fig. 5.

Steady airflow is maintained by regulating the pressure upstream of an orifice plate. The stagnation pressure and temperature upstream of the orifice plate are monitored by a Bourdon pressure gauge and a thermistor probe. Two orifice plates were machined to form convergent-divergent nozzles with throat area openings measuring 0.125" and 0.136" in diameter. The smaller orifice is used for the smooth wall experiment and the other one for the rough wall experiment. A large enough pressure difference between the upstream and downstream of the orifice is provided to keep the choked condition at the throat.

The mass flow is calculated by the following relationship

$$\dot{m} = \rho^* a^* A^* = \sqrt{\frac{\gamma}{R}} \frac{p^*}{\sqrt{T^*}} A^* = \left(\frac{2}{\gamma+1}\right)^{\frac{1}{2}\frac{\gamma+1}{\gamma-1}} \sqrt{\frac{\gamma}{R}} \frac{p_t}{\sqrt{T_t}} A^* \quad (1)$$

where $A^*$ is the minimum area at the throat; $P_t$ and $T_t$ are the stagnation pressure and temperature respectively. Since the air supply line

has a large area in contact with the room air, and the temperature difference at the end of the model is found to be small, no air heater is necessary to reduce the temperature difference in the freestream and in the jet.

# CHAPTER III

# INSTRUMENTATION

## 3.1. Data Acquisition

Outputs from the instruments were read by two Keithley Model 160 Digital Voltmeters and their Binary Coded Decimal outputs were interfaced into Interdata Model 70 Mini-Computer for an on-line data processing. The system included a central processor unit with 32K bytes core memory, dual cassette tape drive, line printer, x-y recorder and A-D, D-A converters. Keithley DVM digitized data every half second and the mean and variation were computed from data sampled for 10 ~ 20 seconds.

The accuracy of measurements on mean velocity, mean static pressure and velocity fluctuations is discussed in detail in Appendix B. In summary, as for the mean velocity, an instrumental error is within 0.05%, the effect of the temperature variation in the wake is within 0.2% and the effect of turbulence is 1.45% in the near wake and 0.01% at far downstream.

As for the static pressure, the instrument is accurate within $\delta C_p \sim 2 \times 10^{-4}$, where $C_p$ is normalized by the free stream dynamic pressure, but nonsteadiness and nonuniformity at static pressure in the wind tunnel caused an inaccuracy of about $\delta C_p \sim 0.6 \times 10^{-3} \sim 1 \times 10^{-3}$. Presence of turbulence in the wake may cause up to $\delta C_p \sim 1.4 \times 10^{-2}$ at the highest turbulence intensity observed and $\delta C_p \sim 1 \times 10^{-3}$ at the 40 diameter station and downstream in the wake.

As for the turbulence intensity measurements, the calibration procedure for the hot-wire anemometer system is estimated to be

accurate within 2% if the dynamic calibration is assumed to be identical to the static calibration. The effect of temperature variation is within 0.7%.

Instrumentation for intermittency measurement, power spectra, x-wire measurement and the flow visualization will be discussed at each section together with the results.

3.2. Mean Velocity and Mean Static Pressure Measurements

A Pitot-static probe fabricated for this experiment is shown in Fig. 6. The length of the supporting tube was required to avoid the interference with the presence of the traverse system downstream.

The tygon tubing leading to the pressure sensor was kept as short as possible and also was kept from vibration to avoid the unnecessary time lag and fluctuation on readings. A Barocel Type 538-10 Pressure Sensor (10 mm Hg max) and Datametrix Type 1014A Electronic Manometer were used for all the pressure measurements except the absolute room pressure which was measured by a Bendix Aviation Type 172 Aneroid Barometer. The accuracy of the aneroid barometer was checked with a mercury tube, and they agreed within 0.1%. The calibration constant supplied by the manufacturer for the Barocel Pressure Sensor was checked by a precision U-tube manometer, measuring the pressure drop produced by the laminar flow meter at different flow rates of air.

Density of the air was computed from the ambient pressure and temperature at the time. For the static pressure measurement,

the room pressure was taken as a reference pressure. The time lag between the probe and the sensor was equalized by connecting on the reference pressure side the tygon tube of the same length as on the probe side with a small opening at the end in order to minimize the effect of the room pressure changes. The remaining high-frequency fluctuation in output was removed electronically by passing the output from the electronic manometer into a 10 Hz low-pass RC filter before it is read by the data acquisition system.

3.3. Velocity Fluctuation Measurements

Turbulent quantities were measured by means of a DISA Type 55A01 constant temperature anemometer. A major part of the measurements was done in combination with a DISA type 55D10 Linearizer. The hot wire probe used for the axial velocity fluctuation measurement was platinum wire 0.00254 mm in diameter with aspect ratio 400. The wire was annealed before usage to relieve the thermal stress which causes calibration drift. An overheat ratio of 1.5 was chosen. The exponent in the King's law was determined from the calibration, and the setting of the linearizer was adjusted. A typical calibration curve of the hot wire output with the linearizer is shown in Fig. 7. The program for data acquisition takes the free stream velocity data and resets the slope of the linearizer output each time before the wake survey to compensate for a possible drift. Frequency response of the system was checked by the square wave test, and the upper limit of frequency response was 16 kHz. A 10 kHz low-pass filter was used to eliminate the electronic noise at high

frequencies. DC fluctuation was eliminated by the 5Hz high-pass filter. The DC output of the bridge voltage was read by a DVM. The fluctuation voltage was fed into a DISA Model 55D35 RMS voltmeter. Analog output proportional to the mean square value of the input was measured by DVM.

Calibration of the RMS meter was carried out with a sine wave produced by a Wavetek Model 164 sweep generator and with a Fluke 8375A Digital Multimeter. A satisfactory result was obtained except in the lowest end, 5 to 10% of full scale, where a slight non-linearity was observed. Therefore, the appropriate range was set so that measurements could be made at the upper portion of the scale.

### 3.4. Free Stream Conditions

#### 3.4.1. Mean Velocity and Mean Static Pressure in Free Stream

As stated earlier, enough warmup time was allowed for the temperature to obtain its equilibrium value, then the measurements were started. Also a major part of the experiments was conducted with fully engaged magnetic clutch between the motor and the fan. Fan speed was constant within less than 10 RPM at 1300 RPM when measured by Strobotak. Temperature variation was kept within $1^{o}$ after warmup time. The ambient pressure was constant during the run within 0.4 mm Hg.

The bottom wall of the wind tunnel was adjusted until the minimum variation in the free stream static pressure was obtained. The results of the mean static pressure in the free stream are presented in Fig. 8. These are plotted in terms of deviation from the

average value. The station X = 0 corresponds to the trailing edge of the model. The flow was sensitive to the local slope of the wall. The bottom wall consisted of three parts, and here the first and last elements are seen causing the variation from the mean at $X/D < 10$ and $X/D > 65$. Also at the farthest downstream point, the end effect due to the absence of the diffuser downstream from the test section also was responsible for the variation in mean static pressure. Nevertheless, the maximum difference in static pressure for an entire length of the test section was within 1% of the free stream dynamic pressure. The variation in the transverse direction in the free stream was within 0.2% of the dynamic pressure.

The effect of the longitudinal pressure gradient on the behavior of the wake takes place in the following manner: The longitudinal pressure gradient affects $\partial u/\partial x$ and then affects $\partial u/\partial r$. The change in $\partial u/\partial r$ will affect the production of turbulent energy. Changes of the turbulent energy and the shear stress in turn change the mean velocity profile. To estimate the degree of influence by the present pressure gradient is not trivial due to the indirect process involved as shown above; but interpolating the experimental results by Gartshore (1967) in adverse pressure gradients and by Narasimha and Prabhu (1972) under an impulsive pressure gradient, a pressure gradient of as much as 1% of the dynamic pressure may be considered to give no significant influence on the wake. To double check the measurement above, the mean velocity profile in the test section was also measured. The variation in the entire test section is within

0.1 m/sec at the nominal velocity 16.20 m/sec (0.6% variation).

3.4.2. Free Stream Turbulence Level and the Wake of a Vertical Strut

When the bridge output from the hot wire anemometer is contaminated by the electronic noise of the system, the signal may be sorted out as follows, provided the signal and the noise are not correlated:

Since

$$\overline{e'^2_{total}} = \overline{(e'_{signal} + e'_{noise})^2} \simeq \overline{e'^2_{signal}} + \overline{e'^2_{noise}}$$

we get

$$\overline{(e'^2_{signal})}^{\frac{1}{2}} = (\overline{e'^2_{total}} - \overline{e'^2_{noise}})^{\frac{1}{2}} .$$

However, when the level of the noise is not small, it is important to make an accurate estimate of its magnitude. The electronic noise with a probe in no flow condition is not necessarily the noise with flow because of the large difference in the DC component of the output between zero velocity and the test condition. The method mentioned by Demin et al. (1973) was utilized here. To simulate an operating condition, the same amount of heat transfer from the wire should be made as in the case of a forced convection. This was realized by heat conduction from a hot wire placed in liquid nitrogen. For a maximum conduction, the hot wire was placed in a test tube and then the gap was filled with 0.3μ fine carborundum powder. Decrease of the noise level with the increase of the bridge DC voltage was observed. The noise level of the system at the operating DC bridge output was 0.33 mV, compared with 0.44 mV from a hot wire placed in a wind tunnel without flow. Using this value, the free-

stream turbulence level was found to be 0.11%. The value 0.083% by Sigal (1971) apparently comes from an inaccurate treatment of the noise level. In order to study the effect of the vertical strut used for the air supply line, a horizontal traverse of a hot wire probe was made in the free stream across the wake of the strut. The turbulence profile in the strut wake was not clearly discernible, since it was buried in the freestream turbulence level and the electronic noise. However, both at X/D = 10 and 75 the profiles have a Gaussian shape of about 3/4" width, and the maximum RMS axial velocity fluctuation is found to be approximately 0.13%, including the freestream turbulence level. Only a slight variation of this turbulence level in the axial direction was noticed. When a $\frac{1}{2}$" circular tube was placed in the settling chamber as a preliminary study the maximum turbulence level in the test section was as high as 0.4%. The effect of the airfoil shape fairing and the damping effect of a fine screen downstream were proved. A traverse was made to study the effect of 0.006" supporting wires in the contraction section, but with the present system no wake was detected in the test section.

3.4.3. Temperature Variation in the Wake

A temperature survey was made to examine the effect of the temperature difference between the freestream and the jet since no cooling or heating was provided for the air supply. Temperature was measured with a probe equipped with a Fenwell G-320 bead type thermistor which was calibrated in water with a mercury thermometer. The jet was found to be cooler than the freestream, and the wake had Gaussian temperature profiles at each station. The axial variation of the centerline temperature defect is plotted in Fig. 9.

Fluctuations in the data are shown by the error bars.

Except for the initial and the final data points, the data follow the slope $x^{-0.8}$. Because of the response time of the thermistor and of non-stationary free stream temperature, these data are meant to be for reference only, but they follow the same power law as observed in the wake behind a heated sphere (Gibson et al. 1968). The maximum temperature difference between the centerline and the edge of the wake was about $1^{\circ}C$ at $x/D = 5$ and was $0.2^{\circ}C$ at $x/D = 70$. As shown in Appendix B, the effects of this magnitude of temperature difference on the total pressure, static pressure and hot-wire measurements are negligible. A Richardson number at $X/D = 5$ based on the radial velocity gradient was estimated to be

$$R_i = \frac{g}{T_r}\frac{\partial T}{\partial r}\Big/\left(\frac{\partial U}{\partial r}\right)^2 \sim \frac{g}{\Delta T}\frac{\Delta T_{\mathbb{C}}}{r_o}\Big/\left(\frac{\Delta u_{\mathbb{C}}}{r_o}\right) \sim 3.15\times10^{-3},$$

and the buoyancy effect was judged to be negligible.

3.4.4. Steadiness of the Air Injection

The steadiness of the jet was not directly monitored and the variation was not noticeable in the course of the experiment but it can be estimated as follows.

Since the strength of the jet is governed by Eq. (1), we get

$$\dot{m} = \rho U \sim P_t/T_t^{\frac{1}{2}}$$

$$\therefore \quad U \sim \frac{T}{P}\frac{P_t}{T_t^{\frac{1}{2}}} = \frac{T}{P}\frac{(P_r+P)^{\frac{1}{2}}}{T_t^{\frac{1}{2}}},$$

where $P_r = P_t - P$ and is kept constant by the regulator.

Hence

$$U \sim \frac{T}{T_t^{\frac{1}{2}}} \left( \frac{P_r}{P} + 1 \right)$$

$$\frac{\delta(U)}{U} \sim \frac{\delta(T)}{T} + \frac{\delta\left( \frac{P_r}{P} + 1 \right)}{\frac{P_r}{P} + 1} + \frac{1}{2} \frac{\delta(T_t)}{T_t}$$

$$\therefore \quad \left| \frac{\delta(U)}{U} \right| \sim \left| \frac{\delta(T)}{T} \right| + \left| \frac{\delta(P)/P}{1+P_r/P} \right| + \frac{\left| \delta(P_r)/P \right|}{\left| 1+P_r/P \right|}$$

Here ambient pressure was constant within $\pm$ 2 mb $\sim \pm 0.003$ psi and the temperature variation was within $\pm$ 0.5°C. The pressure regulator kept $P_r$ within 0.1 psi. Therefore, the variation of the jet speed was estimated to be

$$\frac{\delta u_{jet}}{u_{jet}} \sim 0.9\%$$

3.4.5. Axisymmetry of the Wake

A considerable amount of time and effort were spent in order to establish the axisymmetry of the flow both in the mean flow quantities and the fluctuation quantity. First the direction of the jet had to be adjusted to become in alignment with the wake of the body, and secondly the boundary layer on the model tube was required to be symmetric around the tube. With nonsymmetric boundary layer, a thinner boundary layer produced a higher turbulence intensity because of the higher velocity shear. On the other hand, the shear flow between the misaligned jet and the boundary layer produced an opposite asymmetry in turbulence intensity. When the jet was in a crosswind with respect to the free stream, the higher turbulence intensity occurred on the leeside of the cross flow.

Alignment of the model was mainly made by adjusting the tension of each of the 4 x 0.006" music wires attached to the taper

section of the tube in the contraction section (see Fig. 2). Also it was necessary to re-align the test section itself to ensure the parallel free stream with respect to the model, which was supported at the settling chamber and the contraction section independent of the test section. The bending of the model by gravitational force was not detected in the measurements.

Horizontal and vertical traverse of the wake were made at several axial stations, and the contour mapping of mean velocity and fluctuation were taken at chosen stations. The results exhibited a satisfactory symmetry as shown by the comparison between the horizontal and the vertical traverse at X/D = 1 in Figs. 10 and 11 and by the contour mapping of the mean velocity at X/D = 40 presented in Fig. 12.

The single element hot wire was rotated by 90° on its axis and the mean velocity profiles were compared between these two probe orientations. No change was noticeable, and it was judged that the flowfield is free from the swirling motion.

3.5. Momentum Balance in the Wake and Adjustment of the Jet

When the flow is axisymmetric and has no swirl, the momentum integral equation in the axial direction is given by

$$\frac{d}{dx}\int_0^\infty u(u-u_e)rdr+\frac{du_e}{dx}\int_0^\infty (u-u_e)rdr+\frac{d}{dx}\int_0^\infty \frac{P-P_e}{\rho}rdr+\frac{d}{dx}\int_0^\infty \overline{u'^2}\,rdr=0 \qquad (2)$$

If there is no pressure gradient in the free stream ($du_e/dx$), the above equation can be integrated and the momentum flux in the flow is given by

$$M = 2\pi \left\{ \int_0^\infty u(u-U_\infty)rdr + \int_0^\infty \frac{P-P_\infty}{\rho} rdr + \int_0^\infty (\overline{u'^2} - \overline{u'^2_\infty})rdr \right\} = \text{const.}$$

where $U_\infty = u_e = \text{const}$, $p_\infty \equiv p_e = \text{const.}$

If the momentum coefficient is defined by

$$C_m = \frac{M}{\frac{1}{2}\rho U_\infty^2 \pi(D^2/4)} ,$$

where D is a body diameter, the non-dimensional momentum integral in the flow is given by

$$C_m = 16 \left\{ \int_0^\infty \frac{u}{U_\infty}\left(\frac{u}{U_\infty} - 1\right)\frac{r}{D}\frac{dr}{D} + \int_0^\infty \frac{P-P_\infty}{\rho U_\infty^2}\frac{r}{D}\frac{dr}{D} + \int_0^\infty \left(\frac{\overline{u'^2}}{U_\infty^2} - \frac{\overline{u'^2}}{U_\infty^2}\right)\frac{r}{D}\frac{dr}{D} \right\}. \quad (3)$$

A survey of the wake was conducted with the online data processing system, and the data of the mean velocity, mean static pressure and the velocity fluctuations were numerically integrated according to each term in Eq. (3). Then the strength of the jet was changed, and the momentum integral in the wake was computed. This process was repeated until a condition with virtually zero momentum defect was obtained. In the present study, this is designated as the matched injection case.

The axial variation of the total momentum integral in the matched injection case is presented in Fig. 13 together with individual contributions from the mean velocity, mean static pressure and the axial velocity fluctuation.

At X/D = 5, the velocity integral and the static pressure integral are slightly off the trend. It is believed that the cause is

that the integrations were not carried out far enough into the free-stream. Except for this station, the overall variation in momentum is within 1% of the drag of the model itself, and this was judged to be satisfactory.*

The momentum fluxes in the wake at various injection rates were obtained in a similar way and their axial variations were checked for a consistency of the data. The momentum integral thus obtained will be discussed together with the presentation of each result.

---

* In the propeller driven body reported by Chieng et al. (1974), their calculation showed a large positive contribution from the static pressure integral, whereas they showed that the pressure is lower in the wake than at the edge, and this may have caused a slower decay of the centerline velocity (cf. Fig. 1).

# CHAPTER IV

# RESULTS

## 4.1. Mean Velocity Profiles in Boundary Layers and Jet

### 4.1.1. Turbulent Boundary Layers on the Models

Both the smooth wall model and the rough wall model were tested, and the velocity profiles of the turbulent boundary layer on these models were measured by a Pitot-static probe traversed immediately downstream of the model trailing edge ($X/D \sim 0.01$). A jet injection from the model kept the separation streamline closely parallel to the model axis. Mean velocity profiles on the smooth wall and on the rough wall are shown in Fig. 14. Owing to the satisfactory axi-symmetry of the boundary layer, results in one radial direction are presented. The boundary layer thickness, displacement thickness and momentum thickness for each model are tabulated in the figure. A significant effect of the boundary layer thickness due to the rough wall is noticed.

The friction velocity for each case was determined by fitting the universal velocity defect law,

$$\frac{u_\infty - u}{u_\tau} = -\frac{1}{\kappa} \ell n \frac{y}{\delta} + \frac{2\pi}{\kappa}, \quad \kappa = 0.41$$

to the measured profile.

The value of $\pi$ was chosen in conjunction with the law of the wall and was set to be 0.35. This is considerably lower than the value for the flat plate boundary layer at the same value of $Re_\theta$, which was 0.62 for $Re_\theta = 14,000$ (Coles 1968), and this was mainly attributed to the effect of the curvature. Fig. 15 shows the velocity profiles in terms

of the velocity defect law and Fig. 16 shows the law of the wall. Except for the value of $\pi$, the effect of the curvature of the model is negligible with these small boundary layer thicknesses. According to the results by Willmarth et al. (1975) the boundary layer thickness was more than 9 times the model diameter before the departure from the law of the wall profile for the flat plate became prominent.

For the rough wall model, the equivalent sand grain roughness was found to be $k_s = 0.285$, which is about 3 times the roughness height, and it compared well with the empirical law for the completely rough wall by Nikuradse (Schlichting 1968). For the roughness element other than sand grain roughness, Dvorak (1969) proposed an empirical formula for the wall profile with zero pressure gradient. For a roughness density $\lambda < 4.68$, we have

$$\frac{u}{u_\tau} = \frac{1}{\kappa} \ell n \frac{y u_\tau}{\nu} + C - \frac{\Delta u_1}{u_\tau}$$

where

$$\frac{\Delta u_1}{u_\tau} = \frac{1}{\kappa} \ell n \frac{u_\tau k}{\nu} + 17.35(1.625 \log \lambda - 1)$$

and k is a physical roughness height. Fig. 16 shows the present result, and it compares well with the empirical law above for given $k = 3/32''$ and $\lambda = 4$.

4.1.2. Mean Exit Velocity Profile of Jet

The mean velocity profile of the jet is presented in Fig. 17. A measurement was taken immediately downstream of the trailing edge of the model tube. Fig. 18 shows the profile in terms of the velocity defect law and is compared with the formula for the equilibrium pipe flow (Hinze 1959)

$$\frac{u_{\mathcal{L}} - u}{u_2} = -\frac{1}{\kappa} \ell n \frac{r}{R} + 0.8$$

The velocity profile in the law of the wall coordinate is plotted in Fig. 19 and is compared with the law of the wall with $\kappa = 0.41$ and $C = 5.0$.

4.2. Pure Wake

As a basis for subsequent experiments, the wake of a smooth wall model tube with no injection was first investigated. The mean velocity, the mean static pressure and the axial velocity fluctuation were integrated across the wake, and the resulting momentum integral at several axial stations is plotted in Fig. 20. The contributions from the pressure and the velocity fluctuation are negligible compared to the velocity defect in the wake. The measured momentum flux is reasonably constant along the wake, and the drag coefficient of the body is found to be $C_D \sim 0.68$.

This rather high value for a slender body is partially due to a thick axisymmetric turbulent boundary layer starting to develop from the upstream section and partially to a low base pressure. The momentum thickness of the boundary layer was $\theta = 0.0538''$ as stated, and the base pressure coefficient $C_{P_B} = \frac{p_{s\,base} - p_{s\infty}}{\frac{1}{2} \rho U_\infty^2}$ was measured to be $-0.110$. The drag coefficient estimated from these values are close to the drag coefficient obtained from the wake momentum defect, which proves the consistency in measurements.

The mean velocity profiles covering from X/D = 5 to X/D = 89 are shown in Fig. 21. If the centerline velocity defect and the radius, $r_o$, which is defined where the turbulence intensity is half the maximum

value, are taken as the velocity scale and the length scale respectively, the normalized velocity profiles at various axial stations collapse into a typical Gaussian-like profile as shown in Fig. 22.*

The RMS axial velocity fluctuations are shown in Fig. 23. Slight asymmetry in profiles are caused by an imperfect alignment for this run, but the magnitude of the asymmetry was tolerated as insignificant. In the following presentations of turbulent intensities, the free stream turbulence level is removed from the signals.

The normalized turbulence intensity profiles are plotted in Fig. 24. Immediately noticeable is the overall self-preservation in profiles. With a closer look, initial twin peak profiles at X/D = 5 and 10 are seen relaxing into the flat top bell-shaped profile. This makes an interesting comparison with the wake of a sphere measured by Uberoi and Freymuth (1970). They observed a self-similar profile from X/D = 50 to X/D = 150, and the shape of the profile remains to have a distinct twin peak. The wake behind a slender body (Chevray 1968) exhibited a similar relaxation process toward the flat top profile as in the present study, even though Chevray's measurements did not go far enough to give evidence on the far wake. The difference from Uberoi and Freymuth's result is considered to be due to the persistence of the turbulent structure based on the large scale vortex shedding from a bluff body. The structure in the far wake, which is traceable to the initial vortex shedding, was observed by Oswald and Kibens (1971) in the wake behind a disk.

---

* A label $u_d$ used in the figure is interchangeable with a symbol $\Delta u$, i.e, $u_d \equiv \Delta u = u - u_\infty$.

The decay of centerline velocity defect and the maximum turbulence intensity decay are plotted in Figs. 41 and 42, and the decay laws are compared with the established law $\sim x^{-2/3}$ in Fig. 25.

The virtual origins for the similar velocity profile and the velocity fluctuation profile are obtained as is shown. They do not exactly agree, partly due to the fact that the measurement has not extended far enough downstream.

The balance between the mean flow quantities and the fluctuation quantities is discussed later.

4.3. Matched Injection - Smooth Wall

The mean velocity profiles in the wake are presented in Fig. 26a for X/D = 5 to 40 and in Fig. 26b for X/D = 40 to 89. A very rapid decay of the centerline velocity is noticed. This centerline velocity is plotted against the streamline station in Fig. 41. The failure of the decay law prediction by Prandtl's eddy viscosity model or by the mixing length theory (see Appendix A) is clearly seen. In Fig. 52 the decay law by Prandtl's eddy viscosity model is compared with the experimental data.

The velocity profiles are normalized by the centerline velocity difference and the wake width $r_o$, and the results of the normalized profiles are shown in Fig. 27. Stations from X/D = 5 to X/D = 20 have slowly varying profiles near the edges, but at X/D = 30 and downstream a fairly good self-similar nature in the profile is noticeable. Some scatter in the data, particularly at X/D = 89, is within the estimated error of the measurement.

It should be mentioned that at X/D = 75 and 89, approximately 0.1% of difference in the free stream velocity was measured between one edge of the wake and another edge, and that the velocity difference was computed subtracting the velocity obtained by linearly interpolating between two edge values from the measured velocity within the wake.

The shape of the self-preserving profile is comparable to the eigenfunction obtained from the simple turbulence modelings such as the eddy viscosity model presented in Appendix A. (See Figs. 88 and 90).

Naudascher's experimental results (Naudascher 1965) show an existence of a self-similar velocity profile among four stations from X/D = 10 to 25, and his profile compares well with the present result. Ridjanovic (1963) reported the results farther downstream which depart from the self-similar profile, and at X/D = 50 the centerline velocity becomes negative. However, as pointed out by Naudascher, Ridjanovic's last two measurements are of the same order as the experimental error. Since the present results also demonstrated the presence of a self-similar profile as far downstream as possible with reasonable accuracy, it can be concluded that the self-similar velocity profile exists in a matched injection wake extending farthest downstream until the velocity profile becomes indistinguishable from that of a uniform stream.

Results of the axial turbulence intensities are shown in Fig. 28 and in Fig. 29, the latter in normalized coordinate systems. Overall similarity appears to exist. In more detail, however, the plateau regions appearing near the edges are due to the turbulence in the

boundary layer, i.e., a turbulence corresponds to the second inflection point in the velocity profile near the edge and they diminish and disappear before X/D = 30. In the center region, the twin peak profile due to the initial mixing of the jet and boundary layer gets smoothed out, and the profile becomes bell-shaped and is approaching Gaussian profile. Naudascher's results extend to X/D = 130 and exhibit a similar Gaussian type profile. A Gaussian shape profile of turbulence intensity is to be distinguished from the twin peak type or flat top bell-shaped profiles observed in ordinary wakes and jets which have a strong production of turbulence due to the large velocity shear.

The maximum turbulence intensity decays more rapidly than in pure wake or in co-flowing jet as shown in Fig. 42.

4.4. Weak Injection

When the jet injection is slightly weaker than the matched case, it leaves the momentum deficit in the wake. The momentum in the wake was measured to be $C_m = -0.38\ C_d$, where $C_d$ is the drag coefficient of the smooth wall model and the negative sign indicates the momentum deficit.

The mean velocity profiles are presented in Figs. 30a and 30b. The initial profiles resemble those of the matched injection case, but the centerline velocity decays more rapidly, and farther downstream the velocity profile approaches the pure wake profiles as shown in Fig. 30b.

The rapid decay of the centerline velocity in the relaxation process is demonstrated in Fig. 41. After X/D=40, the velocity peak on the centerline diminishes rapidly and disappears at X/D=75.

Farther downstream the velocity defect is expected to decay as in an ordinary wake, but the length of the test section prevented following this last stage of behavior.

Even though the direct comparison is not possible because of the different external conditions, it is worthwhile to refer to Eggers' results in compressible hydrogen-air jet because of their similar velocity profile to the current data (Eggers 1971). In his experiment, the near-sonic jet of hydrogen was mixed into a supersonic parallel stream of air at M = 2.50 or M = 1.32 with external boundary layer of an appreciable thickness. For M = 1.32 airstream with the jet exit velocity ratio $u_j/u_\infty$ = 2.78, the result was similar to the present strong injection case which is discussed in the next section. For M = 2.50 airstream the jet exit velocity ratio $u_j/u_\infty$ was 1.98, and the velocity profiles are similar to the present weak injection case and are seen to be relaxing into the wake profile downstream. After the velocity profile becomes a pure wake type, the centerline velocity defect varies very little up to the farthest point of their observation (58 diameters). Prior to these results, Eggers and Torrence reported an air-air mixing with jet exit velocities smaller than the freestream (Eggers and Torrence 1969), and it was found that the flow relaxed into a pure profile sooner and followed the behavior of the pure wake downstream.

The axial velocity fluctuations of the present weak injection case are presented in Fig. 31 and in normalized scale in Fig. 32. Plateaus in the turbulence profile near the edges are prominent,

indicating the contribution from the wake of the body over the mixing of the jet. Existence of self-preservation is not evident, and this represents the relaxation process in a wake type behavior. The maximum turbulence decay is plotted in Fig. 42. The lower maximum turbulence level at the initial stage is due to the smaller velocity shear by the jet mixing, but otherwise the decay rate at upstream stages is similar to the matched injection case. At downstream stages the decay rate is slightly slower, and if the measurement were continued farther downstream, the decay rate would have reached the equilibrium region with pure wake decay rate.

4.5. Strong Injection

In the strong injection case the total momentum was measured to be $C_m = 0.40\ C_d$; that is, the thrust is larger than the drag by 40%.

The mean velocity profiles are given in Figs. 33a and 33b. Close to the body, the velocity profiles are similar to those of the zero-momentum case, but farther downstream ($x/D \geq 40$) the flow relaxes into a self-similar weak jet profile as demonstrated in the normalized coordinates in Fig. 34.

Even though the wake momentum $C_m$ for this strong injection case was almost equal in magnitude with the momentum for the weak injection case ($C_m \approx -0.38\ C_d$), the relaxation period was considerably shorter than in the weak injection case.

It is interesting to see whether the relaxation period in the weak injection case becomes shorter if the initial velocity profile has a deficit near the center and an excess toward the edge which

still result in the same amount of momentum defect.

The centerline velocity, plotted against axial positions in Fig. 41, shows a slower decay rate than for the matched injection case. The departure becomes clear beyond X/D = 30.

The axial velocity fluctuation profiles are shown in Figs. 35 and 36, the latter in the normalized coordinate system. Plateau regions which correspond to the outer inflection point of the velocity get smoothed away very quickly. The dip in the center of the wake is filled in rapidly, and from X/D = 40 onward the profile reaches the similar flat-top bell-shaped profile.

In regard to the maximum turbulence level, Fig. 42 shows that the initial turbulence level is higher but that the decay rate is quite similar to the matched injection case. However, a closer look reveals a slight slowdown in the decay rate beyond 60 diameters downstream, and this corresponds to the region where the velocity profile becomes a self-preserving weak jet.

In order to determine the virtual origins for these self-similar profiles, the centerline velocity and the maximum axial velocity fluctuation were plotted in terms of the inverse power of the decay rate. The results, according to $\Delta u_{\mathcal{L}}/U_\infty$, $\frac{u'_{max}}{U_\infty} \sim x^{-\frac{2}{3}}$ are shown in Fig. 37. The mean velocity seems to follow this law in three segments. The turbulent intensity decay has two distinct regions. The asymptotic law for the coflowing jet $\Delta u_{\mathcal{L}}/U_\infty$, $\frac{u'_{max}}{U_\infty} \sim x^{-1}$ was tried, but data points showed a somewhat larger scatter from a straight line.

Antonia and Bilger (1974) indicated doubt as to the universal similarity rule for the coflowing jet approaching the asymptotic,

self-preserving, axisymmetric positive wake. The present data seem to imply the existence of the self-similar velocity profile and velocity fluctuation profile for the weak jet or positive wake, but in order to be able to answer the independence on the initial conditions, measurements in a region farther downstream are required.

4.6. Very Strong Injection

In addition to the pure wake, another well-known axisymmetric turbulent free shear flow is the jet in a coflowing stream. (The presence of the tunnel walls did not allow experiments on pure jet.)

A very strong injection of jet was introduced from the model into the same freestream as in other cases. The exit velocity at the centerline was approximately $u_j/u_\infty = 2.1$.

The survey at X/D = 20 was made with an on-line data acquisition system, and the momentum integral of the flow was found to be $C_m = 1.52$, i.e. 2.20 times the drag coefficient of the pure wake case. In this case the hot wire probe was continuously traversed across the wake, and the linearizer outputs were recorded on an X-Y plotter. The results of the mean velocity and the velocity fluctuation were read off from the plottings by the digitizer.

The normalized mean velocity profiles are shown in Fig. 38, and the normalized axial velocity fluctuation profiles are given in Fig. 39. Somewhat larger scatterings in data points are due to the simplified data acquisition procedure for this particular case.

The mean velocity profiles at upstream stages exhibit the velocity defect near the edge due to the boundary layer on the model, but at X/D = 20 and downstream the velocity profiles are found to be

self-preserving.

Similarly, at the initial stages the axial velocity fluctuation profiles have plateaus near the edge which are the reminiscence of the turbulent boundary layer on the model and sharp twin-peak profile due to the mixing regions. However, they quickly disappear, and the flow attains a self-preserving profile downstream.

The centerline velocity decay and maximum turbulence decay are plotted in Fig. 40. Even though the mean velocity and the velocity flucations did not render a common virtual origin, the decay rates agree with the available data on the higher exit velocity ratios (Harsha 1971). It should be pointed out that even with this relatively low exit velocity, the flow does not behave as a small-increment jet, but it behaves as $\Delta u_{\mathcal{L}}/U_\infty$, $\frac{u'_{max}}{U_\infty} \sim x^{-1}$ and not as $x^{-\frac{2}{3}}$ as in a pure wake case.

Also, comparing the results between the very strong injection case and the strong injection case, the transition process from the strong jet, which decays as $\Delta u_{\mathcal{L}}$, $u'_{max} \sim x^{-1}$, into the self-preserving weak jet, if it exists, which decays $\Delta u_{\mathcal{L}}$, $u'_{max} \sim x^{-\frac{2}{3}}$, are to be answered in the study on the coflowing jets.

4.7. Matched Injection-Rough Wall

The rough wall model described in chapter II was substituted for the smooth wall model. The objective of this study is to increase the boundary-layer drag while matching the strength of the jet to produce a zero momentum defect and to see the effect on the behavior of the wake.

4.7.1 Pure Wake

The pure wake behind the rough wall model was investigated first. The drag coefficient computed from the wake survey was found to be $C_d = 0.89$ based on the body diameter including the roughness height ($D = 1.19''$). This is 1.3 times the drag coefficient of the smooth wall model. It should be mentioned that the result of pure wake in the following is that of a model with equivalent O-rings, but that the difference in flow parameters such as boundary layer thickness and turbulence intensity from the square roughness elements were not noticeable. The twin peak in the turbulent intensity profile was found to disappear quickly and to approach a bell-shaped profile. Aside from this, the mean velocity profile and the turbulent intensity profile, respectively, were of the same shape as in the wake of a smooth wall model.

As for the centerline velocity and the maximum turbulence level, the same decay rates as in the smooth wall case were observed. When the axial stations were expressed as $x/\sqrt{C_d}D$, axial decay rates of centerline velocity and maximum turbulence intensity come to overlap respectively between the smooth wall and the rough wall models for sufficiently large $x$.

However, it should be noted that this is not the universal rule among the pure wake data available. The constants $\Delta u_{\mathbb{Q}}$ and $\frac{u'_{max}}{U_c}$, where $U_c = U_\infty [(x-x_o)/\sqrt{C_d}D]^{-\frac{2}{3}}$ and $x_o$ is the virtual origin, depend on the various body shapes as seen by Bukreev et al. between the spheroid and the sphere. (Bukreev, Vasil'ev and Lytkin 1972).

4.7.2. Matched Injection

The strength of the jet was adjusted in the same way as in the smooth wall body case, and the result of the momentum integral obtained from the wake survey is shown in Fig. 43. A large streamwise decrease in the total momentum balance was observed, which at first was thought to be the result of the streamwise pressure gradient in the freestream. The effect of the variation in the freestream velocity estimated from Eq. 2 in Sec. 3.5 was too small to account for the observed variation in the momentum integral. No definite cause was found.

The results of the mean velocity distribution and the axial turbulence intensity are shown in Figs. 44 ~ 47.

The mean velocity profiles are presented in a normalized coordinate system in Fig. 45. In spite of the larger scatter in the mean velocity data, the overall characteristics of the self-preservation in the velocity profile are seen, and the profile is found to be of the same shape as in the smooth wall model case.

In the normalized turbulence intensity profiles (Fig. 47), twin peaks are present only at X/D = 5, and the profile reaches the bell-shaped one and then into a Gaussian-like profile sooner than in the smooth wall case. The centerline velocity and the maximum axial turbulence intensity are presented in Figs. 52 and 53, together with the results for the smooth-wall model and Naudascher's results behind a circular-disk. Both the centerline velocity and turbulence intensity show that the rough-wall case has a shorter relaxation period prior to the final decay stage as compared with the smooth-wall case.

Naudascher's results show that the wake appears to reach the final decay rate as early as X/D = 5. The decay rates in the final stage are seen to be the same for all cases. An interesting observation is that behind a circular disk the initial turbulence level reaches the final decay rate from above, while the initial level for the slender body is low and the decay rates gradually increase until they reach the final decay region.

The processes involved here may be described as follows. For a smooth wall body, turbulent boundary-layer flow and a jet-flow merge at the end of the tube. The characteristic length scale in the boundary layer is of the order of the boundary layer thickness, and that of a jet (or pipe flow) is of the order of the pipe radius. These relatively small scale eddies that are in equilibrium in themselves merge together, and then the eddies have to adjust their size to a scale which is compatible with the wake width before the flow establishes asymptotic behavior as a fully developed free shear layer. The wake reaches its final stage sooner when the initial eddy sizes are large and closer to those of the far wake, and the intensity is higher. This explains the shorter relaxation region in the rough wall case compared to the smooth wall case. If the body is bluff like a circular disk, the large energetic vortices are shed from the body, and the relaxation is reduced to a few body-diameter lengths.

4.8. Matched Injection - Low Free Stream Velocity

In order to examine the effect of the Reynolds number, a momentumless wake behind a smooth wall model at a freestream velocity 8.5 m/sec was studied. The Reynolds number was 13,400

based on the body diameter.

The flow in the pure wake was first measured, and the drag coefficient was found to be $C_D = 0.68$, which agrees with the result at a freestream velocity 16.2 m/sec.

The zero momentum defect in the wake was realized by adjusting the strength of the jet, and the survey of the wake at several downstream locations was conducted. The results of the mean velocity distribution and the axial turbulence intensity distribution are presented in Figs. 48 and 50. It is found that the self-preservation exists both in the mean velocity profile and in the RMS axial velocity fluctuation as shown in Figs. 49 and 51. Scatter among the data points was slightly larger because of a small dynamic pressure in the flow, and the mean static pressure measurement was particularly vulnerable to the ambient pressure fluctuation.

The axial decay of the centerline mean velocity difference and the decay of the maximum RMS velocity fluctuation are plotted in Figs. 52 and 53. The decay of the centerline mean velocity and also of the maximum velocity fluctuation are identical with the higher freestream velocity case. The lack of flow sensitivity to a change of Reynolds number is not surprising from the viewpoint of the universal equilibrium hypothesis (see e.g. Townsend 1976), even though the behavior of the zero momentum wake is dominated by the dissipation of energy. The increase in Reynolds number extends the higher end of the wave numbers in the energy containing eddies.

However, at sufficiently large Reynolds number, the size of the dissipating eddies is orders of magnitude smaller than that of the energy containing eddies. Therefore, since the dissipation rate is governed by the rate of the energy supply from the large scale eddies which are independent of viscosity, the dissipation rate remains unaffected.

Wang (1965) also observed the identical asymptotic behavior of turbulence decay between $Re_d$ = 55,000 and $Re_d$ = 6,850 based on the disk diameter. His results of the spectra at two Reynolds numbers indicates the similar profiles. (The spectra at lower Reynolds number is seen extending to higher frequency, but this is judged to be caused by the inadequate value for the integral scale L used for normalization.)

4.9. Mean Static Pressure

The results of the mean static pressure measurements in the wakes are presented in Figs. 54 ~ 60. The pressure coefficient is defined as,

$$C_p = \frac{\overline{p}_s - \overline{p}_{s\infty}}{\frac{1}{2}\rho U_\infty^2}$$

where $p_{s\infty}$ is the static pressure outside of the wake and varies slightly with x as shown in Fig. 8. The freestream static pressure varied as much as 0.001 $C_p$ also with the transverse distance. For clarity of presentation, the local freestream static pressures used in the above formula were defined as a linear interpolation between the values at the opposite edges of the wake.

In general all static pressure distributions are Gaussian-like until the profile becomes unrecognizable under the scatter in the data

far downstream. Less resolution was achieved in the low freestream velocity case. Immediately downstream of the rough wall model, the profile was not similar to those in the wake because of the higher turbulence level in the boundary layer compared to the turbulence in the jet.

The momentum equation in the radial direction without swirl is

$$\bar{u}\frac{\partial \bar{v}}{\partial x} + \bar{v}\frac{\partial \bar{v}}{\partial r} = -\frac{1}{\rho}\frac{\partial \bar{p}}{\partial r} - \frac{\partial \overline{u'v'}}{\partial x} - \frac{\partial \overline{v'^2}}{\partial r} - \frac{\overline{v'^2} - \overline{w'^2}}{r}$$

With the boundary layer approximation and the assumption that $\overline{v'^2} \sim \overline{w'^2}$, this equation is readily integrated to give

$$p - p_\infty = -\rho\,\overline{v'^2}$$

or

$$C_p = 2\left(\frac{\overline{v'^2}}{U_\infty^2}\right)$$

The ratio $-C_{p_{min}} \Big/ 2\left(\frac{\overline{v'^2_{max}}}{U_\infty^2}\right)$ from Naudascher's experiment is included in Fig. 60. Except at X/D = 5, where $C_p$ is lower from the streamline curvature effect behind a disk, the ratio is nearly a constant around unity. Since the radial velocity fluctuations were not measured in the present experiment, the axial velocity fluctuations are used instead, and Fig. 60 shows the ratio between the minimum static pressure and the maximum axial velocity fluctuations. The accuracy is indicated by the error bars. Departure of the ratio from unity is caused either by the curvature in the streamline or by the lack of equilibrium between the axial and radial turbulence components. When the wake reaches an equilibrium, the axial and

radial turbulence intensities should attain a constant ratio, and in the case of an isotropic turbulence, the ratio is unity. Fig. 60 shows a gradual increase of the ratios from the present experiments. The result is consistent with the above equation. Between the matched injection cases, an earlier approach toward the final stage behind the rough wall model is suggested by a faster rise of the ratio than is seen behind a smooth wall model. The most rapid increase is seen in a pure wake. An intermediary trend exists in a weak injection and a strong injection case, but the results are omitted from the figure for simplicity. Because of the ambiguity in the pressure data at the farthest stations, it was not possible to determine the asymptotic value for $-C_{p_{min}}/2(\frac{\overline{u'^2}_{max}}{U_\infty})$, which is expected to be below unity.

4.10. Intermittency Factor

The intermittency factor was obtained using a Philco-Ford Model ADP-11 intermittency meter. A signal from the hot wire anemometer was amplified to a suitable amplitude with a DISA Model 55D25 Auxiliary unit and an HP-450 Amplifier (Gain 40 db) connected in series. The signal was AC coupled, and the component of low frequency potential fluctuation was removed by the Krohn-Hite Model 330 MR Band-Pass Filter set for 600 Hz High-Pass Filter and 3 kHz Low-Pass Filter. A value of the capacitor for the low pass filter in the intermittency meter was chosen between .05 $\mu$f ~ .1$\mu$f, which corresponds to the time constant 0.5 msec to 1 msec, and the trigger level was set to count each turbulent burst which was distinguished from the potential fluctuation. The comparator output and the input

signal were monitored on the oscilloscope, and the intermittency factor was read on an X-Y plotter at each radial position of the wake.

Fig. 61a shows a typical oscilloscope trace of the signal in the matched injection case on top and the result of the differentation at the bottom. Fig. 61b shows the signal and the intermittency meter comparator output. The horizontal scale is 5 msec/cm in all traces. Here the probe is located 89 diameters downstream near the edge of the wake. The comparator output in Fig. 61b indicates that the time constant is too short because the comparator output does not stay high through the period during which one would consider the flow to be turbulent. However, the final result of the intermittency factor distribution was found to be virtually identical with the one obtained with a more appropriate time constant.

Fig. 62 shows the oscilloscope traces of the velocity fluctuations in a pure wake (2), a strong injection (b), and a matched injection (c), with X/D = 60 at their respective edges of the turbulent region. One significant characteristic is that, while the turbulent velocity fluctuates in both upward and downward directions near the edge of a matched injection wake, the velocity has exclusively downward-going turbulent bursts near the edge of the pure-drag wake, and it has the upward-going bursts in the strong injection wake. This behavior is consistent with the velocity bias expected in the turbulent region for each case. Also, the scale of the turbulent region in the matched case appears to be small compared with those in the pure wake and the strong injection case.

The result at X/D = 60 is shown in Fig. 63. In addition to the matched injection case, the results of the pure wake, strong injection

and weak injection cases are also presented. The wake radius is normalized by the respective half-width of the axial turbulent intensity profile. In the pure wake a wide intermittently turbulent region and a narrow turbulent core region near the centerline are noticeable. On the other hand, the strong injection case has a sharply falling off boundary between the turbulent and nonturbulent regions and a widest fully turbulent region near the centerline. The widths of the fully turbulent region in both the weak injection and the matched injection cases fall between the strong injection case and the pure wake. The slope of the matched injection case is parallel to that of the pure wake, and the slope of the weak injection case is parallel to that of the strong injection case.

The result of the pure wake case indicates that the potential flow region exists even close to the centerline, while the result of the strong injection case shows that the flow has a definite turbulence or highly turbulent region near the centerline and that the boundary between the turbulent and nonturbulent region is rather sharp. Therefore, the size of the indentations of the boundary in a pure wake appears to be much larger than that in the strong or weak injection cases at this axial station and so is the size of the eddies. The matched injection case exhibits an intermediary behavior, with its relatively wide, highly turbulent region near the centerline and a wide intermittent region outside. The result of flow visualization supports this conclusion.

At a station farther downstream, X/D = 89; these distinctions among the various cases cease to be clear (Fig. 64). A flat top distribution is gone even from the strong injection case, and the

measurements for all cases indicate the intermittent turbulence even near the centerline of the wake and a gentler slope toward the edges. This intermittent nature near the centerline of the wakes was also seen in the flow visualization.

The intermittency factor on the wake centerline does not remain unity but decreases downstream. For a matched injection case this is shown in Fig. 65 at three streamwise stations. The same trend was observed in Wang's result at two stations behind a disk with a matched injection. Also, in the pure wake the intermittency factor in the centerline decreased downstream. Riddhagni et al. (1971) reported that the fully turbulent core behind the sphere was limited up to X/D = 20 and that afterward the intermittency factor on the centerline decayed as $x^{-0.15}$. From the present results, the decay of the centerline intermittency factor seems to differ depending on the type of the flow, but not enough data were taken to verify their observation. It should also be mentioned that at a position very far downstream the turbulence level in the wake becomes very low, causing some difficulties with accurate signal resolution.

From the present results no self-similarity of the profiles was detected in the matched injection case, in the weak injection case or in the strong injection case. But in the pure wake case when the vertical scale is normalized by the value of the intermittency factor on the centerline, the intermittency factor profiles at X/D = 60 and 89 collapse into a self-similar profile.

4.11. Energy Spectra of Velocity Fluctuations

The one-dimensional energy spectra of the axial velocity fluctuations were obtained by digitizing the signal and performing the Fast Fourier Transform on the data with Interdata Model 70 computer. The software was provided by J. Kendall of JPL. The program digitizes the signal at a specified sampling rate and displays the results on an X-Y plotter. The Wavetek Model 103 function generator feeds the square wave signal into an A/D converter as a sampling trigger. After it was shown that most of the turbulent energy is contained in the region less than 500 Hz, the data were digitized at the rate of 2 kHz, and a total of $2^{15}$, i.e. 32,768, points were sampled. A hot wire signal was passed through a 600 Hz low-pass filter in order to avoid an aliasing effect. The results in the pure wake case are shown in Figs. 66a, b, c, and the results in the matched injection case are shown in Figs. 67a, b, c.

Comparisons are made between the pure wake case and the matched injection case at various locations. At the radial position where the turbulent intensity profile exhibits the maximum value, the difference between the two types of wakes is easily noticeable. At 10 diameters, (Figs. 66a, 67a), the pure wake case shows a rather sharp peak around 110 Hz, which gives the Strouhal number 0.17 based on the body diameter, while the matched injection case has a more widely diffused peak around 220 Hz. On the centerline and near the edge of the wakes, the spectra in both flows are free of peaks and monotonically decrease with increasing frequency. Farther downstream at X/D = 40 in the pure wake (Fig. 66b) the

spectra at the maximum turbulent intensity point have their region below the peak filled up. The frequency at the peak decreases as the wake grows downstream, but the decrease in the peak frequency is not as remarkable as that in the mixing layer observed by Kolpin (1962). The peak is still noticeable at the farthest edge of the wake, but the energy spectral density decreases monotonically with increasing frequencies.

In the matched injection case at the same axial station, X/D=40, (Fig. 67b), the power spectra taken near the centerline and the edge are nearly constant in a low frequency region and then decrease with increasing frequency. Still farther downstream at X/D = 75, (Figs. 66c and 67c), the spectra in the pure wake also have a plateau before they start decaying with increasing frequency, similar to the spectra observed in the matched injection case at X/D = 40.

Summing up, the energy spectra measurements showed the following. The pure wake has a distinct organized wave structure at the initial region and then turbulent process fills in the low frequency range of power spectra until it produces a flat plateau region. The matched injection case has a more dispersed eddy structure at the beginning and quickly reaches the spectra which monotically decrease with increasing frequencies.

Finally, the peak at the frequency range of about 20 Hz was observed invariably, and this phenomenon was taken up separately. When the hot wire probe was placed just behind the tube wall where the mixing of the boundary layer on the model and the jet flow from the pipe occurs, a sharp peak in the power spectra was found even

when the wind tunnel was off. Hence it was deduced that the room vibration caused by the adjacent utility room was exciting the instability mode in the jet and the boundary layer. However, the contribution of this peak to the turbulent energy is judged to be negligible.

4.12. Reynolds Stress

The Reynolds shear stress was computed from the data on the mean velocity, mean static pressure and the axial velocity fluctuation. By integrating the momentum equation, the x-wise momentum equation

$$\frac{\partial \overline{u^2}}{\partial x} + \bar{v}\frac{\partial \bar{u}\bar{v}}{\partial r} = -\frac{1}{\rho}\frac{\partial \bar{p}}{\partial x} - \frac{\partial \overline{u'^2}}{\partial x} - \frac{1}{r}\frac{\partial r\overline{u'v'}}{\partial r}$$

from r = 0 to r = r, we obtain

$$-\overline{u'v'}\,r = \int_o^r \frac{\partial u^2}{\partial x} r\,dr - u_{r=r}\int_o^r \frac{\partial \bar{u}}{\partial x} r\,dr - \int_o^r \frac{1}{\rho}\frac{\partial \bar{p}}{\partial x} r\,dr - \int_o^r \frac{\partial \overline{u'^2}}{\partial x} r\,dr \qquad (4)$$

The data obtained for the matched injection case and pure wake demonstrate the existence of the similarity of the form

$$\bar{u} = \bar{u}_\infty + \Delta u_{\mathcal{L}}(x) f(\eta)$$

$$\overline{u'^2} = \overline{u'^2_m}(x) g(\eta)$$

$$\bar{p} = \bar{p}_\infty + p_m(x) h(\eta)$$

where $\eta = r/r_o(x)$. When these are substituted into Eq. (4), we obtain

$$-\frac{\overline{u'v'}}{U_\infty^2} = \frac{1}{r}\left\{\left(1-\frac{\Delta u_{\mathcal{L}}\, f}{U_\infty}\right)\left[\left(\frac{d\Delta u_{\mathcal{L}}/U_\infty}{dx} r_o^2 + 2\frac{\Delta u_{\mathcal{L}}}{U_\infty} r_o \dot{r}_o\right)\int_o^\eta f\eta d\eta - \frac{\Delta u_{\mathcal{L}}}{U_\infty} r_o \dot{r}_o f\eta^2\right]\right.$$

$$+\left(\frac{d\,\Delta u_{\mathcal{L}}^2/U_\infty^2}{dx} r_o^2 + 2\frac{\Delta u_{\mathcal{L}}^2}{U_\infty^2} r_o \dot{r}_o\right)\int_o^\eta f^2\eta d\eta - \frac{\Delta u_{\mathcal{L}}^2}{U_\infty^2} r_o \dot{r}_o f^2\eta^2$$

$$-\left(\frac{d\,p_m/\rho U_\infty^2}{dx} r_o^2 + 2\frac{p_m}{\rho U_\infty^2} r_o \dot{r}_o\right)\int_o^\eta h\eta d\eta + \frac{p_m}{\rho U_\infty^2} r_o \dot{r}_o h\eta^2$$

$$\left.-\left(\frac{d\,\overline{u'^2}/U_\infty^2}{dx} r_o^2 + 2\frac{\overline{u'^2}_m}{U_\infty^2} r_o \dot{r}_o\right)\int_o^\eta g\eta\, d\eta + \frac{\overline{u'^2}_m}{U_\infty^2} r_o \dot{r}_o g\eta^2\right\} \qquad (5)$$

The forms of second order in $\Delta u_{\mathcal{L}}/U_\infty$ may be neglected in the far wake, but they are kept for computation.

The computed results in the matched injection case at X/D = 20 and 40 are presented in Figs. 68 and 69. The results at other stations have similar profiles. A cartesian coordinate system is employed here for clarity of presentation. It is noted that the contributions to turbulent shear stress from the mean static pressure and the velocity fluctuation are small, nearly cancelling each other, and that the main contribution is from the mean velocity profile. For comparison, the results of the pure wake at X/D = 40 are presented in Fig. 70. Here again the contribution to the shear stress is predominantly from the mean velocity profile.

The shear stress profiles at these streamwise stations appear to be self-similar. Eq. (5) shows that the shear stress profile is not necessarily similar even with the similar velocity profile. For the non-zero drag case, such as a pure wake, the coefficient of the first

term $\frac{d}{dx}(\Delta u_{\mathcal{L}} r_o^2)$ vanishes from the condition of Drag = const., and the shear-stress profile becomes similar when $u_d \ll U_\infty$.

Axial variation of the maximum shear stress is shown in Fig. 71 and compared with Naudascher's result from x-wire measurement. (To check the consistency, Naudascher's velocity profile was integrated using Eq. (5), and a satisfactory agreement with his results from x-wire were observed.) A similar decay law in shear stress between the present result and Naudascher's result is obtained.

The results in the pure wake are also shown. In the equilibrium wake, it is expected that $\Delta u_{\mathcal{L}} \sim u'_{max} \sim x^{-\frac{2}{3}}$, hence $\overline{u'v'}_{max} \sim x^{-4/3}$. The present results show a fairly good agreement with this prediction.

The relation between the Reynolds shear stress and other flow quantities particularly in the matched injection case will be discussed in chapter VI.

Reynolds stress measurement in the matched injection case and in the pure wake was also attempted using the x-wire procedure and is discussed in Appendix C.

4.13. Wake Spreading

The half radii which are defined where the RMS velocity fluctuation is one-half the maximum value are plotted in Figs. 72 and 73 for various injection cases. The wake spreading rate in the pure wake approximately follows $r_o \sim x^{\frac{1}{3}}$, and in the very strong injection case it follows $r_o \sim x^{\frac{1}{2}}$. The former is a well established spreading rate, but a few words are necessary for the latter. According to Fejer et al. (1967), when the centerline velocity decays

$$\frac{u_{\mathcal{L}}-u_e}{u_j-u_e} = \left(\frac{x/D}{L_v}\right)^{-m}$$

where $L_v$ is a constant, and the similar velocity profile is assumed. The wake radius is obtained by integrating a condition of the constant momentum flux, and for a Gaussian velocity profile, the result is

$$\frac{r_o}{D} = \left(\frac{x/D}{L_v}\right)^{m} \left[ \frac{\left(\frac{u_j}{u_e} - 1\right) + 2}{\left(\frac{u_j}{u_e} - 1\right) + 2\left(\frac{x/D}{L_v}\right)^{m}} \right]^{\frac{1}{2}}$$

In the present case we have $m \sim +1$, $u_j/u_e \sim 2.1$ and $L_v \sim 6$.

Hence

$$\frac{r_o}{D} \sim \left(\frac{x}{D}\right)^{+1} \frac{3.1}{1.1+2\left(\frac{x/D}{L_v}\right)}^{\frac{1}{2}} \sim \left(\frac{x}{D}\right)^{\frac{1}{2}}$$

which agrees with the present data.

The differences among the matched injection, strong injection and weak injection cases are slight. Slow starting of an initial wake spreading in the matched injection and the weak injection corresponds well with relaxation regions in maximum velocity fluctuation decay rate in both cases. In the matched injection cases, as shown in Fig. 73, all the spreading rates following approximately $X^{1/3.2}$, except the low velocity case in which the accuracy is less. As for the magnitude of the wake width with respect to the body diameter, the disk gives the largest $r_o/D$, while the smooth wall model gives the smallest $r_o/D$, and the rough wall gives the intermediate value. Behind the smooth wall, essentially no spreading is observed up to 10 diameters. The rough wall case has a slow spreading rate between X/D = 5 and 10. On the other hand, a circular disk produces a rapid

initial spreading and gradually approaches the asymptotic spreading rate. According to Ridjanovic's result, the spreading rate slows down still further and follows $X^{1/4.5}$ between X/D = 50 and X/D = 130. This region corresponds to that where the production is completely negligible following the region where the production is rapidly decreasing. The present investigation did not extend far enough downstream to verify Ridjanovic's result in shear free regime.

# CHAPTER V

# FLOW VISUALIZATION

## 5.1. Photographic Arrangement

Recent techniques of correlation measurement and conditional sampling have shown the significance of the large structures in the turbulent shear layer. However, the flow visualization technique still is a valuable technique to obtain insight into the nature of the flow, even though it often remains qualitative rather than quantitative.

Most of the photographs available on the axisymmetric turbulent flow are not distinct due to their uniform illumination and the three-dimensionality of the flow. In the present investigation, a vertical thin sheet of light is produced in the plane of symmetry of the flow as illustrated in Fig. 74. The light source is a Coherent Radiation Model 53 Argon-ion laser. The prism wave selector in the system was replaced by a flat mirror to obtain the maximum illumination. The resulting beam intensity was 8.5w consisting mainly of two frequencies, 4880 Å (blue) and 5145 Å (green). The laser beam was passed through a cylindrical lens with focal length 22.2 mm to diverge the light only in the vertical direction. A concave spherical mirror with focal length 20' is placed to reflect the light and give a sheet of light converging in height in the upstream direction. Width of the light sheet was less than 1/8".

Aerosol of dibutyl phthalate (density 1.04 gr/cm$^3$) is employed as light scattering particles. An aerosol generator similar to that described by Griffin and Votaw (1973) was fabricated. The aerosol particles are estimated to average 0.5$\mu$ in diameter. They are mixed

with the jet air supply and injected from the end of the tube model.

According to the results of Mazumder et al. (1974), the frequency response of the droplets of uniform density and of 0.5$\mu$ in diameter is better than 4 kHz for an exact coincidence (20 kHz if 2% slippage is allowed). Therefore, the present aerosol particles are considered to have an excellent flow tracking fidelity.

All of the photographs were taken at right angles to the flow direction to avoid distortion of the image. Consequently, the lack of illumination even with an 8.5W laser was noticed, since the maximum intensity is obtained in the forward scattering. A fast shutter speed was necessary to record the flow motions without blur, but the sensitivity of the available film was limited (Polaroid Type 410 film has ASA 10,000 sensitivity, but it produced very grainy images). Therefore the flow visualization was conducted at reduced free stream velocities.

The free stream velocity ranged from 1.6 m/sec to 6.5 m/sec for still pictures and 2.2 m/sec for motion pictures. With unaided eyes, it was possible to follow the large eddies up to 7 m/sec. A hot wire survey was made at these low velocities to check the difference in flow characteristics. Very close to the body, the flow is laminar and is not representative of the flow in which the other flow measurements were taken. Sufficiently downstream from the body, however, the hot wire signal and its spectra indicate that the flow was fully turbulent. Therefore, it is hoped that the results of the flow visualization will give qualitative, if not quantitative, information of the turbulent wakes currently measured.

The photographic systems used for still pictures included a Graphlex camera mounted with an F2.5, f=85 mm Aero Ektar lens and a Nikkormat FTN with an F1.4, f = 50 mm Nikkor lens. Polaroid films with ASA 3,000 sensitivity and Kodak 2475 recording film with ASA 1,000 sensitivity were used.

In addition to the still pictures, 16 mm motion pictures were taken in order to follow the motion of the large eddies as they are converted downstream. For this purpose, an I-beam rail was placed parallel to the wind tunnel front wall, and a Bolex 16 mm movie camera was mounted on a carriage which is driven in synchronization with the flow by a variable speed DC motor on the rail through a cable. An f=25 mm, F1.5 lens was used, and the filming speed of 64 frames per second was selected. At the processing, Double X film was pushed to ASA 500 sensitivity. The freestream velocity of 2.2 m/sec was chosen which gave the Reynolds number $Re_D$ = 3600 based on the body diameter. The results were studied with a 16 mm motion analyzer.

5.2. Results

The flow in the test section as viewed from the downstream end is shown in Fig. 75. The flow is a strong injection case with $u_j/u_\infty$ = 1.5, and the free stream velocity is 2 m/sec. Organized structures are observed extending to x/D = 80, the farthest downstream in the view.

The recirculating base flow region in the pure wake case was visualized by the aerosol diffusing from the inner wall of the model without injection. Fig. 76 is an example at low velocity, 1.6 m/sec.

(The rings seen on the model were those tested for a preliminary measurement of roughness effect.) The amount of scattering particles in the flow was not sufficient to study the far wake region. Therefore, a slight amount of aerosol was injected for light scattering, but the momentum input with this injection was found to be negligible. Representative still pictures with free stream velocity 1.6 m/sec. are presented in Fig. 77a to 20 diameters and Fig. 77b from X/D = 50 to 80. Together with the movie, the following can be observed. In the initial region, the flow is laminar due to the lower Reynolds number. Asymmetric sinuous transition waves are seen travelling downstream. Shortly, they form crests, and the waves break up. The wake "whips off" chains of alternating waves. Amalgamation of neighboring eddies was seen in this region. As the eddies travel downstream, they grow in size and engulf the outside flow by their rotation. The motion of these eddies is illustrated in Fig. 81.

In the weak injection case, instability in the mixing region quickly formed a train of eddies which were symmetrical with respect to the centerline of the wake. These eddies were seen forming from the core region of the wake and subsequently overtook the potential flow ad they grew outward and engulfed it by their rotation as is illustrated in Fig. 81. At the farthest point downstream, these rotations were not as vigorous but the large motions still continued.

In the strong injection case, still photographs are presented to show the region X/D = 0 ~20 and X/D = 50~80 in Figs. 78 a, b. Freestream velocity was again 1.6 m/sec. The results of the movie

($U_\infty \sim 2.2$ m/sec) follow. The initial region of the jet had a variety of small scale eddies, but shortly downstream, $X/D \sim 10$, they reshaped themselves and started the organized rotations. At the edge of the turbulent core, large symmetrical eddies rotated in the opposite sense compared with those in the weak injection cases, as shown in Fig. 81. They engulfed the potential fluid from the downstream side. Eddies in the center region went through constant deformations and the center region was less intermittent than in other types of flow.

Immediately noticeable in the matched injection case was the lack of organized large eddy rotations. Still pictures are shown in Fig. 79. The freestream velocity was 1.6 m/sec. Cases with a higher freestream velocity, 4 m/sec, are shown in Fig. 80. At this higher Reynolds number ($Re_D = 6,550$), the wake contained a finer structure of eddies, but the global structures were observed to be of the same nature among the various velocities. The examination of the movie shows the following. Very close to the body, the symmetrical oscillation and occurrence of bulges were seen. Shortly downstream, the jet rapidly broke up into pieces, and the motions of eddies were without any organized direction. The eddy motion then settled down and the pattern of eddies were roughly kept as they were convected downstream and diffused outward. Mushroom-shaped eddies were characteristic of this wake, and they were seen growing in an outward direction without rotation (Fig. 81). Also, the centerline region became more intermittent as the wake grew downstream. The flow speed was increased, but any change in this intermittent nature was not

observed (unfilled spots in terms of the visualization) near the centerline of the wake.

The symmetric structure of rolling vortices on the symmetry plane in the strong and weak injection cases is considered to be the sliced view of the ring vortex structures. Becker and Massaro (H. A. Becker and T. A. Massaro 1968) conducted flow visualizations of a tone-excited round jet into still air with Reynolds number up to 10,000 based on the nozzle diameter. Even though their observations are limited to the proximity of the nozzle, very similar symmetrical vortex structures, as in the present strong injection case, were observed in a symmetry plane of pure jets. They identified these as ring vortices by a general illumination. They also observed vortex amalgamation processes in pure jets. However, because of the slow rate of the wake growth in the present strong injection case, these were not evident in the present case.

On the other hand, in the symmetry plane of the pure wake (very weak injection), vortices were asymmetrical about the centerline of the wake. The vortices appeared to be connected with each other to form a single helix, but that is not possible if the flow is to be free of angular momentum. The model was carefully aligned including the strut upstream of the screen, and the hot wire survey with different wire orientation revealed no swirl motion in the mean flow.

A portion of the vertical sheet of light was spread in a horizontal direction with another cylindrical lens. The clear observation was difficult due to the lack of light, but there were indications that the vortices were rolling in the opposite directions one after another.

Thus, the vortices appeared to have a double helical structure. One of them is assumed to have a smaller radius than the other, for the intersection of two vortex filaments is not possible. However, little is known about the vortex structure in axisymmetric flow (see e.g. H. Gold (1963) for transition of axisymmetric wake), and the statement above remains to be only speculative.

# CHAPTER VI

# DISCUSSIONS

## 6.1. Equilibrium between Mean Flow and Turbulent Flow

### 6.1.1. The Wake of Various Bodies

Townsend (1947) first investigated the wake of a cylinder and concluded that it takes in excess of 1,000 diameters before the total kinetic energy of the turbulent motion and the total kinetic energy of the mean flow reach a complete equilibrium. It was indicated in the present investigation that the process of attaining the asymptotic behavior of the turbulent free shear flow is dependent on the initial condition, particularly on the shape of the body. Therefore, it is of interest to study the existence of the equilibrium between mean flow and turbulent motion and to investigate the process to attain the equilibrium state in axisymmetric wake flows. First this is carried out in the pure wake with various initial conditions. It is assumed that the turbulent motion is characterized by the maximum axial turbulent intensity and that the mean flow motion is characterized by the centerline velocity defect. Then the ratio formed by these two parameters is obtained from the various data available including the present data and is presented in Fig. 82. If the axial turbulent intensity is proportional to the total turbulent energy, this ratio becomes a square root of the ratio between turbulent energy and the total mean flow energy as used by Townsend.

It is immediately noticeable that the wake behind the slender bodies (Chevray (1968), Schetz (1975)) does not attain equilibrium even at the 40 diameter station. On the other hand the wakes behind

bluff bodies, such as disk and sphere, exhibit the constant value of the parameter as close to the body as 5 diameters downstream. (Due to the inaccuracy in reading data from the published figures, some fluctuations in the results are seen but they are not necessarily representative of the original accuracy.)

The present results behind a smooth wall model and a rough wall model show gradual increase in the ratio. The difference between the two cases is small. At X/D = 60 and downstream, the ratio seems to level off indicating the flow to be approaching the equilibrium.

The differences in the flow processes between behind a bluff body and behind a smooth wall body was discussed previously together with the results behind a rough wall model. For a slender body, the separation region is minimal and so is the vortex shedding. Therefore, these vortices have to grow in their size and get concentrated to the size inherent to the given type of free shear flow. On the other hand, behind a bluff body, large and vigorous asymmetric vortex sheddings with their spacing compatible to the scale of the body itself induce large scale velocity fluctuations, and thus enhance a stronger mixing to attain an asymptotic behavior sooner.

Behind bluff bodies the ratio between the maximum axial turbulent intensity and the centerline velocity defect attains the value $0.9 \sim 1.0$. The results by Cooper and Lutzky (1955) behind a square disk achieve the same value. The wakes behind slender bodies observed by Schetz et al. and Carmody may be considered to be developing to reach the same value. Also, the present cases may reach the same value at a slower rate. However, behind a porous disk the final

values are much smaller than in other cases. Bevilaqua (1975) reported the slower development of the wake behind a porous disk starting with smaller scale motion than the wake behind a sphere. (Bevilaqua chose the porosity of the disk so that it has a drag coefficient equal with the sphere. Therefore, the difference in behaviors is due to the initial eddy sizes and not the magnitude of the drag which was used successfully to normalize the wake of a rough wall in the previous chapter.)

Townsend (1970) examined the conditions for the self-preserving development in axisymmetric wakes. Following his analysis, but using a different notation, the necessary condition is

$$q_o^2/\tau_m \geq 2K\sqrt{\frac{J}{I_2}}\ \frac{L}{r_o}$$

where $u - U_\infty = \Delta u_o f(\eta)$, $f(0) = 1$ and $\eta = r/r_o$

$$q^2 = \overline{u'^2} + \overline{v'^2} + \overline{w'^2} = q_o^2 g(\eta),\ g(0) = 1$$

$$\tau = \tau_m h(\eta),\quad \tau_m = -\overline{u'v'}_{max}$$

$$I_2 = \int f^2 \cdot \eta d\eta$$

$$J = \int g \cdot \eta\, d\eta$$

$$K = \int f' \cdot h \cdot \eta d\eta$$

$$L = q_o^3 r_o^2 / \int \epsilon\, r dr \text{ and } \epsilon \text{ is the energy dissipation.}$$

Uberoi and Freymuth's data (1970) behind a sphere at X/D = 100 give the value of 7.9 for the right hand side of the inequality while their $q_o^2/\tau_m$ is 8.8 and satisfies the necessary condition above. Chevray's data (1968), behind a slender body, give $q_o^2/\tau_m \sim 6.0$ at the farthest

downstream X/D = 18. The wake behind the smooth wall model in the present investigation gives $q_o^2/\tau_m \sim 3.7$ at X/D = 20, 6.6 at X/D = 40 and 7.2 at X/D = 60. (Here $q_o^2 \sim 3\,\overline{u'^2}_{\mathcal{L}}$ was assumed for the present experimental results.) As is seen in Fig. 82, the flow behind these slender bodies is not in equilibrium yet. Since $q_o^2/\tau_m$ is increasing, the flow may satisfy the necessary condition and may approach the equilibrium sufficiently downstream from the body, and if that is the case, these measurements indicate that the approach to the equilibrium is very slow behind the slender bodies compared with the flow behind the bluff bodies.

For the plane wake, Townsend (1976) gives a universal value of 0.46 for the ratio $q_o/\Delta u_{\mathcal{L}}$, but for an axisymmetric far wake Uberoi and Freymuth's data give 1.41 for this ratio. Further study needs to be conducted to see if a universal ratio exists for axisymmetric wakes.

6.1.2. Equilibrium between Mean Flow and Turbulent Flow in the Matched Injection and in the Unmatched Injection Cases

Fig. 83 shows the axial variation of the quotient $u'_{max}/\Delta u_m$ in the wake for different injection rates from the present experiment. Here $\Delta u_m = u_{max} - u_{min}$. The matched injection case behind a disk by Naudascher is also shown. Downstream of X/D = 10 where the velocity profile becomes self-preserving, the result for the very strong injection case shows a very similar trend as in the pure wake. On the other hand, the values for the matched injection cases show a rapid increase as a function of the axial position and indicate that equilibrium does not exist between the

mean velocity difference and the turbulent velocity fluctuation. The mean velocity difference represents the magnitude of the velocity shear in the wake, which provides a production of turbulence energy. The steady increase in the ratio $u'_{max}/\Delta u_m$ in the matched injection indicates that the rate of production becomes less important in the turbulent energy budget. Among the matched injection cases, the ratio $u'_{max}/\Delta u_m$ is lowest in the smooth wall case, is intermediate in the rough wall case and is highest in the wake behind a disk. This is in accordance with the process of how each wake attains an asymptotic decay law both in terms of the mean velocity and in the turbulent intensity discussion earlier.

The strong injection case shows the intermediate value for the ratio $u'_{max}/\Delta u_m$, characterizing the relaxation process from one type of flow to another. Here three different stages of development can be seen. Up to X/D = 10, the flow is in the relaxation region with only a small increase in $u'_{max}/\Delta u_m$. In this region, strong turbulence is generated by the mean velocity shear. It is followed by the non-equilibrium decay region, which causes a rise in the ratio similar to the case of matched injection. Further downstream, the flow begins to reach the equilibrium region after establishment of the weak jet property, and the behavior of $u'_{max}/\Delta u_m$ is similar to that in the coflowing jet or pure wake.

In the weak injection case, $\Delta u_{\mathbb{C}}$ changes its sign as the flow approaches the pure wake profile, and hence is not a characteristic of the velocity shear in the wake. Therefore, the characteristic velocity $\Delta u_m = u_{max} - u_{min}$ is taken as follows: $u_{max} = u_{\mathbb{C}}$ when

$\Delta u_{\text{℄}} > 0$, but $u_{max} = u_\infty$ when $\Delta u_{\text{℄}} < 0$. Strict equilibrium does not hold because of the lack of the similar profile, but this ratio indicates qualitatively the property of the flow. The ratio $u'_{max}/\Delta u_m$ increases in a similar manner as in the matched injection case and beyond X/D = 40 appears to be approaching the pure wake behavior from above.

6.2. Entrainment Process

In turbulent free shear flows, the surrounding non-turbulent fluid is entrained by the turbulent fluid and this results in the spreading of the wake and jet.

The entrainment rate can be defined as the rate of change of the mass flux $\dot{m}$ inside the turbulent region of the flow. Therefore, the entrainment rate $E=\frac{d\dot{m}}{dx}$ is expressed as

$$\dot{E} = \frac{d\dot{m}}{dx} = \frac{d}{dx}\left(2\pi \int_o^{r_e} \rho u r dr\right)$$

where $r_e$ is the edge of the turbulent region. If the similar velocity profiles exist in the form

$$\Delta u = u - U_\infty = \Delta u_{\text{℄}} f(\eta)$$

$$\text{where } \eta = r/r_e \quad ,$$

then we obtain

$$\dot{E} = \frac{d\dot{m}}{dx} = 2\pi\rho \frac{d}{dx}(\Delta u_{\text{℄}} r_e^2) \int_o^{\eta_e} f\eta d\eta + 2\pi\rho U_e r_e \frac{dr_e}{dx} .$$

For a pure jet, since $U_e = 0$, the above expression reduces to

$$\dot{E} = \frac{d\dot{m}}{dx} = 2\pi\rho \frac{d}{dx}(U_{\text{℄}} r_e^2) \int_o^{\eta_e} f\eta d\eta \quad .$$

Since the condition of a constant momentum flux gives $\Delta u_{\mathcal{L}} r_e^2 = \text{constant}$ for an ordinary wake, and $\int_0^{\eta_e} f\eta d\eta = 0$ approximately for a zero momentum wake, in these two cases the expression for $\dot{E}$ becomes

$$\dot{E} = U_e r_e \frac{dr_e}{dx} \quad . \tag{6}$$

If the edge of the turbulent region in average is proportional to the wake width $r_o$ where the turbulence level is half the maximum value, the entrainment rate in the wakes can be estimated from the growth of the wake width.

The present investigation has shown that the difference in the wake growth among the variable injection cases was slight. This implies that the entrainment rate as computed from Eq. (6) does not differ much in various cases. The result of the flow visualization, however, has shown that for the pure wake and unmatched injection cases, the rotation of large eddies is responsible for the entrainment process, while for the matched injection case, the entrainment is carried out by the diffusion of the turbulent region. Thus, the assumption that the mean position of the turbulent interface is proportional to the wake width $r_o$ requires some reconsideration.

As pointed out by Mobbs (1968) in his experiment behind the two-dimensional composite grid, the wake width can grow if the intermittent region is growing while the fully turbulent region itself is not; and in the present axisymmetric matched injection wake, the results of the intermittency factor measurement and the flow visualization show the increase in the indentations of the interface as the flow moves downstream.

Therefore, it is meaningful to estimate the volume of the fully turbulent region and its growth rate. Using the intermittency factor $\gamma$, the area of the fully turbulent region passing through a fixed cross-sectional plane is estimated to be $S = 2\pi \int_o^\infty \gamma r dr$, and the entrainment rate can be defined as $\dot{E} = U_o \frac{d}{dx}(2\pi \int_o^\infty \gamma r dr)$. The length scale which is the average position of the turbulence interface can thus be defined as

$$\bar{r} = (\int_o^\infty \gamma r dr)^{\frac{1}{2}} .$$

In the matched injection case, this length scale was found to be $\bar{r} = 1.14\, r_o$ at X/D = 20, $0.95\, r_o$ at X/D = 60, and $0.84\, r_o$ at X/D = 89, while the wake width itself grows from $r_o = 0.83$ through 1.25 to 1.39 at the respective axial station. This decrease in the mean position of the interface was observed by Mobbs in his two-dimensional momentumless wake. In the pure wake, the intermittency factor profiles at X/D = 60 and 89 give the nearly proportional increase in $\bar{r}$ with respect to the wake width $r_o$.

Townsend (1970) introduced an entrainment constant which characterizes the entrainment rate as

$$\beta = \frac{U_\infty + \frac{1}{2} u_o}{|u_o|} \frac{d\ell_o}{dx}$$

where $u_o$ is the characteristic velocity in the flow, and $\ell_o$ is the variance of the velocity distribution. This is equal to

$$\beta = \frac{U_\infty}{\Delta u_{\mathfrak{C}}} \frac{d\ell_o}{dx}$$

in the wake where $\Delta u_{\mathfrak{C}} \ll U_\infty$. The length scale $\ell_o$ is found to be

0.6 times the wake width in the present pure wake behind a smooth wall. When the present data are substituted into the above equation, $\beta$ was found approximately constant in the axial direction and was equal to 0.07. The value for the plane wake is given in Townsend's book as 0.08.

For the matched injection case, the length scale $\ell_o$ may not be defined in the same manner as in the pure wake. If $\ell_o$ is proportional to $r_o$ and the wake widths are used to compute $\beta$, the magnitude is not constant but it increases downstream as follows: $\beta \sim 0.12$, 0.24, 0.30, 0.41 at X/D = 20, 40, 60 and 75 respectively. The characteristic velocity governing the entrainment process in the matched injection case seems to be the turbulent intensity rather than the centerline velocity defect. When the axial turbulent intensity $u'_m/U_\infty$ is substituted for the $\Delta u_{\mathcal{L}}$ in the above equation, the entrainment parameter becomes nearly constant in the streamwise direction and is about 0.3 based on the wake width $r_o$.

6.3. Comparison with the Analysis

Prandtl's constant eddy viscosity model and mixing length theory both predict power laws for ordinary jets or wakes satisfactorily. However, as seen in the present results and in the data by other investigators, the axial decay law of the centerline velocity difference and the wake spreading rate do not agree with the prediction obtained by these models. To study this disagreement, the assumption taken in solving the equation of motion are examined below. The outline here is parallel to that given by Tennekes and Lumley (1972).

The equation of motion for axisymmetric wakes without swirl is given by

$$U_\infty \frac{\partial u}{\partial x} = - \frac{\partial r \overline{u'v'}}{\partial r}$$

Here the velocity in the wake is assumed nearly equal to the free-stream velocity $U_\infty$, and the other Reynolds stress term $\overline{u'^2} - \overline{v'^2}$ is neglected.

If it is assumed that the Reynolds stress can be expressed in terms of the characteristic velocity $\Delta u_{\mathbb{C}} = u_{\mathbb{C}} - u_\infty$, namely

$$- \overline{u'v'} = (\Delta u_{\mathbb{C}})^2 \, g(\eta) , \tag{7}$$

and the power law behaviors $\Delta u_{\mathbb{C}} \sim x^{-m}$, $r_o \sim x^n$ and $|\Delta u_{\mathbb{C}} / U_\infty| << |$ are assumed, then it is required for the similarity that $m + n = 1$. Another equation is required to determine the exponent. For a nonzero drag case this is obtained from a momentum integral as

$$U_\infty \, \Delta u_{\mathbb{C}} \, r_o^2 = \text{const.} \quad \text{which gives } m + 2n = 0 .$$

Hence

$$\Delta u_{\mathbb{C}} \sim x^{-\frac{2}{3}}, \quad r_o \sim x^{\frac{1}{3}} .$$

However, for a momentumless wake, the last equation is not applicable because of Drag $\sim U_\infty \Delta u_{\mathbb{C}} r_o^2 \int_o^\infty f\eta d\eta = 0$. The equation for the moments of velocity obtained from the momentum equation is

$$U_\infty \frac{d}{dx} \int_o^\infty \Delta u \cdot r^{2n} \, r dr = 2n \int_o^\infty \overline{u'v'} \, r^{2n} \, dr . \tag{8}$$

The Reynolds stress is expressed as

$$- \overline{u'v'} = \epsilon \frac{\partial u}{\partial r} \tag{9}$$

and if $\epsilon$ is independent of r, Eq. (8) becomes, for n = 1,

$$\frac{d}{dx}\int_o^\infty \Delta u\, r dr = \frac{\epsilon}{U_\infty} 4 \int_o^\infty \Delta u\, r dr \quad .$$

Hence

$$\frac{d}{dx}\int_o^\infty \Delta u\, r^3\, ar = 0, \quad \text{if} \int_o^\infty \Delta u\, r dr = 0 \, .$$

This gives an additional condition on the exponent

$$m + 4n = 0$$

and the exponents in the power laws become

$$m = 4/5, \; n = 1/5,$$

namely,

$$\Delta u_{\mathbb{Q}} \sim x^{-4/5}, \quad r_o \sim x^{1/5} \quad .$$

Eqs. (7) and (9) require the eddy viscosity to have the form

$$\epsilon \sim \Delta u_{\mathbb{Q}} \cdot r_o \quad .$$

This is Prandtl's constant eddy viscosity model. The corresponding velocity profile is

$$\frac{\Delta u}{\Delta u_{\mathbb{Q}}} = f(\eta) = (1 - \frac{\eta^2}{2}) e^{-\eta^2/2} \quad \text{where } \eta = \frac{r}{r_o} \quad .$$

Even though the velocity profile above is similar to those obtained experimentally, the predicted centerline velocity decay is far slower than the experimental results. Also, the predicted growth of the wake width is slower than the experimental results.

The fault of the above analysis stems from the assumption

on the Reynolds stress. The form $\overline{u'v'} = (\Delta u_{\mathfrak{C}})^2 g(\eta)$ is equivalent to the assumption $\overline{u'v'}_{max}/(\Delta u_{\mathfrak{C}})^2 = \text{constant}$. The experimental result of the pure wake behind a smooth wall gives a slight variation as shown in Fig. 84, but the experimental results for the matched injection cases are far from a constant.

The assumption above is equivalent to the condition of the constant turbulent Reynolds number as shown below. Turbulent Reynolds number is defined as

$$R_T = \frac{u_o r_o}{\epsilon} = \frac{\Delta u_{\mathfrak{C}} \cdot r_o}{-\overline{u'v'}/(\frac{\partial u}{\partial r})} \quad .$$

When the similarity profiles for the velocity $\Delta u = \Delta u_{\mathfrak{C}} f(\eta)$ and the shear stress $\overline{u'v'} = \overline{u'v'}_{max} h(\eta)$ are substituted above, the equation becomes

$$R_T = \frac{\Delta u_{\mathfrak{C}}^2}{\overline{u'v'}_{max}} \frac{f'(\eta)}{h(\eta)}$$

and shows the condition for the constant turbulent Reynolds number in the axial direction, $\Delta u_{\mathfrak{C}}^2 \sim \overline{u'v'}_{max}$. (If $R_T$ is also assumed to be constant across the wake, this is equivalent to Prandtl's eddy viscosity model $\epsilon \sim u_o r_o$.) The ratio $\overline{u'v'}_{max}/\overline{u'^2}_{max}$ did not vary much in the experiment (Fig. 85), and if the similarity form $\overline{u'v'} = \overline{u'^2} g(\eta)$ is assumed, this is equivalent to Eq. (7) provided $\Delta u_{\mathfrak{C}} \sim u'_{max}$. This is true if the mean flow is in equilibrium with the turbulent flow, or in other words, if the production of the turbulent energy by the mean flow shear is in balance with the dissipation and convection of the turbulent energy. In the equilibrium flow, the

production term is characterized by $\Delta u_{\mathcal{L}} \cdot u'^2_{max}/r_o$ and the dissipation term by $u'^3_{max}/r_o$ (cf. Townsend 1976). Therefore, the balance between the dissipation and the production is measured by $u'_{max}/\Delta u_{\mathcal{L}}$. The balance between $\Delta u_{\mathcal{L}}$ and $u'_{max}$ does not exist in the momentumless wakes as is shown in Fig. 83, and hence the eddy viscosity model is inappropriate to describe the momentumless wakes. Prandtl's mixing length theory also assumes the equilibrium between the mean flow and the turbulent flow, and therefore it is not surprising that the result $\Delta u_{\mathcal{L}} \sim x^{-0.85}$, $r_o \sim x^{0.15}$ (Appendix A) does not agree with the experiments.

Since the balance of the turbulent energy is essential in the momentumless wakes, any method used to describe the momentumless wake has to include the turbulent energy equation for its closure. Prandtl-Kolomogorov's eddy viscosity model with the turbulent energy term, i.e. $\epsilon = \text{const.} \sqrt{\overline{q'^2}}\ \Lambda$, gives the turbulent Reynolds number as $R_T \sim \Delta u_{\mathcal{L}} / \sqrt{\overline{q^2}}_{max}$. This seems to be a more inclusive model and assumes that turbulent Reynolds number is constant only for free shear layers in equilibrium.

The turbulent kinetic energy model (Bradshaw et al. (1967) and Harsha (1974)) assumes $\frac{\tau}{\rho} = -\overline{u'v'} = a\,\overline{q'^2}$ which is compatible with the observed results $\overline{u'v'}_{max} \sim \overline{u^2}_{max}$ in the matched injection. However, in the momentumless wake, the Reynolds stress changes its sign across the wake, and one has to manipulate the sign of the constant (according to Harsha $a = 0.3\ \frac{\partial u/\partial r}{|\partial u/\partial r|}$).

The evaluation of the second-order closure models such as by Donaldson (Lewellen et al. (1973)) was not tried for the present

experimental case but Lewellen et al. (ibid) applied the model to Naudascher's case, and the computational result shows a slower centerline velocity decay than the experiment, while a good agreement was obtained for the turbulent intensity decay. Recently Finson (1975) carried out an analysis based on the second-order closure model for the zero-momentum wake including the axial and radial turbulent intensity term and neglecting the production term except in the $\overline{u'v'}$-equation. He obtained the exponents for the power law behavior by integrating the equations for momentum, axial turbulent intensity, radial turbulent intensity, turbulent shear stress and length scale. His velocity decay law is compared with the experiments in Fig. 86 and satisfactory agreements are seen. The virtual origin is obtained as X/D = 5 behind a disk, X/D = 14 behind a rough wall model and X/D = 19 behind a smooth wall model. These values are consistent with the establishment of the asymptotic law with various initial conditions discussed earlier. The wake spreading rate is compared with the experiments in Fig. 87. A somewhat larger scatter is seen among the present experimental results, but the agreement is fairly good. Ridjanovic's data for the momentumless wake behind a disk show a different trend downstream; but these may well be removed since the velocity profile is no longer self-preserving and the accuracy of the measurement is not high in this region. Naudascher's data present the same value of the virtual origin as the centerline velocity decay, but the present experiment did not give the same origin as in the velocity partly due to the scattering in data.

# CHAPTER VII

# CONCLUSIONS

(1) A unique self-similar velocity profile in the momentumless wakes was observed, and it was found that the self-similarity of the velocity profile is very sensitive to any mismatch of the momentum balance in the wake.

(2) The centerline velocity in the matched injection cases decays very rapidly compared to the pure wake case or the coflowing jet case. The maximum axial turbulence intensity also decays rapidly, but the difference from the pure wake case or the coflowing case was not as large as for the centerline velocity decays. In the matched injection cases a slightly slower spreading of wake was observed than in the pure wake case or the coflowing jet case.

(3) The relaxation length in which the matched injection wake reaches its final stage depends on the initial conditions. The larger the relative length scale of the eddies at the initial stage, the shorter the relaxation length becomes, but a unique length scale which brings together the axial variations in the various matched injection cases was not found.

(4) Flow visualization in the symmetry plane showed the large eddy rotations engulfing the potential flow in the pure wake and the coflowing jet. In the zero momentum wake these large eddy motions were absent and an increasing indentation of the interface of the turbulent region was observed downstream.

(5) Simple modelings of the Reynolds stress such as Prandtl's eddy viscosity model or mixing length theory predict poorly the power

laws for the momentumless wakes where the equilibrium between production and the dissipation of turbulent energy is absent. The Reynolds shear stress cannot be related only to the mean flow quantity, and it is essential that the model includes the higher-order mechanism of the balance of the turbulent kinetic energy in order to describe the momentumless wakes.

(6) The flow properties in the turbulent wake behind a slender body with well-defined initial conditions were experimentally determined at various injection rates. The data should provide a useful test case for the turbulence-model calculations.

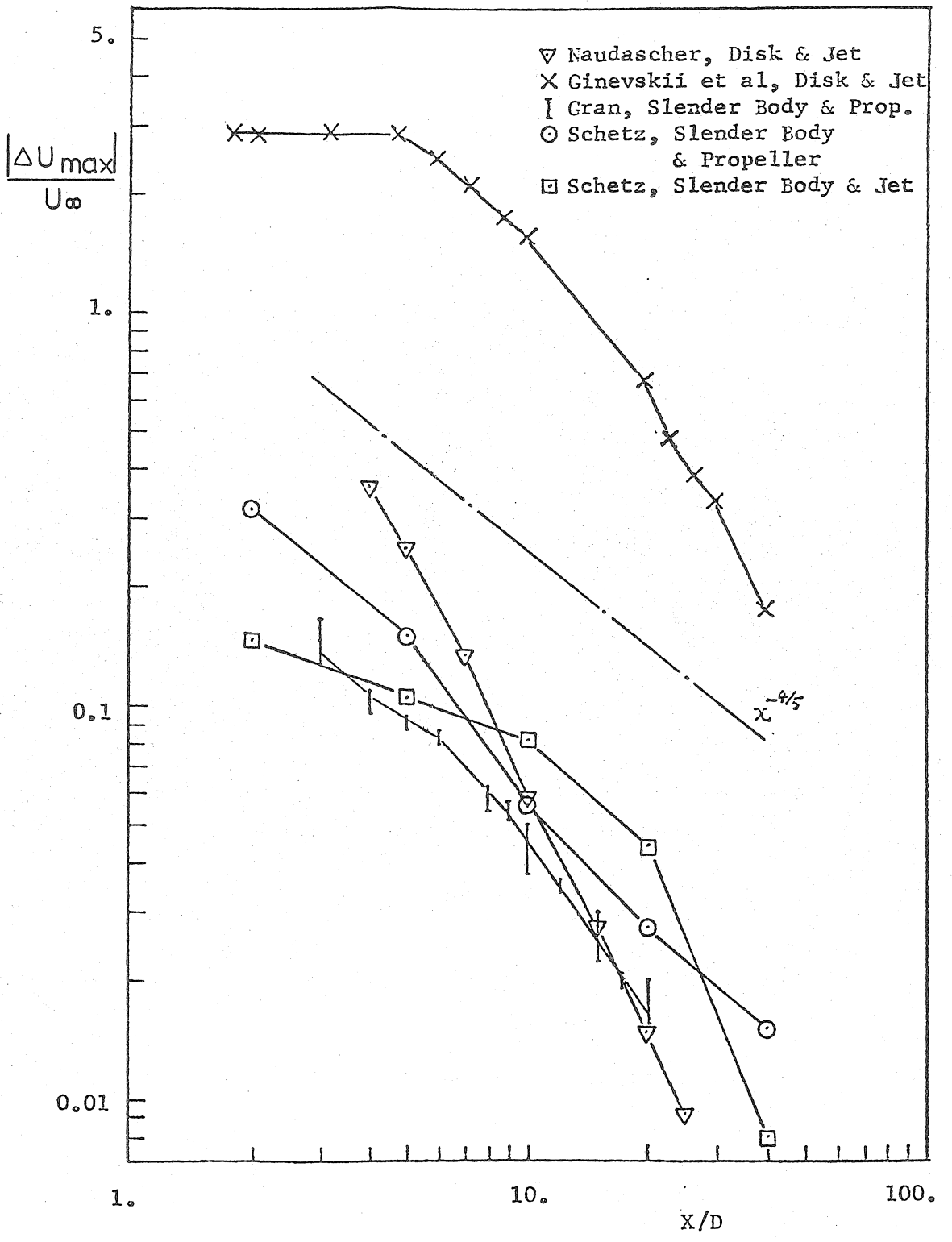


Fig. 1. Axial Variation of the Maximum Velocity Defect in the Momentumless Wake Experiments

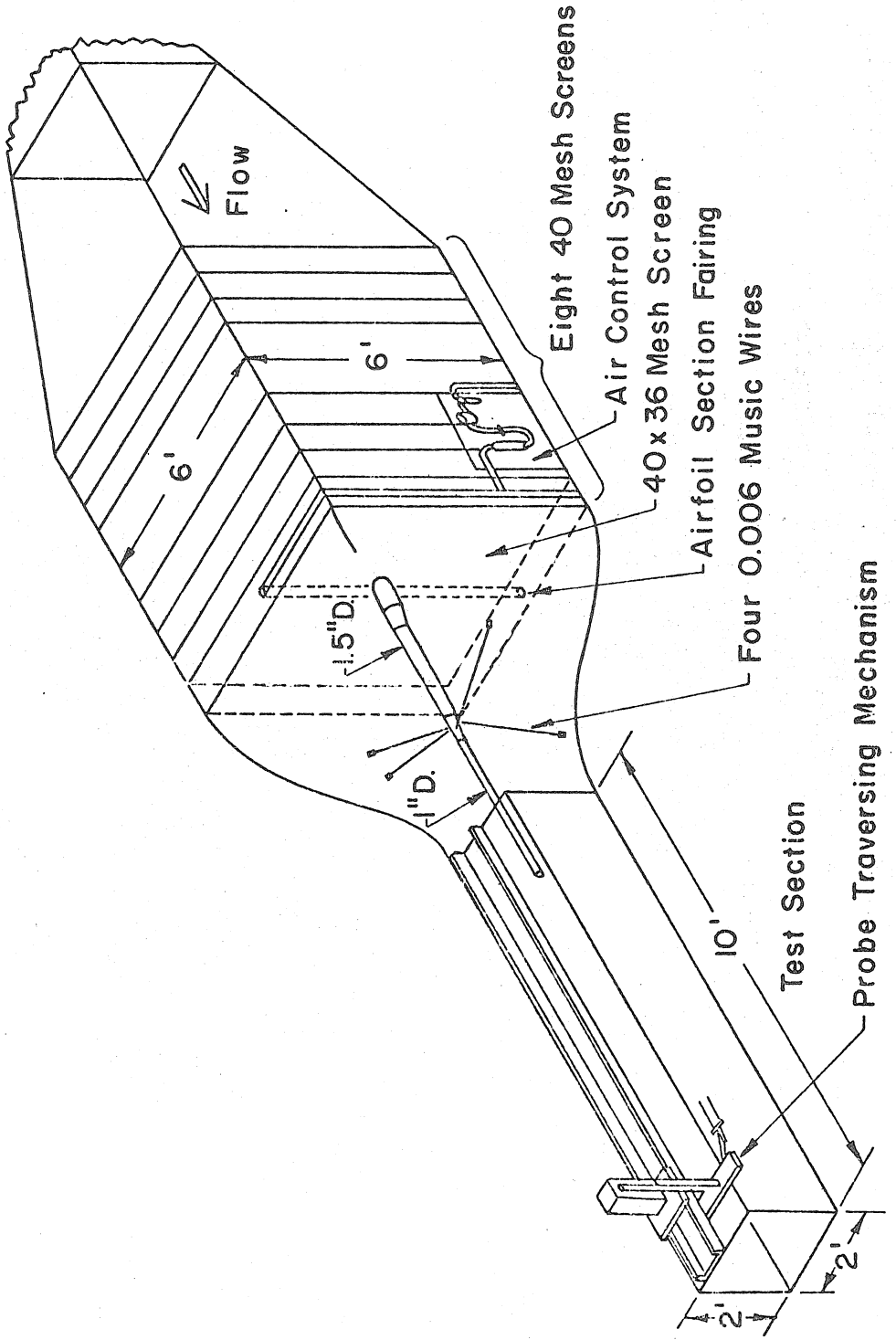


FIG. 2 EXPERIMENTAL SET-UP IN WIND TUNNEL

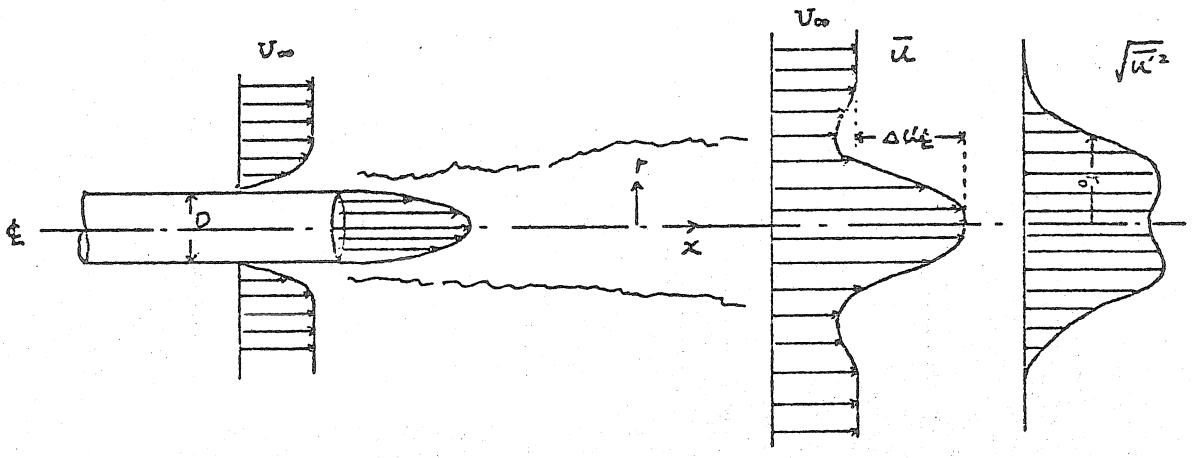


Fig. 3. Definition Sketch with Smooth Wall Model

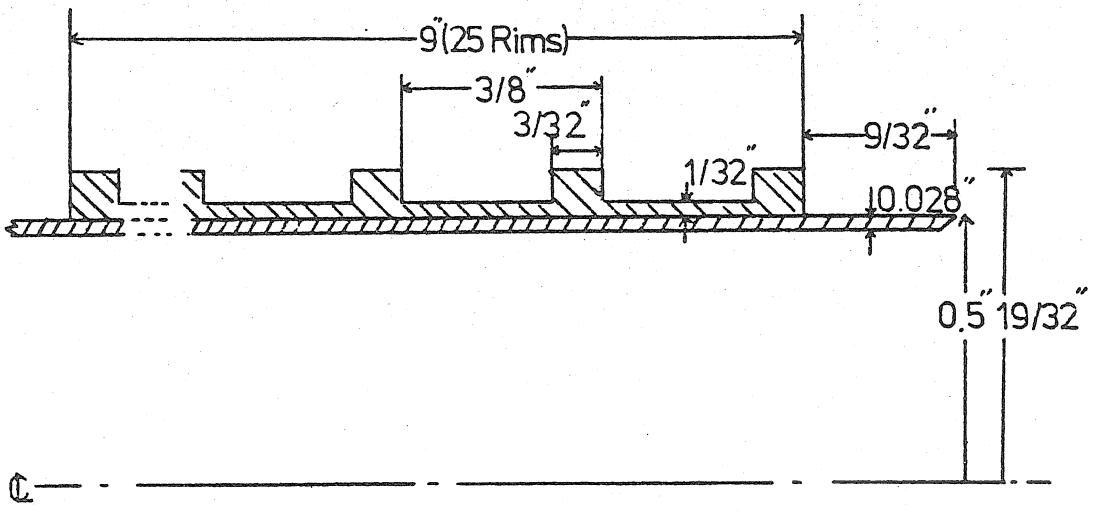


Fig. 4. Rough Wall Model

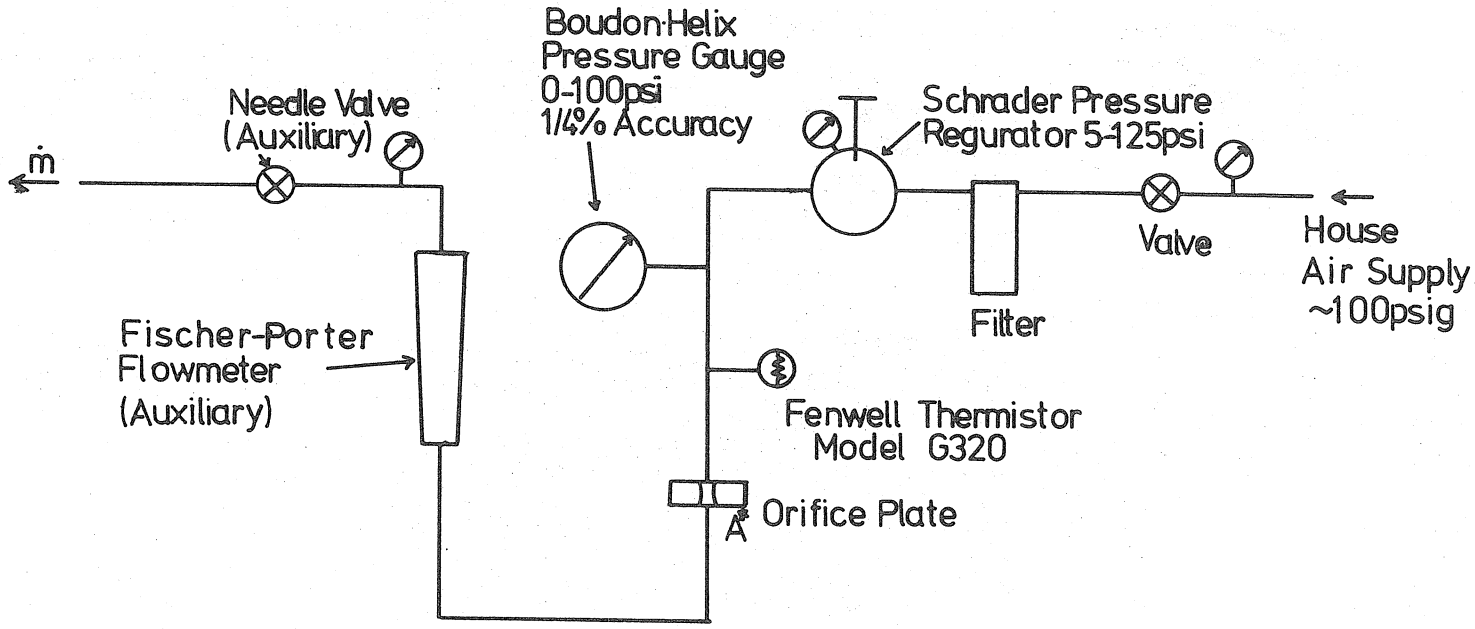


FIG. 5

Air Supply System

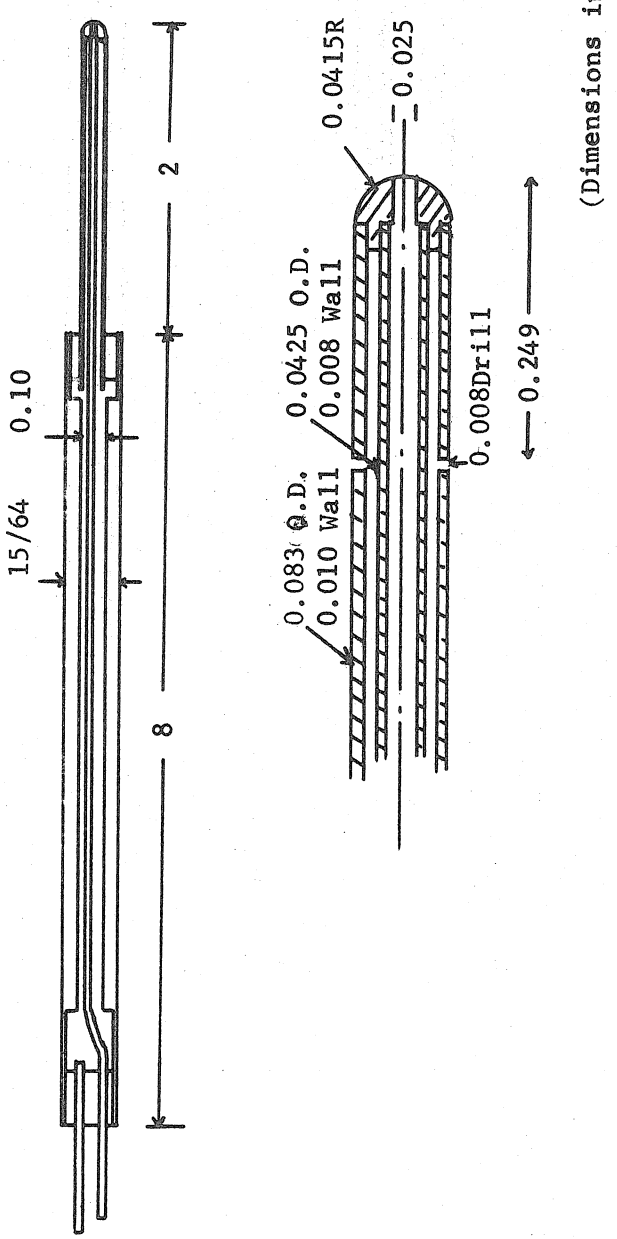


Fig. 6. Pitot-Static Pressure Probe

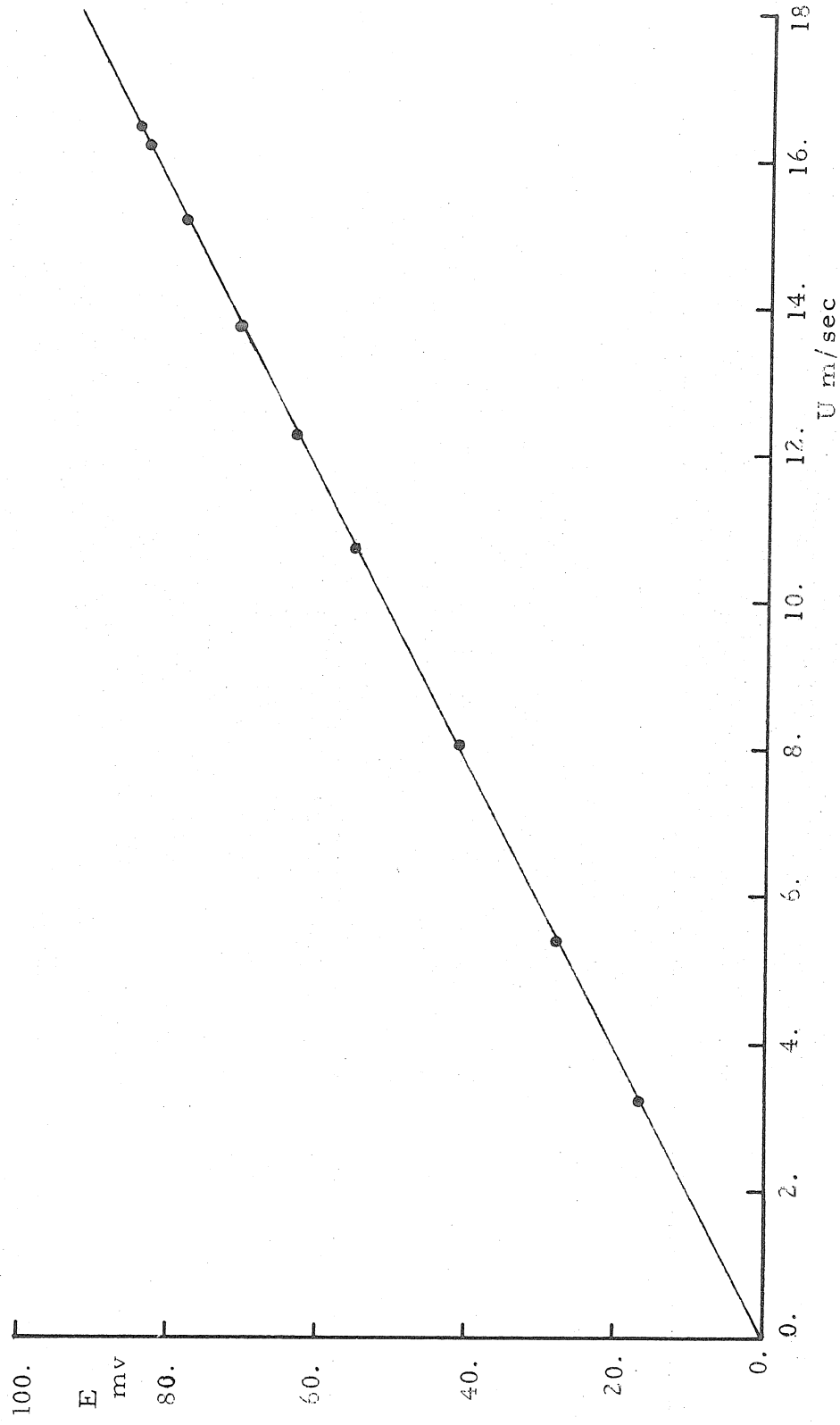


Fig. 7. Calibration of Normal Hot-Wire Probe

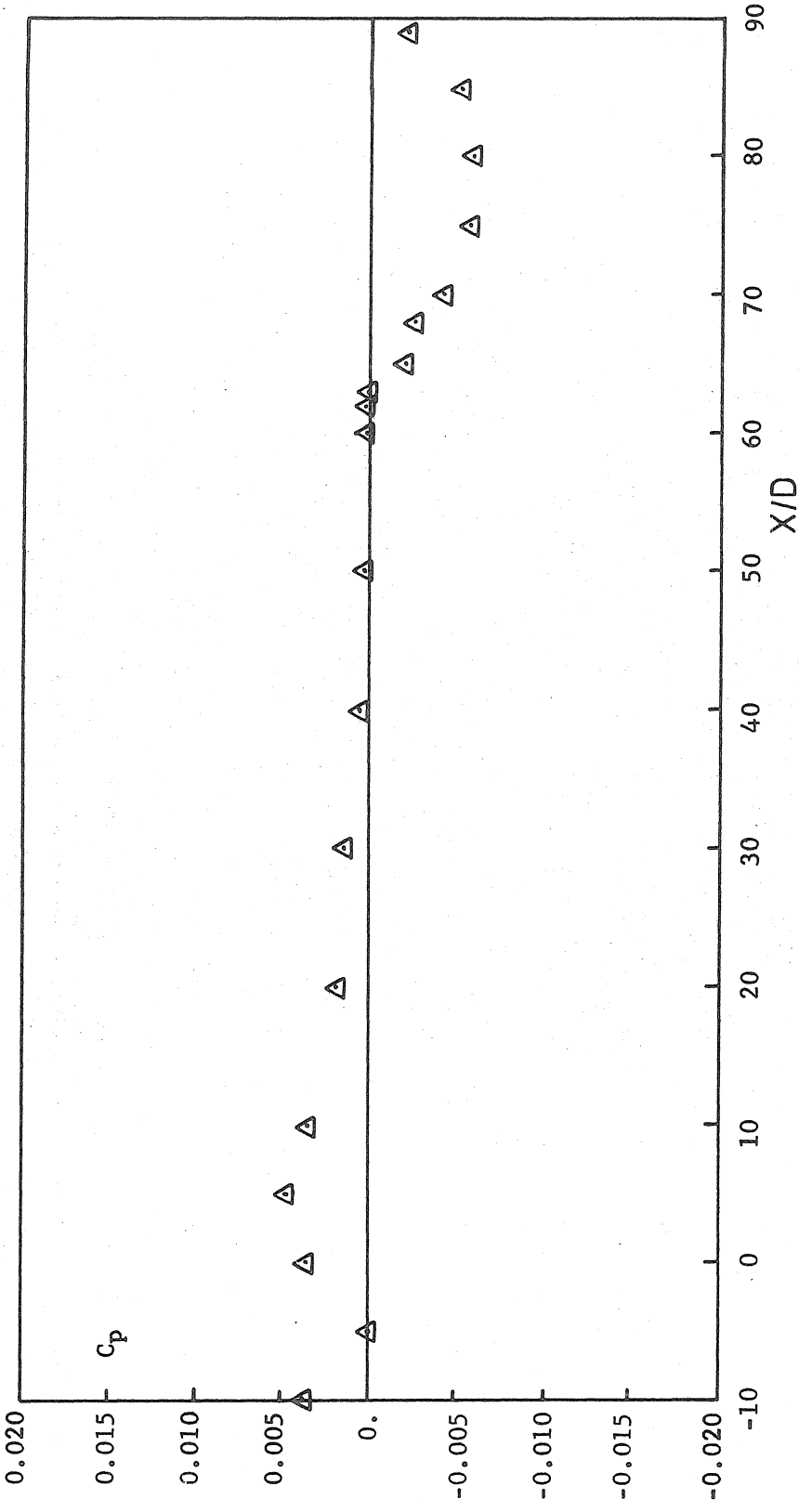


Fig. 8. Free Stream Static Pressure Distribution

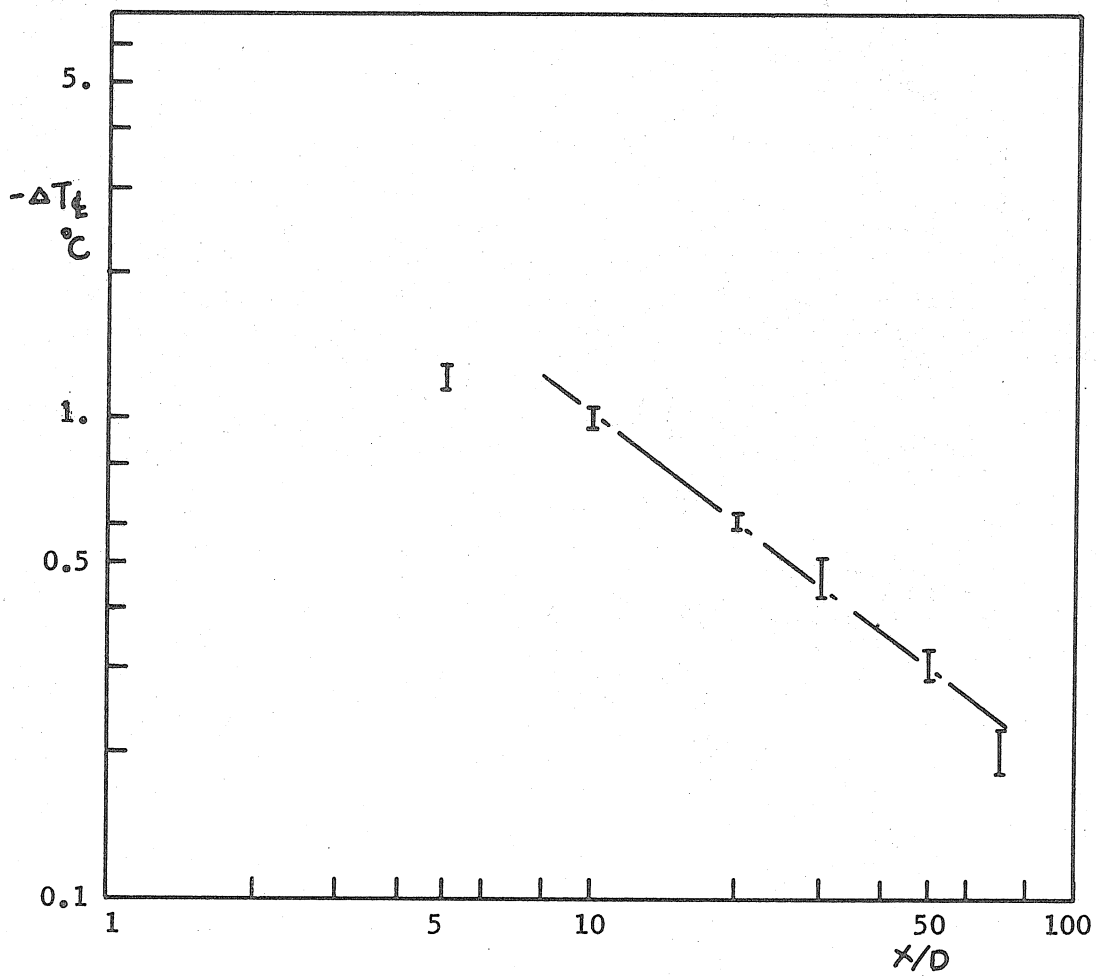


Fig. 9. Axial Variation of Temperature in the Wake

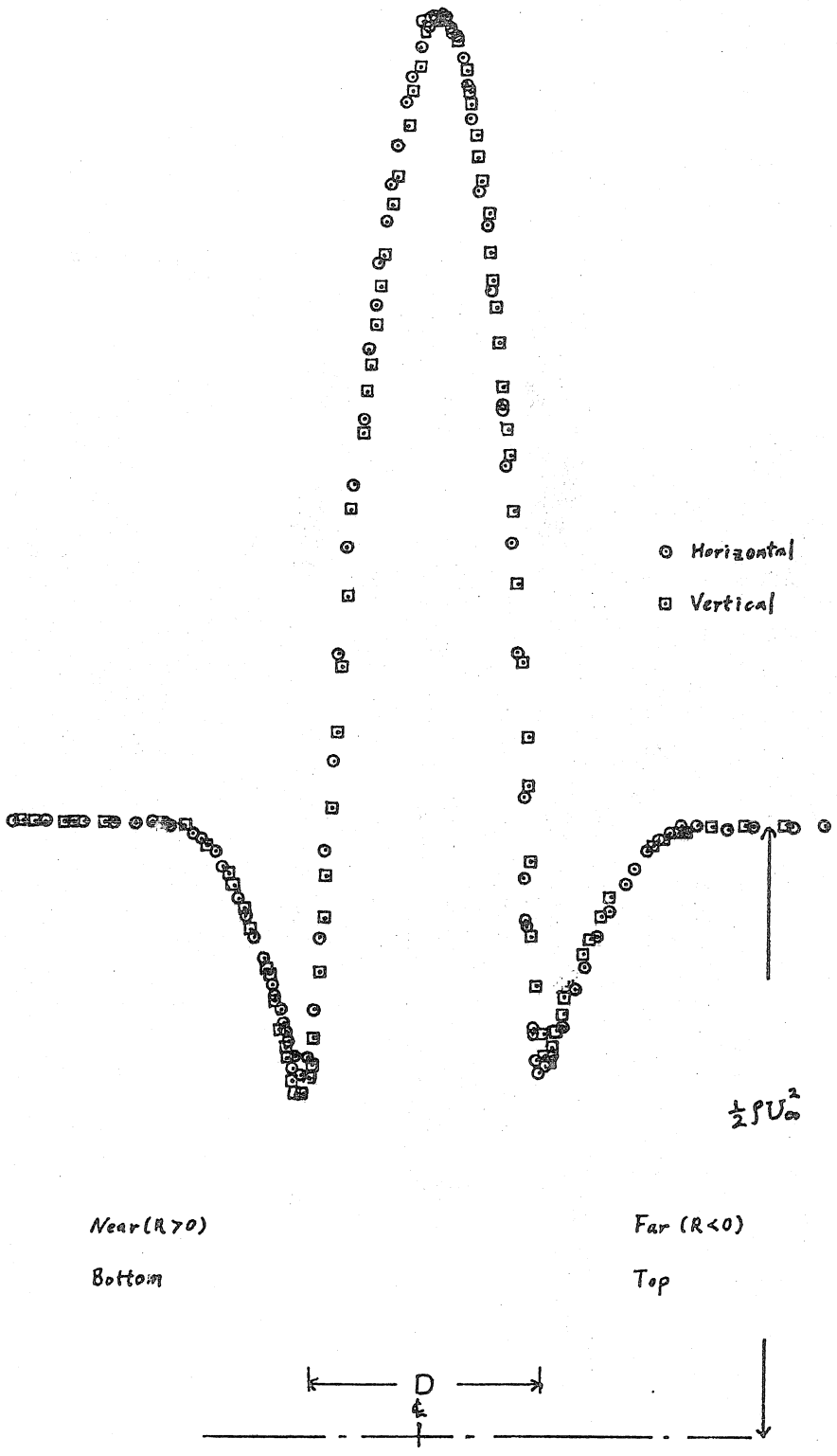


Fig. 10. Axisymmetry of the Wake: Dynamic Pressure Distribution at X/D = 1

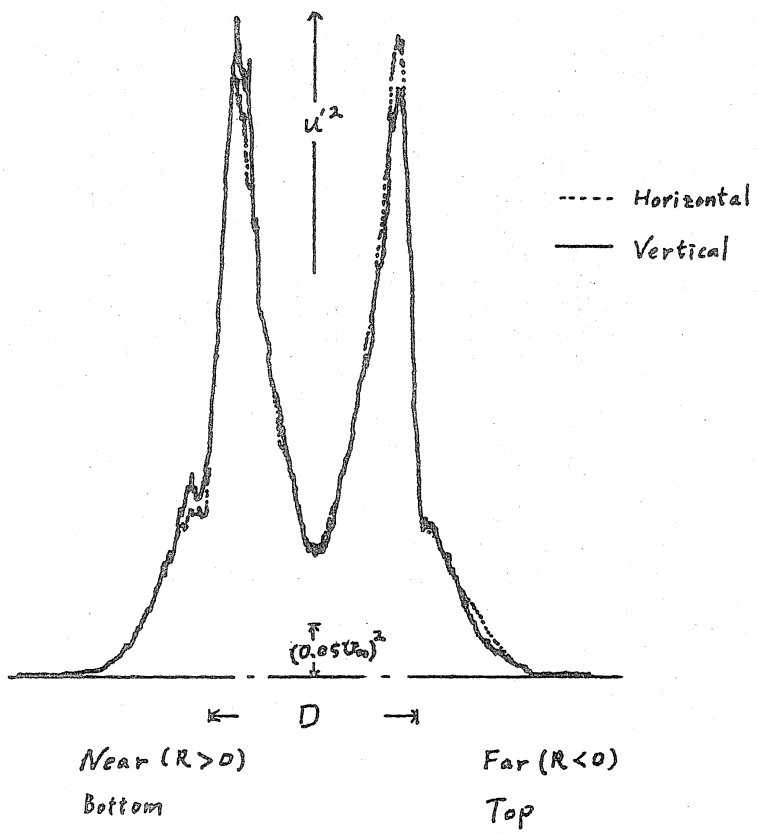


Fig. 11. Axisymmetry of the Wake: Mean Square Axial Turbulent Intensity at X/D = 1

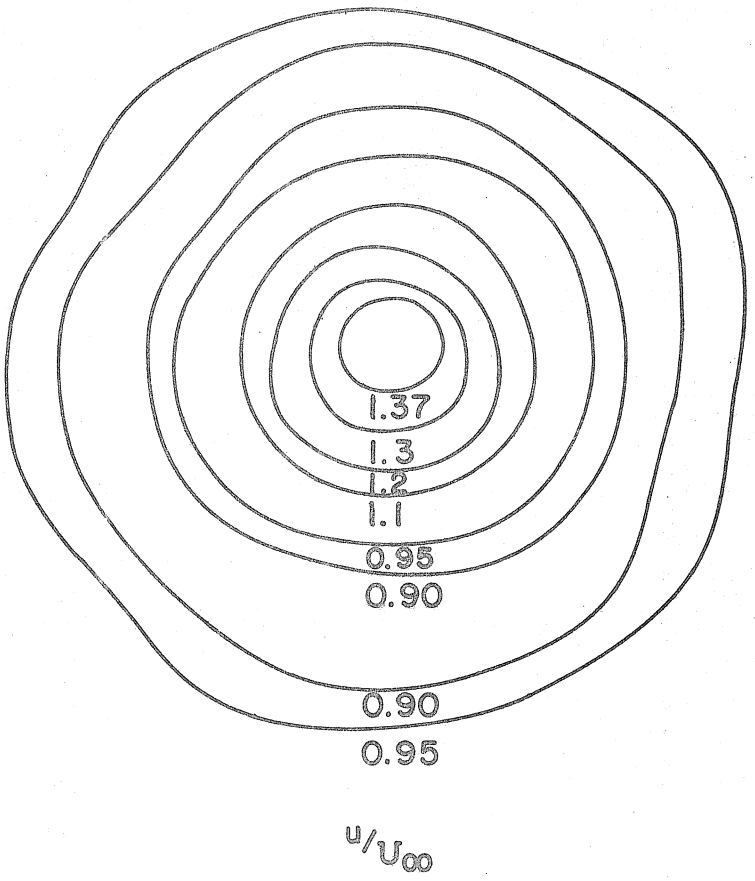


Fig. 12. Mean Velocity Contour Profile at X/D=40

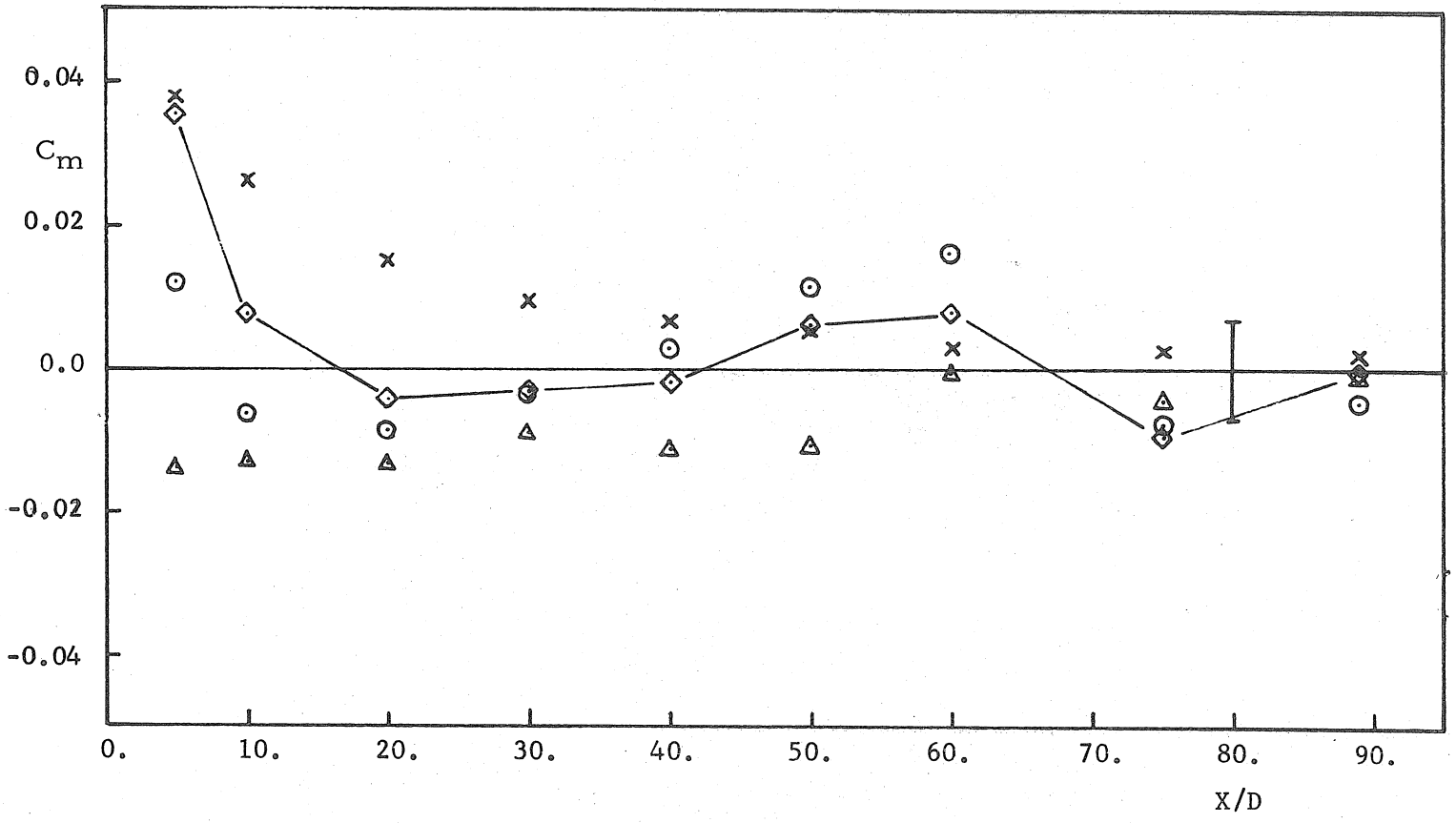


Fig. 13. Momentum Balance in the Smooth Wall Matched Injection Case

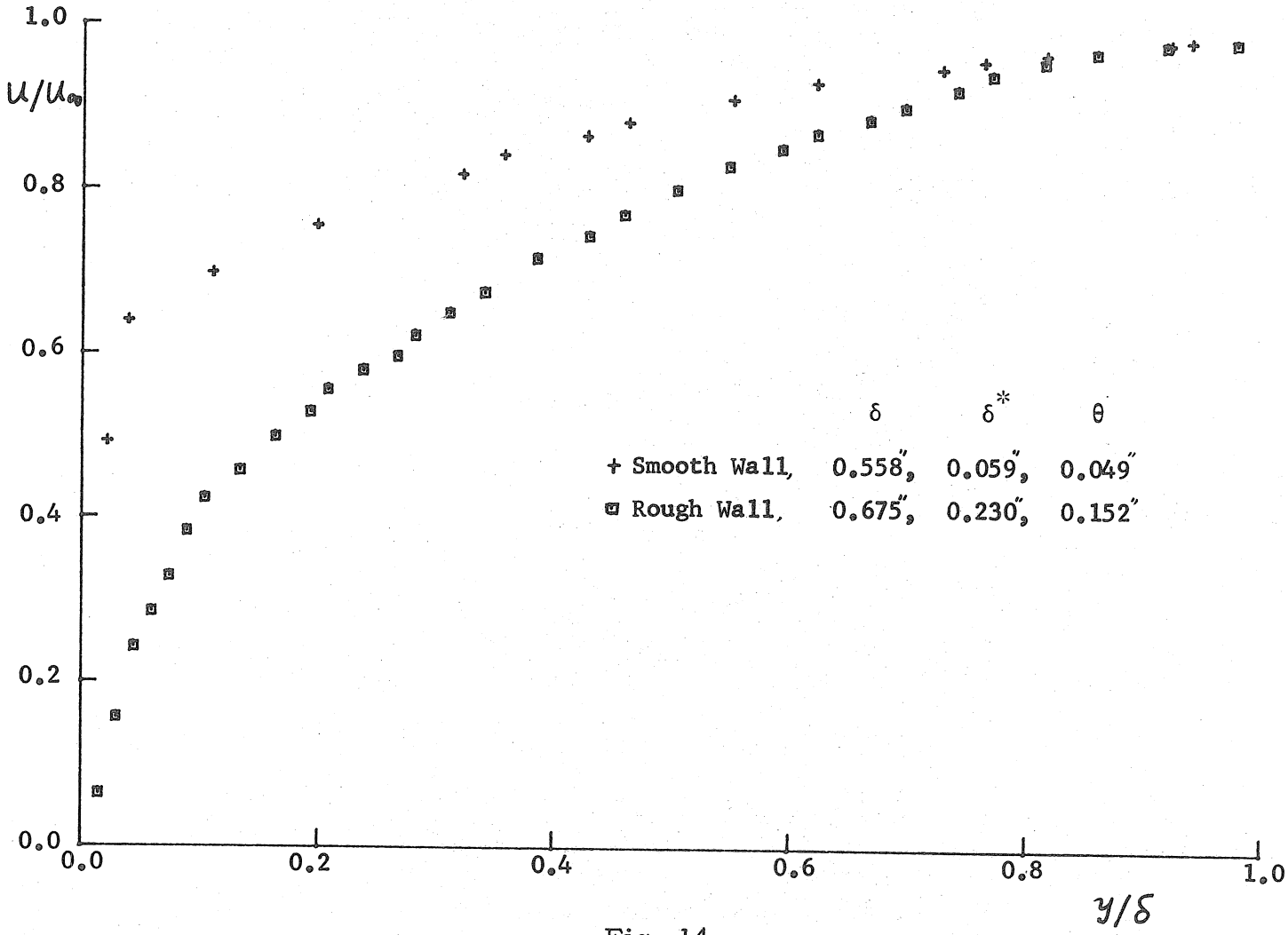


Fig. 14.

Boundary Layer Velocity Profiles on the Models

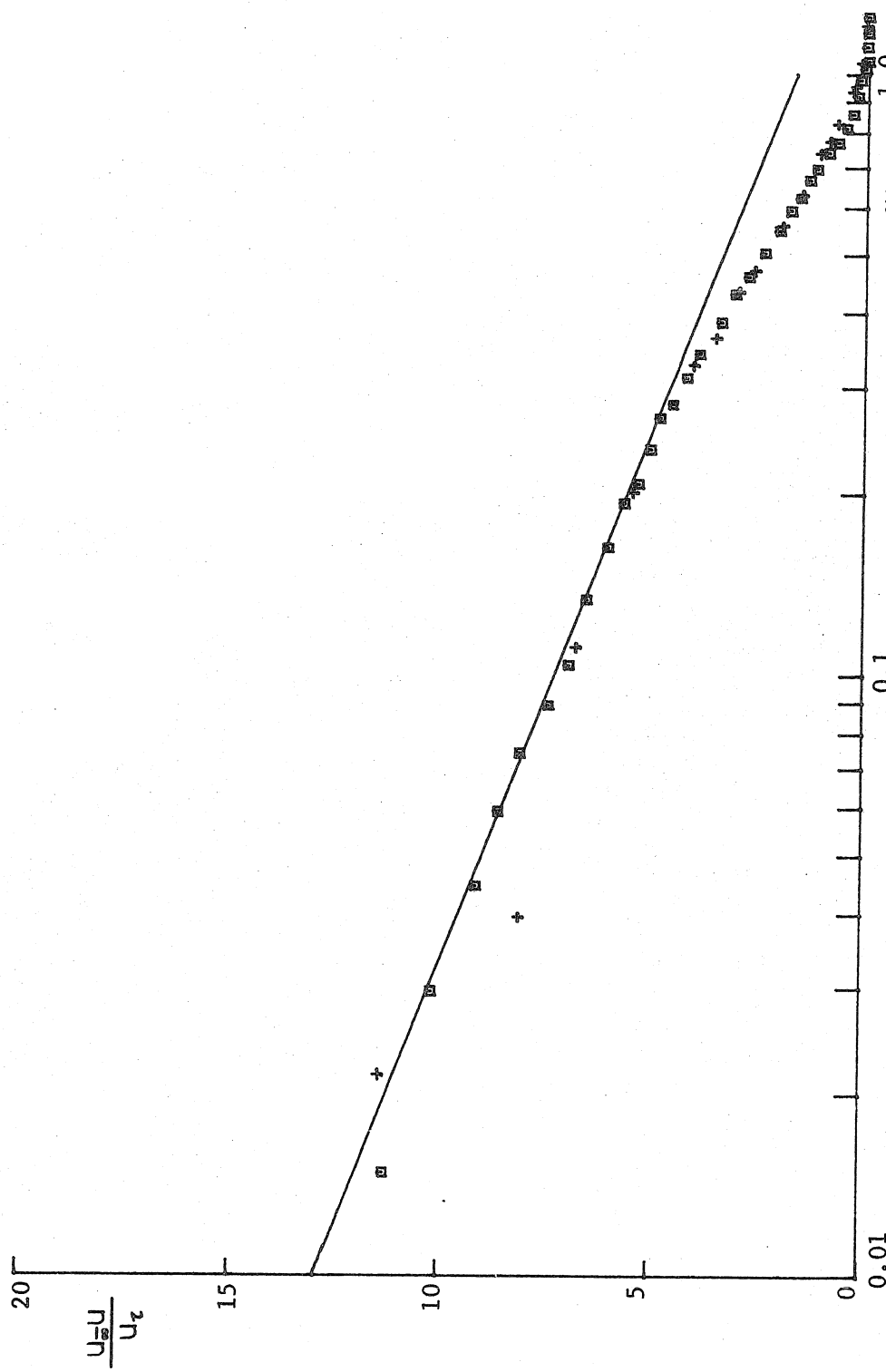


Fig. 15. Velocity Defect Law and the Boundary Layers on the Models

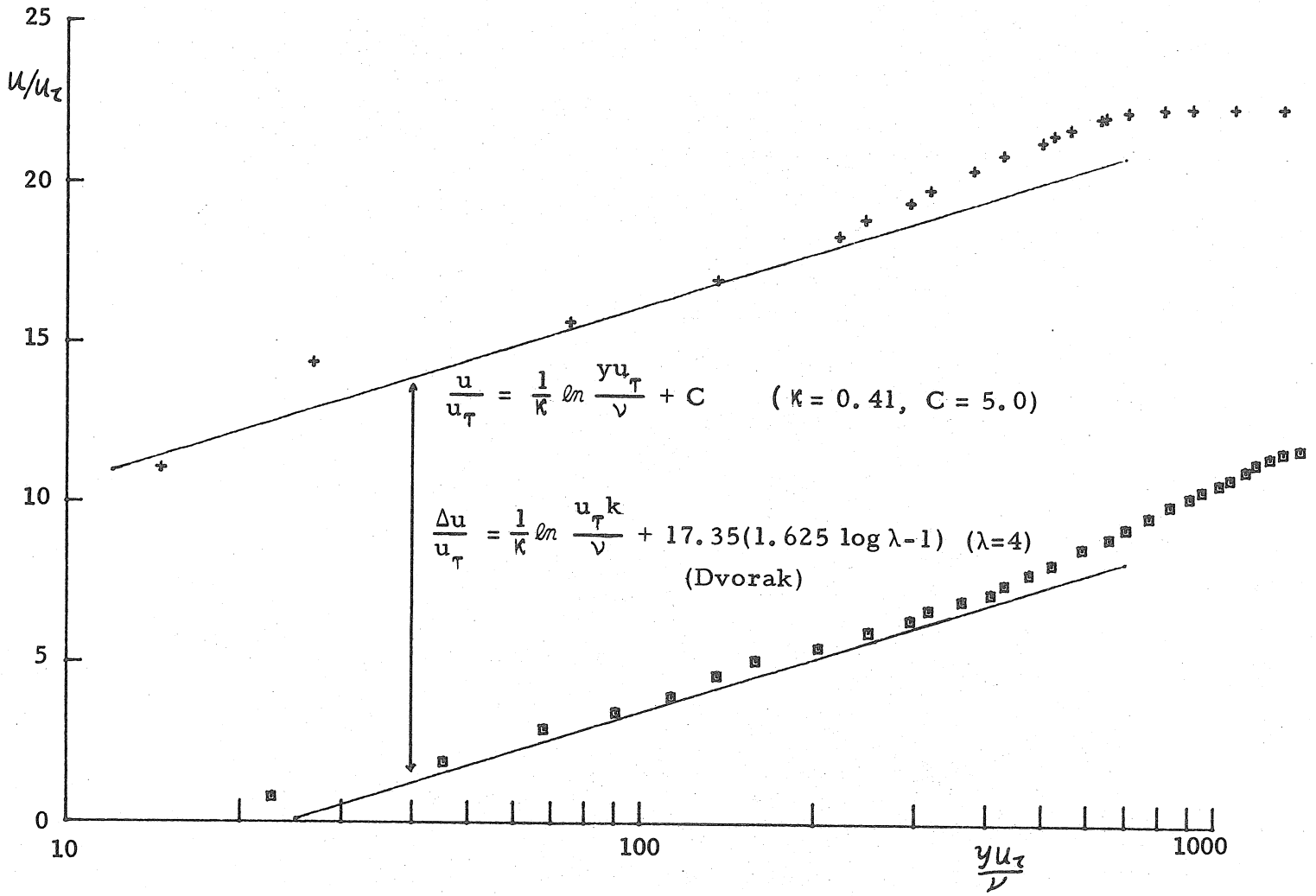


Fig. 16. Law of the Wall and the Boundary Layers on the Models

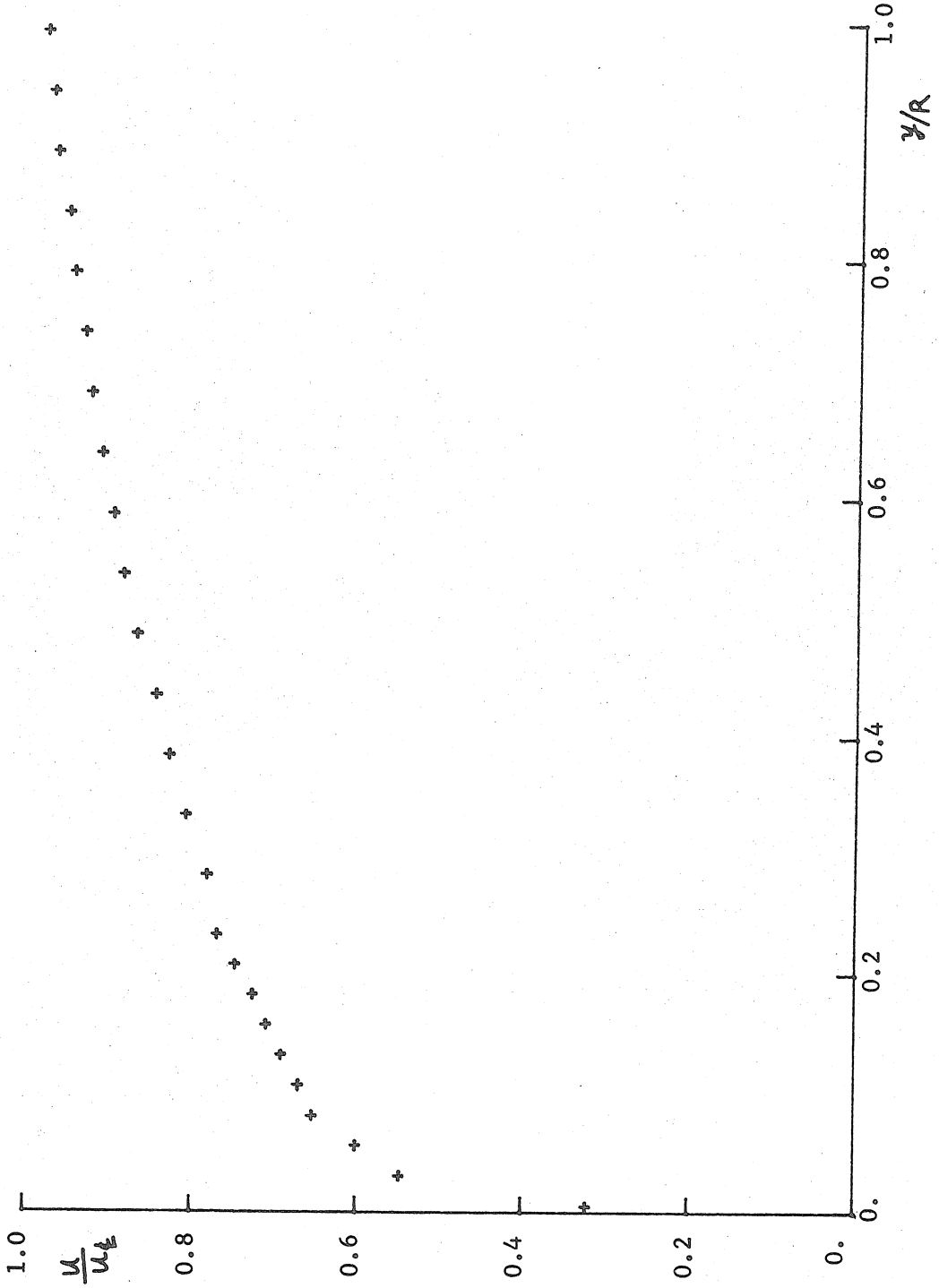


Fig. 17. Mean Velocity Profile of the Jet at the Exit

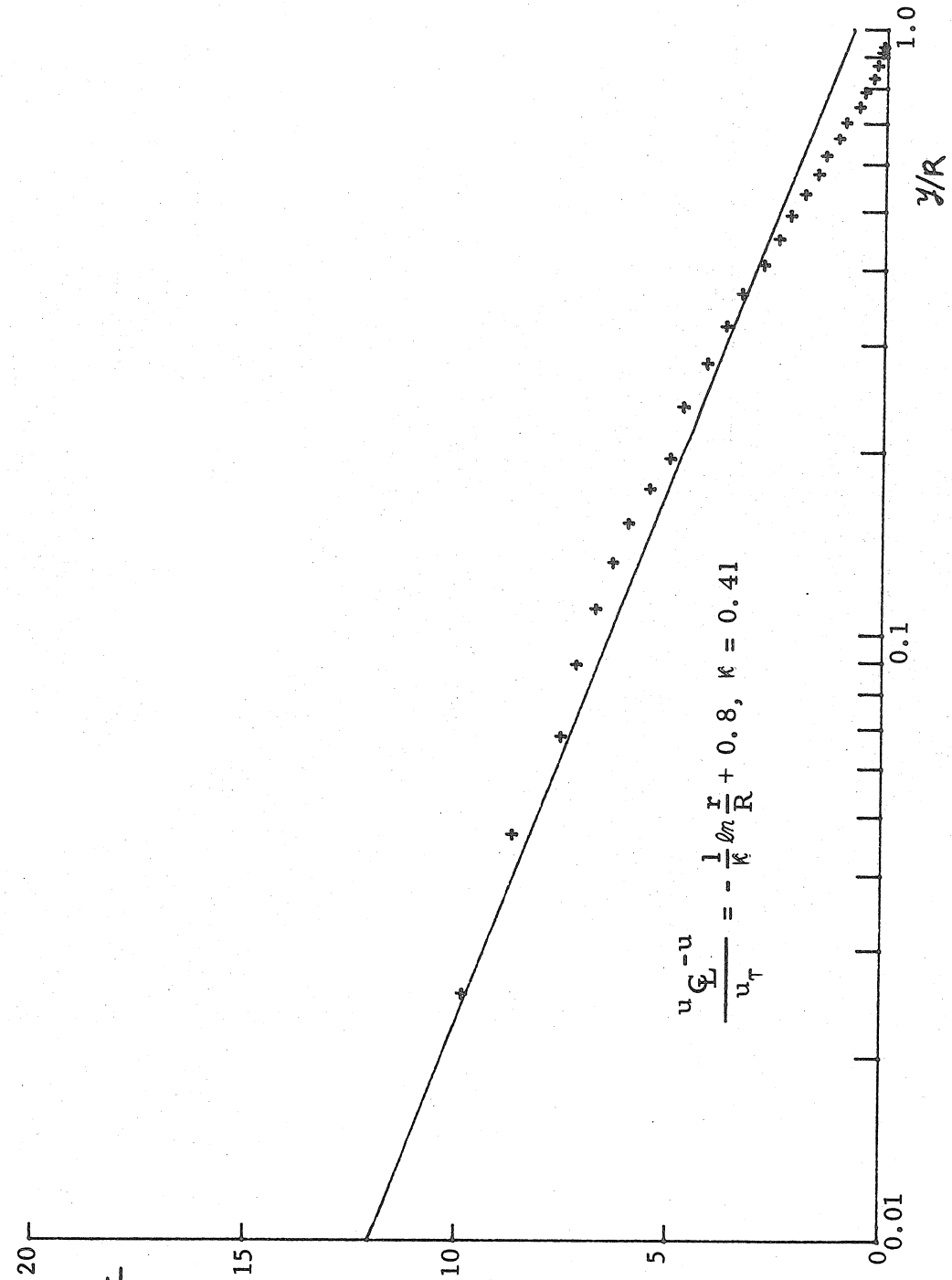


Fig. 18. Velocity Defect Law and Mean Velocity Profile of the Jet

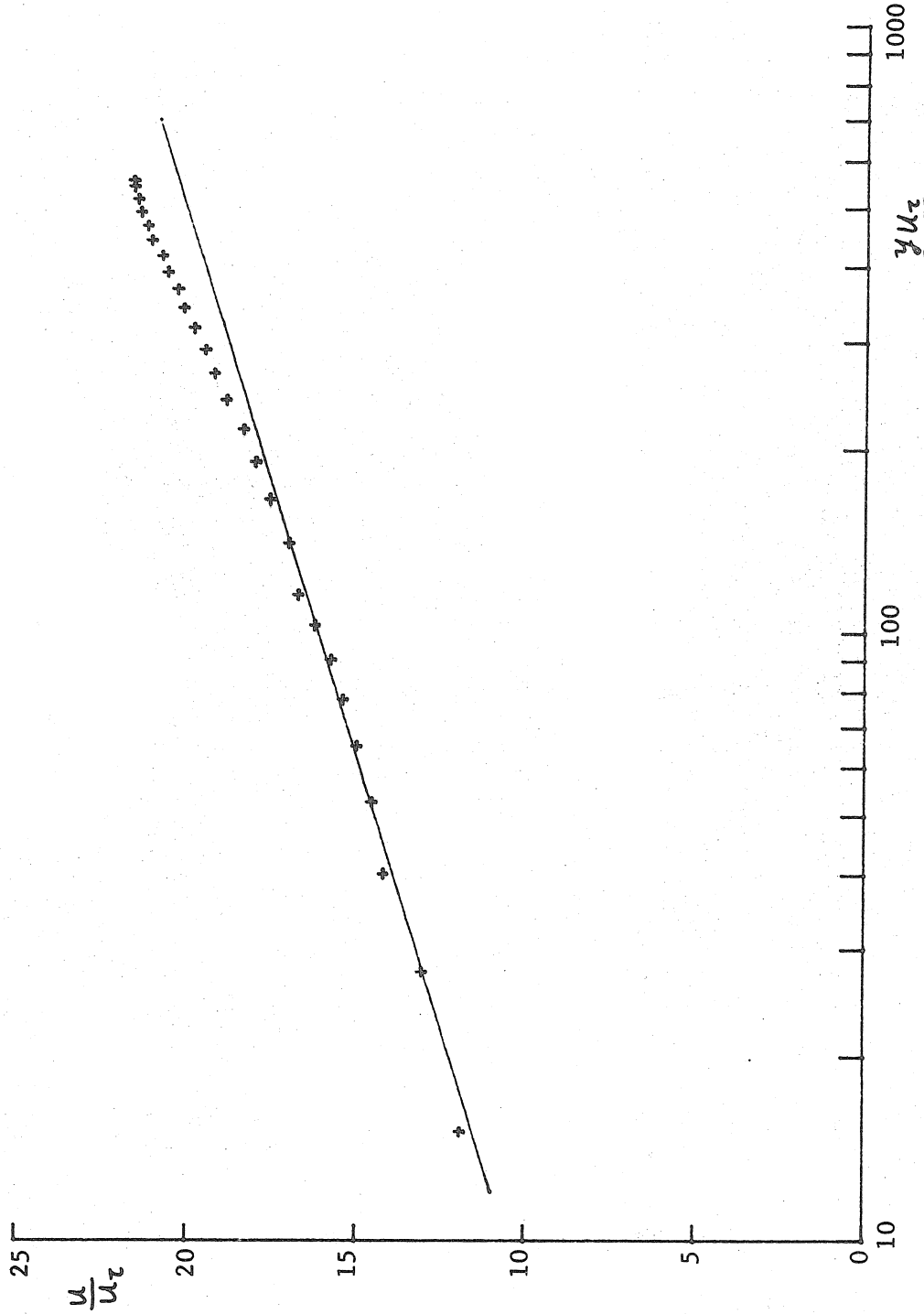


Fig. 19. Law of the Wall and the Velocity Profile of the Jet

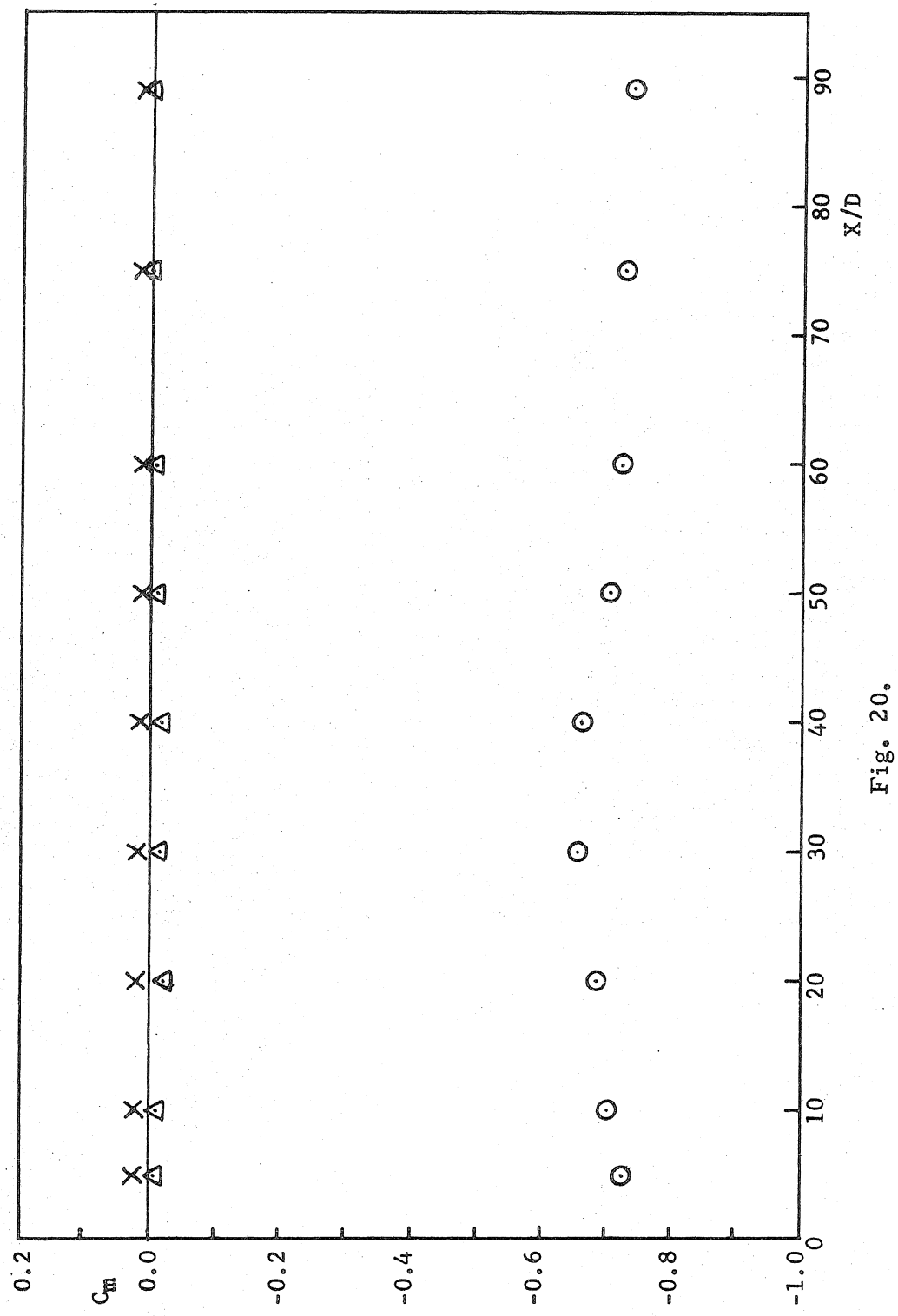


Fig. 20.
Momentum Integral in Pure Wake (Smooth Wall)
⊙ Mean Velocity Integral, △ Mean Static Pressure Integral, × Velocity Fluctuation Integral

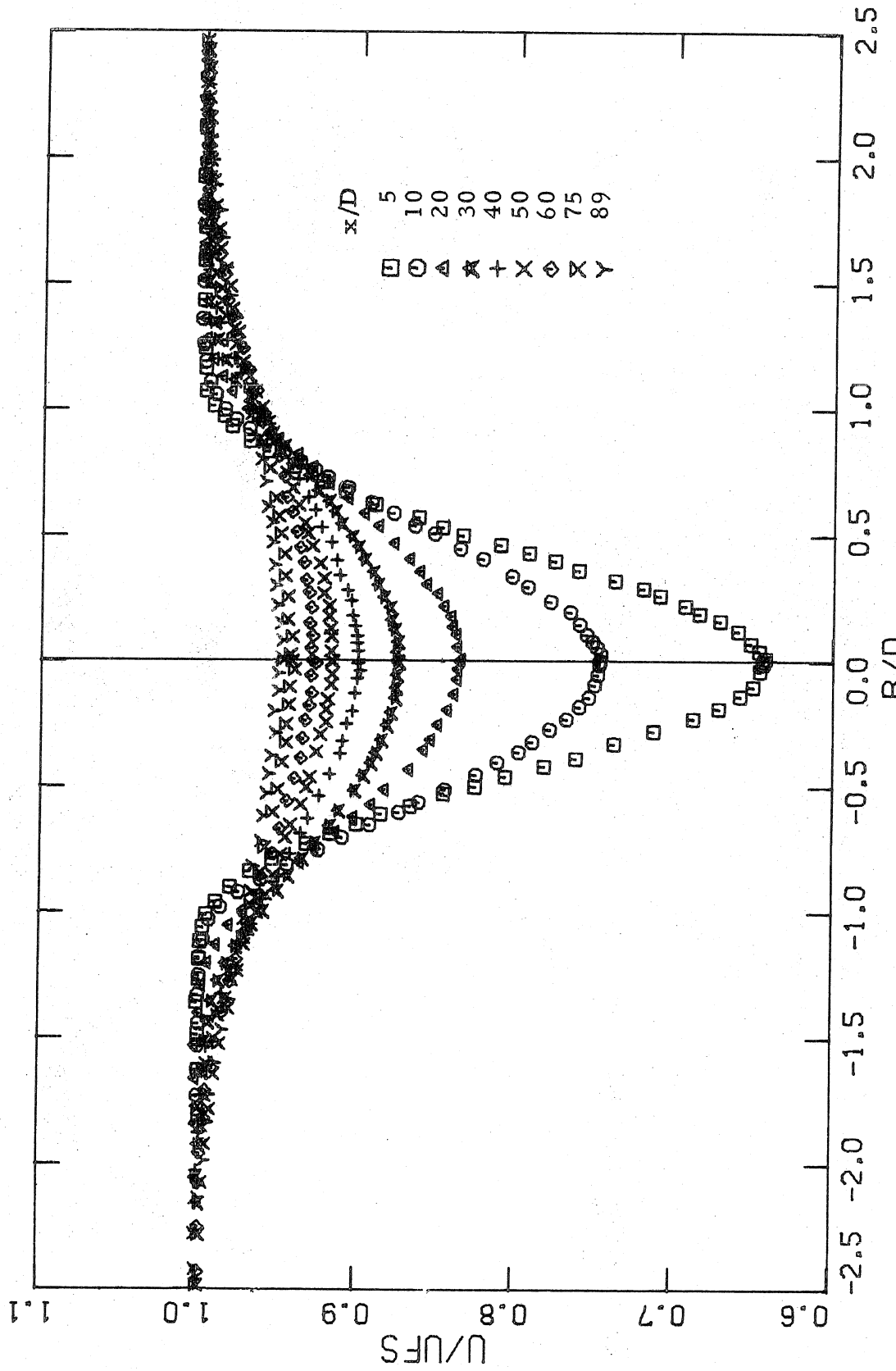


Fig. 21. Pure Wake: Mean Velocity Profiles

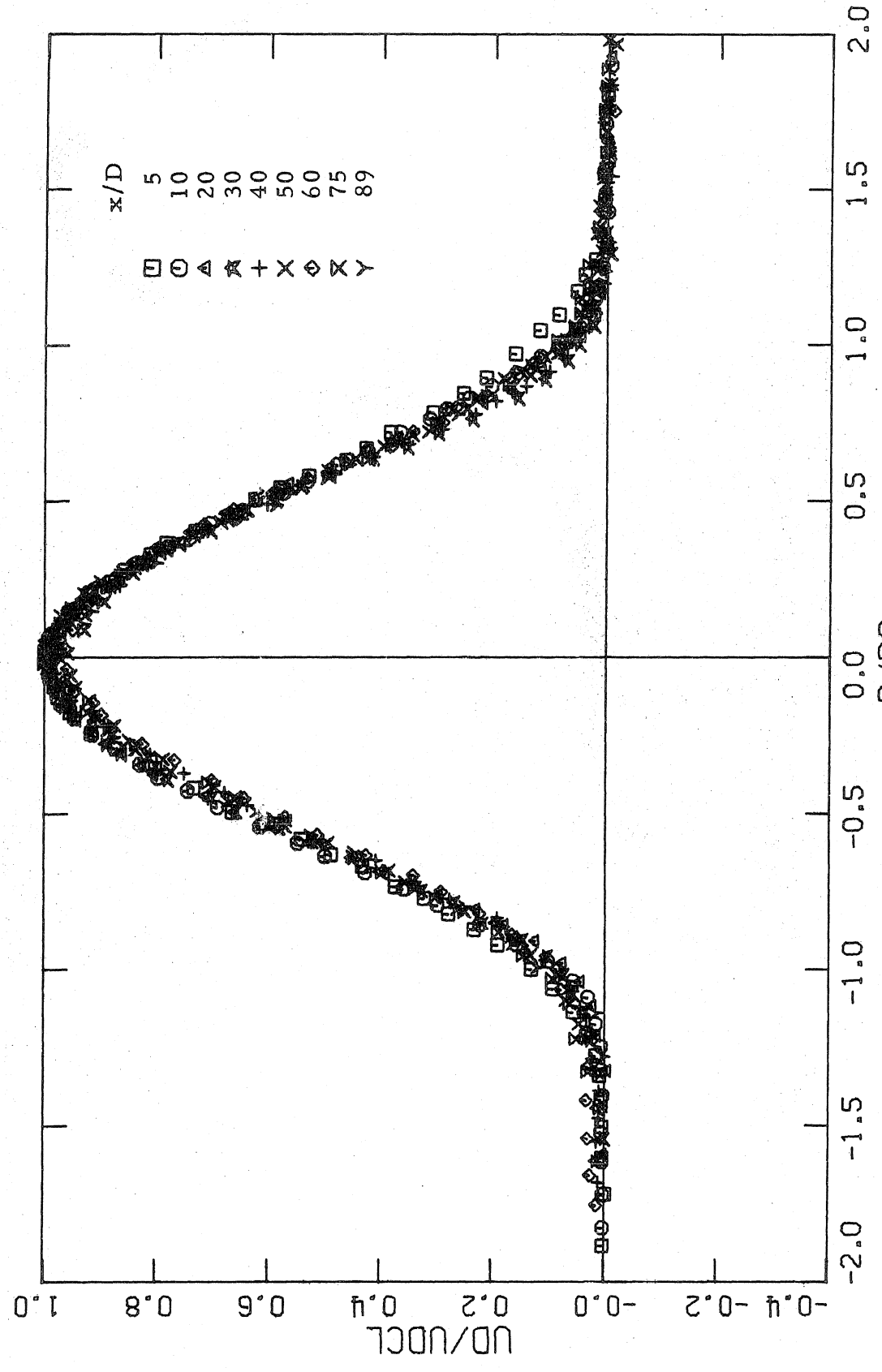


Fig. 22. Pure Wake: Normalized Mean Velocity Profiles

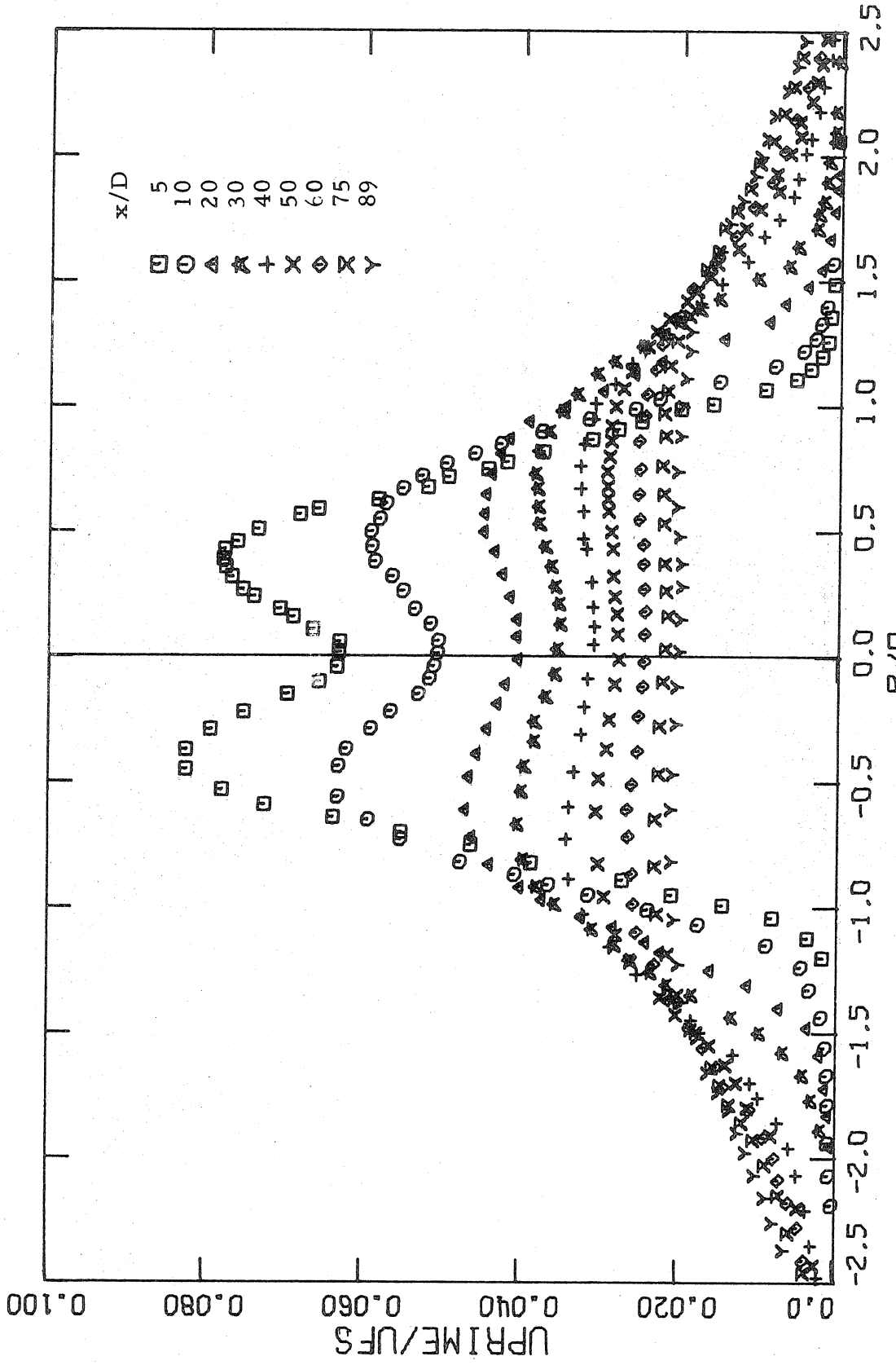


Fig. 23. Pure Wake: Axial Turbulence Intensity Distributions

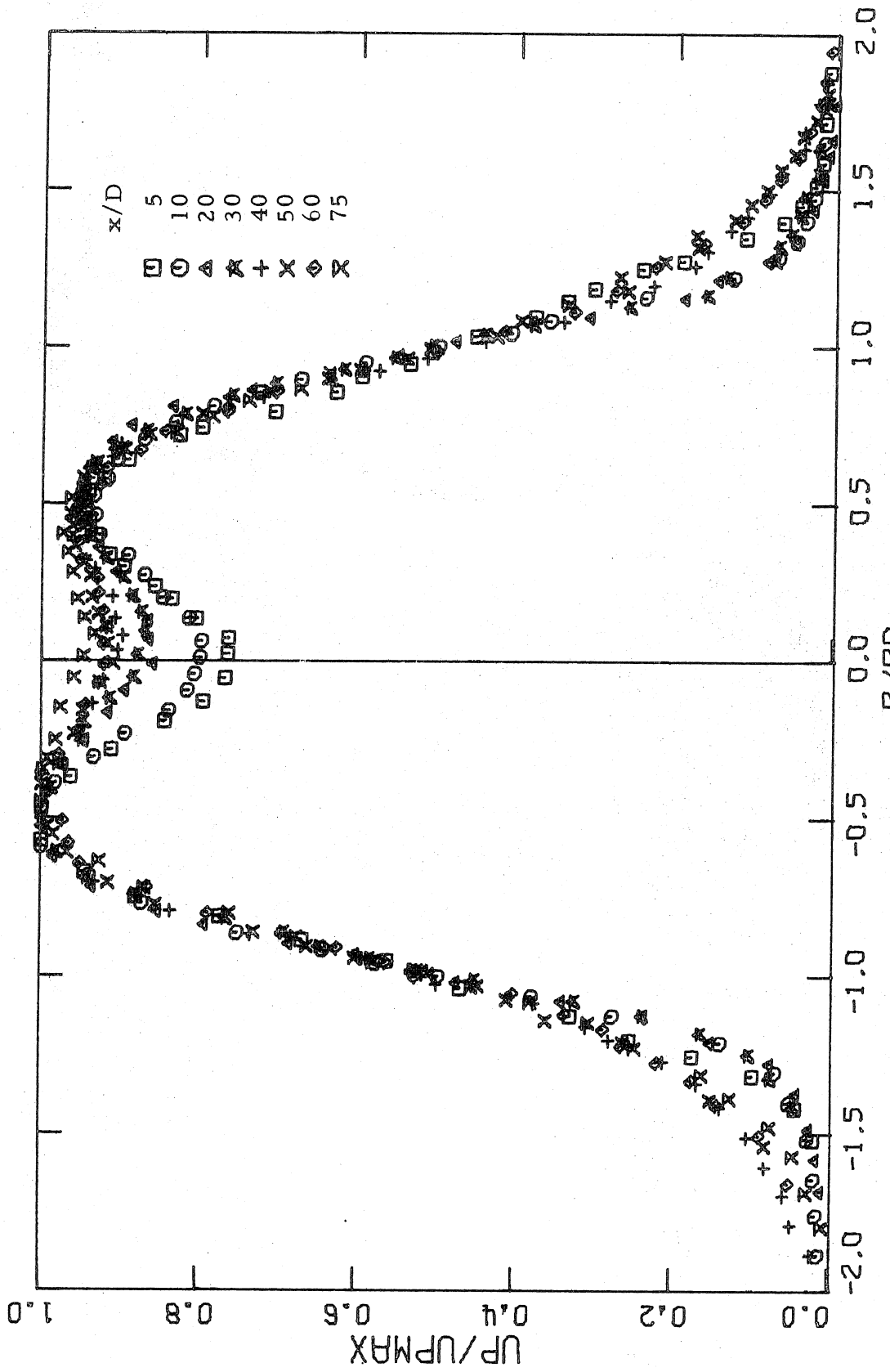


Fig. 24. Pure Wake: Normalized Profile of Axial Turbulent Intensity

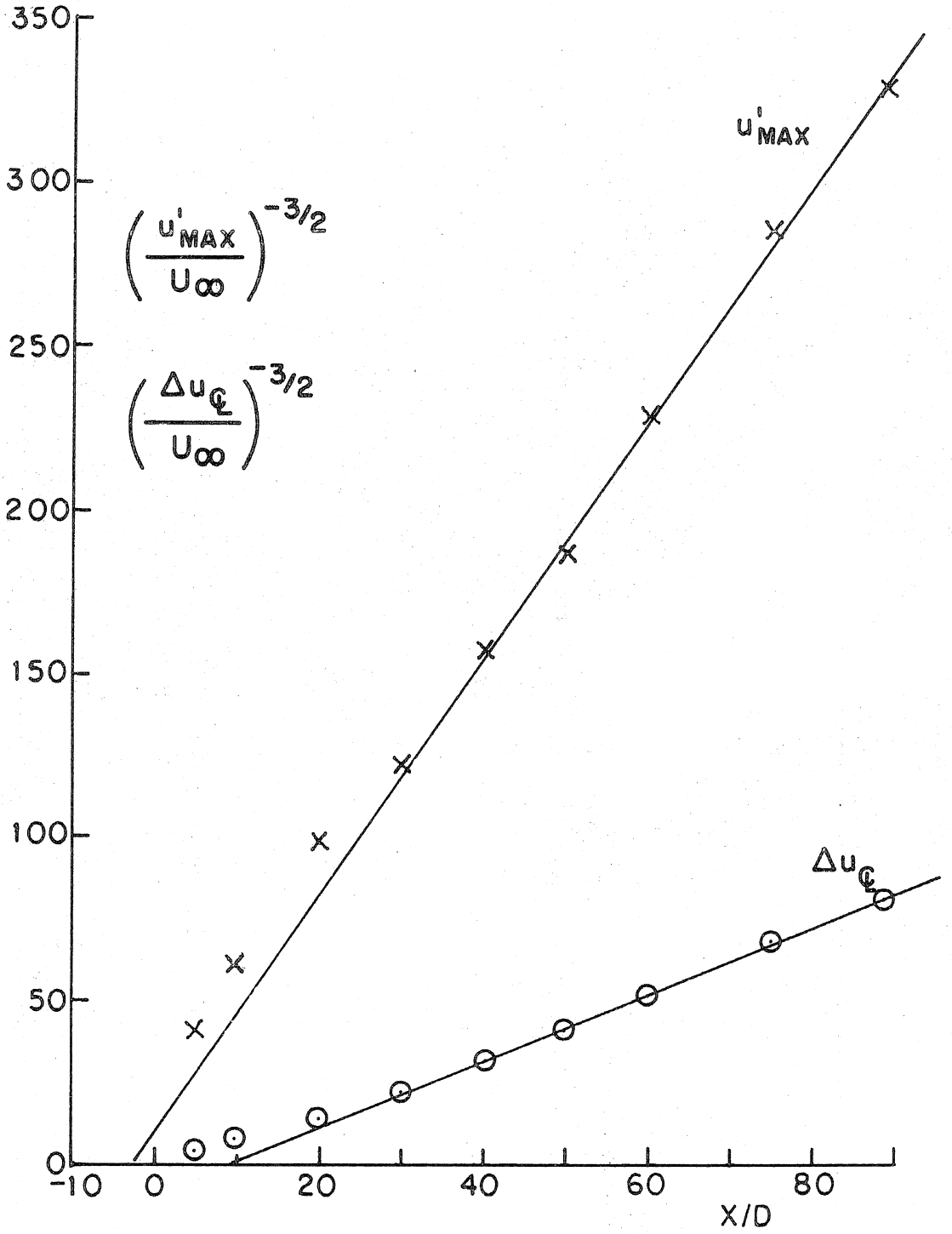


Fig. 25. Virtual Origin of Asymptotic Decay Law in Pure Wake

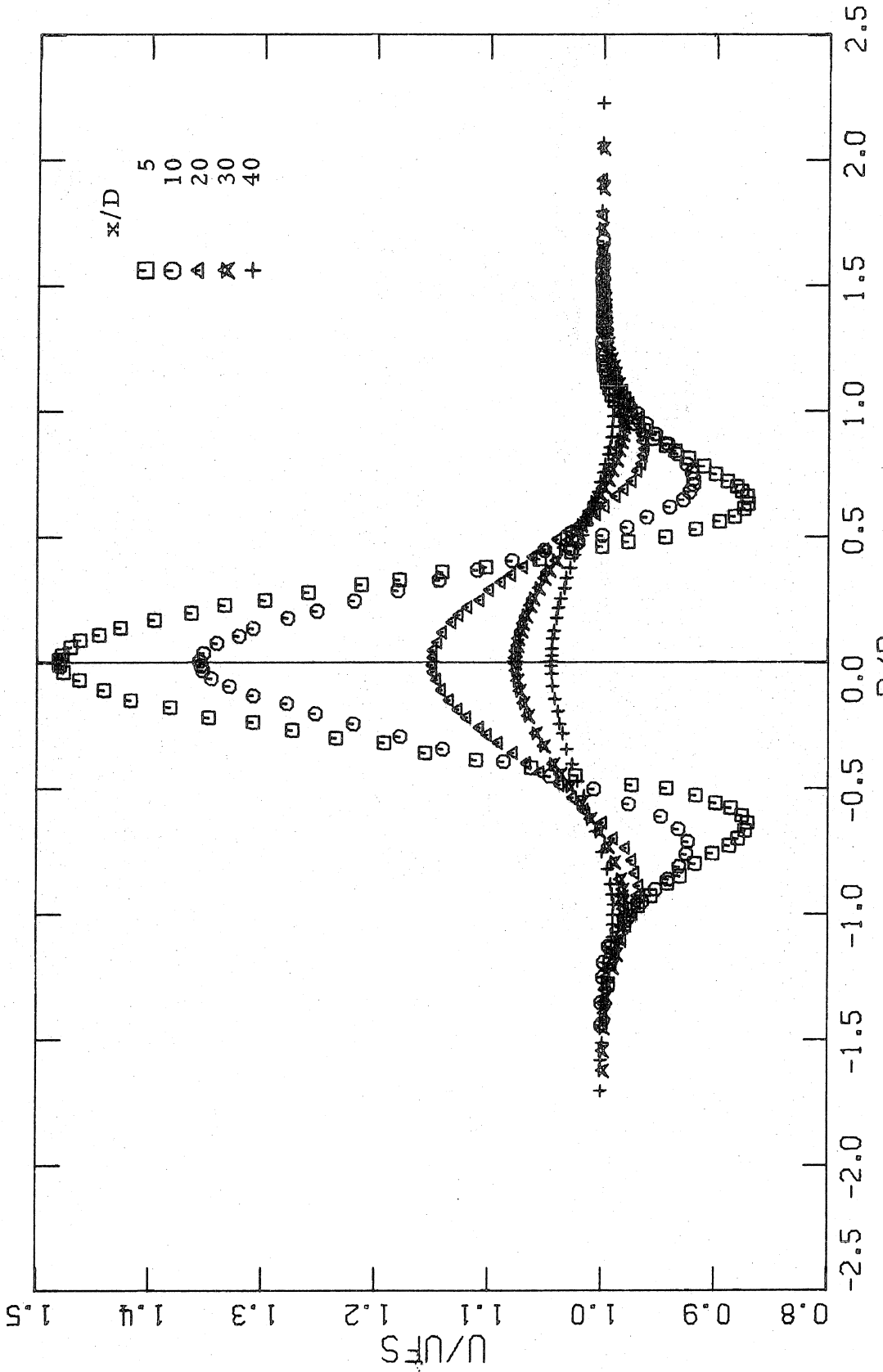


Fig. 26a. Matched Injection: Mean Velocity Profiles X/D = 5-40

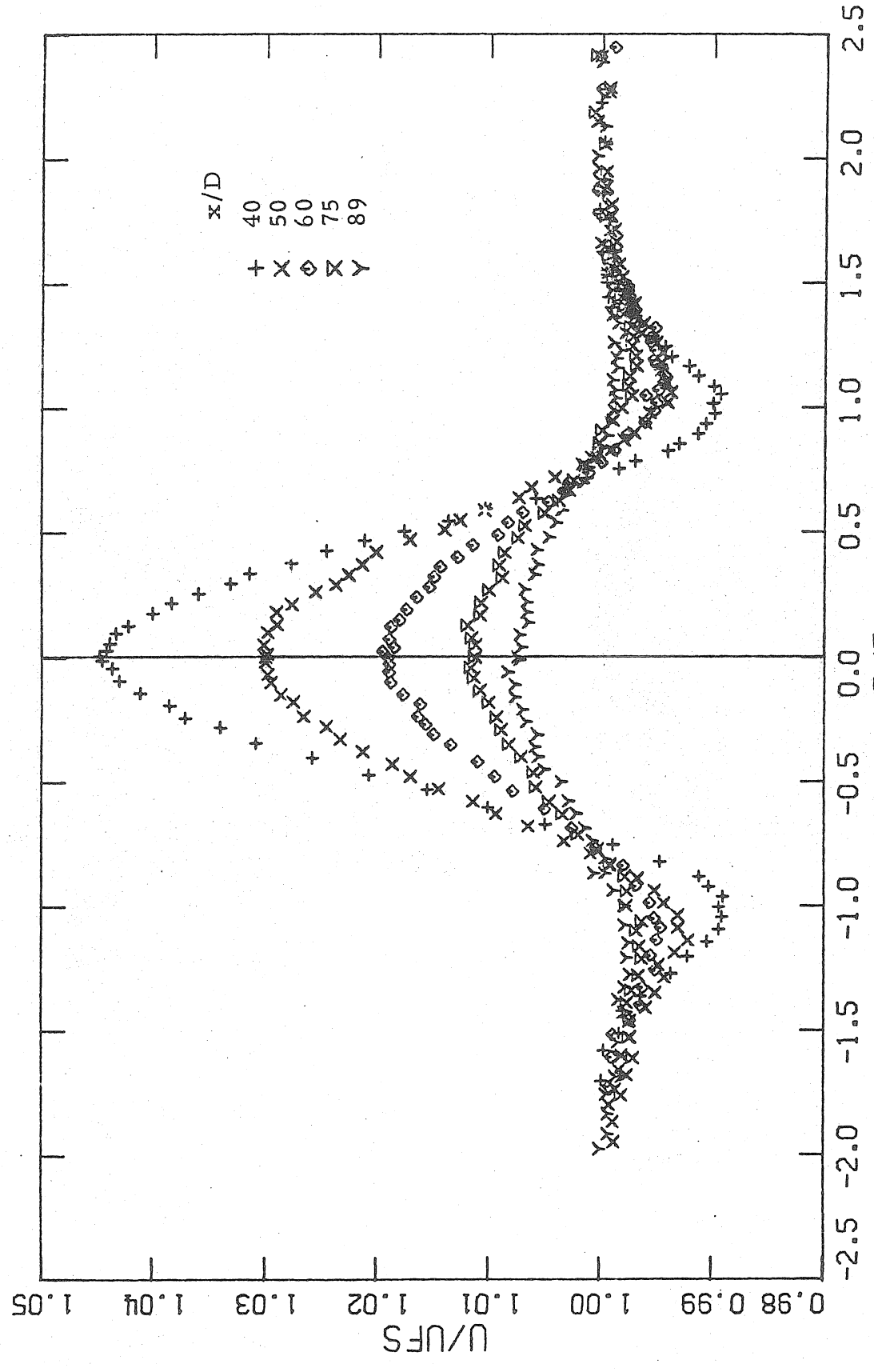


Fig. 26b. Matched Injection: Mean Velocity Profiles X/D = 40-89

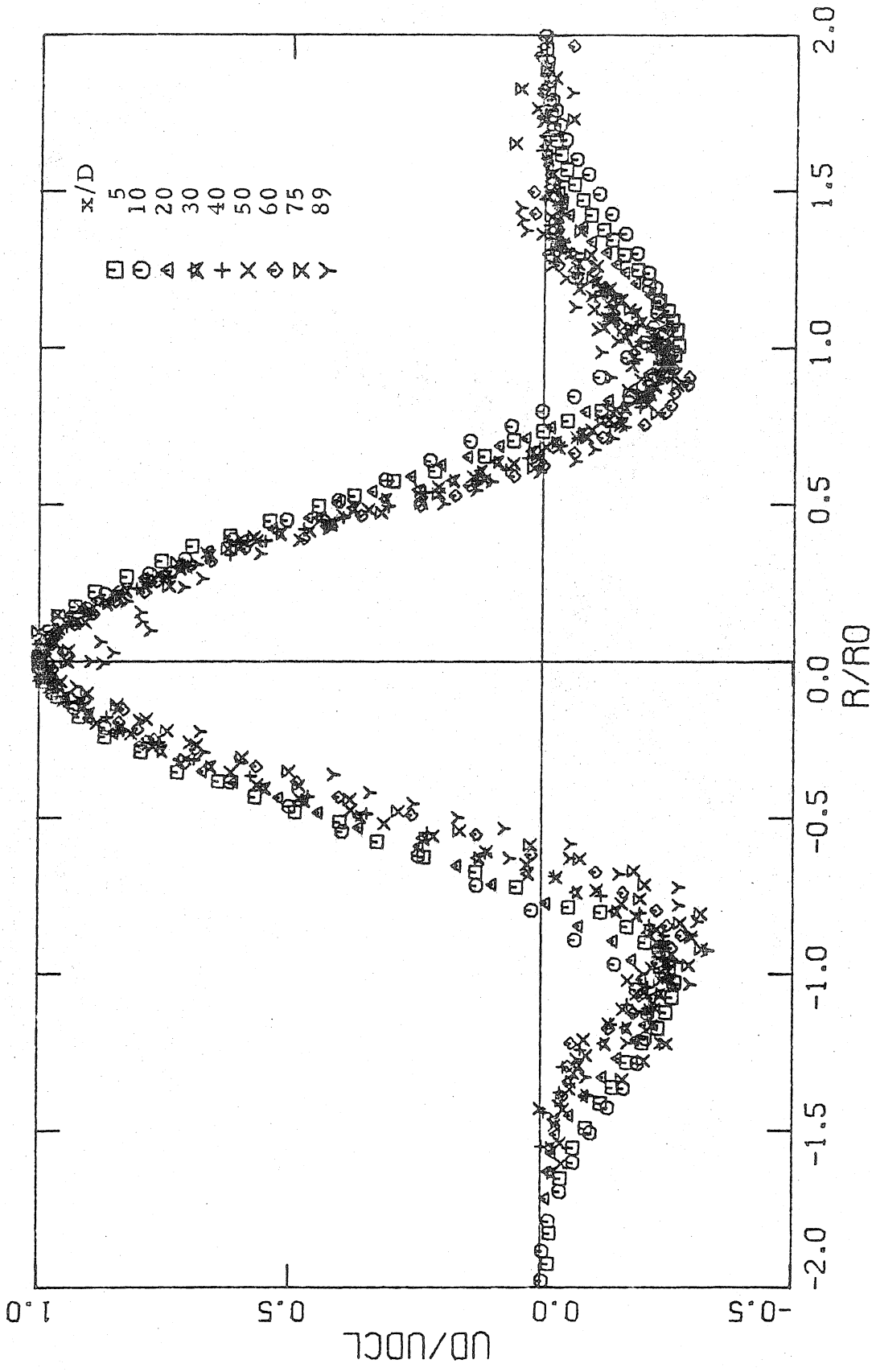


Fig. 27. Matched Injection: Normalized Mean Velocity Profile

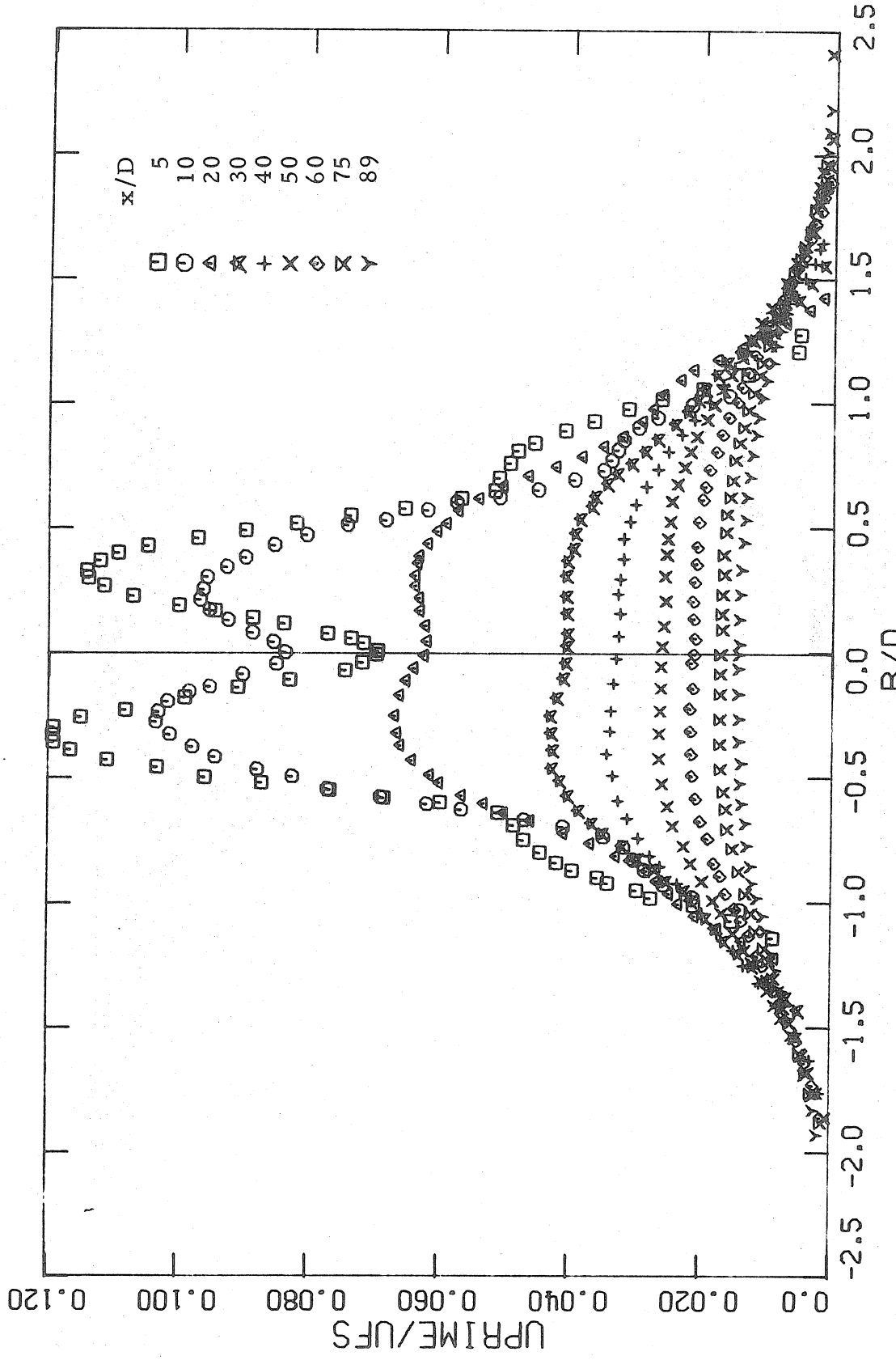


Fig. 28. Matched Injection: Axial Turbulence Intensity

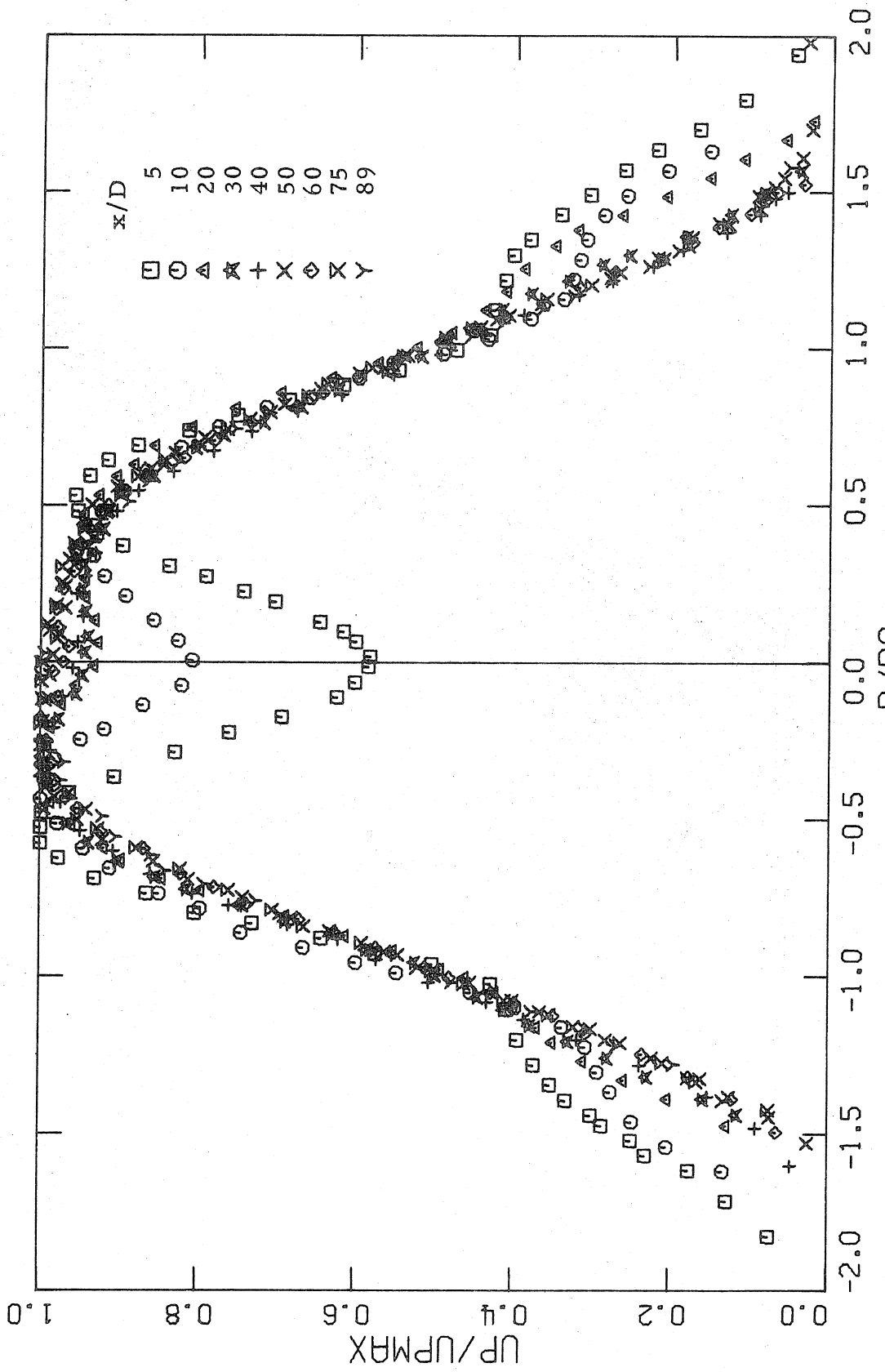


Fig. 29. Matched Injection: Normalized Axial Turbulence Intensity

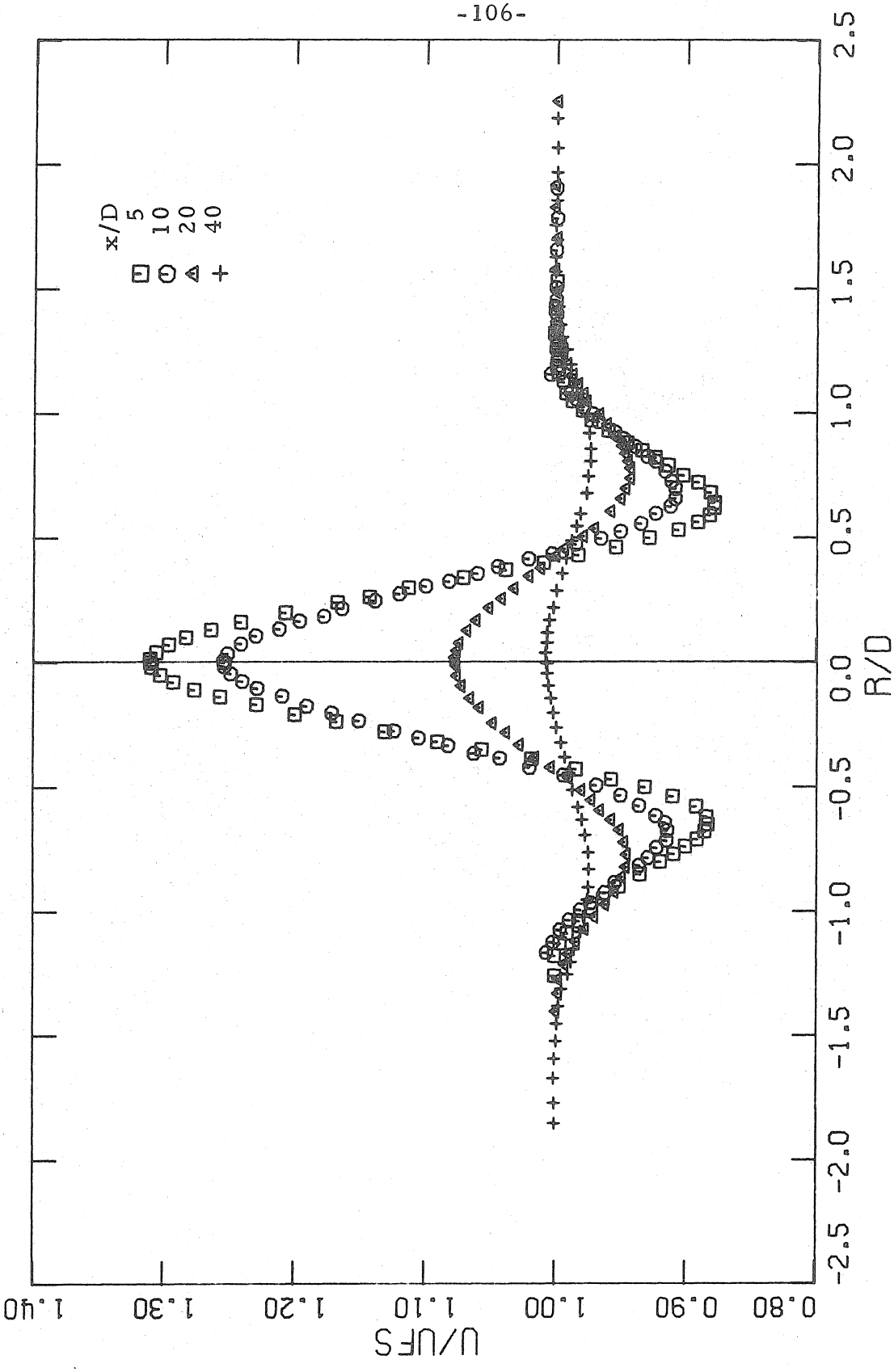


Fig. 30a. Weak Injection: Mean Velocity Profiles, X/D = 5-40

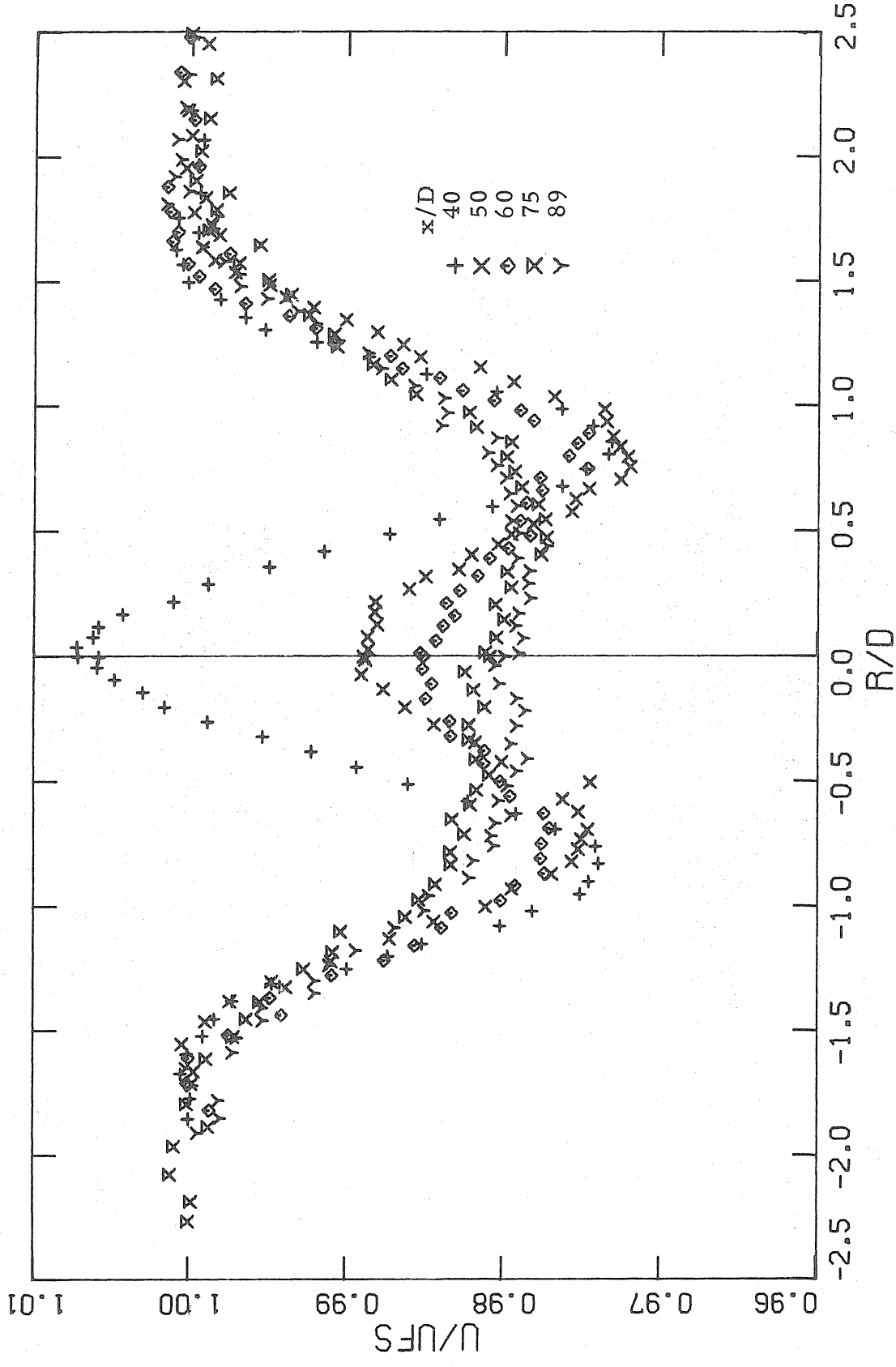


Fig. 30b. Weak Injection: Mean Velocity Profiles, X/D = 40-89

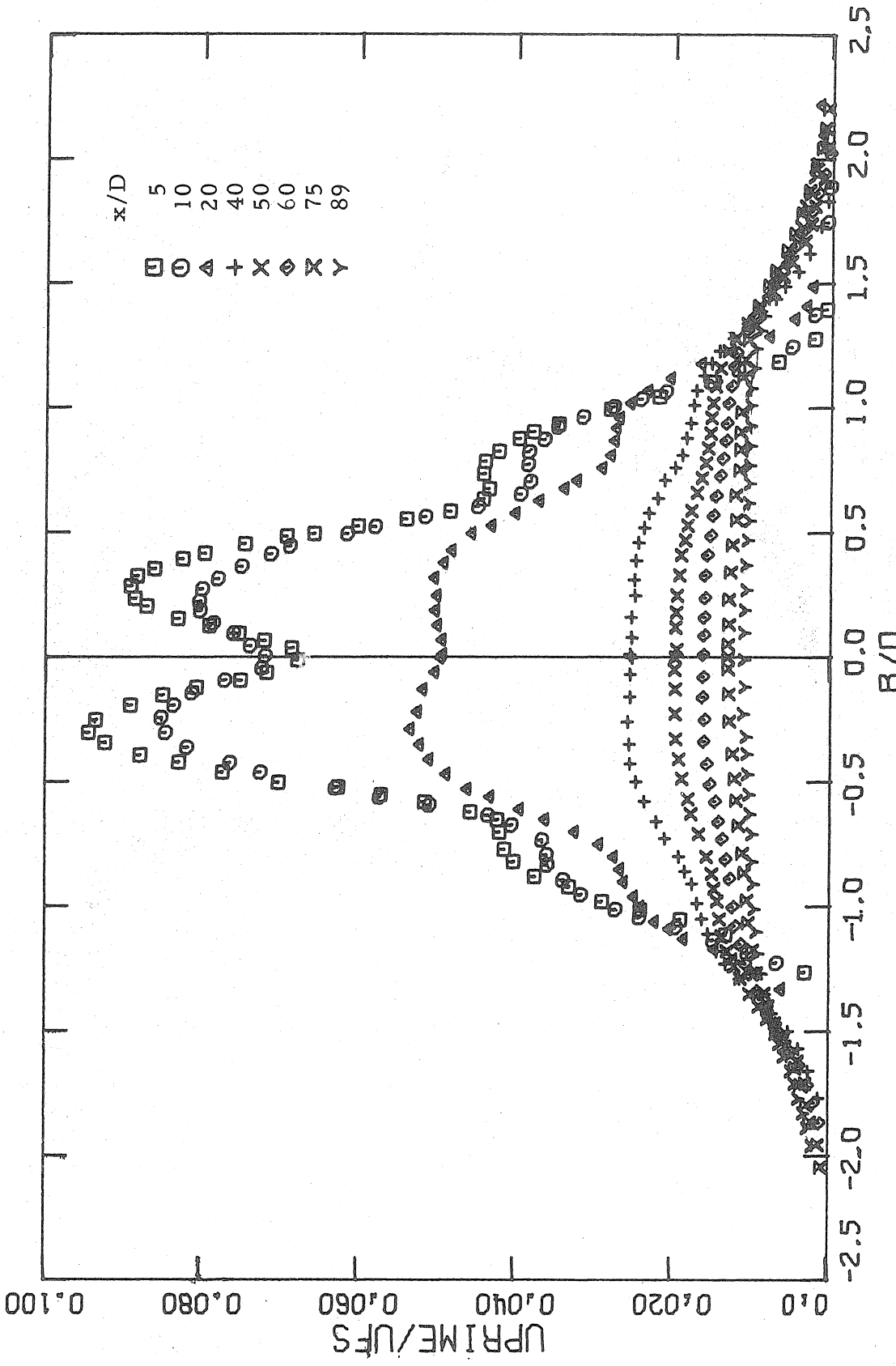


Fig. 31. Weak Injection: Axial Turbulence Intensity

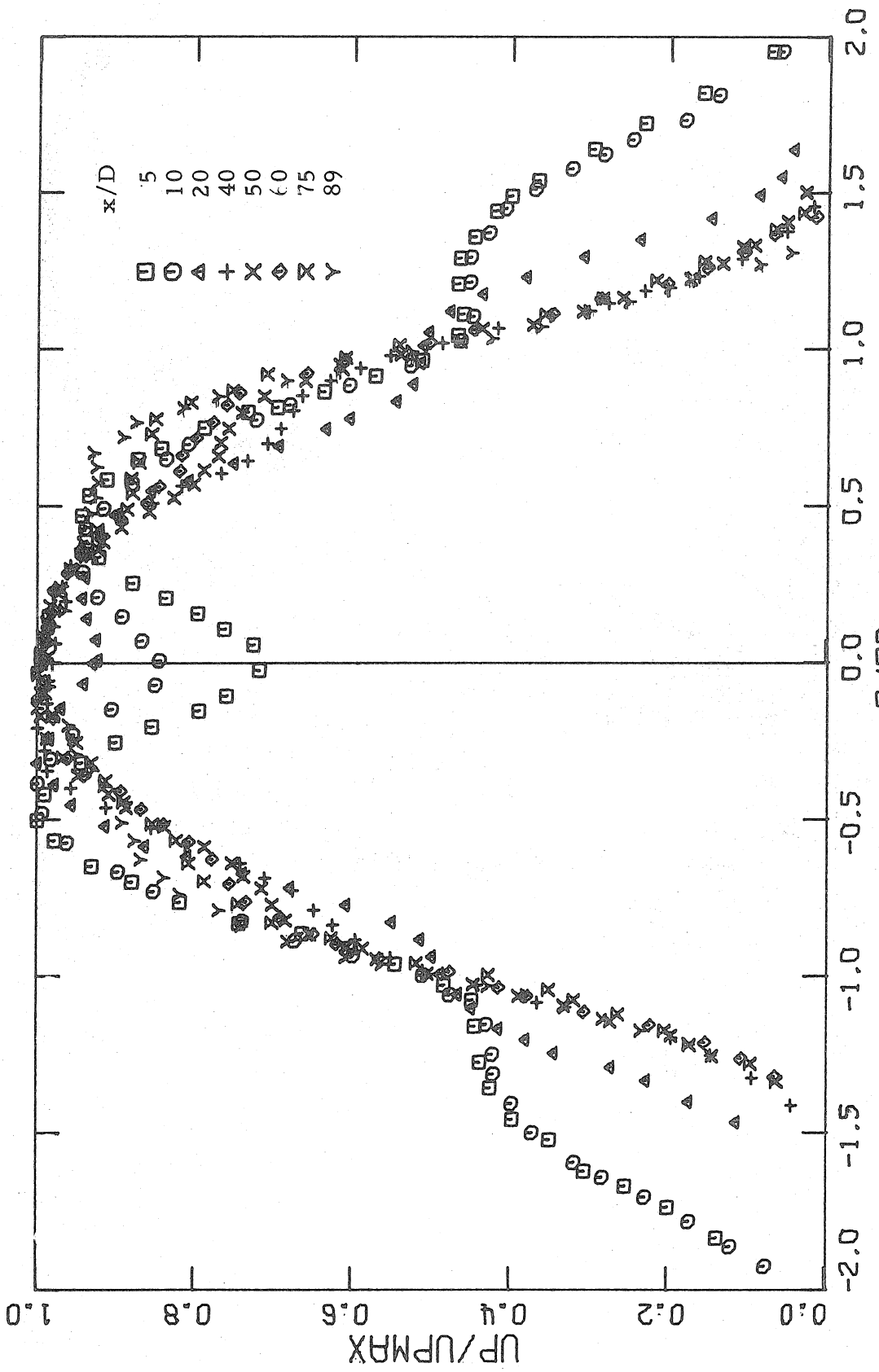


Fig. 32. Weak Injection: Normalized Axial Turbulence Intensity

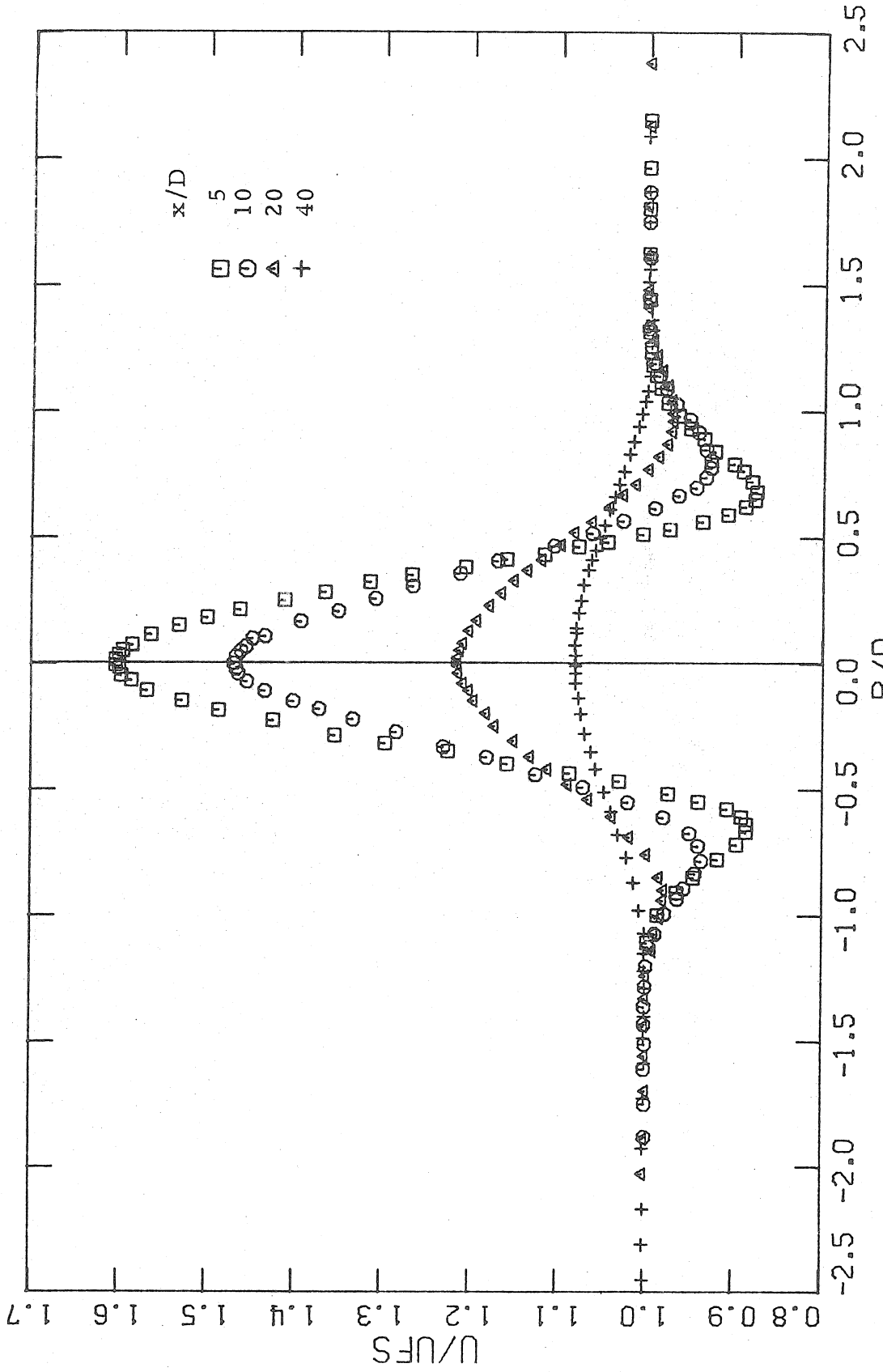


Fig. 33a. Strong Injection: Mean Velocity Profiles X/D = 5-40

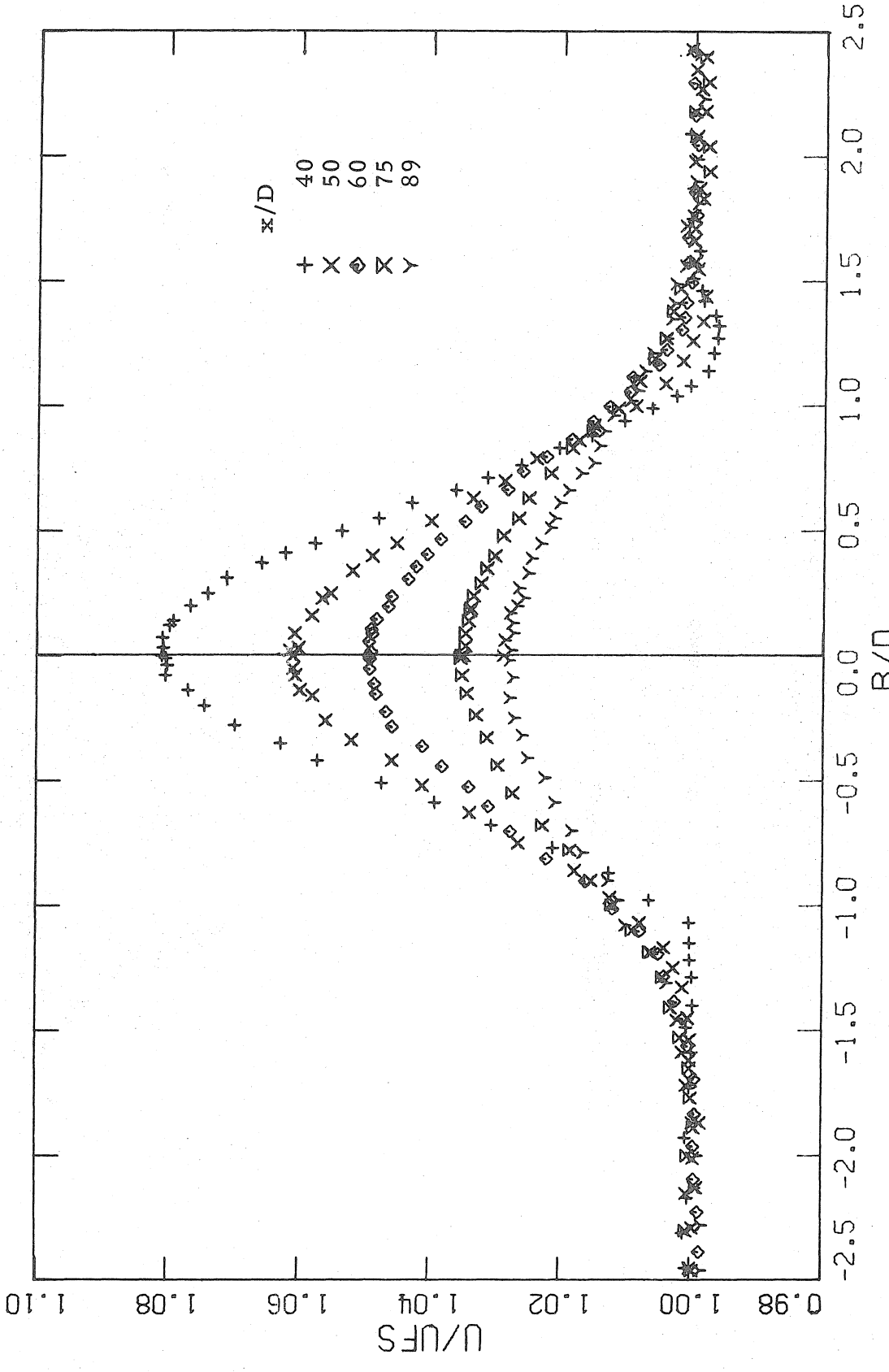


Fig. 33b. Strong Injection: Mean Velocity Profiles X/D = 40-89

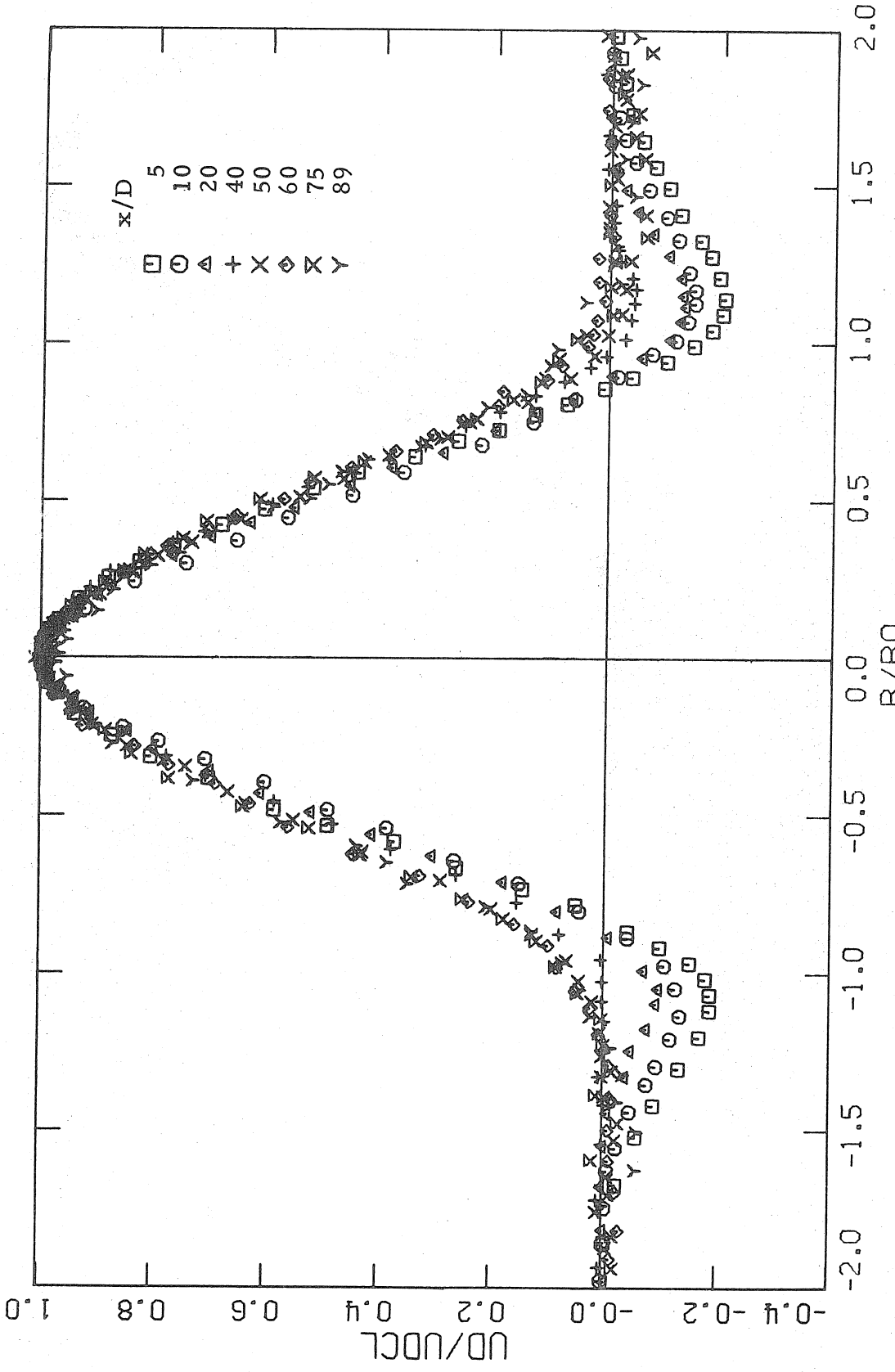


Fig. 34. Strong Injection: Normalized Mean Velocity Profile

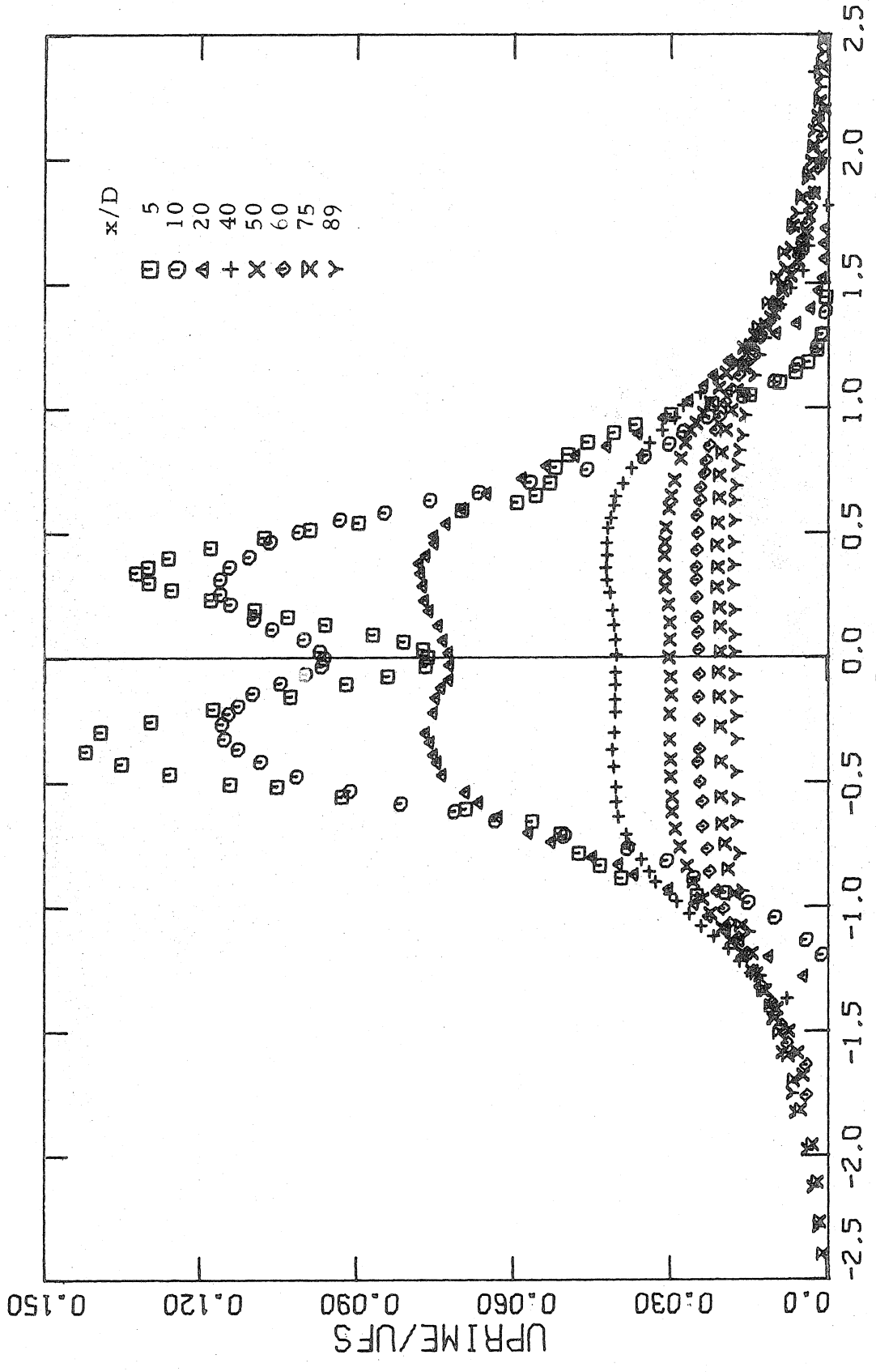


Fig. 35. Strong Injection: Axial Turbulent Intensity

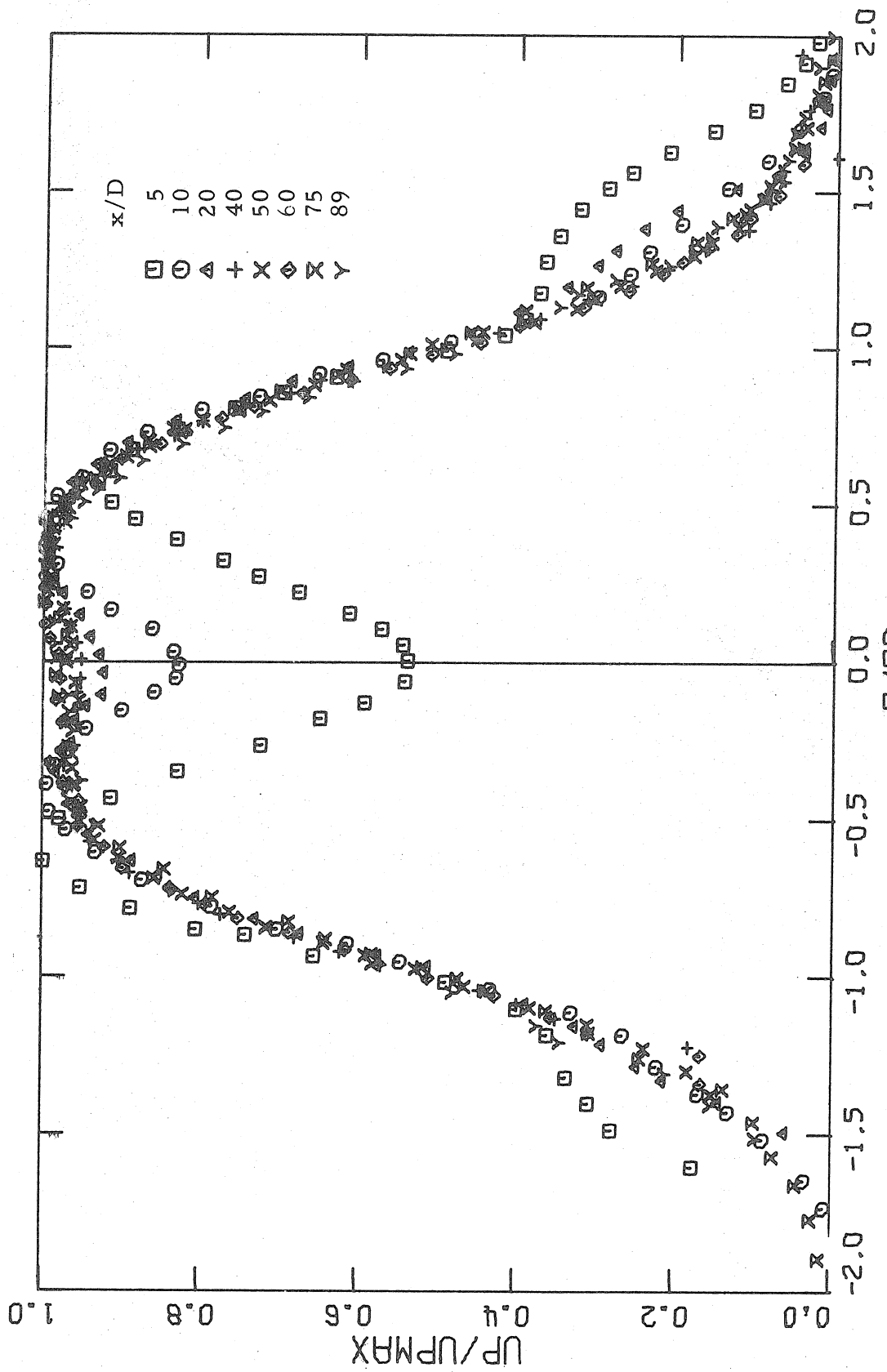


Fig. 36. Strong Injection: Normalized Axial Turbulent Intensity

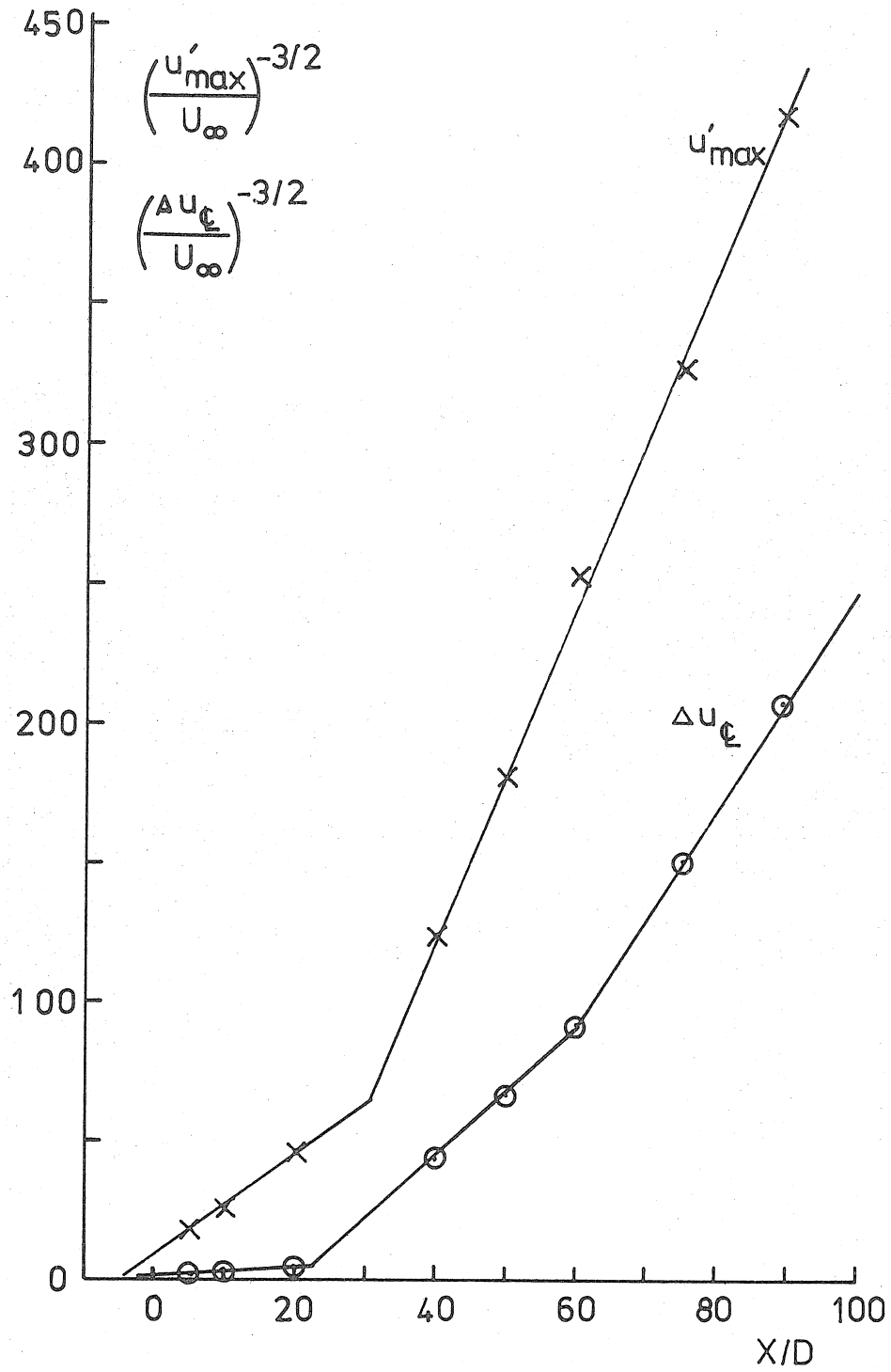


Fig. 37. Strong Injection: Virtual Origin of Asymptotic Decay Law

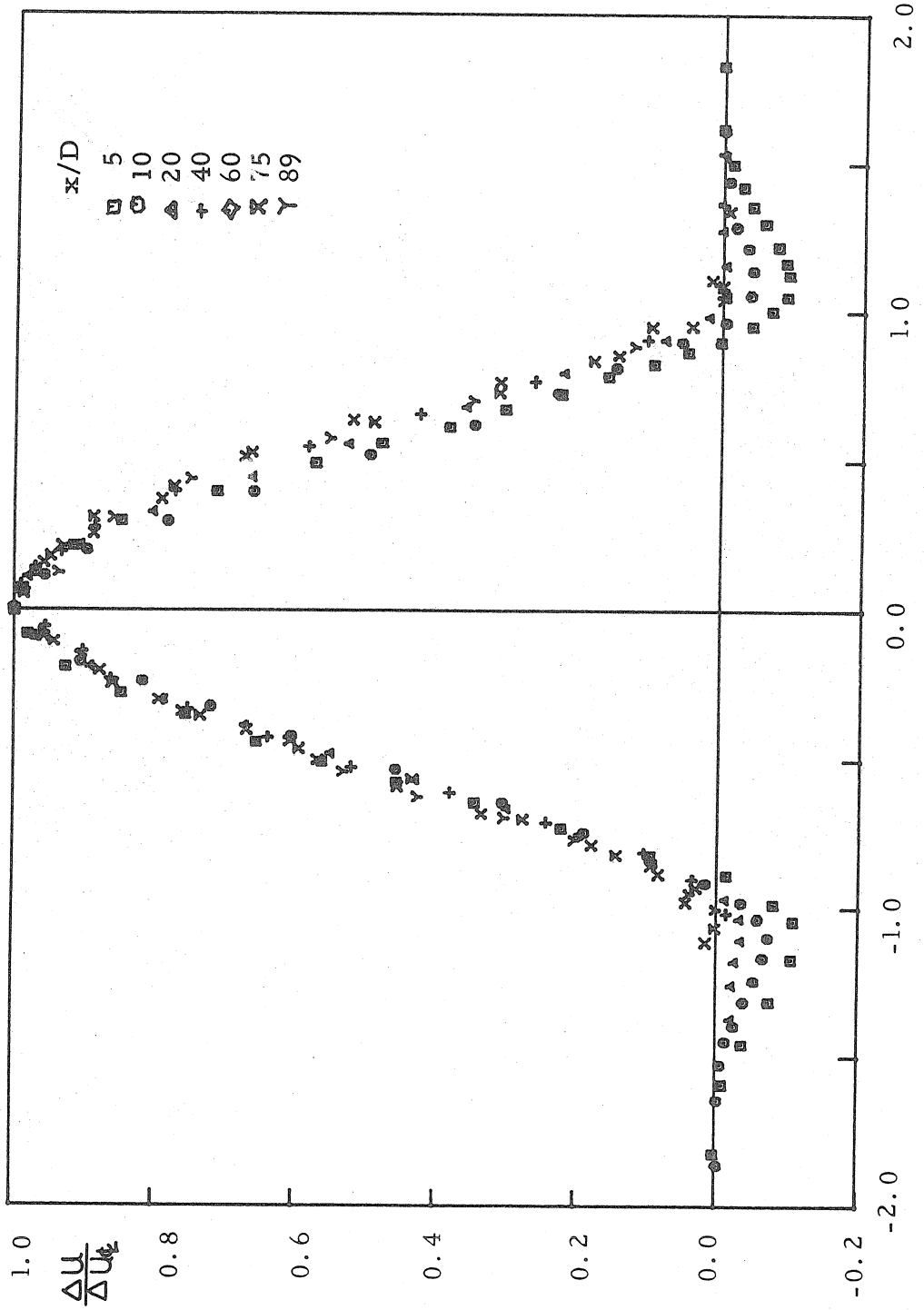


Fig. 38. Very Strong Injection: Normalized Profile of Mean Velocity

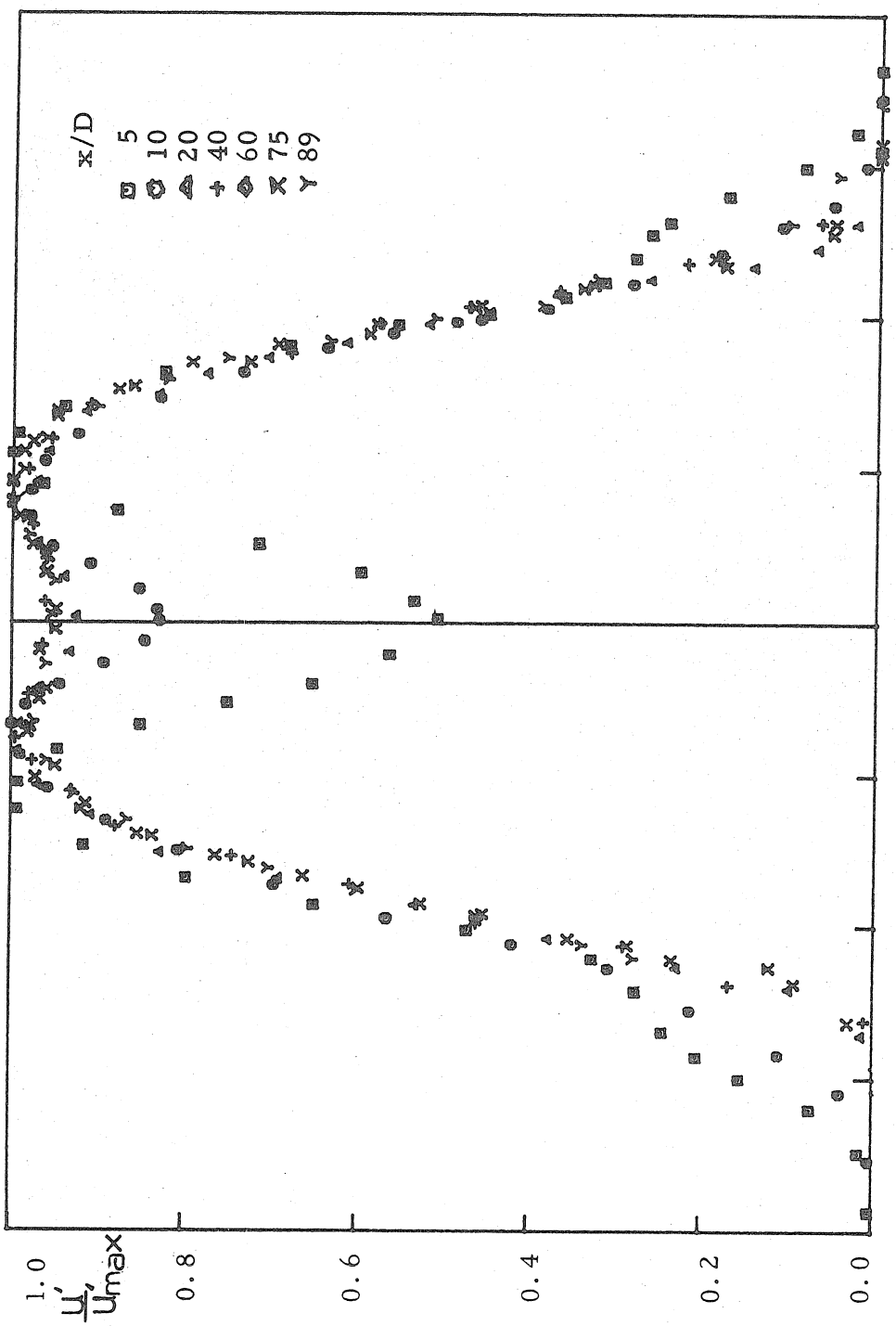


Fig. 39. Very Strong Injection: Normalized Profile of Axial Turbulent Intensity

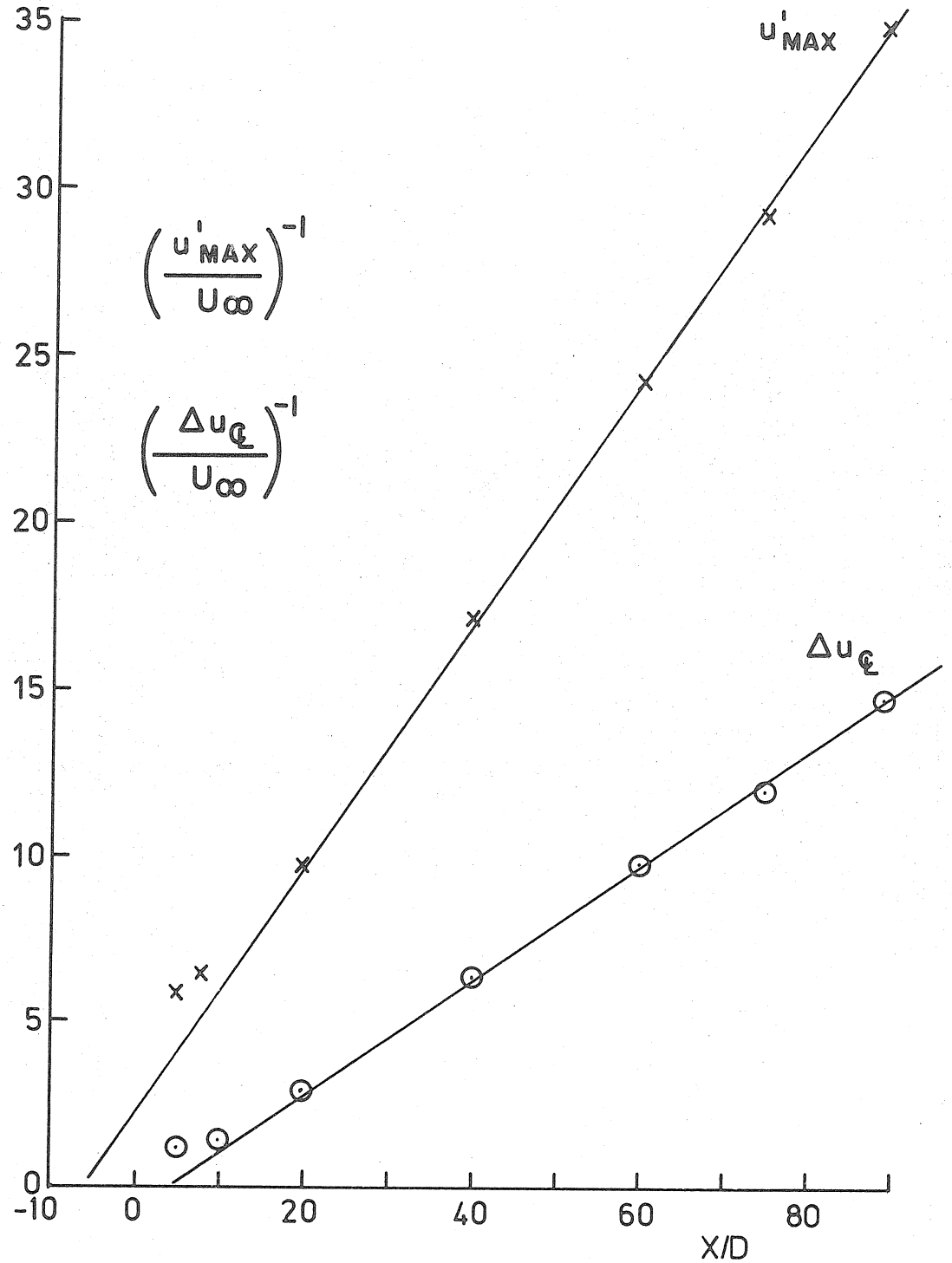


Fig. 40. Very Strong Injection: Virtual Origin of Asymptotic Decay Law

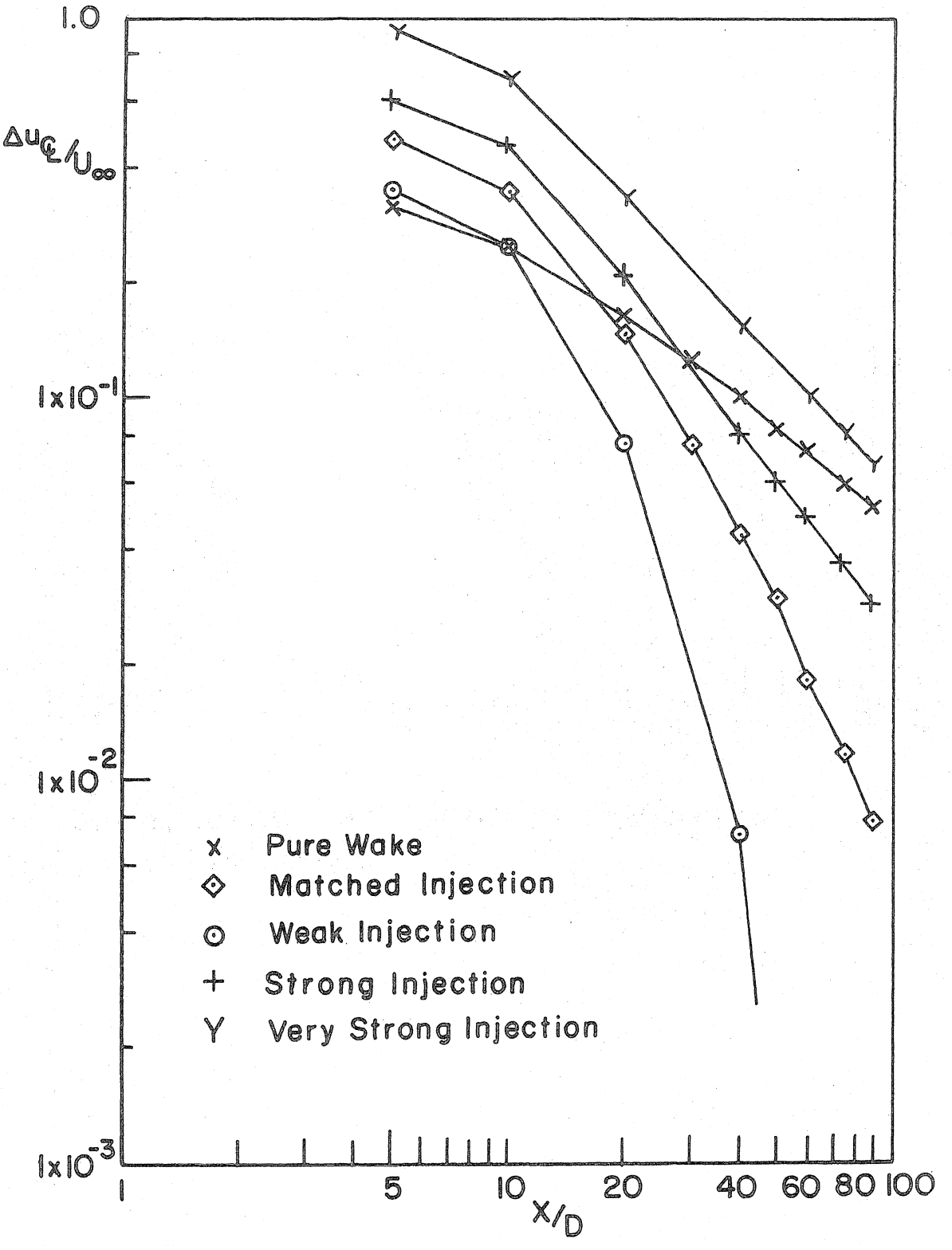


FIG. 41 AXIAL VARIATIONS AT CENTERLINE VELOCITY

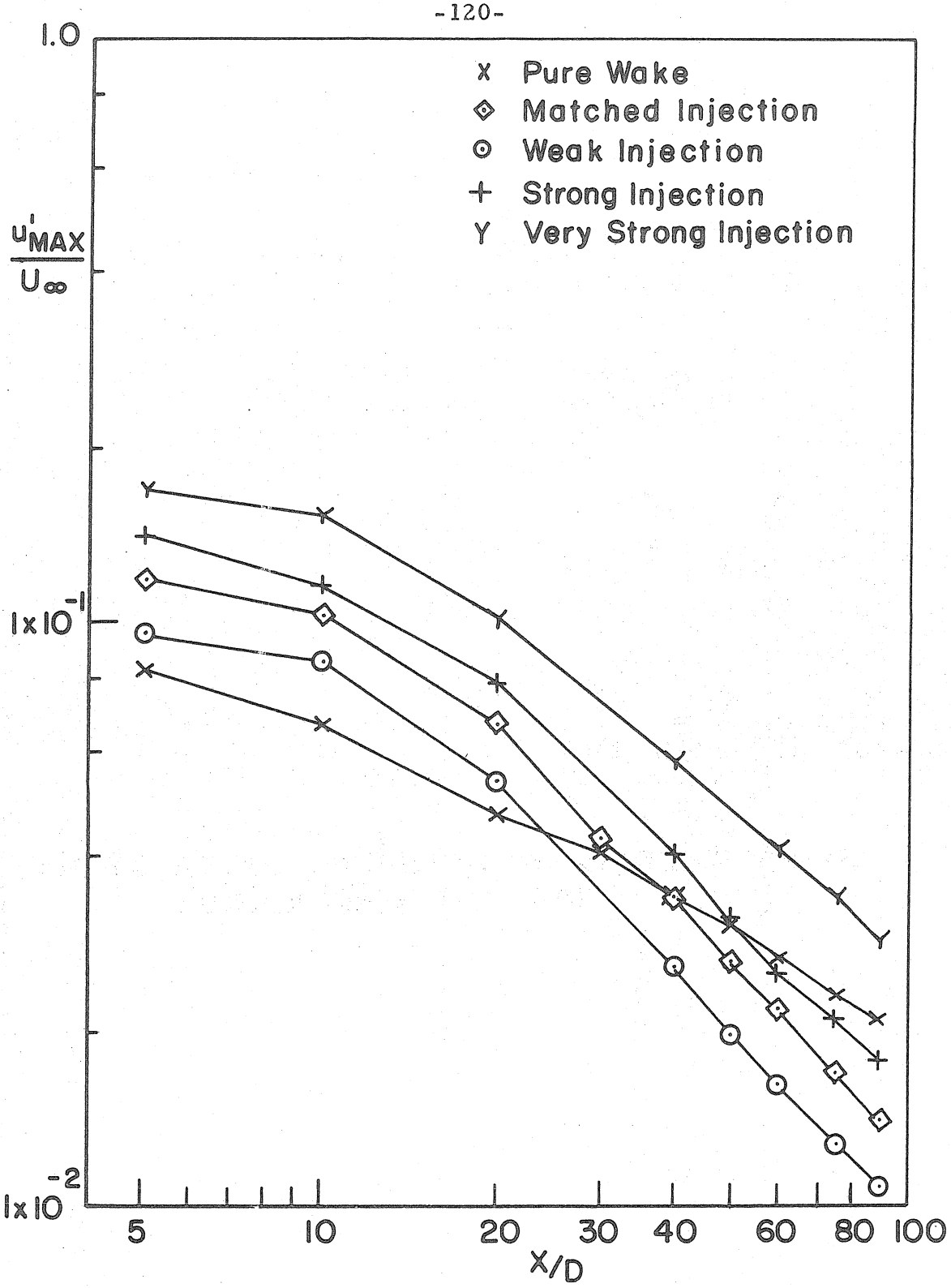


FIG. 42 AXIAL VARIATION AT MAXIMUM AXIAL TURBULENCE INTENSITY

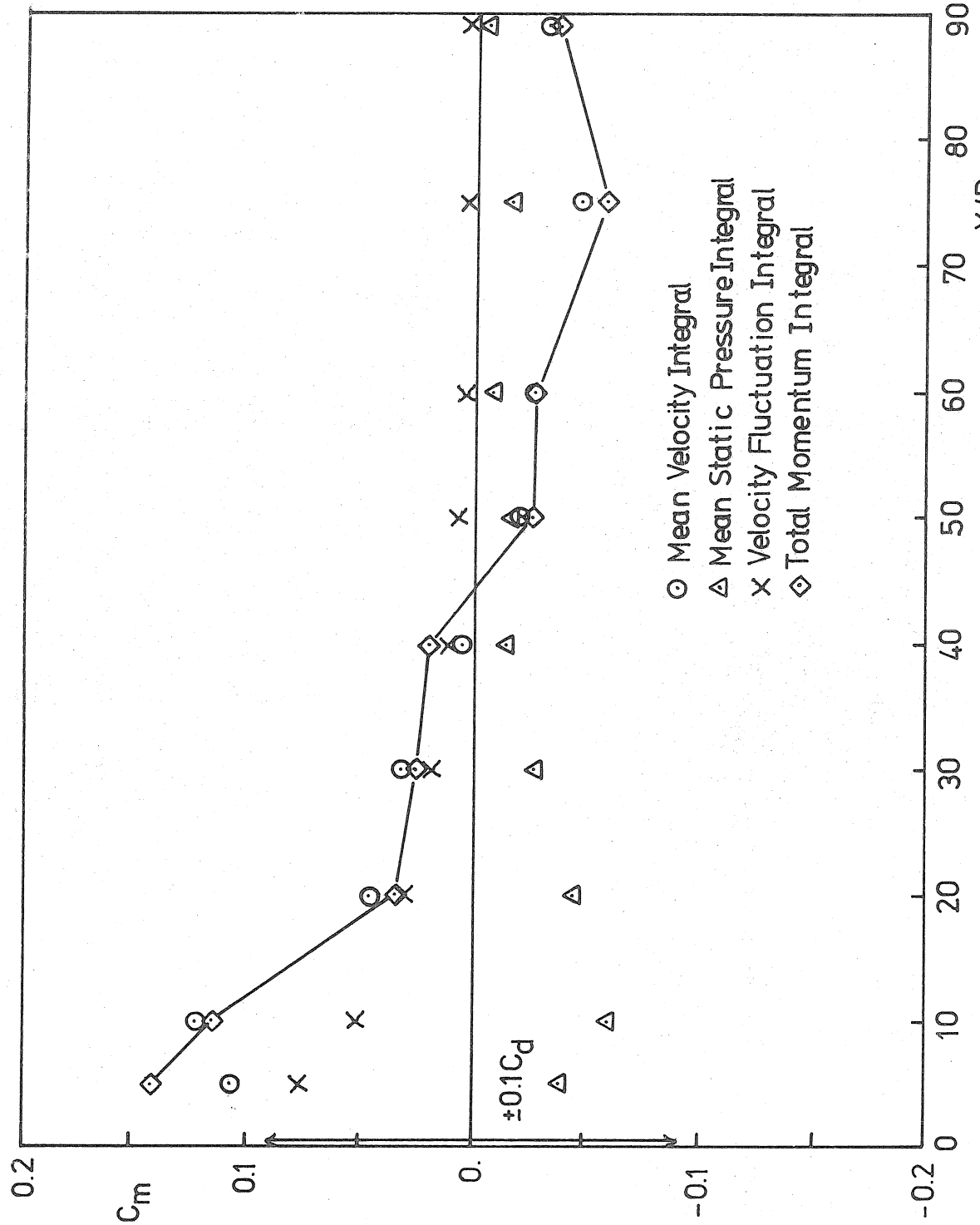


Fig. 43. Momentum Balance in the Rough Wall Matched Injection Case

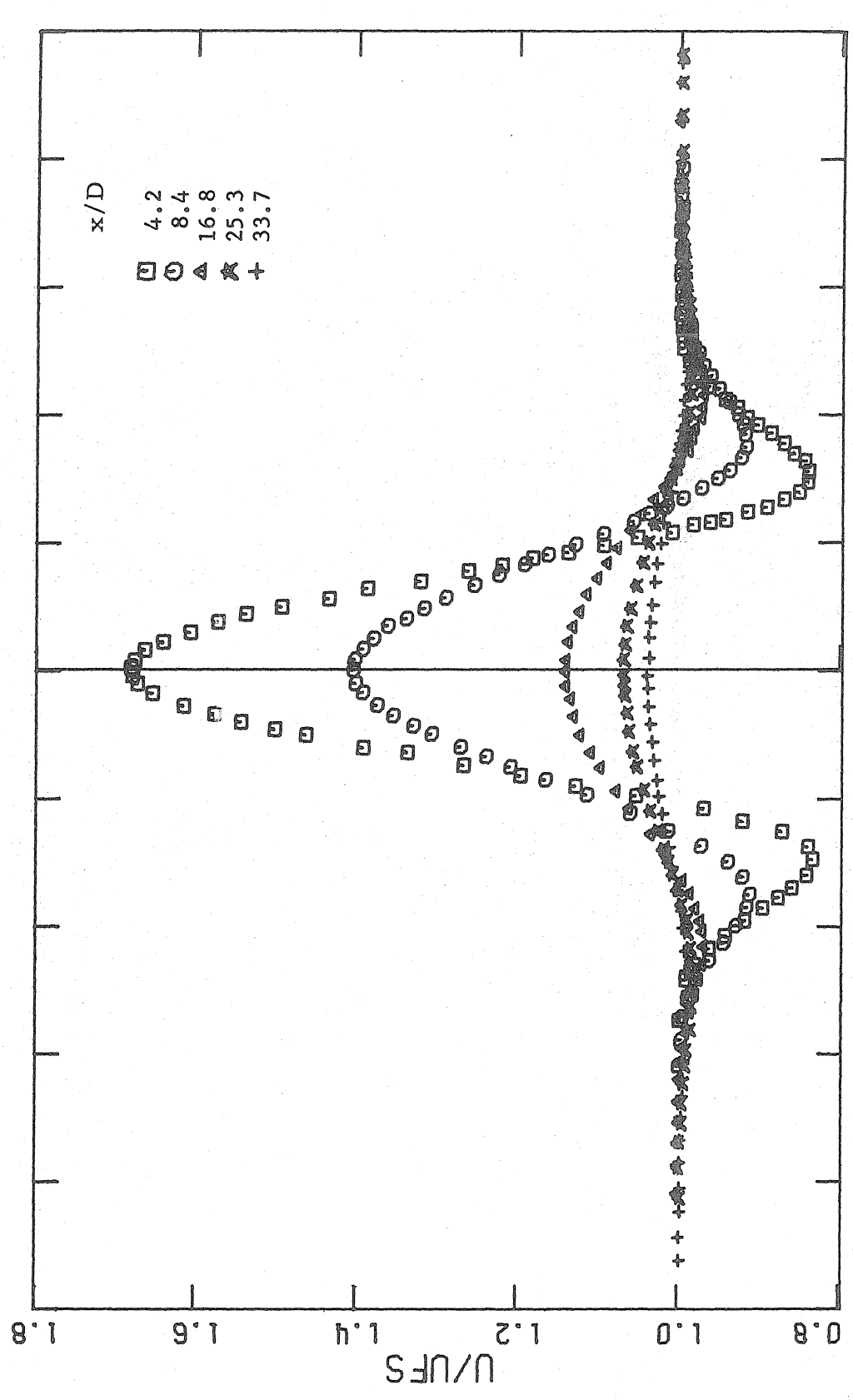


Fig. 44a. Mean Velocity Profile behind a Rough Wall Model, Matched Injection X/D = 4.2-33.7

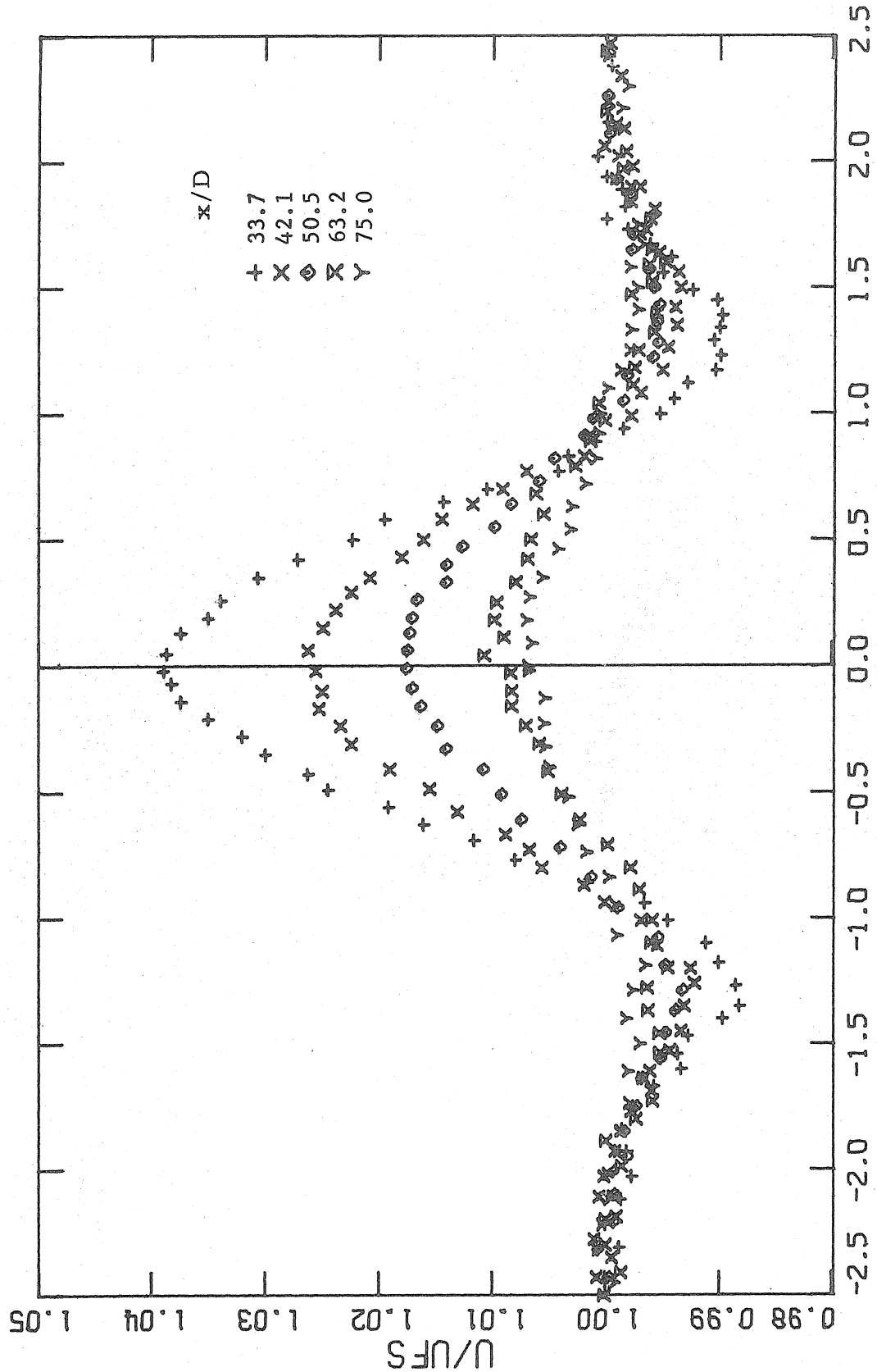


Fig. 44b. Mean Velocity Profile behind a Rough Wall Model, Matched Injection X/D = 33.7-75

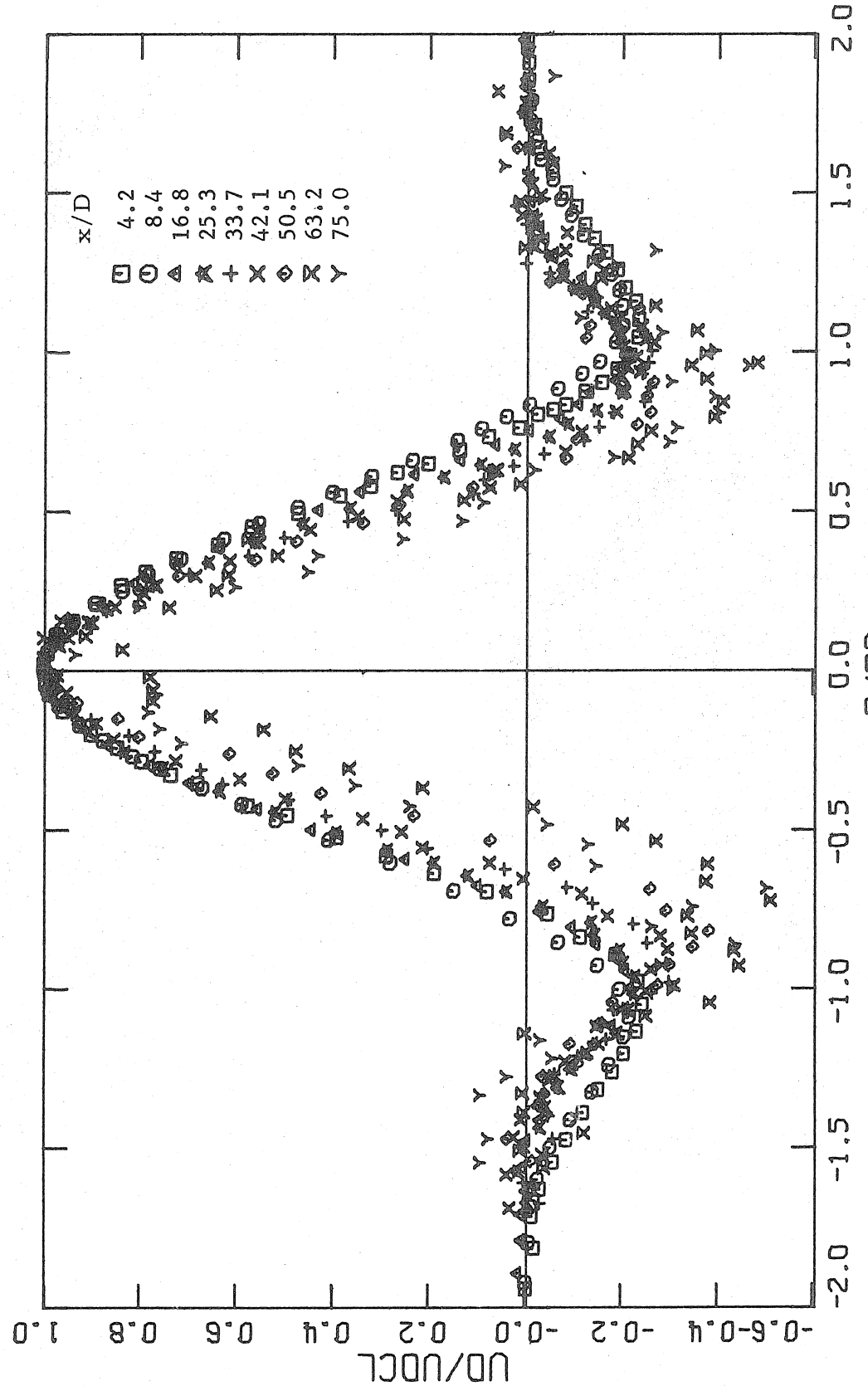


Fig. 45. Normalized Mean Velocity Profile; Rough Wall, Matched Injection

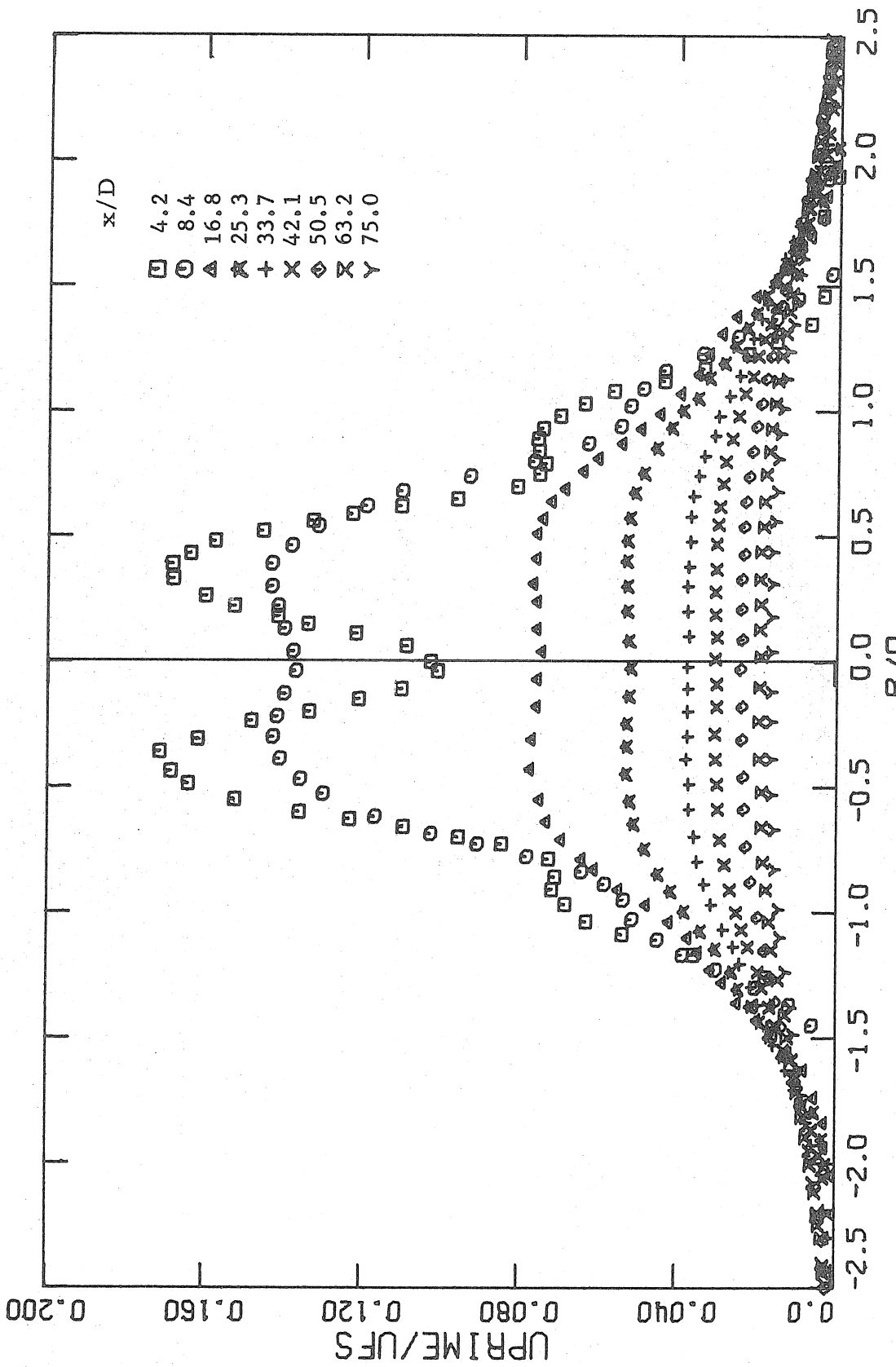


Fig. 46. Axial Turbulence Intensity Distributions; Rough Wall, Matched Injection

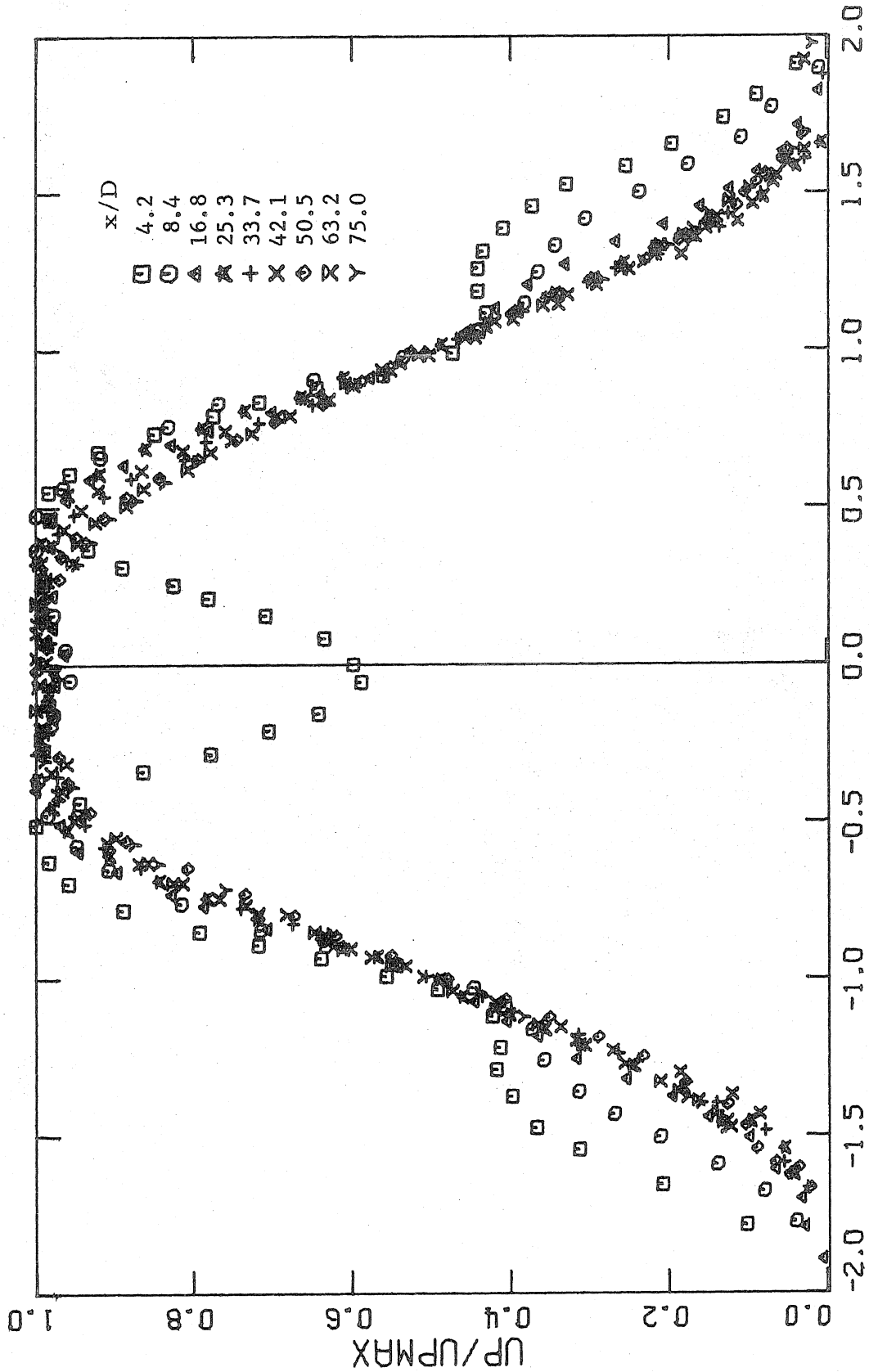


Fig. 47. Normalized Axial Turbulence Intensity Profile; Rough Wall, Matched Injection

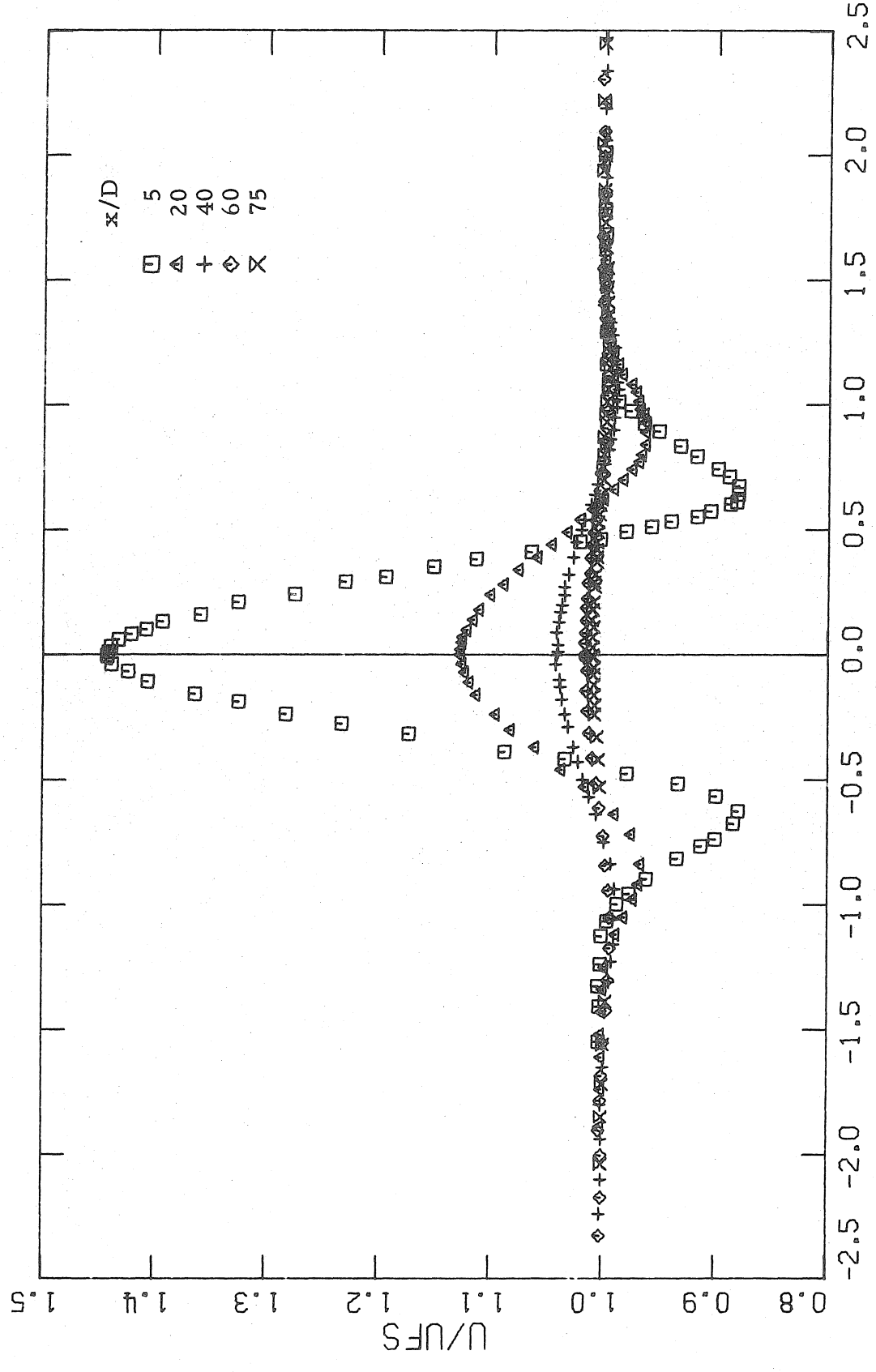


Fig. 48. Mean Velocity Profiles; Matched Injection, Low Free Stream Velocity

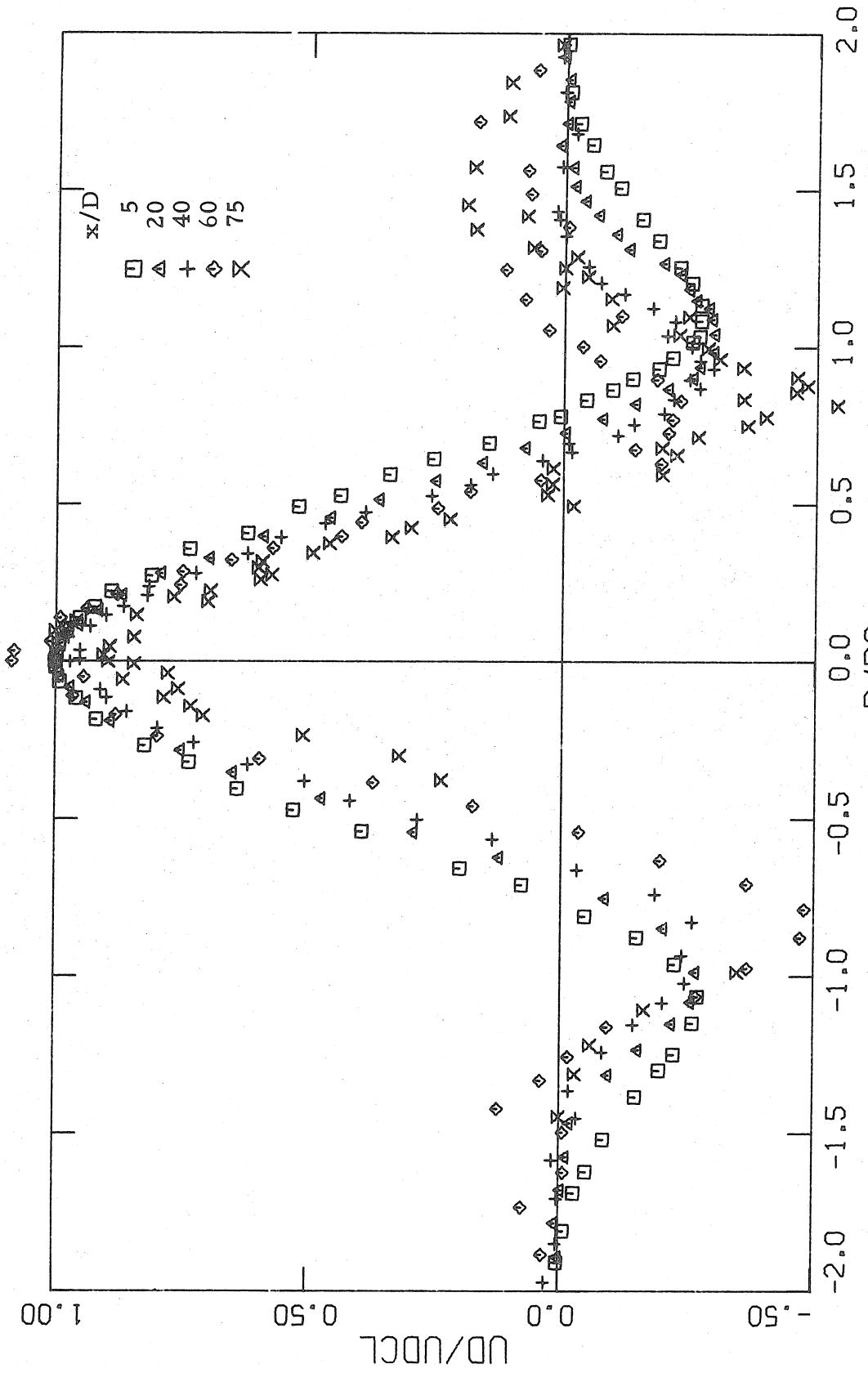


Fig. 49. Normalized Mean Velocity Profile; Matched Injection, Low Free Stream Velocity

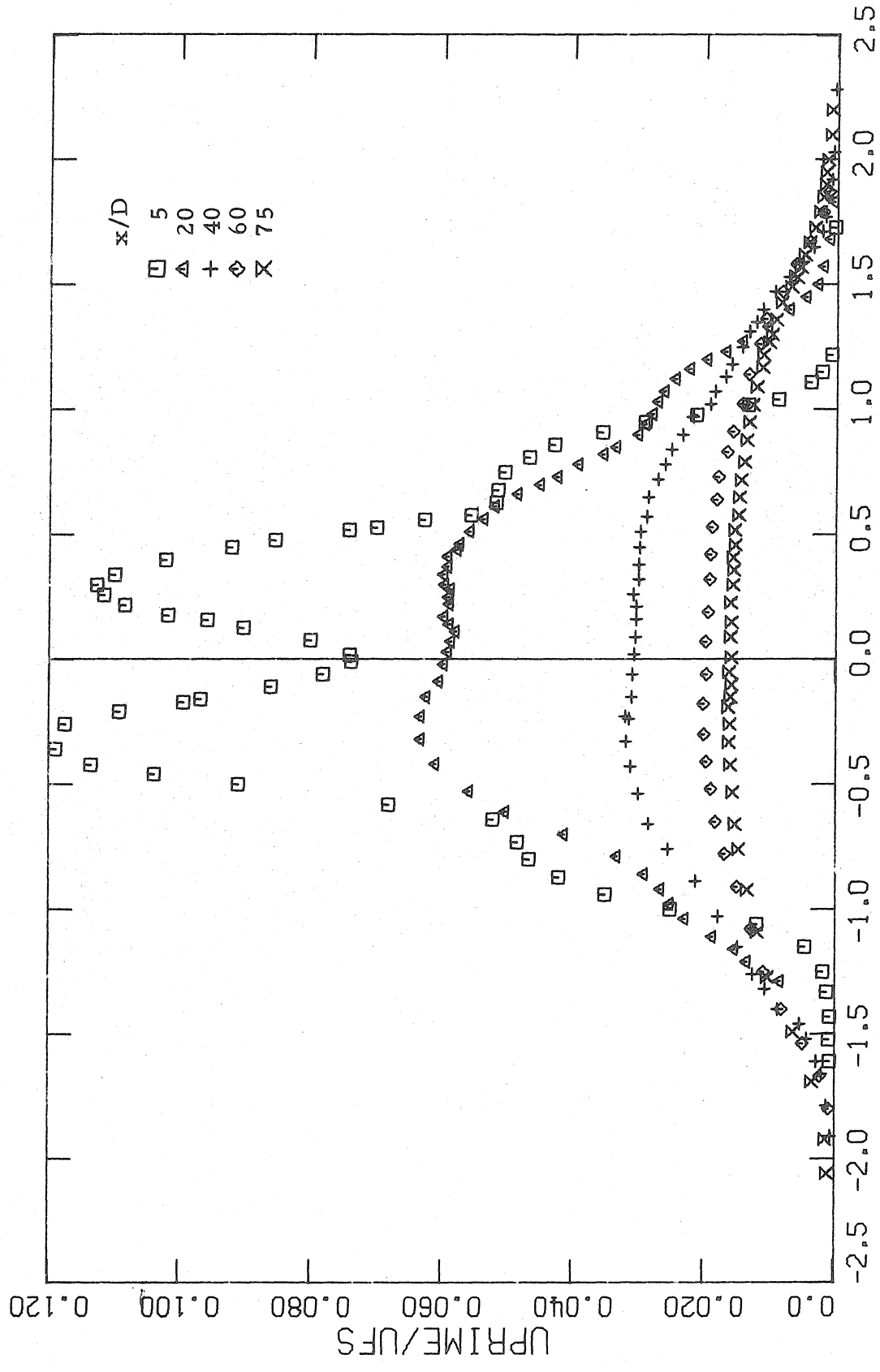


Fig. 50. Axial Turbulence Intensity Distributions; Matched Injection, Low Free Stream Velocity

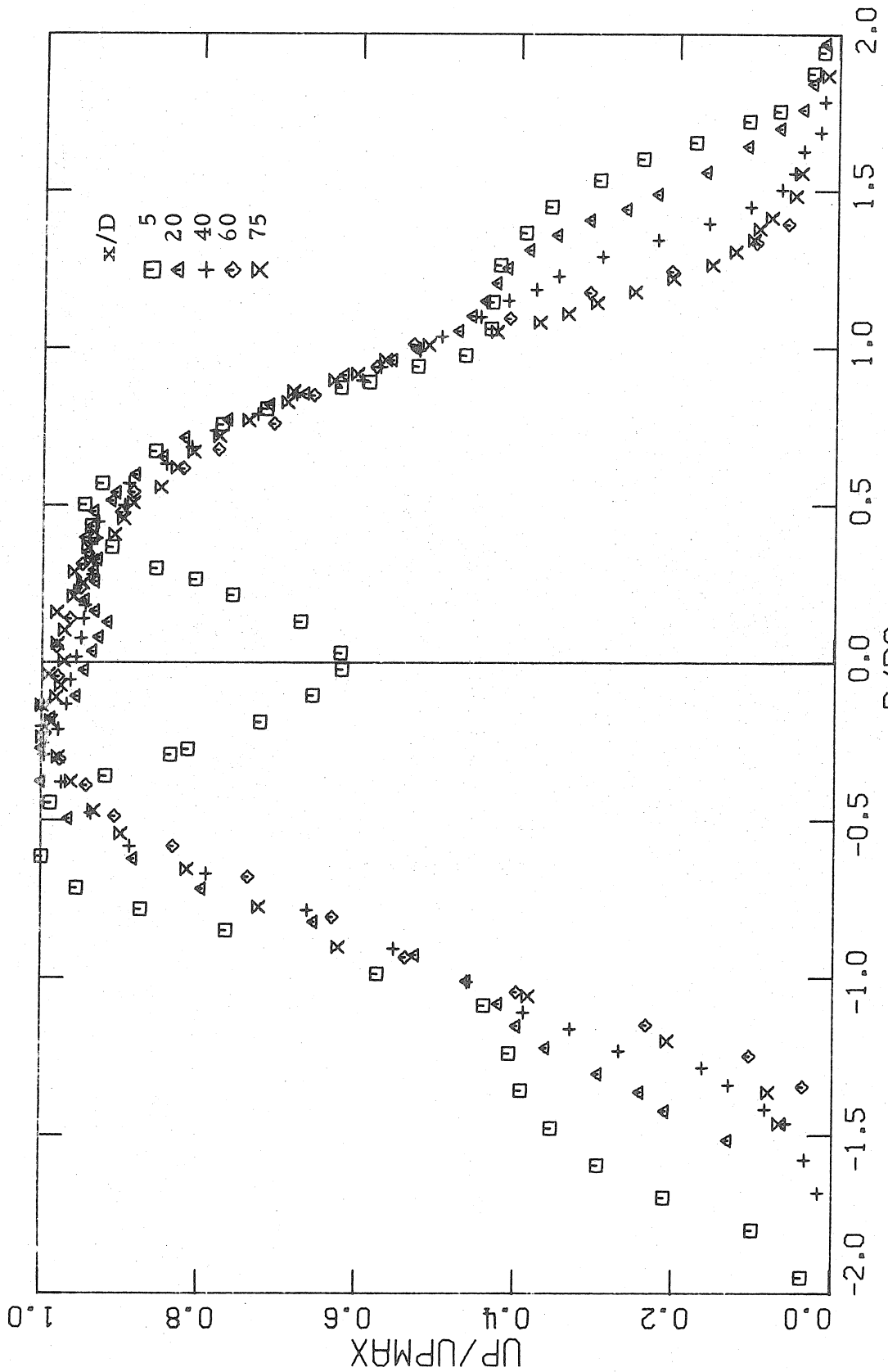


Fig. 51. Normalized Axial Turbulence Intensity; Matched Injection, Low Free Stream Velocity

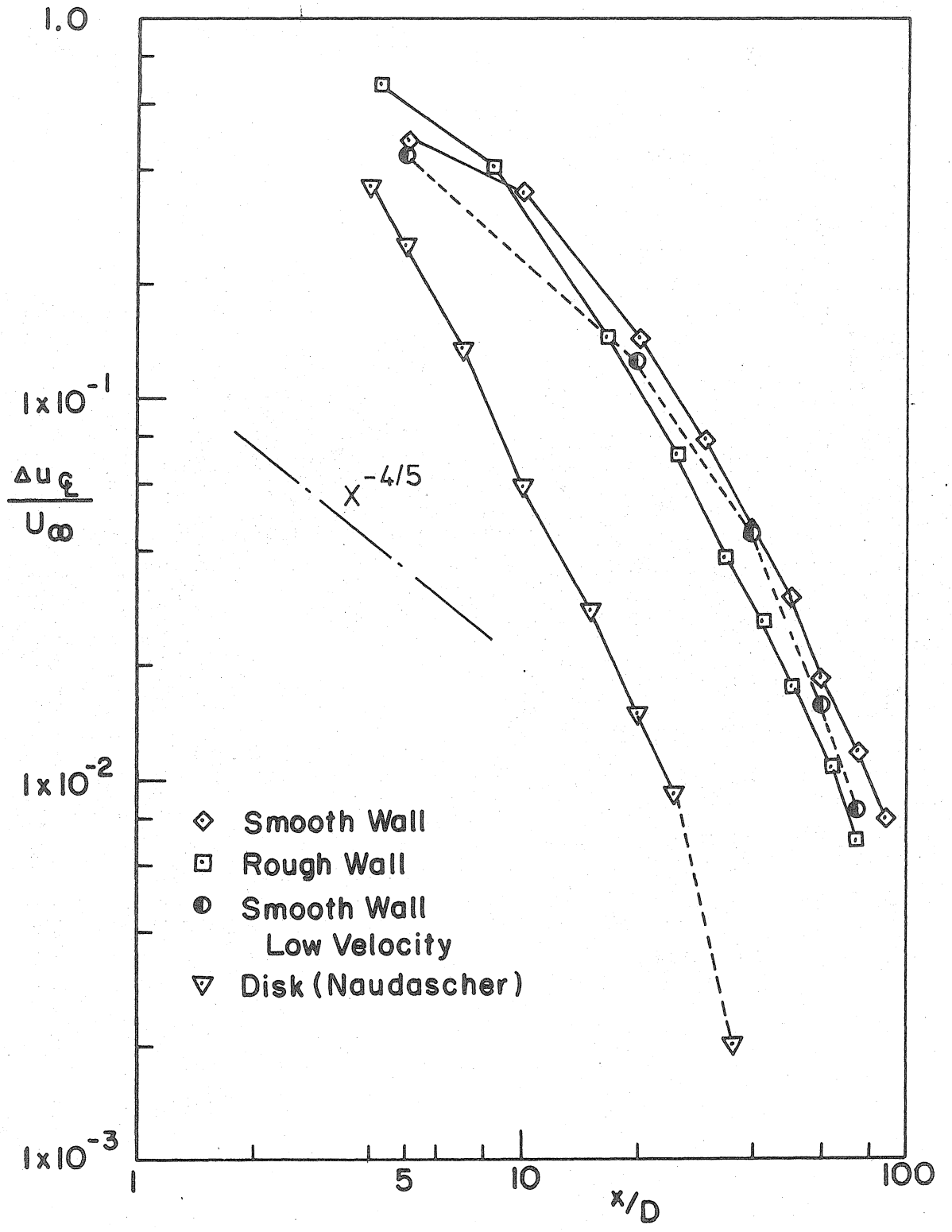


Fig. 52. Axial Variations of Centerline Velocity in Matched Injection Cases

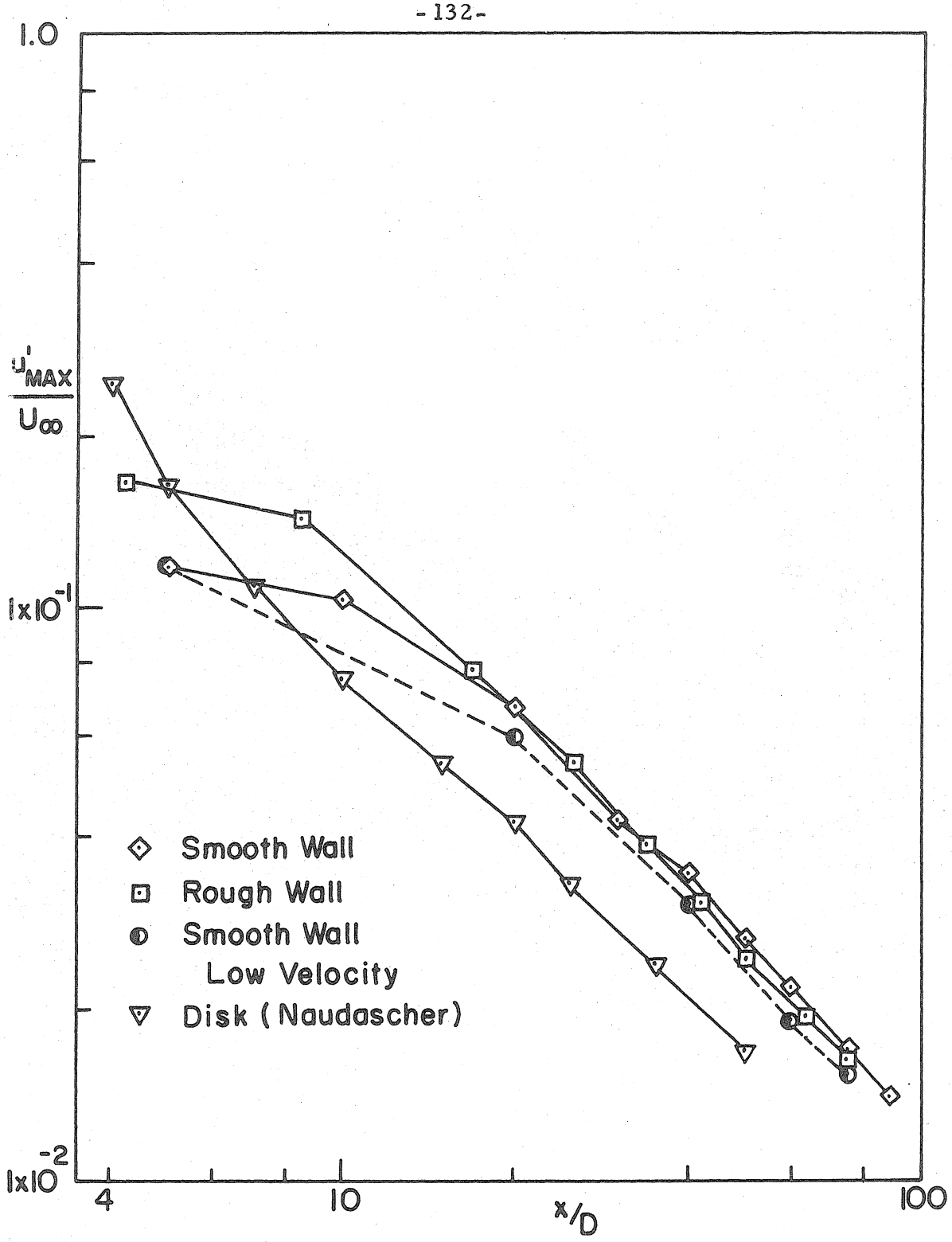


Fig. 53. Axial Variations of Maximum Axial Turbulent Intensity in Matched Injection Cases

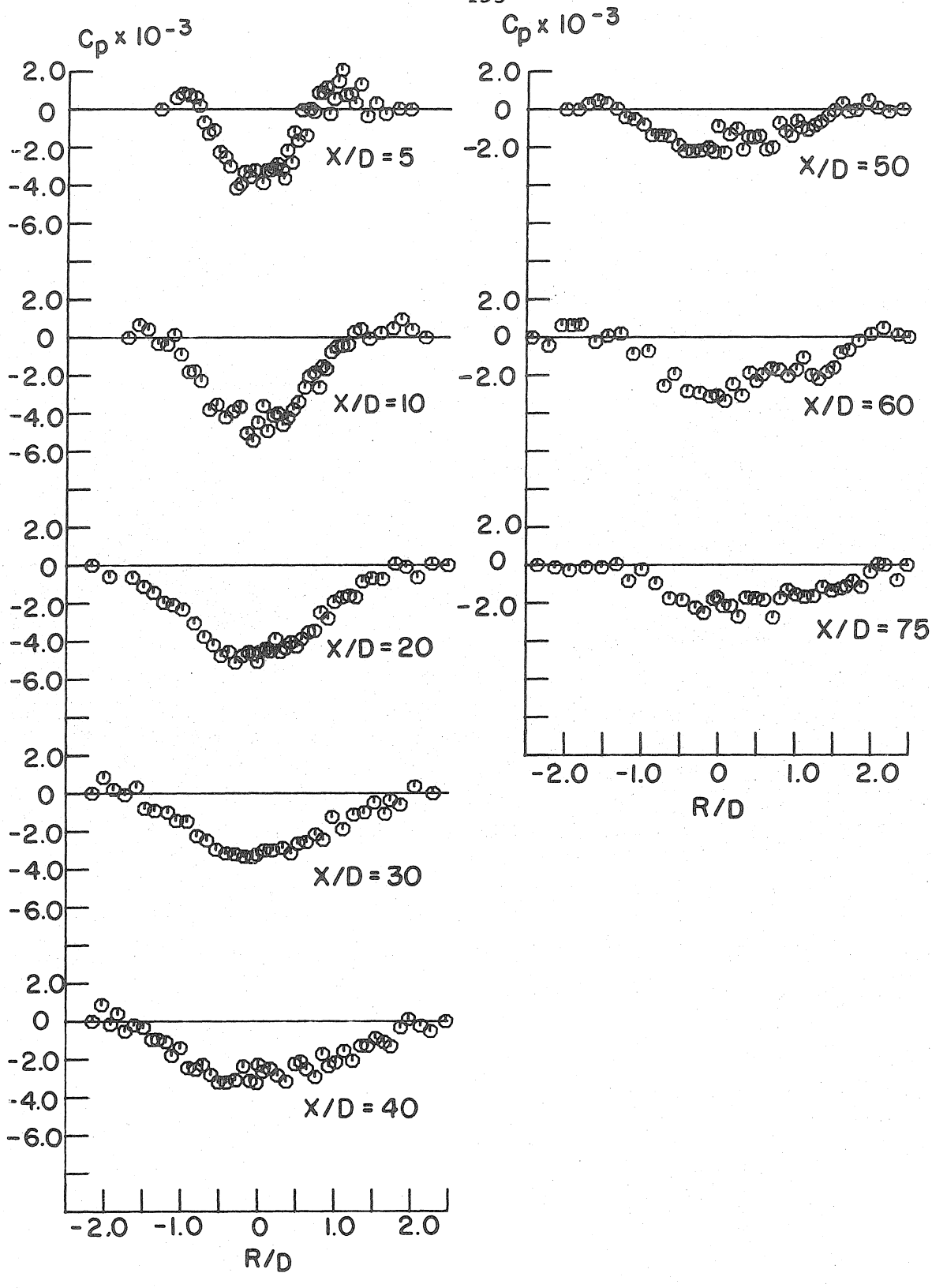


Fig. 54. Mean Static Pressure Distribution, Pure Wake

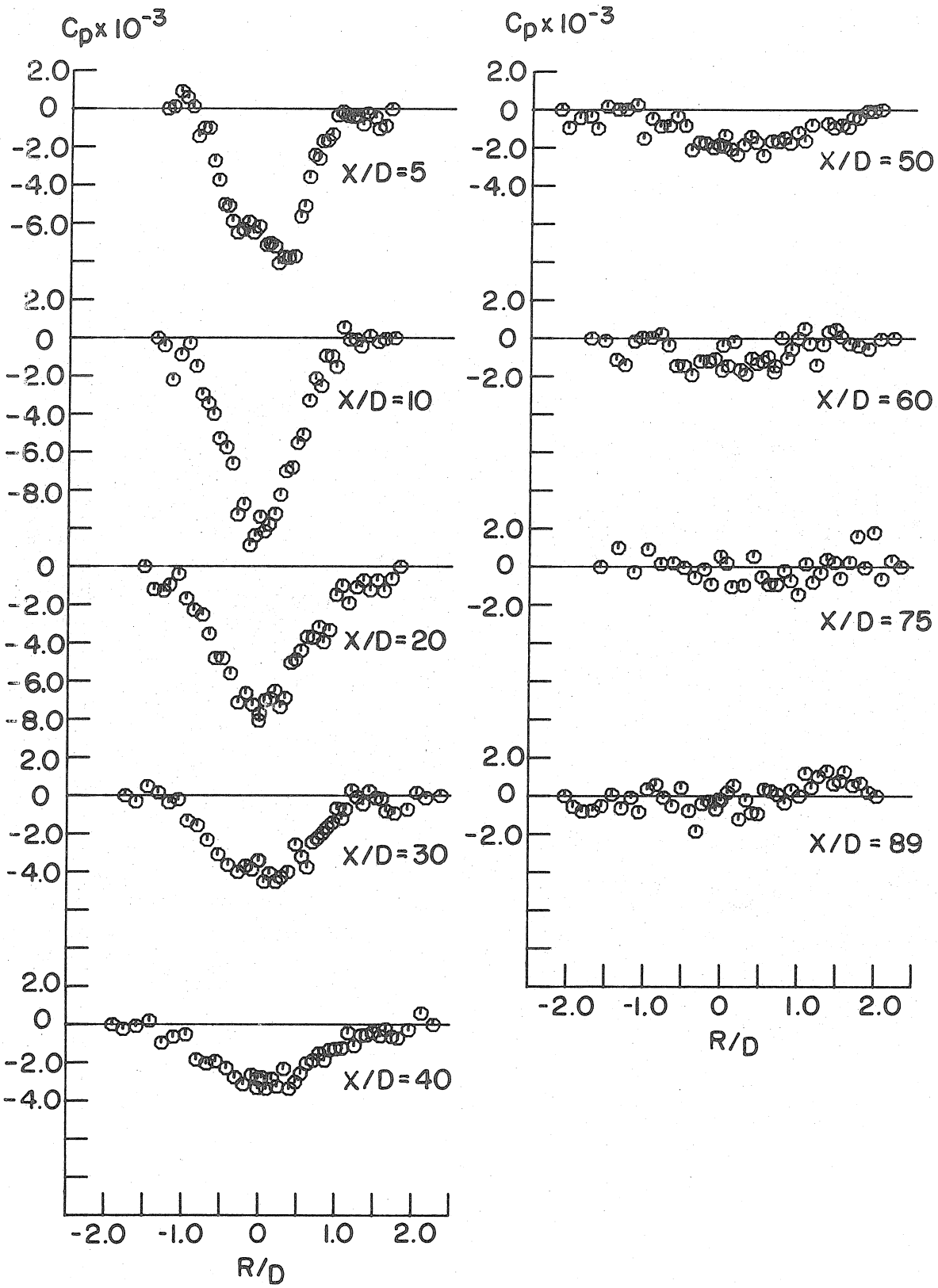


Fig. 55. Mean Static Pressure Distribution, Matched Injection, Smooth Wall

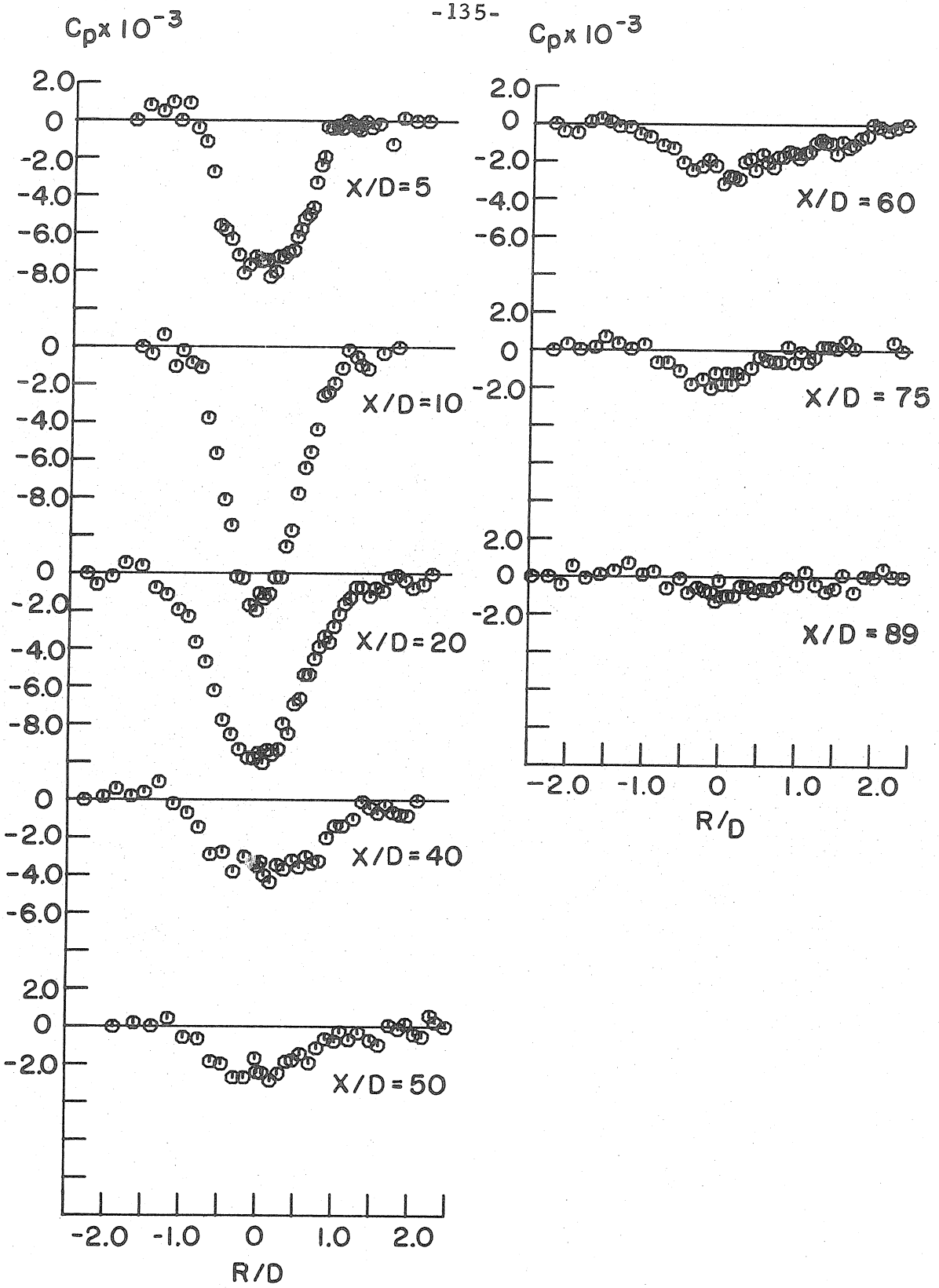


Fig. 56. Mean Static Pressure Distribution, Weak Injection

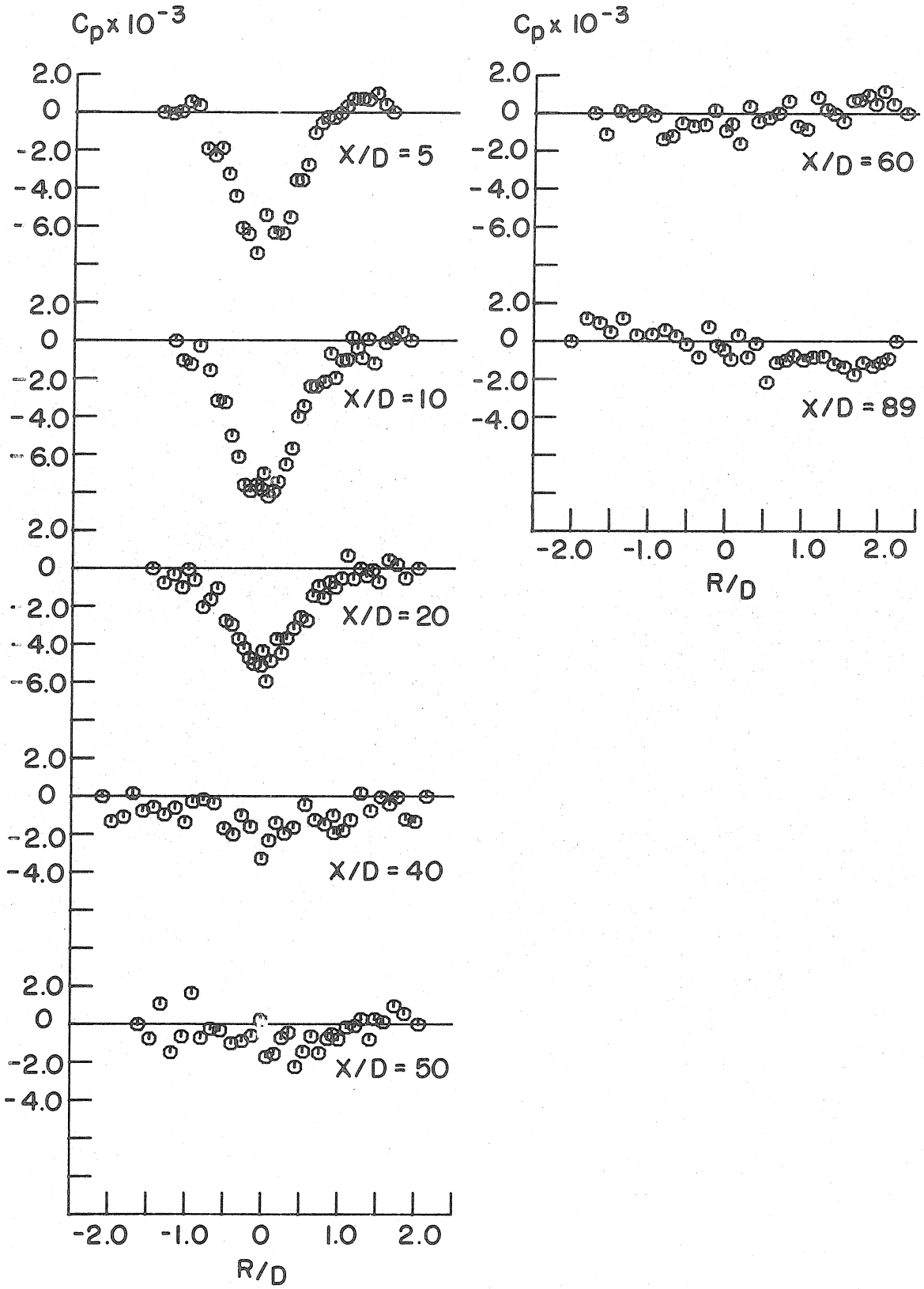


Fig. 57. Mean Static Pressure Distribution, Strong Injection

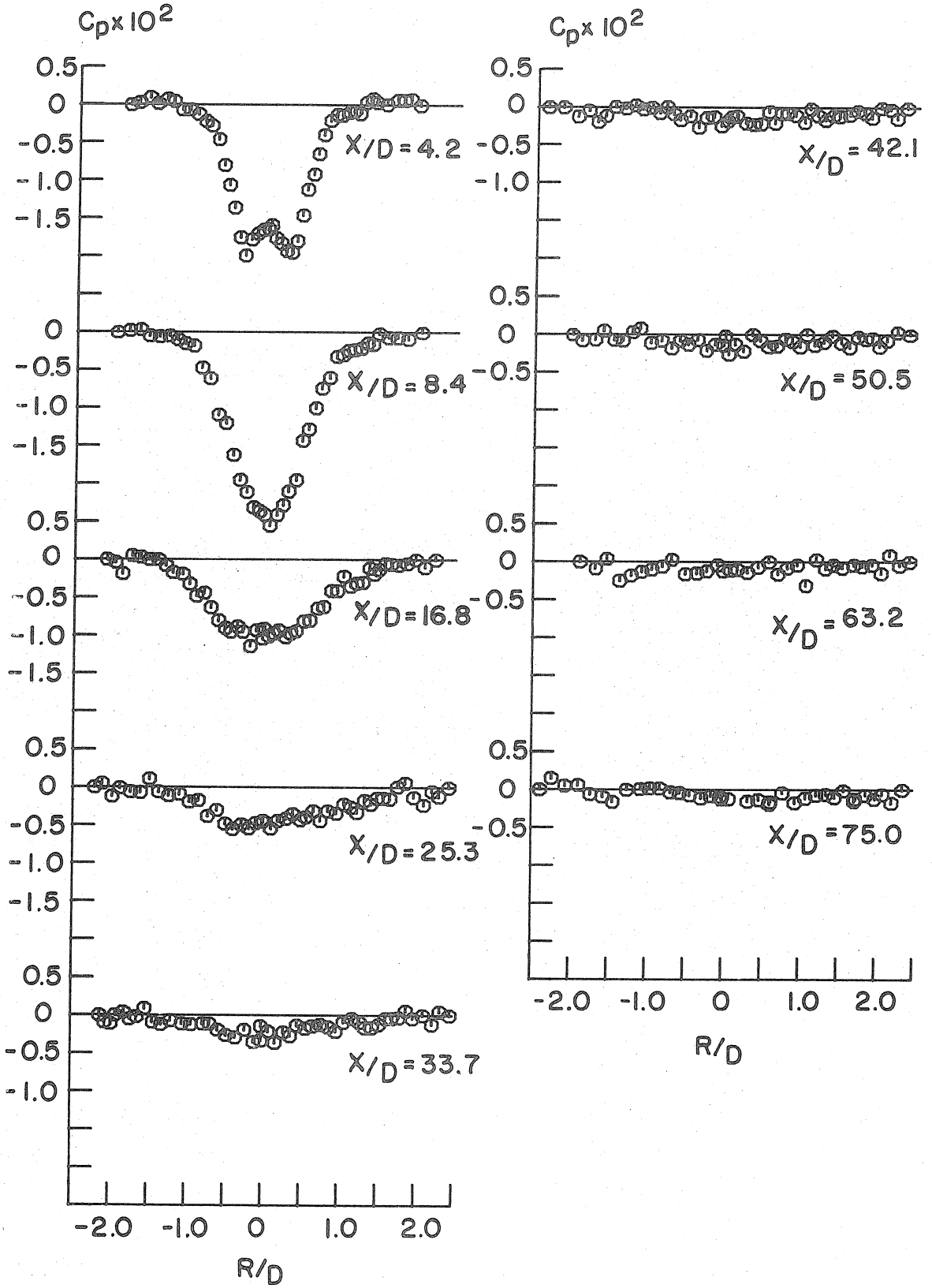


Fig. 58. Mean Static Pressure Distribution, Matched Injection, Rough Wall

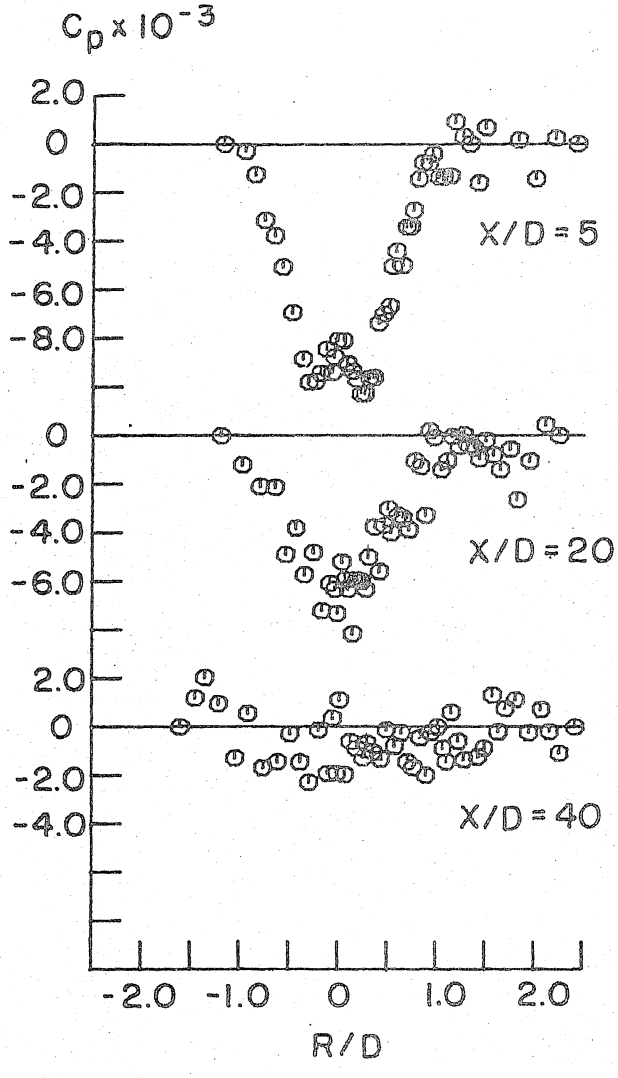


Fig. 59. Mean Static Pressure Distribution, Matched Injection, Low Free Stream Velocity

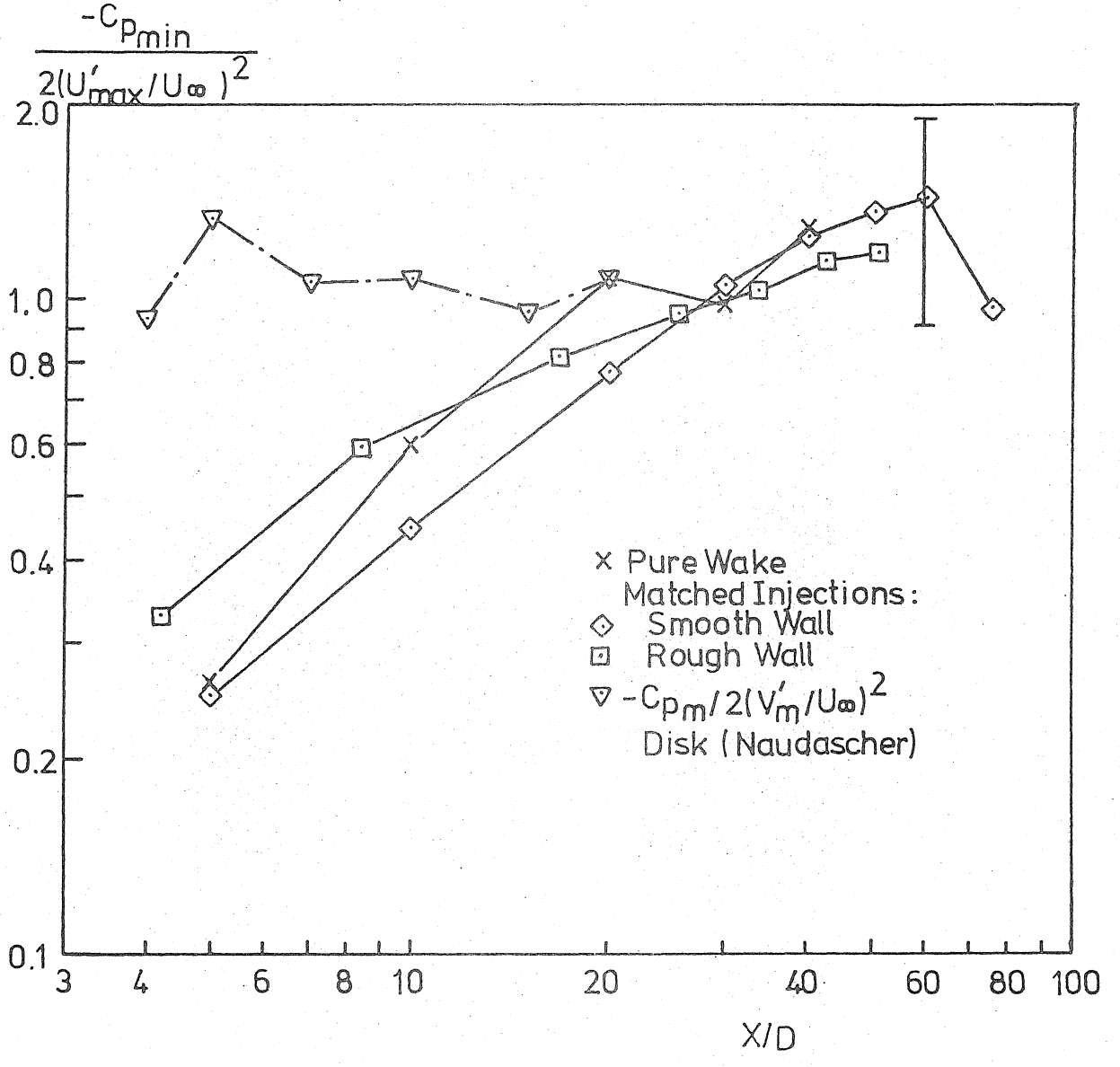


Fig. 60. Variation of $-C_{p_{min}}/2(u'_{max}/U_\infty)^2$ for Various Configurations

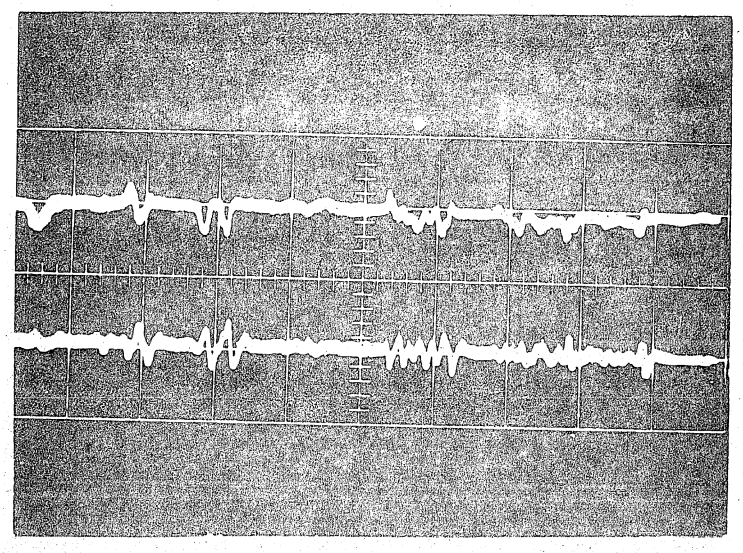


(a)

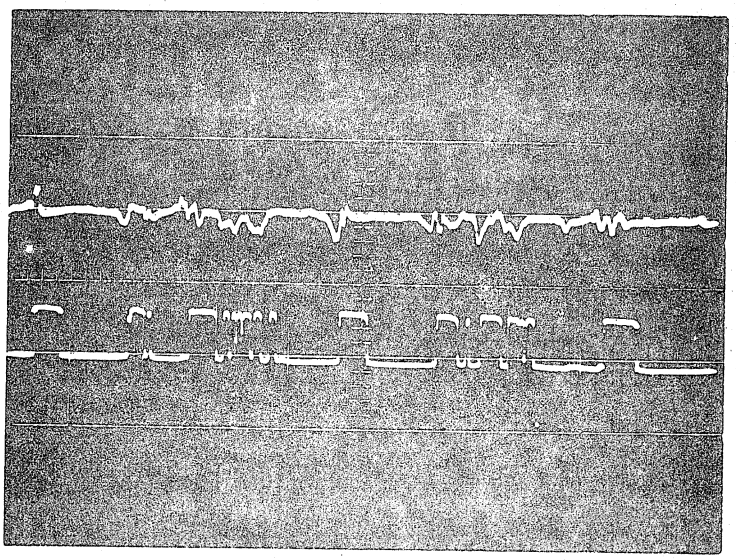


(b)

Fig. 61. Signal Processing for the Intermittency Factor Measurement, Matched Injection X/D = 89

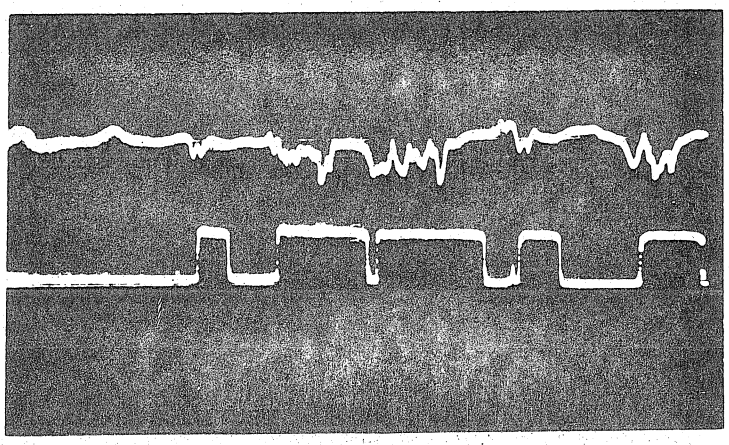

Pure Wake X/D = 60

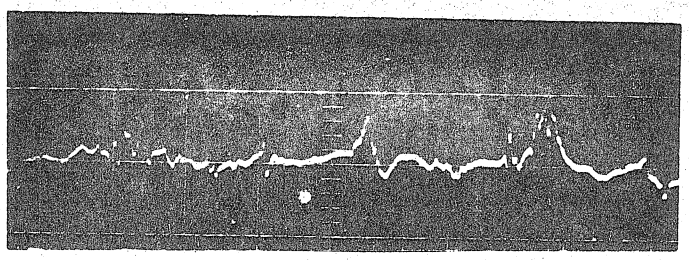

Strong Injection X/D = 60

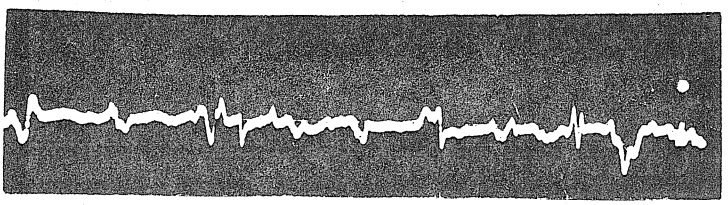

Matched Injection X/D = 60

Fig. 62. Typical Hot Wire Signals in Various Injection Cases

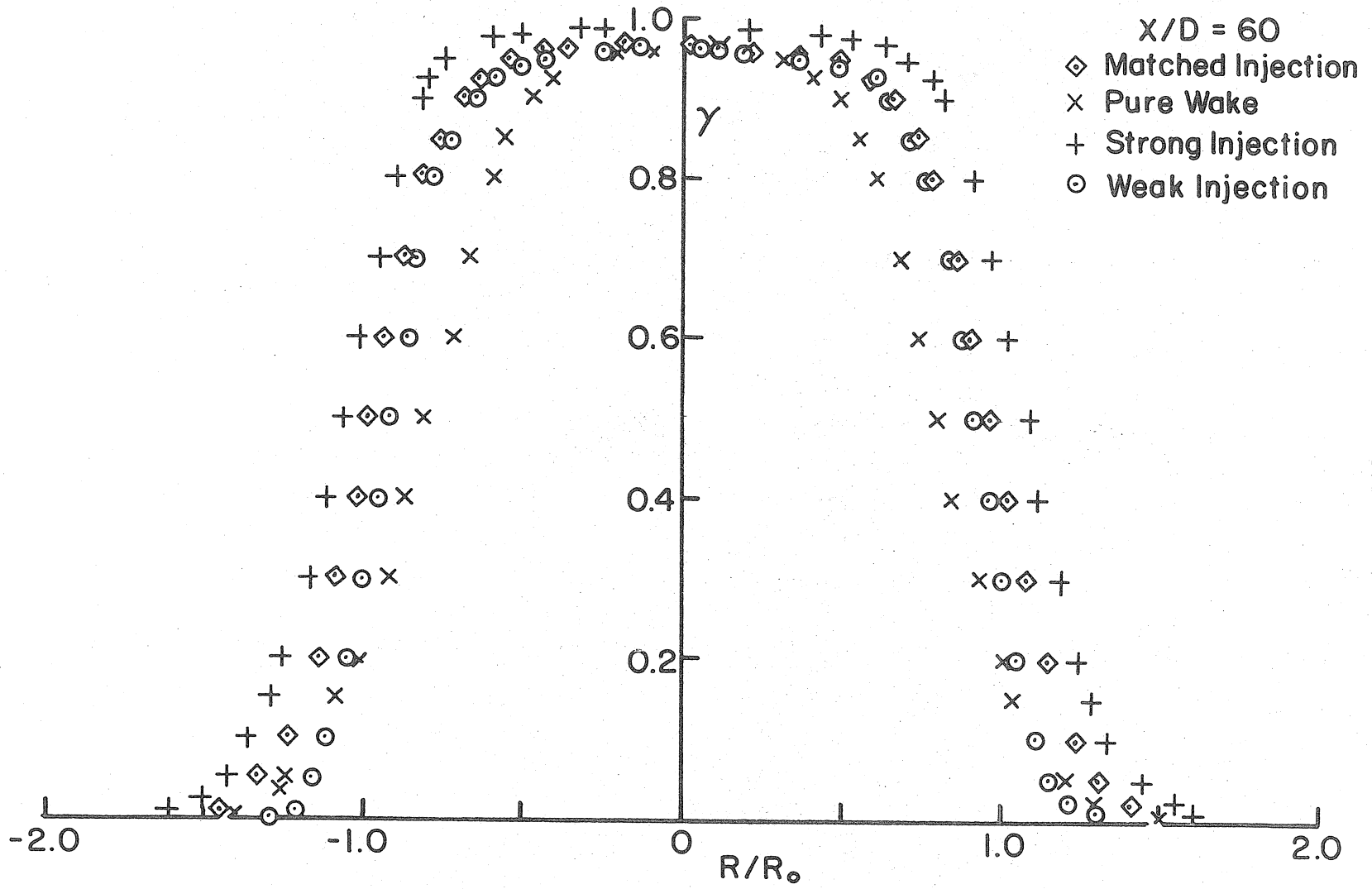


Fig. 63. Intermittency Factor X/D = 60

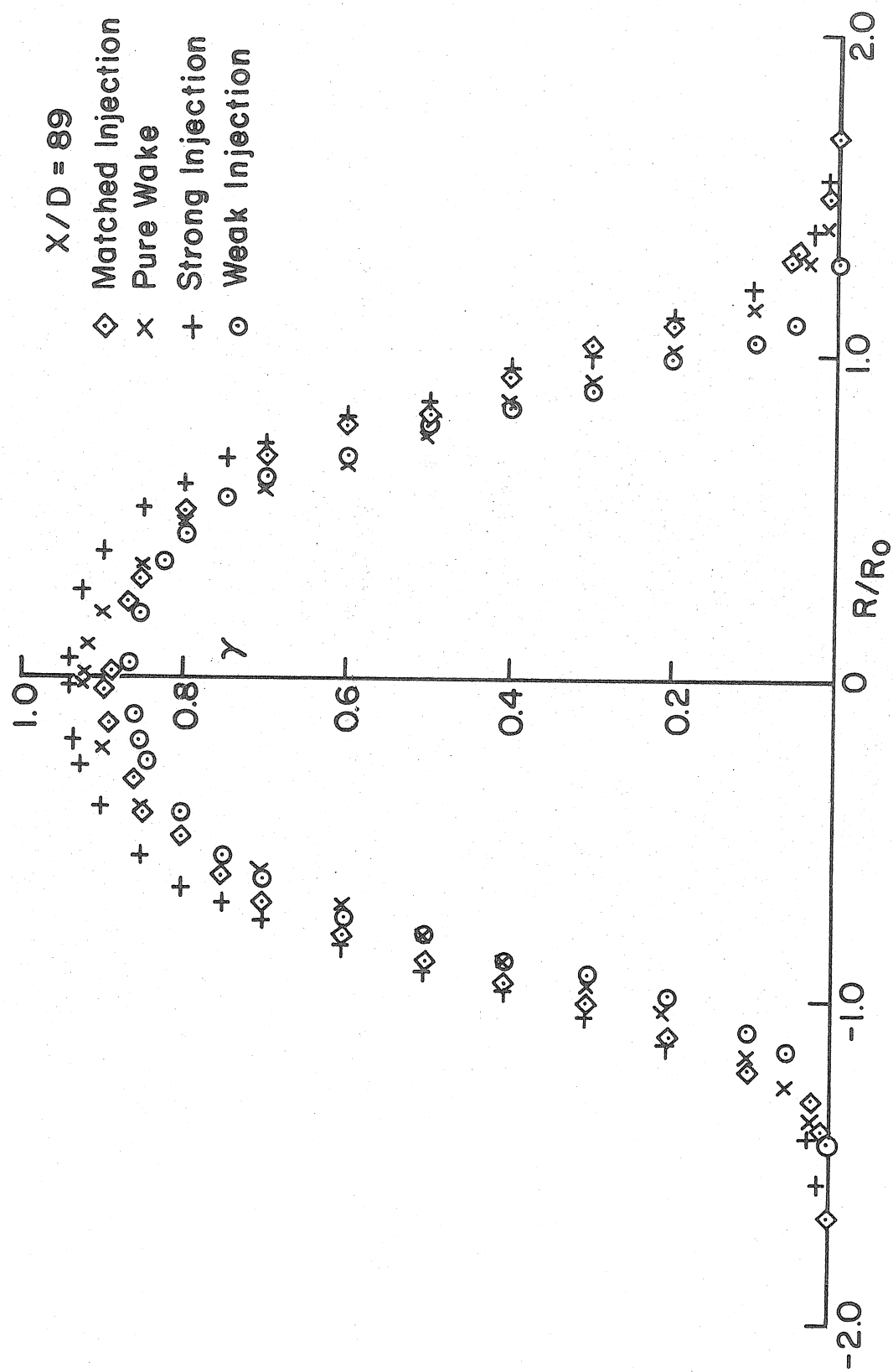


Fig. 64. Intermittency Factor X/D = 89

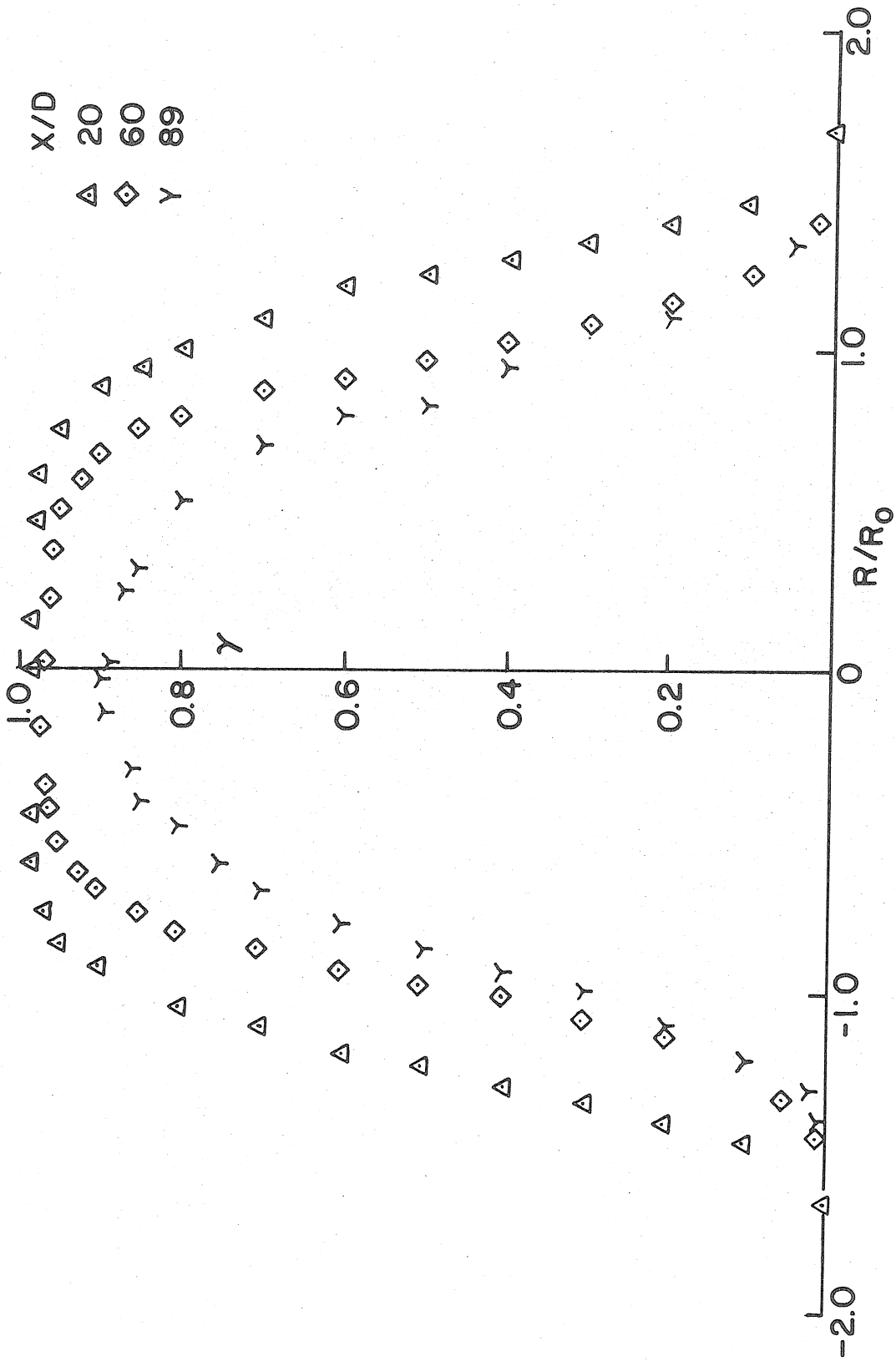


Fig. 65. Intermittency Factor; Matched Injection X/D=20, 60 & 89

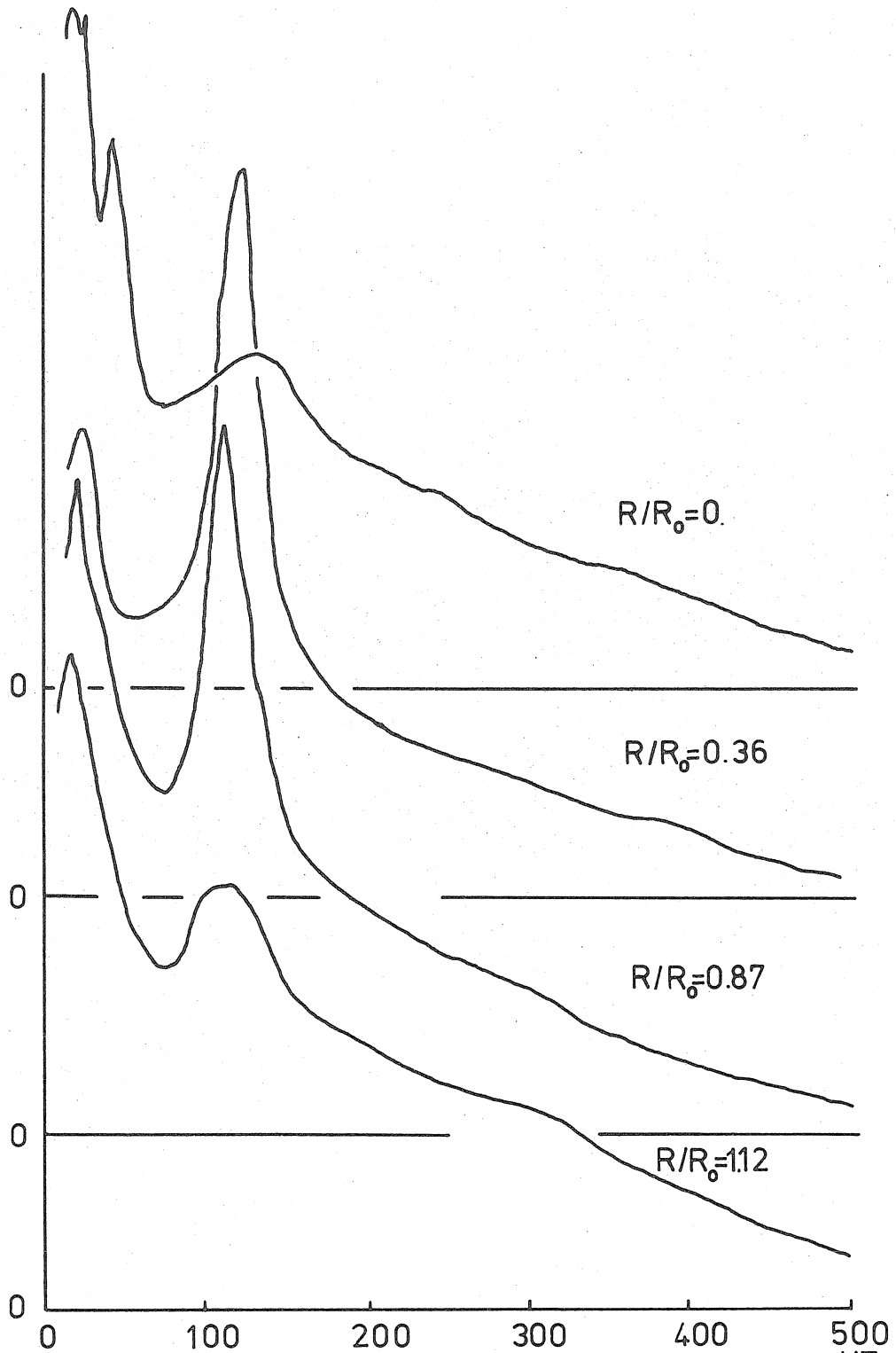


Fig. 66a. Power Spectral Density, Pure Wake X/D= 10

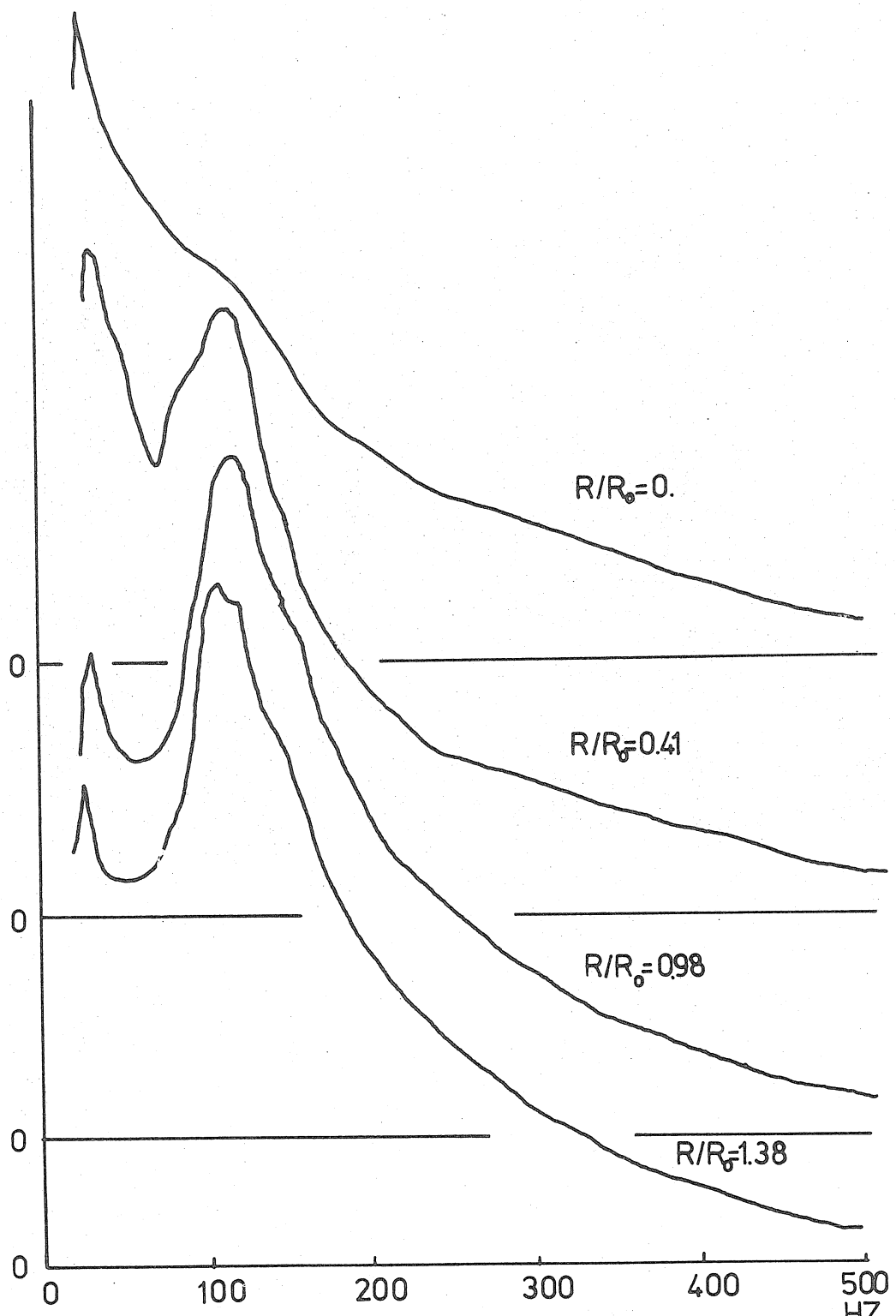


Fig. 66b. Power Spectral Density, Pure Wake X/D = 40

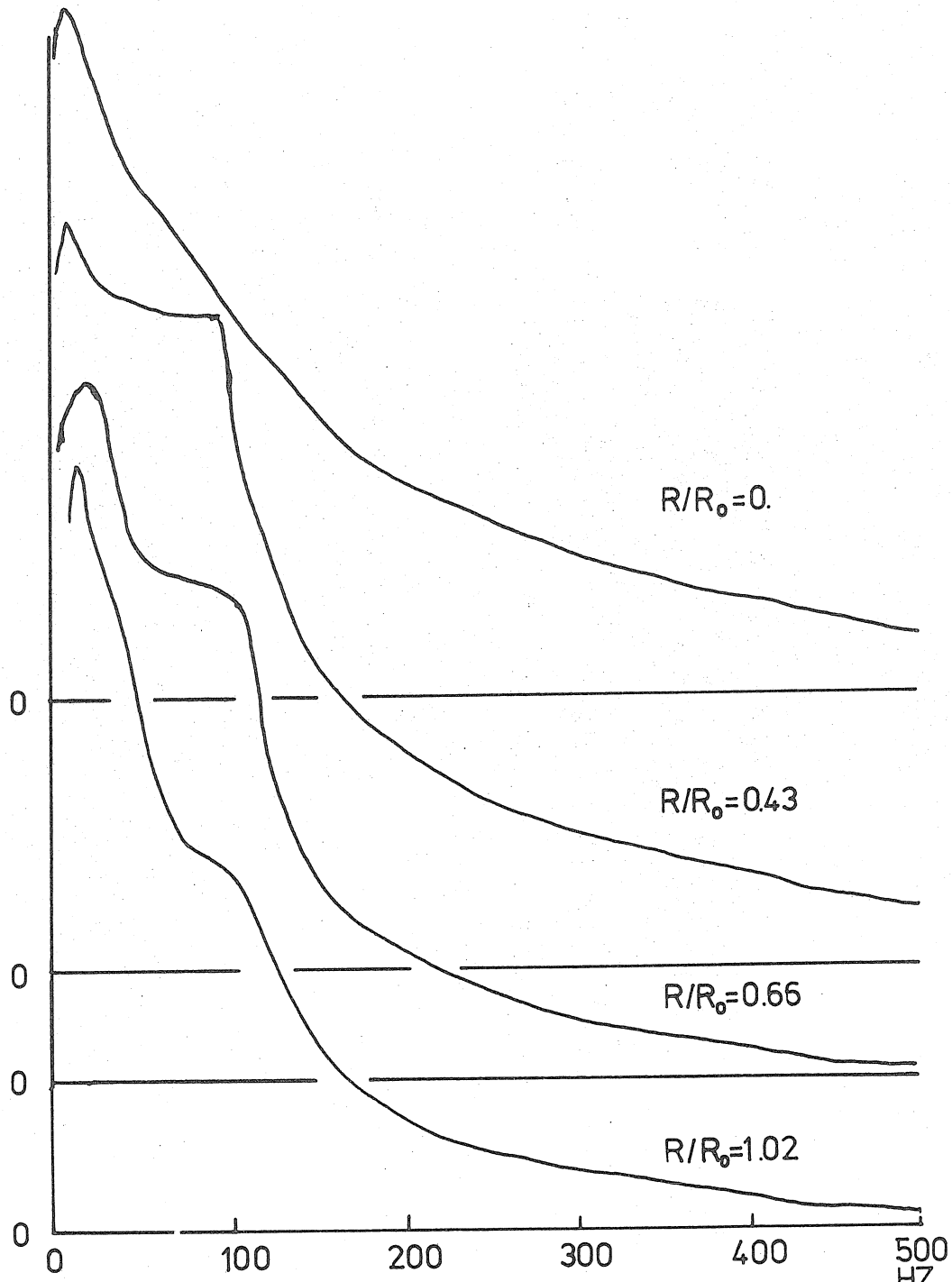


Fig. 66c. Power Spectral Density, Pure Wake X/D = 75

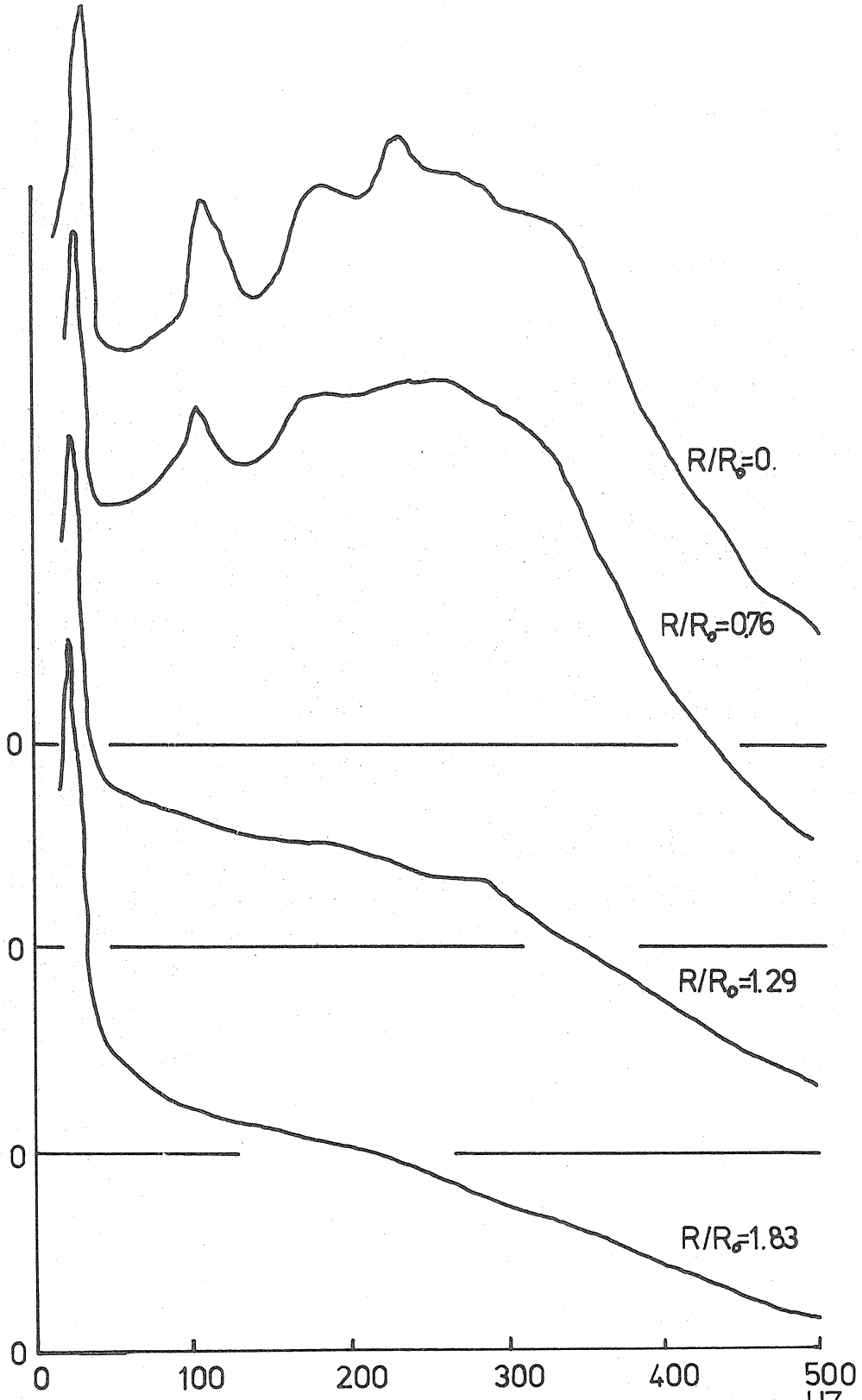


Fig. 67a. Power Spectral Density, Matched Injection
X/D = 10

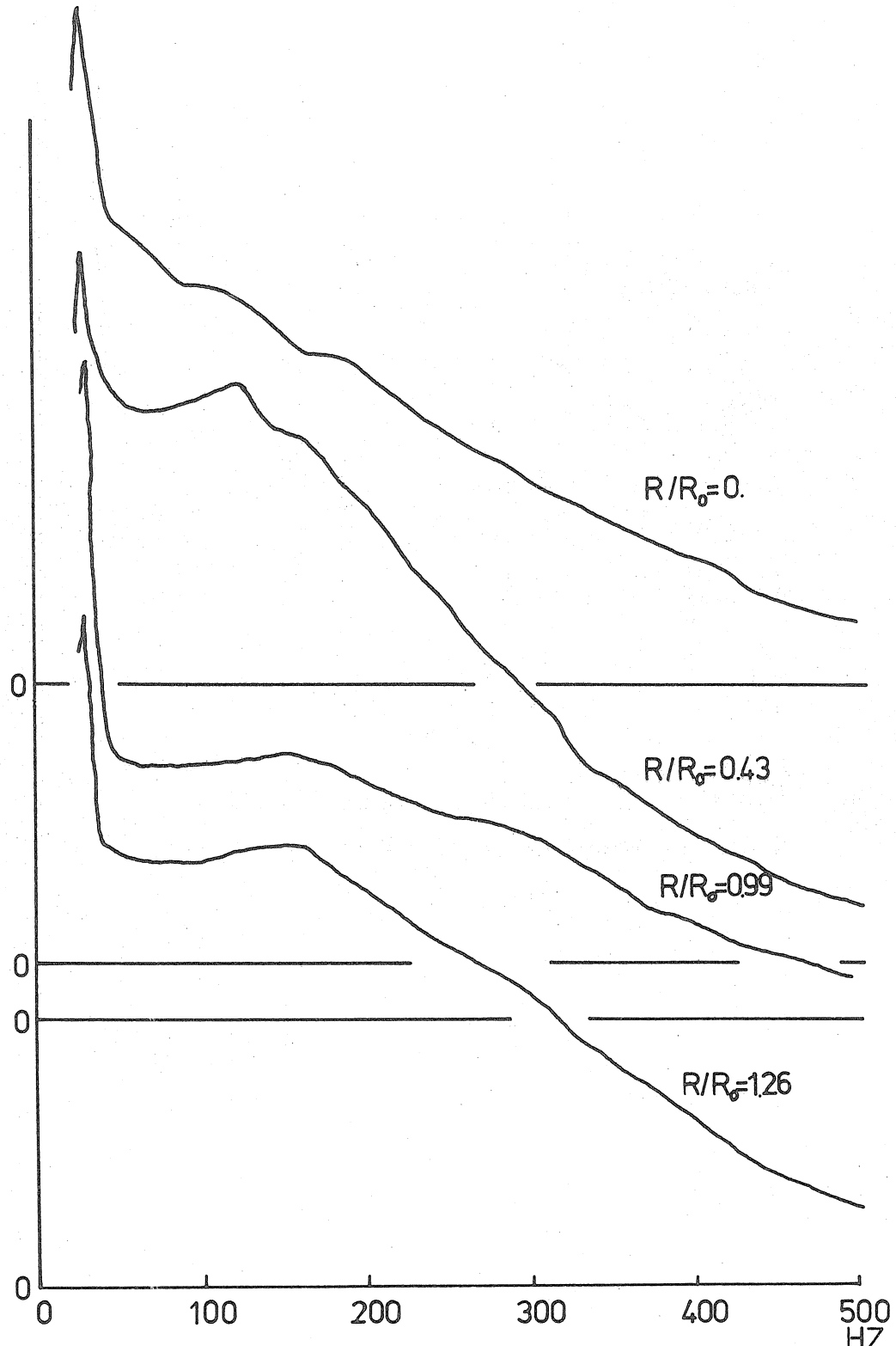


Fig. 67b. Power Spectral Density, Matched Injection
X/D = 40

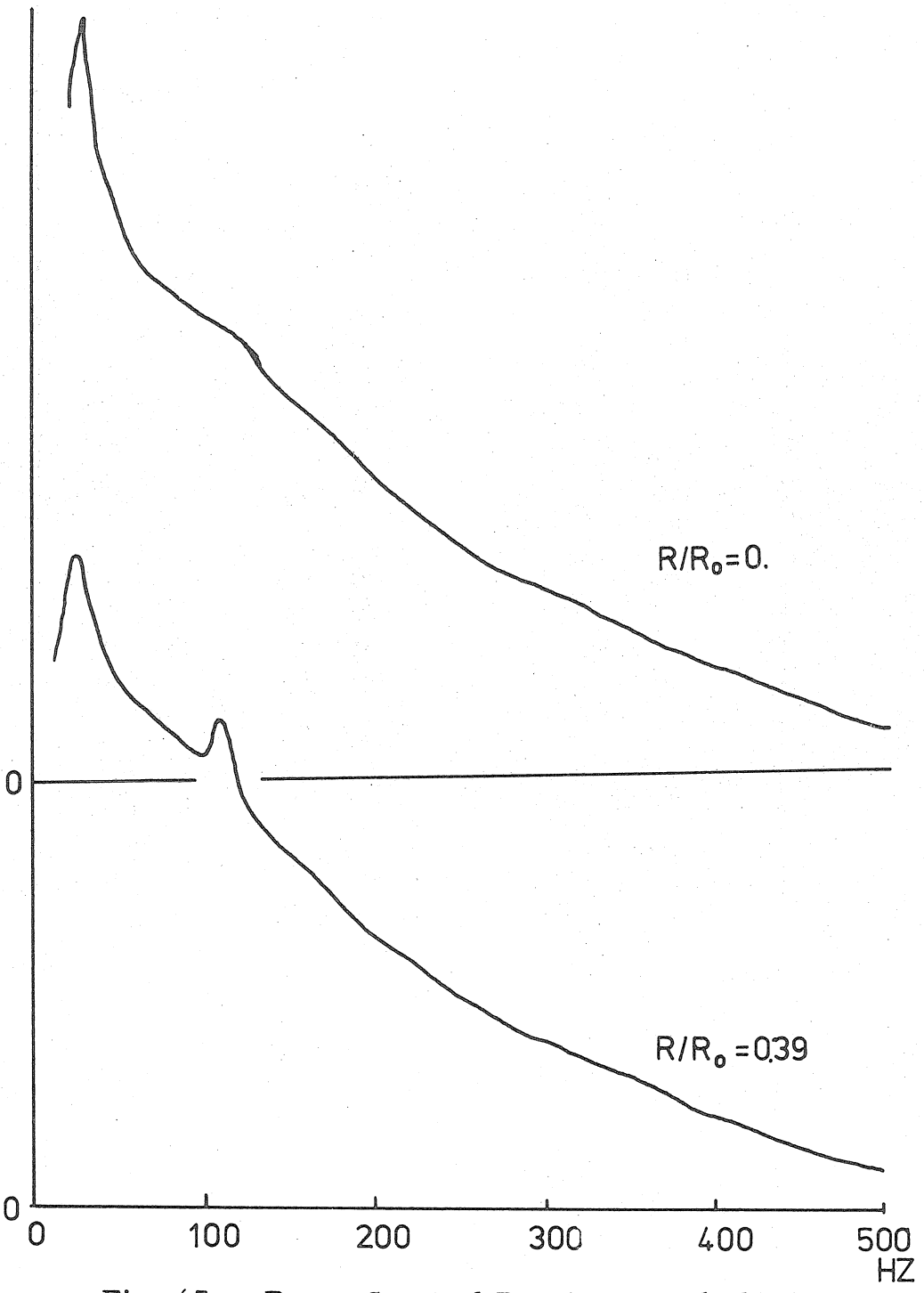


Fig. 67c. Power Spectral Density, Matched Injection
X/D = 75

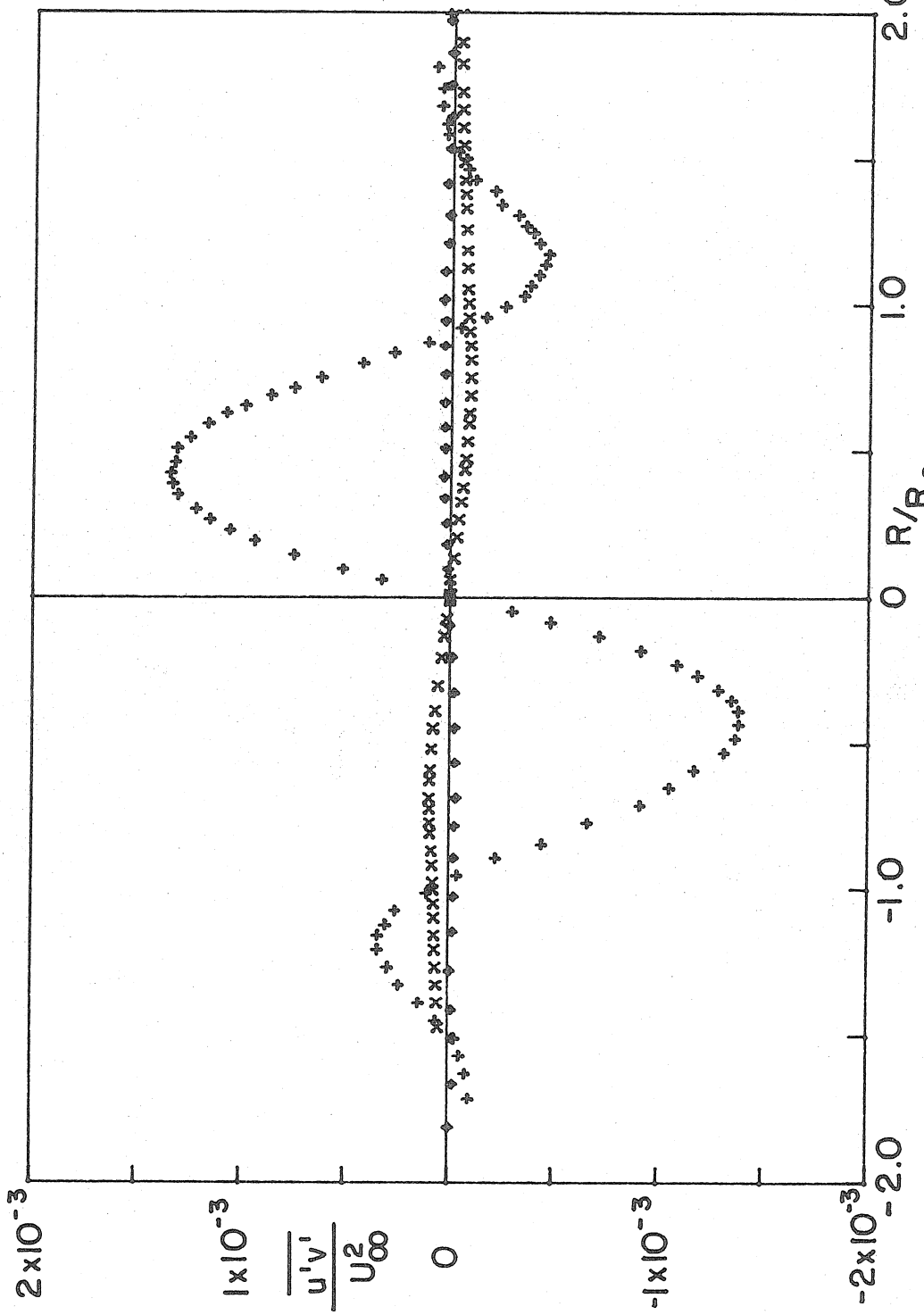


from + Mean Velocity ◆ Mean Static Pressure × Axial Turbulence Intensity

Fig. 68. Turbulent Shear Stress Distribution,(Computed), Matched Injection X/D = 20

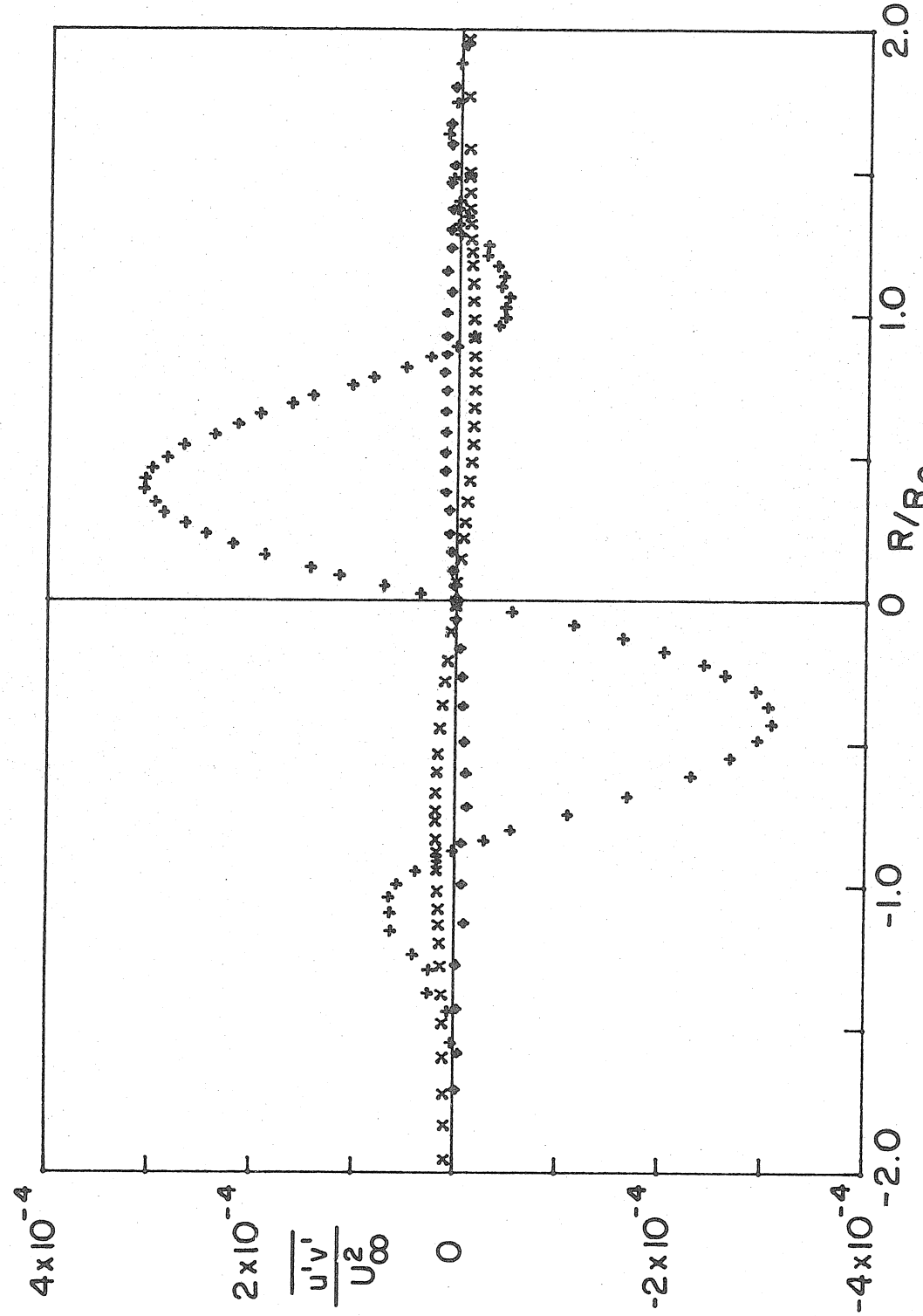


from + Mean Velocity ◆ Mean Static Pressure × Axial Turbulence Intensity

Fig. 69. Turbulent Shear Stress Distribution, (Computed), Matched Injection X/D = 40

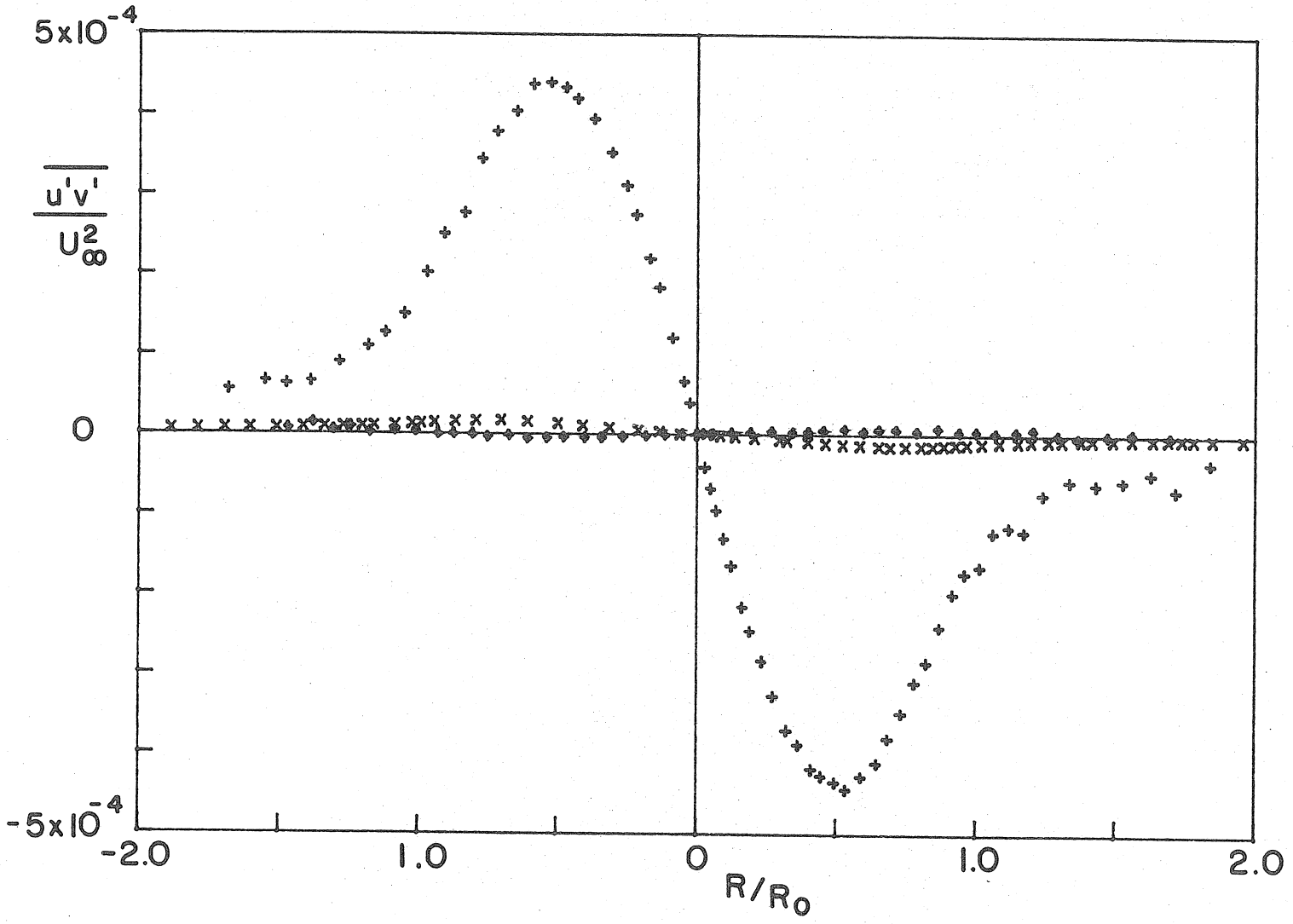


from + Mean Velocity ◇ Mean Static Pressure × Axial Turbulence Intensity

Fig. 70. Turbulent Shear Stress Distribution, (Computed), Pure Wake X/D = 40

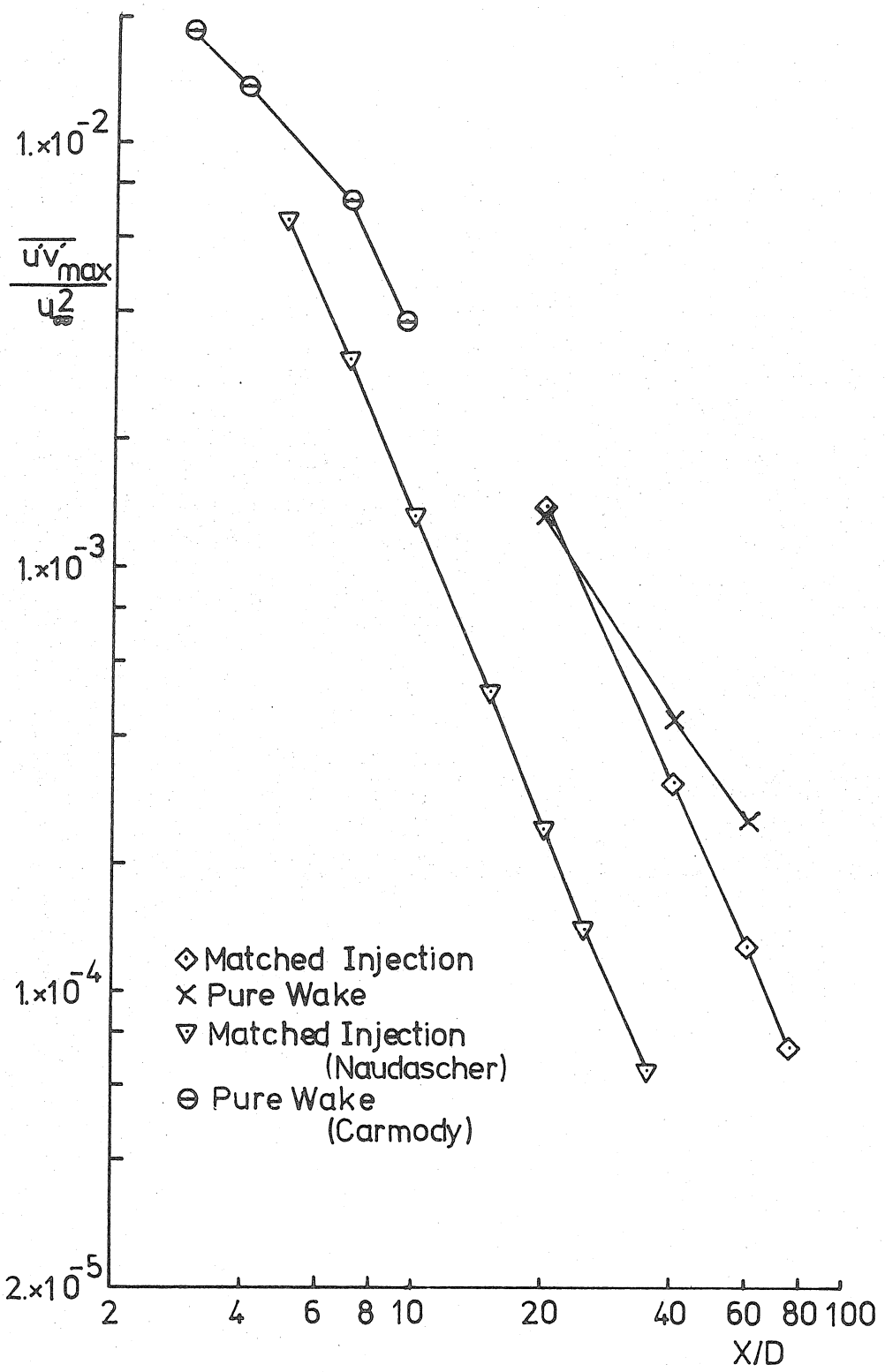


Fig. 71. Axial Variation of Maximum Turbulent Shear Stress

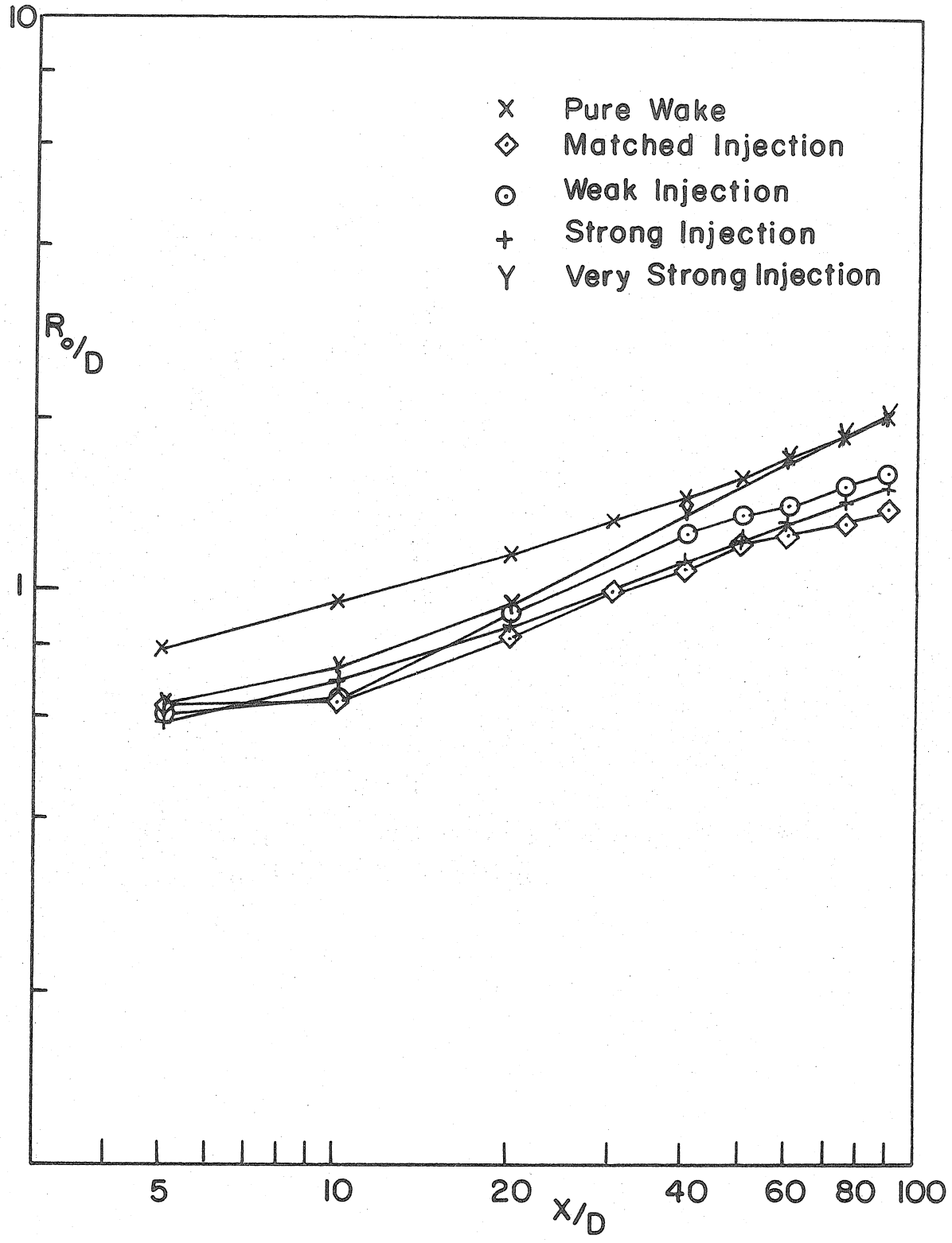


FIG. 72 SPREADING OF THE WAKE IN VARIOUS INJECTION CASES

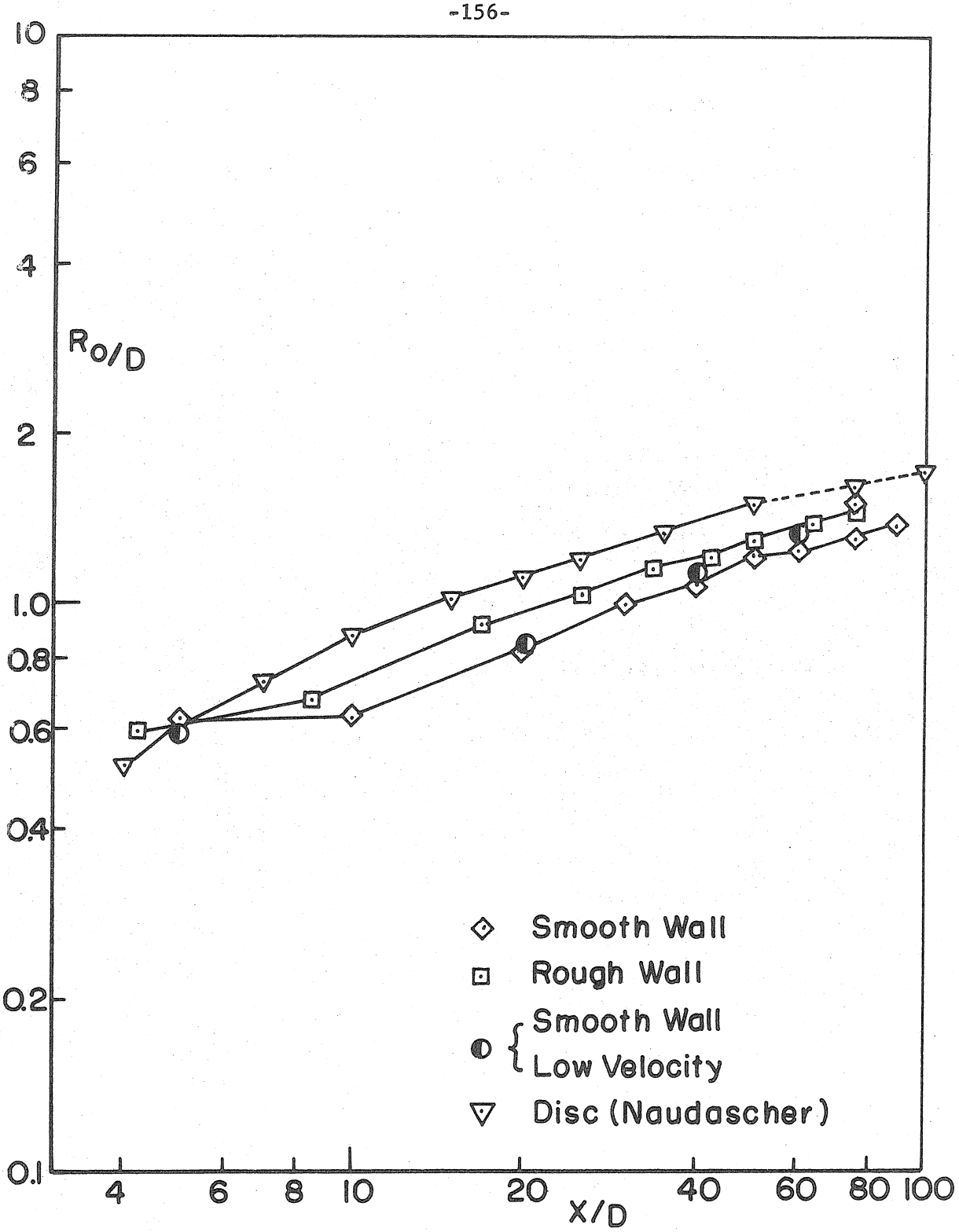


Fig. 73. Spreading of the Wake in Matched Injection Cases

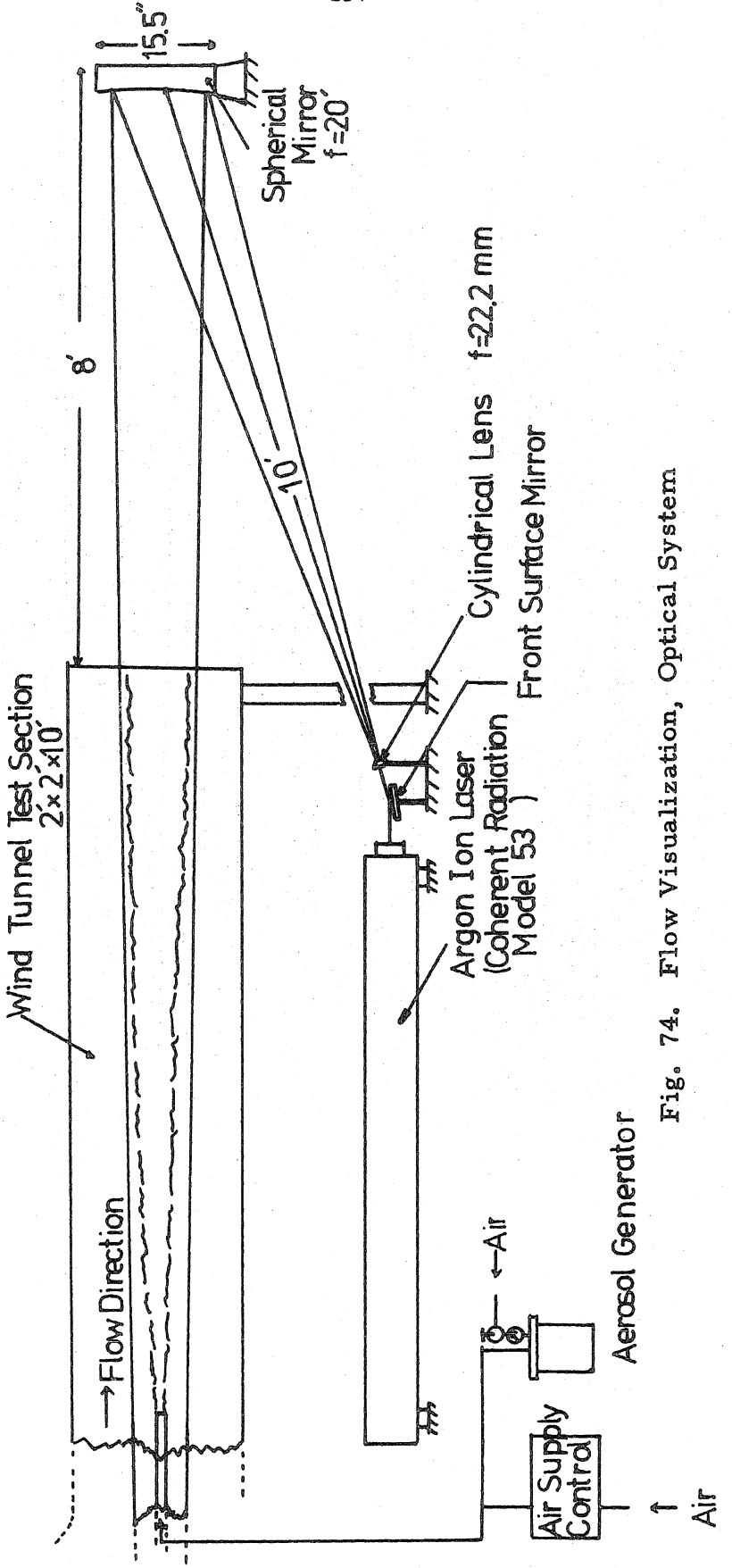


Fig. 74. Flow Visualization, Optical System

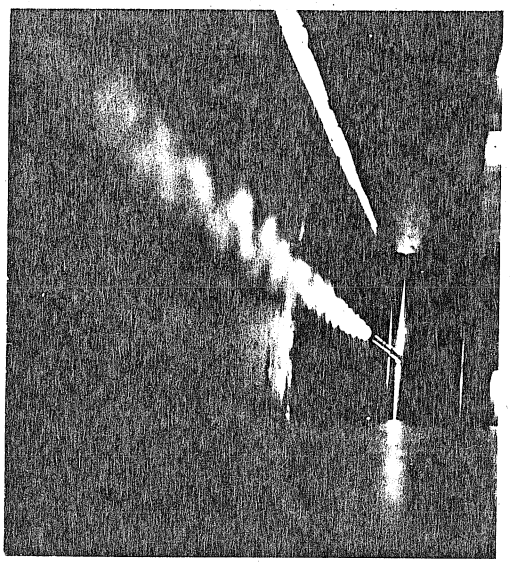

Fig. 75. Overall View of the Flow Visualization, X/D = 0-80, Strong Injection $Re_d$ = 3270

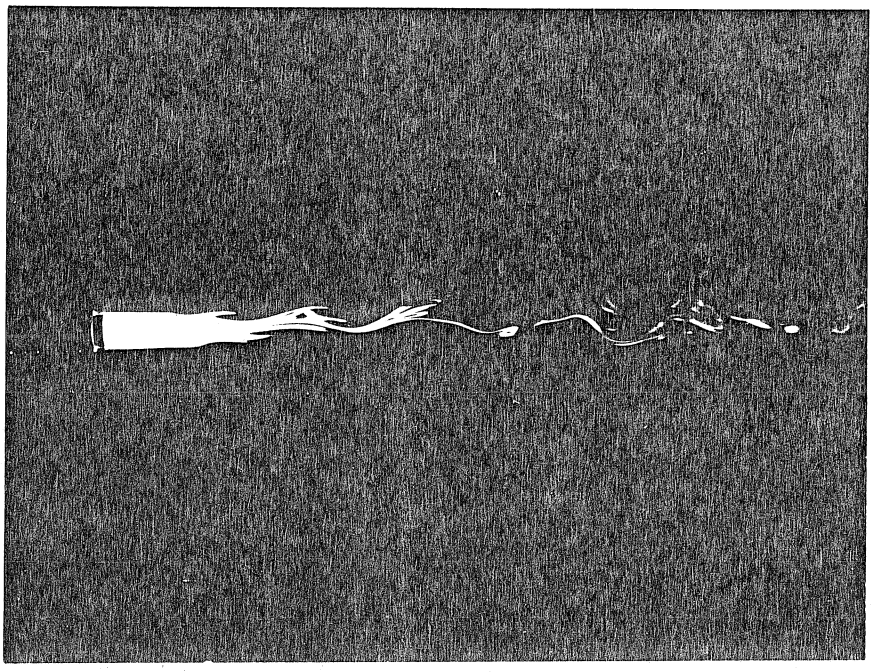

Fig. 76. Near Field of the Pure Wake, $Re_d = 2620$

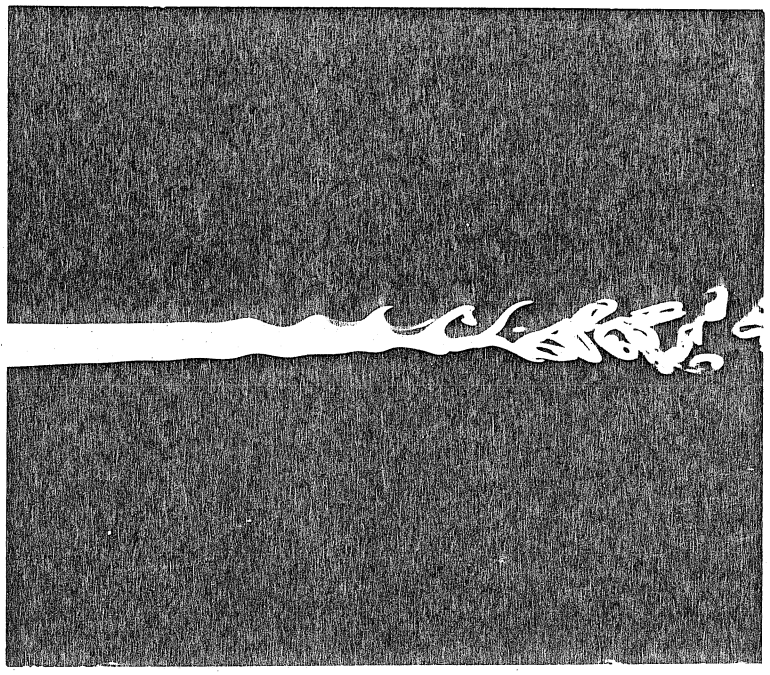

(a) X/D = 0 ~ 20

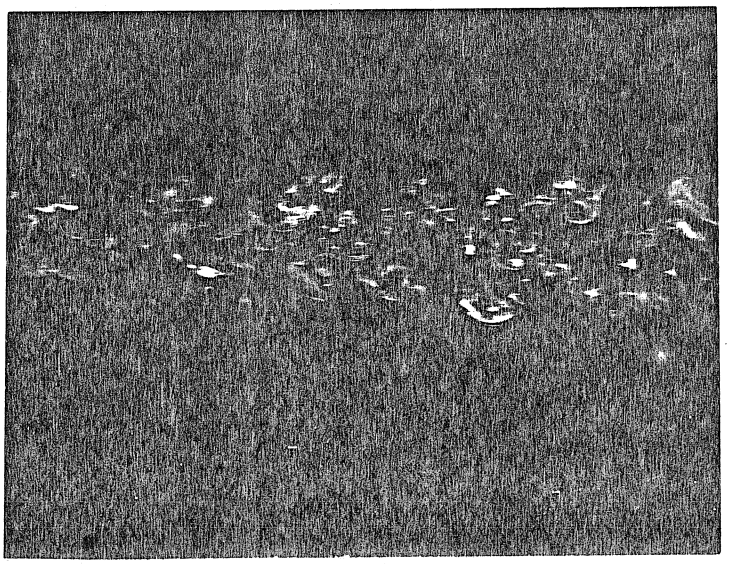

(b) X/D = 50 ~ 80

Fig. 77. Very Weak Injection, a) X/D = 0.20 b) X/D = 50-80, $Re_d$ = 2620

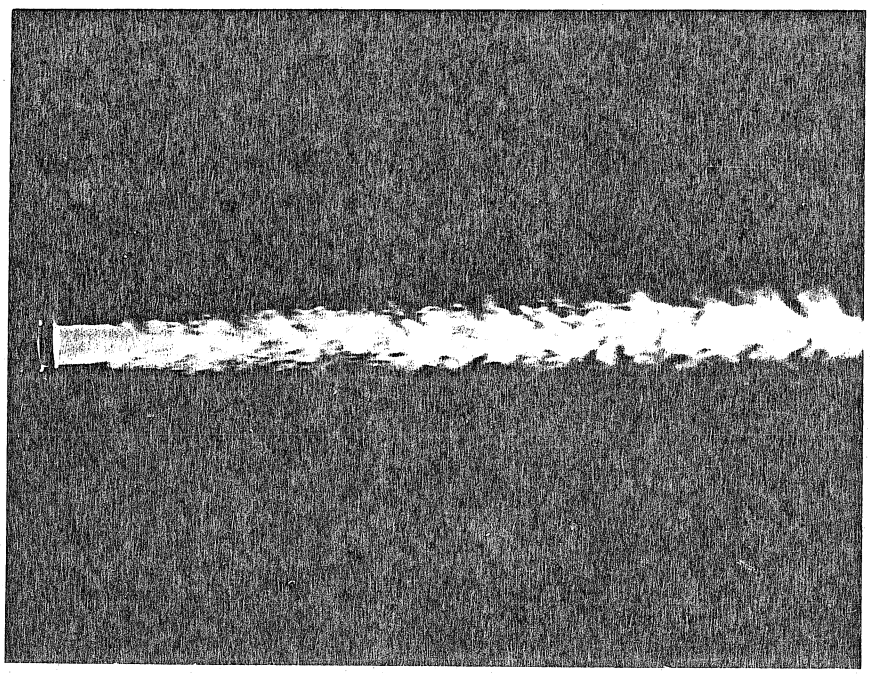

a) X/D = 0 ~ 20

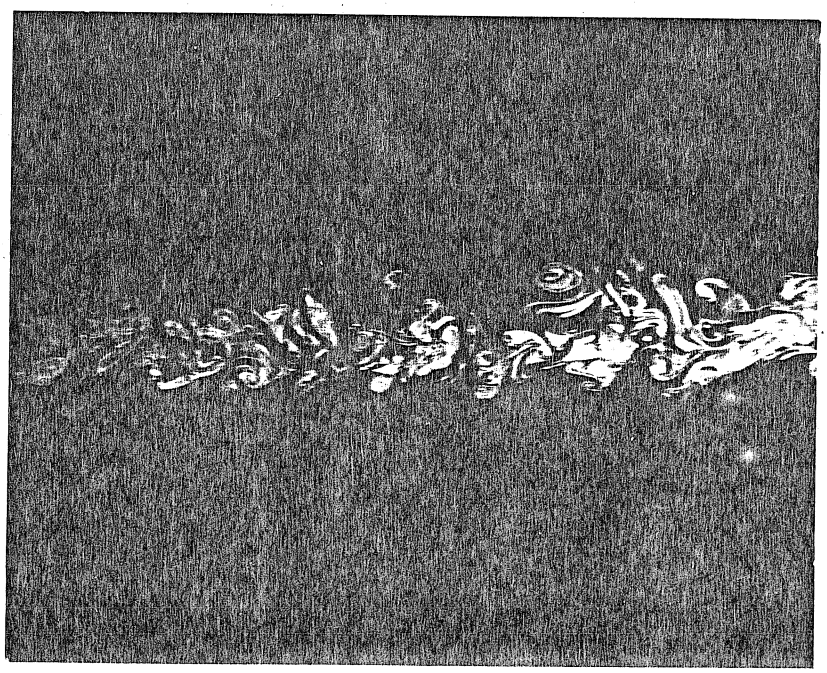

b) X/D = 50 ~ 80

Fig. 78. Strong Injection, a/ X/D = 0-20 b) X/D = 50-80

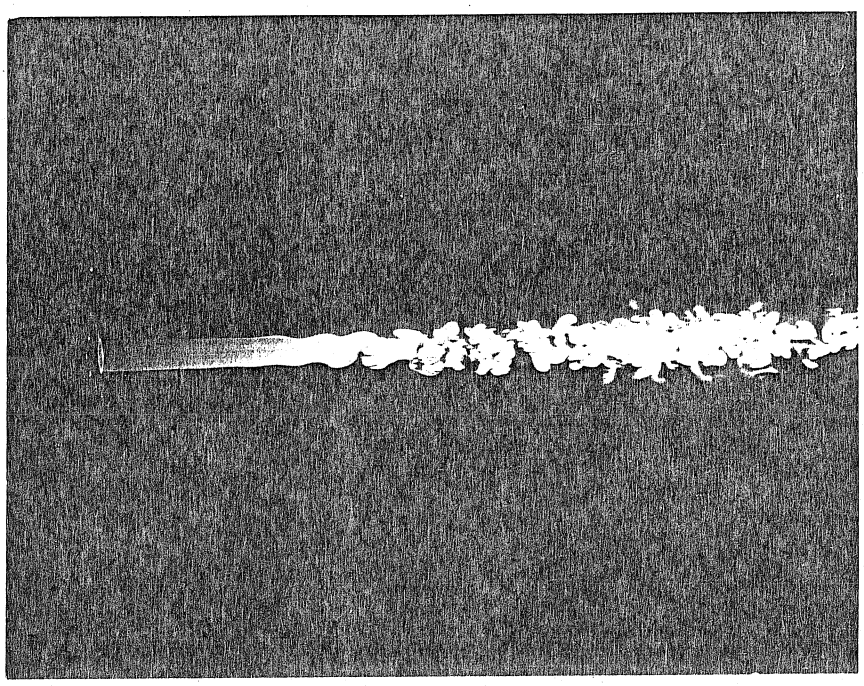

a) X/D = 0 ~ 25

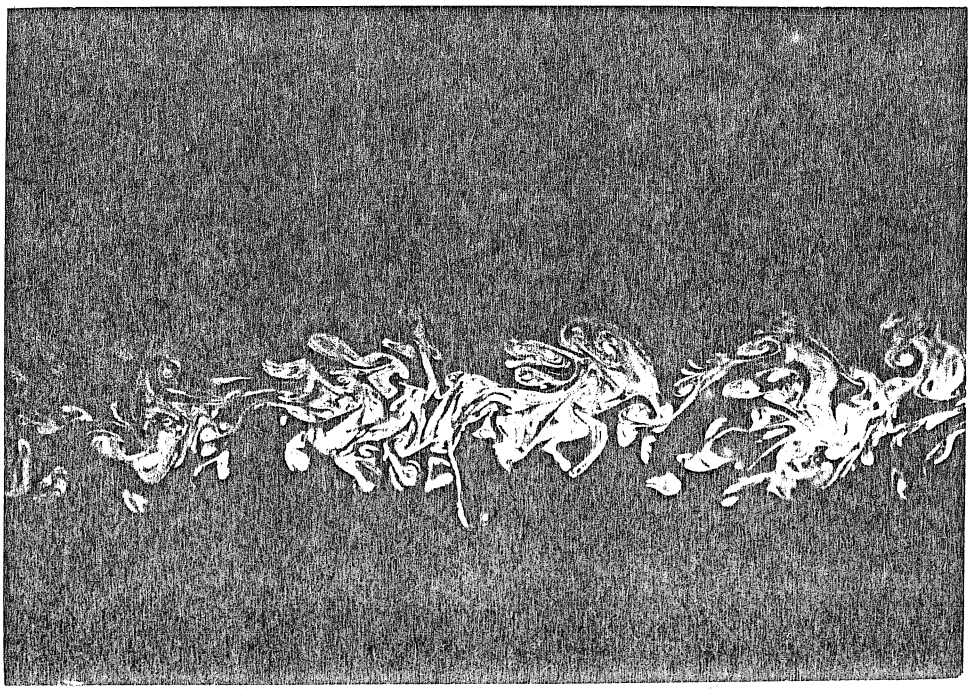

b) X/D = 47 ~ 70

Fig. 79. Matched Injection $Re_d$ = 2620 a) X/D = 0-25 b) X/D = 47-70

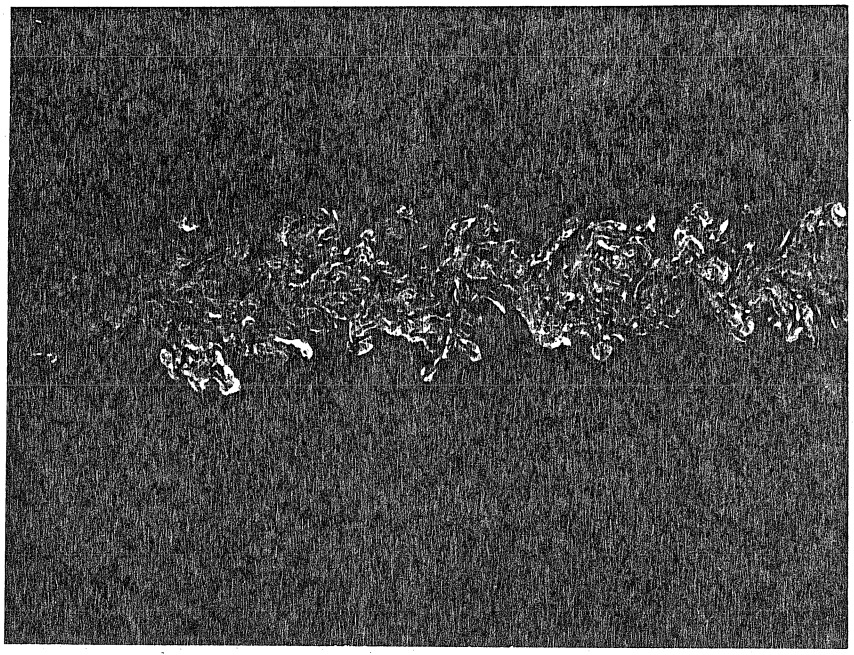

Fig. 80. Matched Injection $Re_d$ = 6550 X/D = 50-80

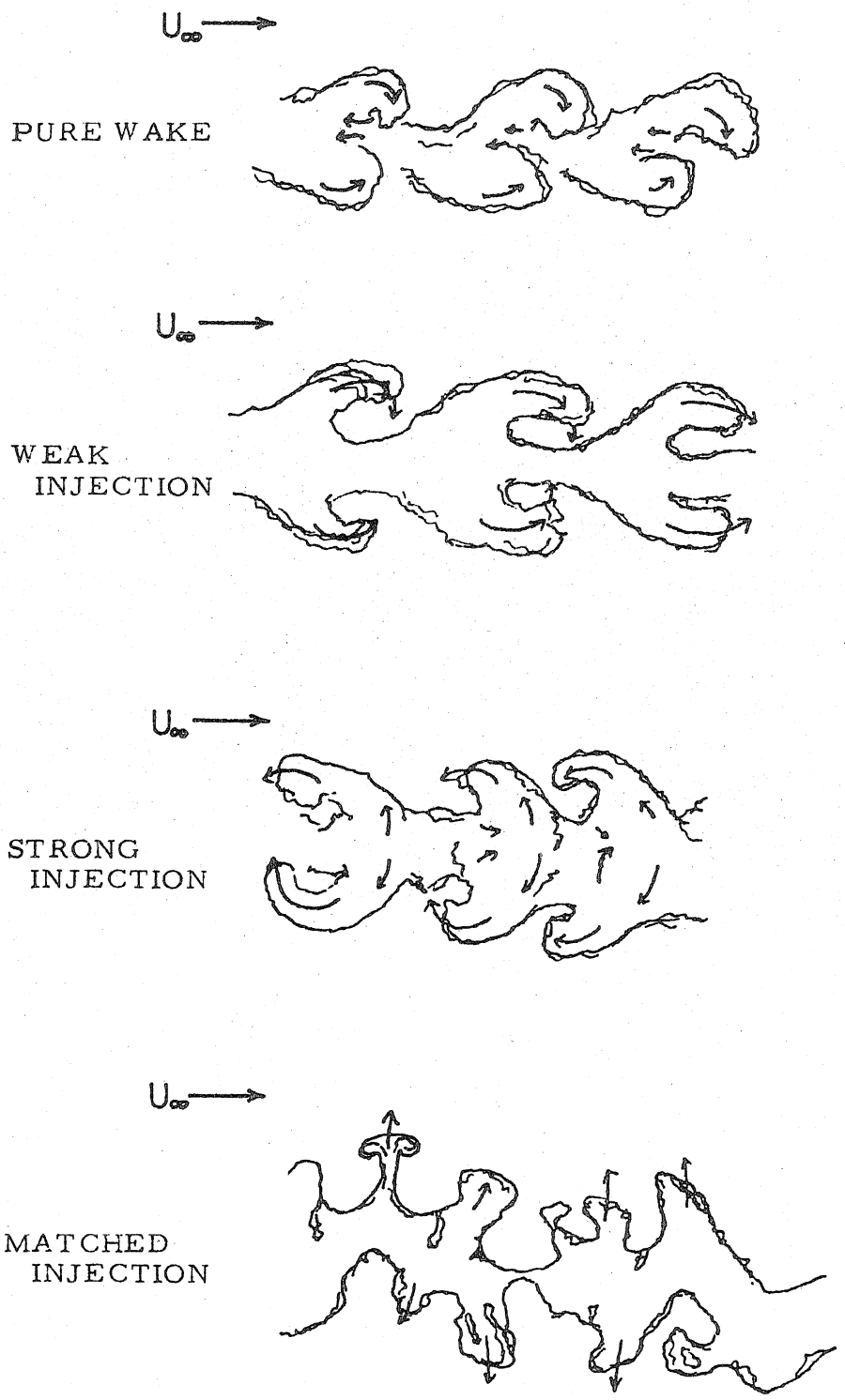


Fig. 81
Sketches of Large Eddy Motions

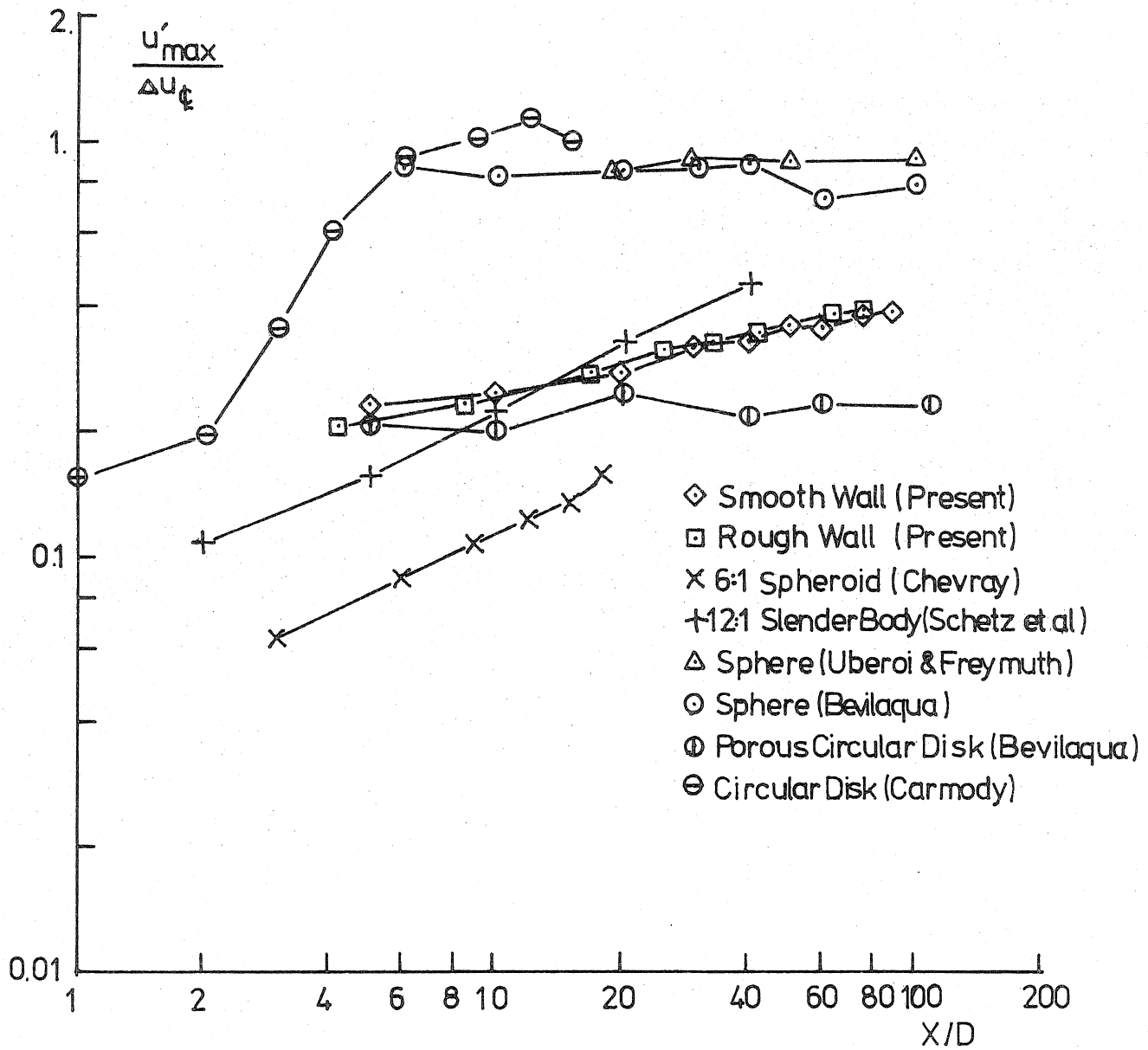


Fig. 82. Balance between Mean Flow and Turbulence in Pure Wakes

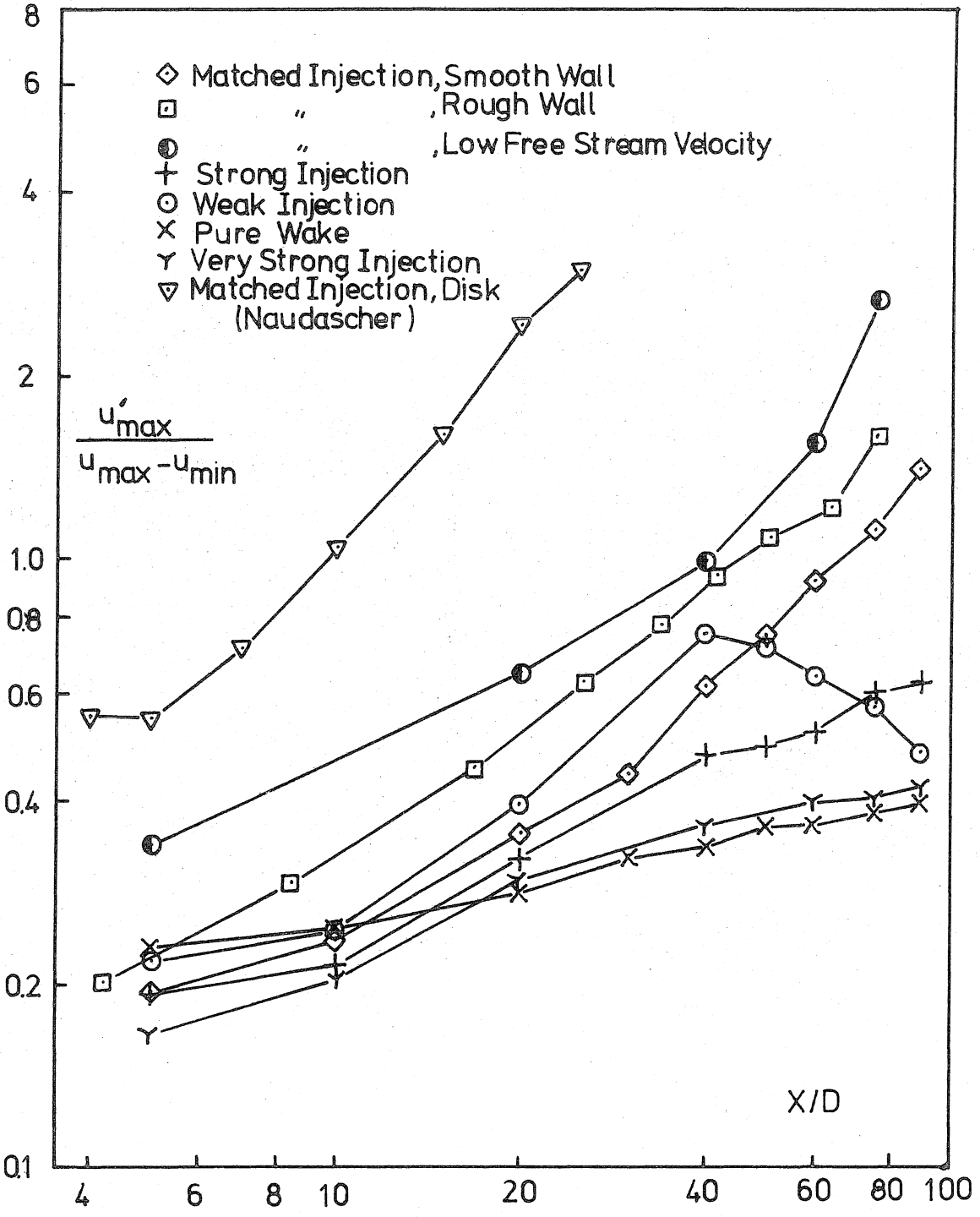


Fig. 83. Balance between Mean Flow and Turbulence in Various Injections

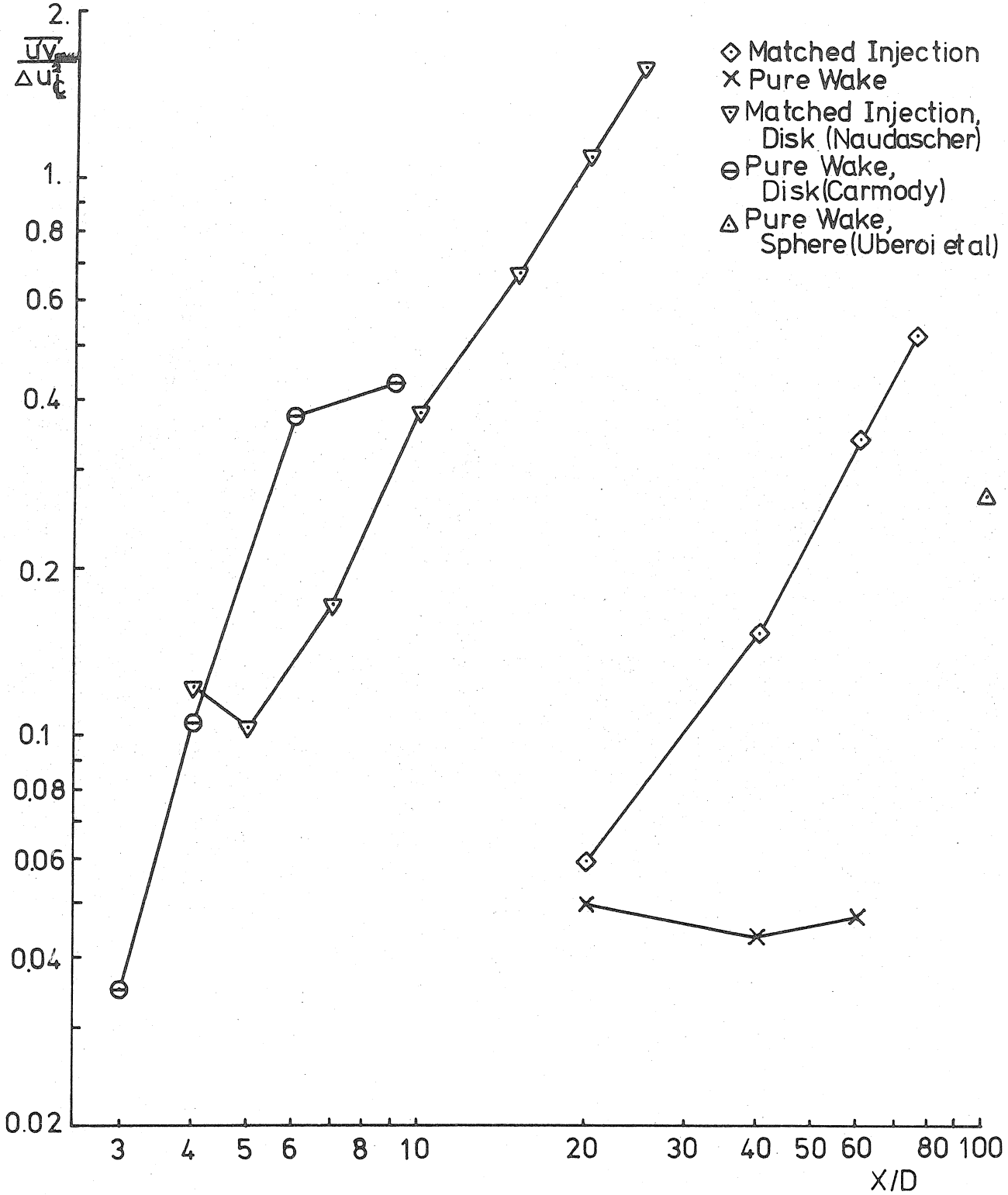


Fig. 84. Ratio between Maximum Turbulent Shear and Centerline Velocity Defect

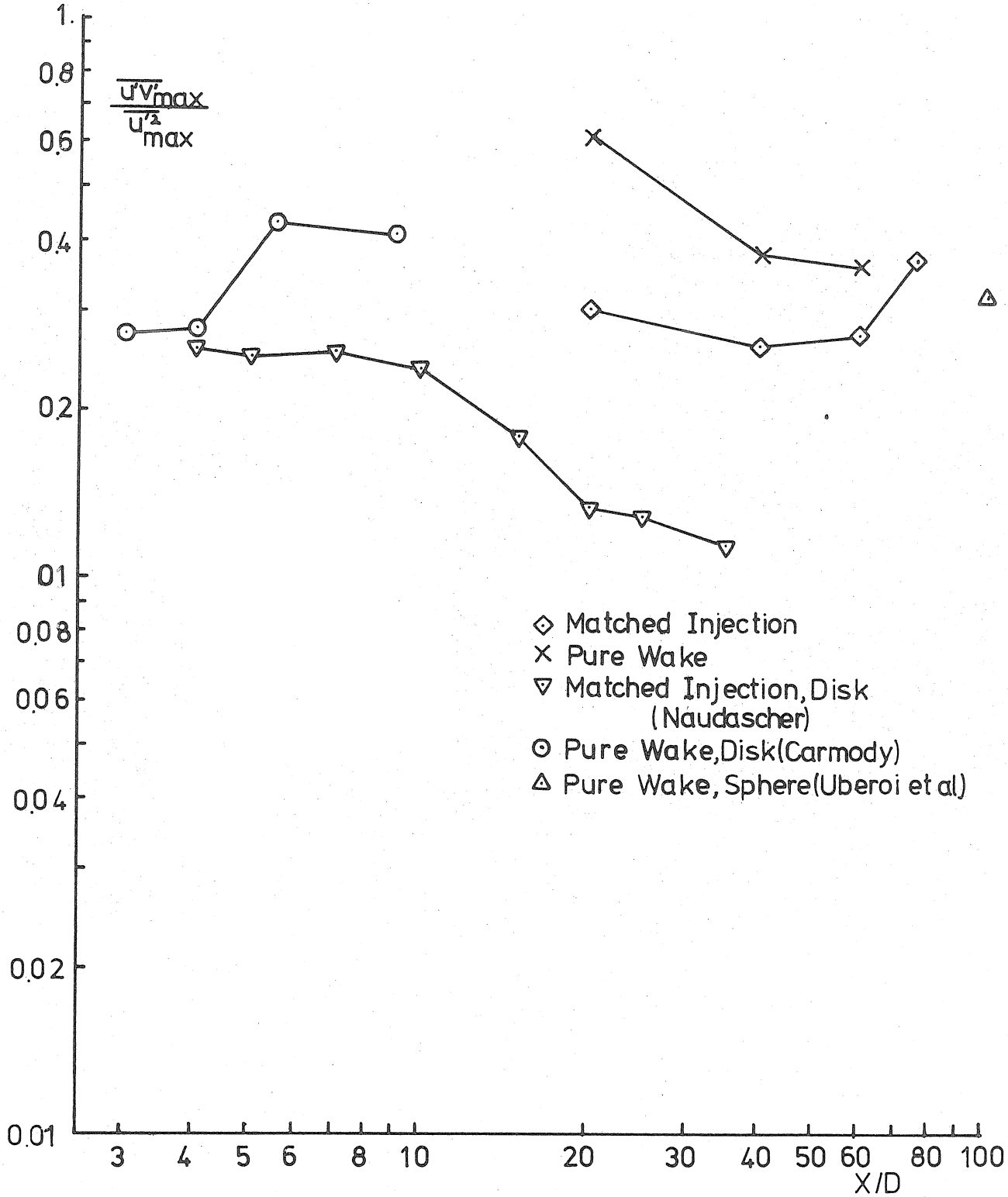


Fig. 85. Ratio between Maximum Turbulent Shear and Maximum Axial Turbulence Intensity

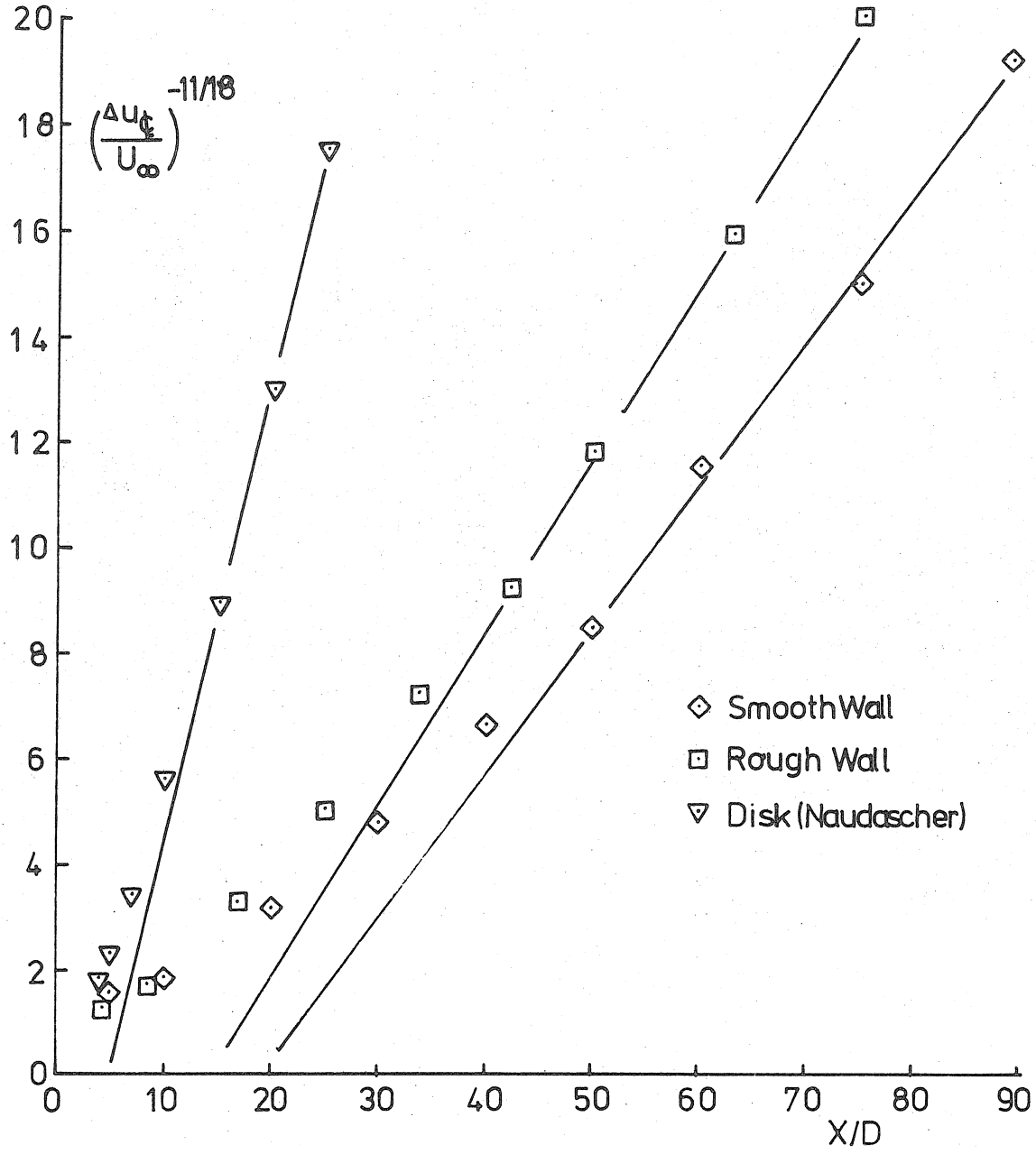


Fig. 86. Comparison with Finson's Analysis, Centerline Velocity

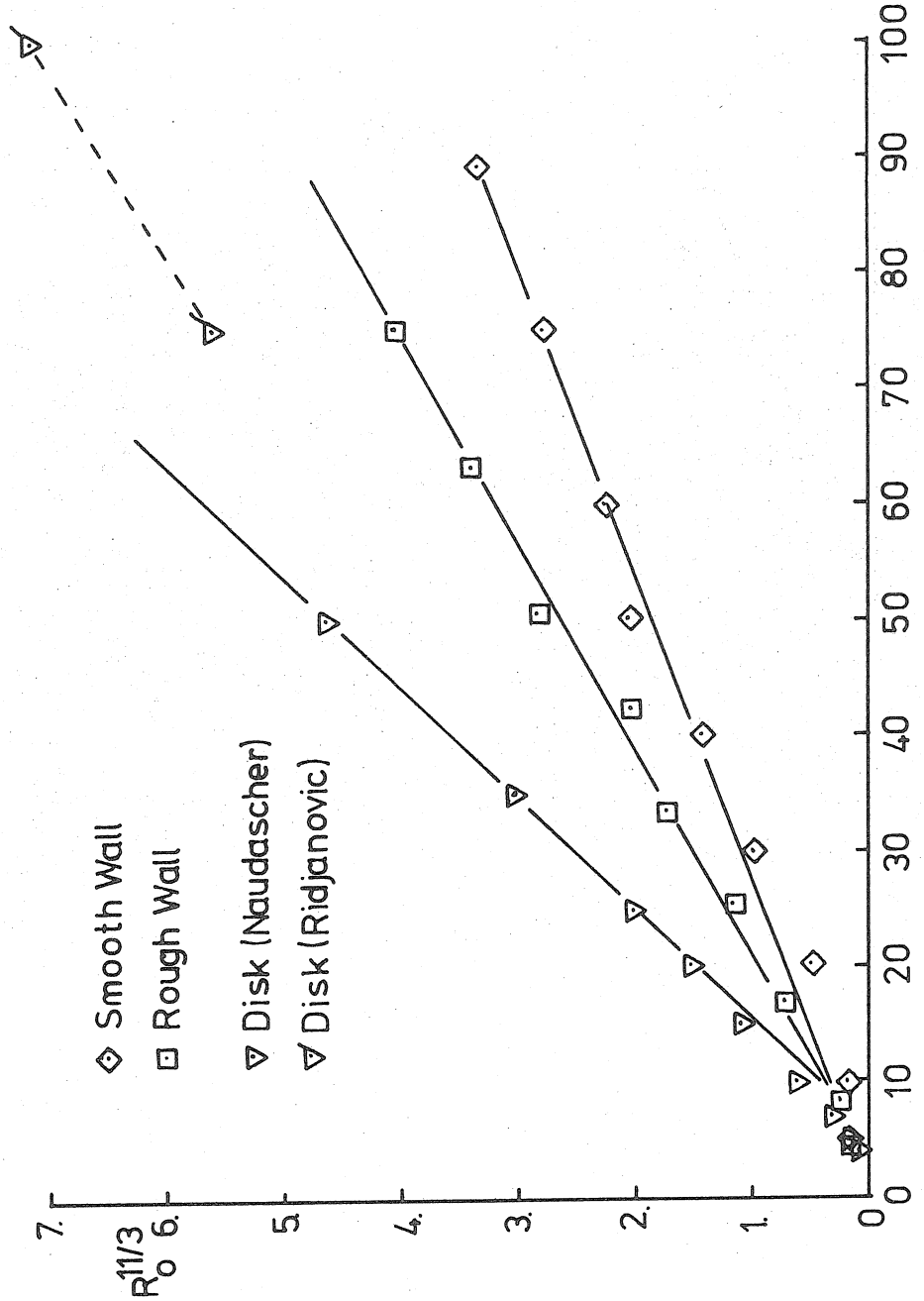


Fig. 87. Comparison with Finson's Analysis, Wake Width

# APPENDIX A - SIMPLE TURBULENCE MODELS

## 1. Prandtl's Eddy Viscosity Model and the Mixed Wake

Here an analysis using a constant eddy viscosity model is presented to study the behavior of the far wake when the momentum flux is not exactly matched and the flow leaves either deficit or excess of momentum in the wake.

The argument here is more straightforward than in Tennekes and Lumley (1972, p. 126). The result yields the similar lower order terms except for the higher order terms of the pure wake which are still dominant over the zero momentum wake terms.

Equation of Motion is

$$u \frac{\partial u}{\partial x} + v \frac{\partial u}{\partial r} = \frac{1}{r^j} \frac{\partial}{\partial r} (r^j \nu_T \frac{\partial u}{\partial r}) \qquad \text{(A-1)}$$

where $j = 0$ for two-dimensional flow ,

and $j = 1$ for axisymmetric flow .

If we define $u_d = u - u_\infty$ and assume $u_d << U_\infty$ we obtain

$$U_\infty \frac{\partial u_d}{\partial x} = \frac{1}{r^j} \frac{\partial}{\partial r} (r^j \nu_T \frac{\partial u_d}{\partial r}) \quad . \qquad \text{(A-2)}$$

If the eddy viscosity is assumed to be constant across the wake, Eq. (A-2) becomes

$$U_\infty \frac{\partial u_d}{\partial x} = \nu_T \frac{1}{r^j} \frac{2}{\partial r} (r^j \frac{\partial u_d}{\partial r}) \quad . \qquad \text{(A-3)}$$

Here we introduce a transformation as

$$\xi = \frac{1}{\nu} \int_o^x \nu_T(x)dx \qquad \text{where } \nu = \text{constant} \quad . \qquad \text{(A-4)}$$

Then Eq. (A-3) becomes

$$U_\infty \frac{\partial u_d}{\partial \xi} = \nu \frac{1}{r^j} \frac{\partial}{\partial r} \left( r^j \frac{\partial u_d}{\partial r} \right) \qquad \text{(A-3')}$$

which is identical with the laminar flow case. When the solution of the form

$$u_d = \sum_{n=0}^{\infty} A_n \xi^{-k_n} f_n(\eta) , \quad \eta = r/b$$
$$b = \sum_{n=0}^{\infty} B_n \xi^{m_n} \qquad \text{(A-4)}$$

is sought, the wake width is obtained for similarity as

$$b(x) = 2\sqrt{\frac{\nu}{U_\infty}} \xi^{\frac{1}{2}} = 2 \frac{\nu}{U_\infty} \xi_*^{\frac{1}{2}} \qquad \text{(A-5)}$$

where $\xi_* = U_o \xi / \nu$ .

The exponent $k_n$'s are determined as follows:

From a condition for momentum flux = constant, we obtain

$$k_o = \frac{j+1}{2} ,$$

since $$(-2 k_o + 1 + j) \int_o^\infty f \eta^j d\eta = 0 . \qquad \text{(A-6)}$$

From the condition for the constant moment of momentum we obtain

$$k_n = \frac{2n+1+j}{2} \qquad n \geq 1 ,$$

since $$(2n+1+j-2k_n) \int_o^\infty f \eta^{2+j} d\eta = 0 . \qquad \text{(A-7)}$$

The equation for the velocity profile is given by

$$f''(\eta) + (2\eta + j\eta^{-1}) f'(\eta) + 4k_n f(\eta) = 0 . \qquad \text{(A-8)}$$

This is subject to the following boundary conditions

$$\begin{cases} f \to 0 \\ f' \to 0 \end{cases} \quad \text{as } \eta \to \infty$$

$$\begin{cases} f = 1 \\ f' = 0 \end{cases} \quad \text{at } \eta = 0 \; .$$

Solutions to Eq. (8) are given by

a. Two-dimensional case

$$f_n(\eta) = H_{2k_n-1}(\eta)e^{-\eta^2}$$

$$\begin{cases} f_o(\eta) = e^{-\eta^2} \\ f_n(\eta) = H_{2n}(\eta)e^{-\eta^2} \qquad n \geq 1 \end{cases} \tag{A-9}$$

where $H_m$ is a Hermite Polynomial and $H_2(\eta) = 1-2\eta^2$ .

b. Axisymmetric case

$$f_n(\eta) = Lk_{n-1}(\eta^2)e$$

$$\begin{cases} f_o(\eta) = e^{-\eta^2} \\ f_n(\eta) = L_n(\eta^2)e^{-\eta^2} \qquad n \geq 1 \end{cases} \tag{A-10}$$

where $L_n$ is a Laguerre polynomial, and $L_1(\eta^2) = 1-\eta^2$. Then the velocity distribution is given as

$$\frac{u_d}{U_\infty} \sim A\, \xi_*^{-\frac{1}{2}(j+1)} \left[ f_o(\eta) + \frac{a_1}{\xi_*} f_1(\eta) + \ldots . \right] \tag{A-11}$$

where $f_0(\eta)$ and $f_1(\eta)$ are given by Eqs. (A-9) and (A-10), and A and $a_1 \ldots .$ are the constants to be determined from the initial velocity profile. (For the higher order terms of $u_d/U_\infty$, see Note 1; for the zero drag case, see Note 2). Now we proceed to express Eqs. (A-5)

and (A-11) in terms of the original axial coordinate x. Prandtl's eddy viscosity model states $\nu_T(x) = \kappa\, u_{d\mathcal{L}}(x) \cdot b(x)$ where $\kappa$ is a constant. Hence

$$\frac{dx}{d\xi} = \frac{\nu^2}{u_\infty \nu_T(x)} = \frac{\nu^2}{U_\infty \kappa u_{d\mathcal{L}}(x) b(x)}$$

$$\therefore \quad \frac{dx}{d\xi_*} = \frac{\nu^2}{U_\infty \kappa A \xi_*^{-\frac{1}{2}(j+1)} U_\infty \left[1+\frac{a_1}{\xi_*}+\ldots\right]\frac{2\nu}{U_\infty}\xi_r^{\frac{1}{2}}}$$

$$= \frac{\nu}{2U_\infty \kappa A} \frac{1}{\xi_*^{-\frac{1}{2}j}\left[1+\frac{a_1}{\xi_*}+\ldots\right]}$$

$$\frac{dx}{d\xi_*} \sim \frac{\nu}{2U_\infty \kappa A}\, \xi_*^{\frac{1}{2}j}\left(1-\frac{a_1}{\xi_*}+\ldots\right) . \qquad \text{(A-12)}$$

Therefore, we obtain

Two dimensional case

$$X = \frac{\nu}{2U_\infty \kappa A}\left(\xi_* - a_1 \ell n\, \xi_* + \ldots\right) \qquad \text{(A-13)}$$

Axisymmetric case

$$X = \frac{\nu}{2U_\infty \kappa A}\left(\frac{3}{2}\xi^{\frac{3}{2}} - 2a_1 \xi^{\frac{1}{2}} + \ldots\right) . \qquad \text{(A-14)}$$

When we define

$$X_* = \frac{2U_\infty \kappa A}{\nu} X ,$$

the transformation is carried out as follows:

(1) Two-dimensional case

$$X_* = \xi_* - a_1 \ell n\, \xi_* + \cdots .$$

$$\therefore \quad \xi_* \doteq X_* + a_1 \ell n\, \xi_* \quad .$$

This is approximated as

$$\xi_{*0} \simeq X_*$$

$$\xi_{*1} \simeq X_* + a_1 \ell n\, X_*$$

$$\xi_{*2} \simeq X_* + a_1 \ell n (X_* + a_1 \ell n\, X_*) \quad .$$

Hence

$$\xi_*^{-\frac{1}{2}} = X_*^{-\frac{1}{2}} \left( 1 + \frac{a_1}{X_*} \ell n\, X_* + \frac{a_1^2}{X_*^2} \ell n X_* + \cdots \right)^{-\frac{1}{2}}$$

$$= X_*^{-\frac{1}{2}} \left[ 1 - \tfrac{1}{2} \left( \frac{a_1}{X_*} \ell n X_* + \frac{a_1^2}{X_*^2} \ell n X_* \right) + \tfrac{1}{2} \left( -\tfrac{1}{2} \right) \left( -\tfrac{3}{2} \right) \frac{a_1^2}{X_*^2} (\ell n X_*)^2 + \cdots \right]$$

and $\xi_*^{-\frac{3}{2}} = X_*^{-\frac{3}{2}} - \cdots .$

Therefore, we get the velocity distribution as

$$\frac{u_d}{U_\infty} \simeq A \Big[ \left( X_*^{-\frac{1}{2}} - \tfrac{1}{2} X_*^{-\frac{3}{2}} \ell n\, X_* - \tfrac{1}{2} X_*^{-\frac{5}{2}} \ell n\, X_* - \cdots \right) e^{-\eta^2}$$

$$+ a_1 \left( X_*^{-\frac{3}{2}} - \cdots \right) (1 - 2\eta^2) e^{-\eta^2} \Big] \quad . \qquad \text{(A-15)}$$

The wake width is obtained from Eq. (A-6) as

$$b(x) = 2 \frac{\nu}{U_\infty} \xi_*^{\frac{1}{2}} \simeq 2 \frac{\nu}{U_\infty} \left[ X_*^{\frac{1}{2}} \left( 1 + \frac{a_1}{2} X_*^{-1} \ell n X_* \cdots \right) \right] \qquad \text{(A-16)}$$

where $$X_* = \frac{2 U_\infty K A}{\nu} X \quad .$$

(2) Axisymmetric Case

$$X_* = \frac{3}{2}\xi_*^{\frac{3}{2}} - 2a_1\xi_*^{\frac{1}{2}} + \cdots .$$

Let

$$\zeta = \xi_*^{\frac{1}{2}} .$$

Then we have

$$\zeta^3 - \frac{4a_1}{3}\zeta - \frac{2}{3}X_* = 0 .$$

Instead of solving the equation above, we proceed as follows:

The solution can be asymptotically expressed by

$$\zeta = X_*^{\frac{1}{3}}(C_0 + C_1 X_*^{-\frac{2}{3}} + C_2 X_*^{-4/3} + \cdots )$$

where $C_0$, $C_1 \cdots$ are constants and determined as

$$C_0^3 X_* + (3C_0^2 C_1 - \frac{4}{3}a_1 C_0)X_*^{\frac{1}{3}} + \left[3(C_0^2 C_2 + C_0 C_1^2) - \frac{4}{3}a_1 C_1\right]X_r^{-\frac{1}{3}} + \cdots$$

$$= \frac{2}{3}X_* .$$

Equating the same power of $X_*$, we obtain

$$C_0 = (\frac{2}{3})^{\frac{1}{3}}$$

$$C_1 = (\frac{2}{3})^{\frac{5}{3}} a_1$$

$$C_2 = 0 .$$

Hence

$$\zeta = \xi_*^{\frac{1}{2}} = X_*^{\frac{1}{3}}\left[1 + (\frac{2}{3})^{4/3} a_1 X_*^{-\frac{2}{3}} + 0 + \cdots\right] .$$

Therefore, the velocity distribution is obtained from

$$\frac{u_d}{U_\infty} \simeq C\,\xi_*^{-1}\left[e^{-\eta^2} + \frac{a_1}{\xi_*}(1-\eta^2)e^{-\eta^2} + \cdots\right]$$

as

$$\frac{u_d}{U_\infty} \simeq C\left(\frac{2}{3}\right)^{-\frac{2}{3}}\left\{\left[X_*^{-\frac{1}{3}} - 2\left(\frac{2}{3}\right)^{4/3} a_1 X_*^{-4/3} + \cdots\right] e^{-\eta^2}\right.$$

$$\left. -\left(\frac{2}{3}\right) a_1 \left[X_*^{-4/3} - 4\left(\frac{2}{3}\right)^{4/3} a_1 X_*^{-2} + \cdots\right](1-\eta^2)e^{-\eta^2}\right\} \cdot \text{(A-17)}$$

The wake width is obtained as

$$b(x) = \frac{2\nu}{U_\infty}\xi_*^{\frac{1}{2}} \simeq 2\left(\frac{2}{3}\right)^{\frac{1}{3}} \frac{\nu}{U_\infty}\left(X_*^{\frac{1}{3}} + \left(\frac{2}{3}\right)^{4/3} a_1 X_*^{-\frac{1}{3}} + \cdots\right). \quad \text{(A-18)}$$

The first three functions in the series for the velocity profile in the axisymmetric case $f_0(\eta) = e^{-\eta^2}$, $f_1(\eta) = L_1(\eta^2)e^{-\eta^2}$, $f_2(\eta) = L_2(\eta^2)e^{-\eta^2}$, are plotted in Fig. 88. As seen in Eqs. (A-15) and (A-17), when the momentum flux is not exactly matched, the pure drag component will dominate the behavior of the wake far downstream. Admitting the inadequacy of the constant eddy viscosity model in the present flow, the behavior obtained above agrees qualitatively with that observed in the present experiment.

Note 1:

When the higher order terms of $u_d/U_\infty$ are included in Eq. (A-1), the equation becomes instead of Eq. (A-2)

$$U_\infty \frac{\partial u_d}{\partial x} - \frac{1}{r^2}\left(r^j \nu \frac{\partial u_d}{\partial r}\right) = -u_d \frac{\partial u_d}{\partial x} - U \frac{\partial u_d}{\partial r} \ .$$

The first terms of the additional expansions due to the right hand side of the above equation are found to be of the order of $\xi_*^{-3}$ in two-dimensional flow and of the order of $\xi_*^{-4}$ in axisymmetric flow. Therefore, we may neglect these as higher order terms in Eq. (A-11).

Note 2:

The solution for zero-momentum wake: When the drag = 0, we do not have the term $\xi^{-(j+1)/2} f_0(\eta)$ in Eq. (A-11), and the solution becomes

$$\begin{cases} \dfrac{U_d}{U_\infty} \simeq C_0 a_1 \xi_*^{-(j+3)/2} f_1(\eta) + \ldots \\ b(x) = 2 \dfrac{\nu}{U_\infty} \xi_*^{\frac{1}{2}} \end{cases} .$$

This yields the solution in terms of the original system as:

(1) Laminar Flow

$$\frac{U_{d\mathbb{L}}}{U_\infty} \sim x^{-(j+3)/2}$$

$$b(x) \sim x^{\frac{1}{2}}$$

$$\frac{u_d}{u_{d\mathbb{L}}} \sim \begin{cases} H_2(\eta)e^{-\eta^2} & \text{Two-dimensional flow} \\ L_1(\eta^2)e^{-\eta^2} & \text{Axisymmetric flow} \end{cases}$$

(2) Turbulent Flow

$$\frac{u_{d\mathbb{L}}}{U_\infty} \sim x^{-(3+j)/(4+j)}$$

$$b(x) \sim x^{1/(4+j)}$$

$$\frac{u_d}{u_{d\mathbb{L}}} \sim \begin{cases} H_2(\eta)e^{-\eta^2} & \text{(Two-dimensional flow } j=0) \\ L_1(\eta^2)e^{-\eta^2} & \text{(Axisymmetric flow } j=1) \end{cases}$$

where $H_2(\eta) = 1-2\eta^2$ and $L_1(\eta^2) = 1-\eta^2$ .

2. Prandtl's Mixing Length Theory

Prandtl's eddy viscosity is independent of r at each cross section. In order to examine the effect of the eddy viscosity that varies in the radial direction, Prandtl's mixing length theory will be applied to the momentumless wake.

Prandtl's mixing length theory assumes

$$\frac{\tau}{\rho} = \ell^2 \left|\frac{\partial u}{\partial r}\right| \frac{\partial u}{\partial r} \quad . \tag{A-19}$$

We take the mixing length proportional to the jet width

$$\ell = c_2\, b(x)$$

and look for the similarity in the form

$$u_d = u - U_o = U_o\, A\, x^{-k}\, f(\zeta) \tag{A-20}$$

where $$\zeta = \frac{r}{b(x)} = \frac{r}{Bx^m} \quad .$$

After we substitute $u_d$ from (A-20) into the linearized momentum equation

$$U_o \frac{\partial u_d}{\partial x} - \frac{1}{r^j} \frac{\partial}{\partial r} \left(r^j \frac{\tau}{\rho}\right) = 0, \begin{cases} j = 0 \text{ (2-dimensional)} \\ j = 1 \text{ (axisymmetric)} \end{cases}$$

we get the condition for similarity

$$m + k = 1 \; ; \tag{A-21}$$

and if we choose

$$B = c_2^2\, A/m \quad , \tag{A-22}$$

the equation for f becomes

$$2f'f'' + j\,\zeta^{-1} f'^2 + \mathrm{sgn}(f')\,[\zeta f' + a f] = 0 \tag{A-23}$$

where $$a = k/m .$$

Boundary conditions are as follows

$$\begin{cases} f(0) = 1 & f'(0) = 0 \\ f(\zeta_e) = 0 & f'(\zeta_e) = 0 \end{cases} \tag{A-24}$$

where $\zeta_e$ denotes the value at the edge of the jet.

If we multiply Eq. (A-23) by $\zeta^j$ and integrate, we obtain

$$[f'^2 \zeta^j]_{\zeta=\zeta_e} + [f \zeta^{1+j}]_{\zeta=\zeta_e} + (a-1-j) \int_o^{\zeta_e} f \zeta^j \, d\zeta = 0.$$

For the momentumless wake the last integral vanishes, and therefore, we require if $\zeta$ should be infinity, then

$$\begin{cases} [f'^2 \zeta^j]_{\zeta=\zeta_e} = 0 \\ [f \zeta^{1+j}]_{\zeta=\zeta_e} = 0 \\ a \neq j + 1 \end{cases} . \tag{A-25}$$

It should be noted that for the non-zero drag case, the exponents m and k are determined from Eq. (A-21) and $a - 1 - j = 0$ as

$$m = \frac{1}{2+j}$$

$$k = \frac{1+j}{2+j} \quad .$$

These exponents are naturally identical with the results from the constant eddy viscosity model.

Eq. (A-23) is a second-order nonlinear ordinary differential equation, and we have four boundary conditions (A-24) to be satisfied. Thus the problem is a nonlinear eigenvalue problem in which a and $\zeta_e$ are the eigenvalues to be determined.

In order to study the behavior of the solution of the nonlinear equation (A-23), we make the following change of variables:

$$s = \frac{f}{\zeta^3}$$
$$t = \frac{f'}{\zeta^2} \qquad \text{(A-26)}$$

Then Eq. (A-23) becomes

$$\frac{dt}{ds} = -\frac{5t^2 + \mathrm{sgn}(t)\cdot(t+as)}{2t(t-3s)} \qquad \text{(A-27)}$$

Integral curves are shown in the following sketch.

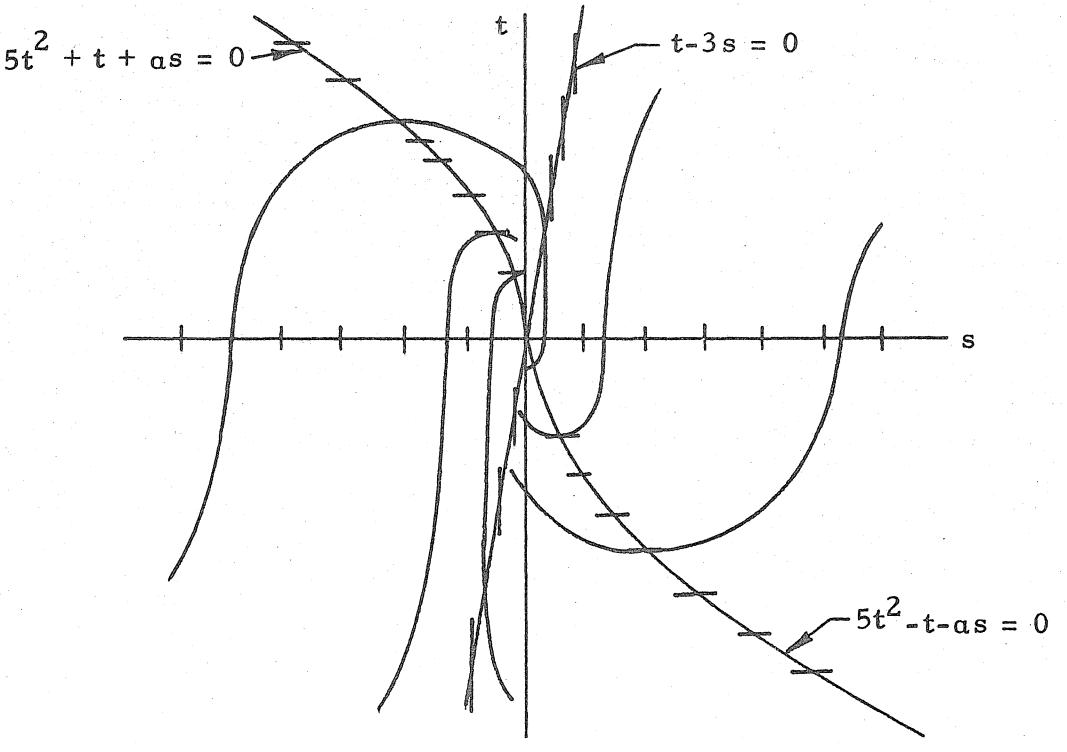


From the boundary condition (A-24), we find $t = -\infty$, $s = +\infty$, $\zeta = 0$, and $t = 0$, $s = 0$ at $\zeta = \zeta_e$. Around the singular point at the origin, we assume first a series expansion as

$$s = a_1 t + a_2 t^2 + a_4 t^4 + \cdots +$$

Substituting into Eq. (A-27) and determining the coefficients, we get

$$s = -t^2 + \frac{2}{3}(2-a)t^3 + \frac{1}{6}(2-a)(3a-7)t^4 + \ldots \qquad \text{(A-28)}$$

or

$$s = -\frac{1}{a}t + \frac{2a+1}{a}t^2 + \frac{2(2a+1)(2a+3)}{a}t^3 + \ldots \qquad \text{(A-29)}$$

Further, when we solve for the deviation $\sigma(t)$ from the above regular solutions

$$s = a_1 t + a_2 t^2 + \ldots + \sigma(t)$$

we get $\sigma(t) \doteq c\, e^{(2a+6)t}$ for Eq. (A-28), and $\sigma(t) \doteq c\, e^{-\frac{1}{(2a+6)}\frac{1}{t}}$ for Eq. (A-29). Therefore, the integral curves passing through the origin have the form either

$$s = -t^2 + \frac{2}{3} + \frac{2}{3}(2-a)t^3 + \frac{1}{6}(2-a)(3a-7)t^4 + \ldots$$

or

$$s = -\frac{1}{a}t + \frac{2a+1}{a}t^2 + \frac{2(2a+1)(2a+3)}{a}t^3 + \ldots + c\, e^{-\frac{1}{2a+6}\frac{1}{t}}$$

where c is a constant. These are illustrated in the following figure:

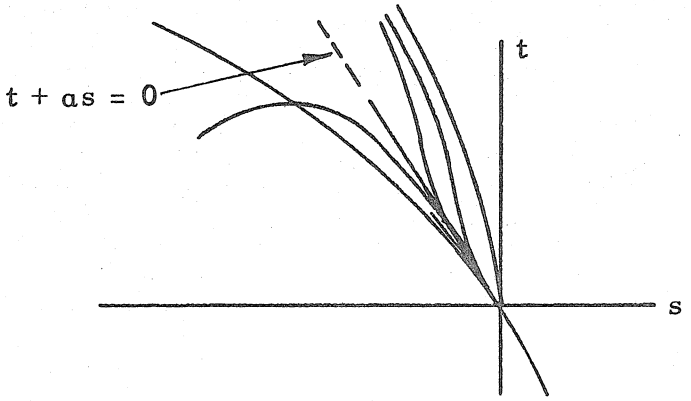


In terms of $f(\zeta)$, we see that

(1) Case $s \sim -\frac{1}{a}t$: we obtain from the definition of s and t,

$$\frac{f'}{f} \sim -a\frac{1}{\zeta}$$

Therefore

$$f \sim \zeta^{-a}$$

Substituting into Eq. (A-25), we obtain

$$f'' \zeta^j \to 0, \; f \zeta^{1+j} \to 0 \text{ as } \zeta \to \infty .$$

Therefore, the drag is zero when $a > 1+j$.

(2) Case $s \sim -t^2$: we obtain

$$f' \sim -\zeta^{\frac{1}{2}} f^{\frac{1}{2}}, \; f^{\frac{1}{2}} \sim -\frac{1}{3}(\zeta^{\frac{3}{2}} + \text{const.}) .$$

Therefore $f = 0$, $f' = 0$ for a finite $\zeta_e$, and the condition of the zero drag is $a \neq 1+j$. For $a = j+1$, the solution for $D \neq 0$ is obtained by Schlichting (1968) for the two-dimensional wake, and Swain (ibid.) for the circular wake. For both cases, the velocity distribution is given by $F = (1 - \frac{1}{3}\zeta^{\frac{1}{2}})^2$.

A numerical integration of the ordinary differential equation was employed to solve the nonlinear eigenvalue problem. In order to avoid two-parameter iteration, the solution for the outer part was obtained in the st-plane and the solution for the inner part was carried out in the $f\zeta$-plane. For the inner part where $f' < 0$, we have from (A-23)

$$\frac{df}{d\zeta} = -\left(\frac{g}{\zeta}\right)^{\frac{1}{2}}$$

$$\frac{dg}{d\zeta} = \zeta\left[-(\zeta g)^{\frac{1}{2}} + af\right] .$$

We integrate the equations from $\zeta = 0$, where $f(0) = 1$, $g(0) = 0$, until we obtain $f' = 0$. Then the numerical integration of Eq. (A-27) starting at $t = s = 0$ along $s \sim -t^2$ is carried out, and the two solutions are

matched on the s-axis, where t = 0 and hence f' = 0. By this shooting method, a was obtained after iterations as

$$a = \frac{k}{m} \doteq 5.538$$

This gives the main characteristic of the momentumless wake as follows:

$$u_{d\mathbb{C}_L} \sim x^{-0.847}$$

$$b \sim x^{0.153}$$

$$\tau_{max} \sim x^{-1.694} \quad .$$

The integral curve and the velocity profiles are given in Figs. 89 and 90. The comparison with Naudascher's experiment is presented. The self-similar velocity profiles are also comparable with the result of the present matched injection cases (see Figs. 27, 45 and 49). It should be noted that both the eddy viscosity and the mixing length theory underpredict the decay of the centerline velocity even though they predict the shape of the velocity profile fairly well.

# APPENDIX B - ACCURACY OF MEASUREMENTS

## 1. Accuracy of Mean Velocity and Static Pressure Measurements

The mean velocity and the mean static pressure were measured by the Barocel sensor and the electronic manometer. According to the operating manual, the accuracy of the Barocel Type 538-10 is $\pm 0.03\%$ of reading and $5 \times 10^{-7}\%$ of sensor full range by setting zero before reading. The CGS Type 1014A-S6 electronic manometer unit has an accuracy of $\pm 0.05\%$ of reading and $\pm 0.01\%$ of range. This gives an accuracy of 0.1% for the dynamic pressure of about 1 mm Hg which was read in the 10 mm Hg range, and 0.05% accuracy for the velocity measurement. Farthest downstream for the matched condition where centerline velocity becomes around 1% above the free stream value, the error estimate above still gives the centerline velocity difference $\Delta u_{\mathcal{L}}$ within the relative error of 10%. The mean static pressure was measured with respect to the room pressure with the manometer range of 0.3 mm Hg. This gives the static pressure measurement an accuracy within $2 \times 10^{-4}$ mm Hg or an accuracy in terms of the pressure coefficient $2 \times 10^{-4}$ based on the dynamic pressure in the flow. Pressure coefficients of maximum static pressure defect observed in the wakes ranged from $2 \times 10^{-2}$ upstream to $1 \times 10^{-3}$ farthest downstream.

The accuracy of the static pressure measurement was largely limited by the room pressure fluctuation and the nonuniformity in the test section in the transverse direction. These effects were estimated to be

$$\delta C_p = 0.6 \times 10^{-3} \sim 1 \times 10^{-3}$$

Averaging the data for a long period with an on-line data acquisition system increased the accuracy of the measurements. We will discuss the other factor to affect the accuracy of measurements.

1a. Effect of the temperature variation on the mean velocity measurement

The spatial variation of the temperature across the wake was measured and was less than 1°C.

The velocity was computed from the relationship

$$u = \sqrt{\frac{2(P_t - P_s)}{\rho}}$$

where the difference between total pressure and the static pressure $P_t - P_s$ was measured by the electronic manometer and the density $\rho$ was computed from the measured ambient temperature and pressure from $\rho = P/RT$.

Since the slight temperature variation mentioned above was not compensated during the run, it is necessary to estimate an error on the measured velocity.

From the above equation, we obtain

$$\frac{\delta u}{u} = \frac{1}{2}\frac{\delta \rho}{\rho} = \frac{1}{2}\frac{\delta T}{T}$$

Therefore, the variation of temperature up to 1°C causes 0.17% of relative error and is negligible.

1b. Effect of the turbulence on the velocity measurement

If Bernoulli's law is applied to the instantaneous velocity, we have

$$P_t - P_s = \tfrac{1}{2}\rho(\bar{u} + u')^2 \quad .$$

The time average of the above is

$$\overline{P_t - P_s} = \tfrac{1}{2}\rho\,\overline{u^2} + \tfrac{1}{2}\rho\,\overline{u'^2}$$

$$\therefore \quad \overline{u^2} = \frac{2(\overline{P_t - P_s})}{\rho} - \overline{u'^2} \qquad (2)$$

Let $\bar{u}_1$ be the calculated velocity neglecting the turbulence level. Then

$$\bar{u}_1 = (\overline{u^2 + u'^2})^{\frac{1}{2}} \doteq \bar{u}\left(1 + \tfrac{1}{2}\frac{\overline{u'^2}}{\overline{u^2}}\right) \quad . \qquad (3)$$

The measured $\frac{u'}{U_\infty}$ was about $1.7 \times 10^{-1}$ in the zero momentum wake behind the rough wall model at $x/D = 5$. Therefore, the error caused by the turbulence $\frac{\delta u}{U}$ is about 1.45% at $x/D = 5$. Farthest downstream where $\Delta u_{\mathit{CL}}/U_\infty$ was about 0.01, $\frac{\delta u}{U}$ is about 0.01%, and hence the relative error $\delta u/\Delta u_{\mathit{CL}}$ is approximately 1% which is entirely negligible compared to the instrument error.

1c. Effect of the turbulence on the static pressure measurements

If the turbulent eddy size is considered small compared to the probe dimensions, the measured static pressure may be thought to read a higher value because of the stress due to velocity fluctuations normal to the probe openings. According to Fage (1936), he

empirically found $P_{s_{meas.}} = P_s + \rho(\overline{v'^2}+\overline{w'^2})$. If $\overline{v'^2} = \overline{w'^2} = 0.7\,\overline{u'^2}$ is assumed in the shear region, this formula gives $P_{s_{meas.}} - P_{s_{true}} = 0.35\,\rho\overline{u'^2}$ or $C_{P_{s_{meas.}}} - C_{P_{s_{true}}} = 0.7\,\frac{\overline{u'^2}}{U_\infty^2}$.

At the maximum turbulence intensity observed in the present matched injection case, this would cause $\delta(C_{p_s})$ up to + 0.01.

However, as pointed out by Bradshaw and Goodman (1968) and others, this argument is valid only when the eddy size is very small. When eddies are large compared with the probe, the effect of the instantaneous flow direction with respect to the probe becomes a dominant factor. From the power spectrum measurement the maximum energy in the pure wake was observed to be around 110 Hz and in the matched injection case around 220 Hz (see Chap. IV). Therefore the size of the energy containing eddies is estimated to be much larger than the probe size. We assume a quasi-steady flow and take the yaw response of the static pressure probe as $P_{s_{meas.}} = P_{s_{true}} - a\psi^2\,\frac{1}{2}\rho\,U_\infty^2$, where $\psi$ is in radians, and we choose a = 0.7 as was taken in the reference above for their probe, which was similar to the present one. The instantaneous yaw caused by the turbulence will be of the order of $(\overline{v'^2}+\overline{w'^2})^{\frac{1}{2}}/U_\infty$. (Since the flow is axisymmetric and the probe is aligned with the mean free stream direction and has pressure holes equally spaced on the periphery, the yaw angle of the probe with respect to the mean flow is considered to be negligible, except at the proximity of the recirculating zone behind a pure wake.) Substituting the above expression, the effect on the static pressure measurement will be $C_{p_{s_{meas.}}} - C_p = -a\psi^2 \sim -0.7(\frac{\overline{v'^2}+\overline{w'^2}}{U_\infty^2})$.

With the measured value for the turbulent intensity in the matched injection case, we obtain $-\delta(C_{p_s}) \sim 0.014$ at highest turbulence intensity and less than 0.001 at X/D = 40 and downstream.

2. Accuracy in Hot Wire Measurement

2a. Hot wire calibration

The bridge output of the hot wire signal was linearized by the linearizer, and the result of the calibration is shown in Fig. 7. The relation between the mean velocity and the mean bridge voltage is given by

$$u = kE$$

Between the fluctuation velocity and the fluctuation voltage, we have

$$(\overline{u'^2})^{\frac{1}{2}} = k'(\overline{e'^2})^{\frac{1}{2}}$$

Therefore the axial turbulence intensity is obtained from

$$\frac{(\overline{u'^2})^{\frac{1}{2}}}{U_\infty} = \frac{k'}{k_\infty}\frac{(\overline{e'^2})^{\frac{1}{2}}}{E_\infty} = \frac{(\overline{e'^2})^{\frac{1}{2}}}{E_\infty} \quad \text{if } \frac{k'}{k} = 1$$

If $\delta(\overline{u'^2})^{\frac{1}{2}}$, $\delta(\overline{e'^2})^{\frac{1}{2}}$, etc. denote the absolute value of error,

$$\frac{\delta((\overline{u'^2})^{\frac{1}{2}}/U_\infty}{(\overline{u'^2})^{\frac{1}{2}}/U_\infty} = \frac{\delta(\overline{e'^2})^{\frac{1}{2}}}{(\overline{e'^2})^{\frac{1}{2}}} + \frac{\delta E}{E_\infty} + \frac{\delta k}{k_\infty} + \frac{\delta k'}{k'}$$

The term $\delta(\overline{e'^2})^{\frac{1}{2}}/(\overline{e'^2})^{\frac{1}{2}}$ represents the error in the fluctuating voltage measurement as measured by the DISA Type 55D35 RMS Voltmeter, at a 0.3 sec time constant setting. From the calibration of the RMS meter, as was mentioned in Chapter II, the accuracy is found to be ± 0.5% except at the lowest end of the scale.

The second term in the right hand side of the above equation is the error in the DC voltage measurement. The standard deviation in the sampled voltage, $E_\infty$, and the accuracy of the measurement system itself give an uncertainty in $\delta E_\infty / E_\infty$ as 0.4%.

The value of the free stream velocity $U_\infty$ was measured from the sampling of the data from the Pitot static probe traversed in the free stream region outside the wake. The DC output of the free stream hot wire signal $E_\infty$ was measured in the same way as the velocity measurement with the hot wire probe placed in the same region. This self-calibrating feature reduces the error in $U_\infty / E_\infty$ to the accuracy of the velocity measurement which is of the order of 0.2% from the argument in the previous section. Hence, $\delta k_\infty / k_\infty \sim 0.2\%$.

We first assume that the velocity fluctuations produce the voltage fluctuations in accordance with the calibration curve done at the static condition (i.e., $k = k'$). Because of the linearized calibration, it is not necessary to take a local slope of the calibration curve which introduces an additional error. However, if the linearization is less than ideal, it will cause an error in velocity fluctuation measurements. At the time of the calibration, the deviation of $u/E$ was within 1% of the mean value in the range of interest. In spite of the filter in the air supply system, oil in the house air supply was detected in the air injection in the form of a mist. The quantity was negligibly small, but it was suspected that fine scale oil particles coat the hot wire and cause the drift of the calibration.

In the present investigation, all the velocity distribution in

the wake was measured in a Pitot tube and in addition with a hot wire to check the accuracy of the measurement. This provided a frequent check during each run against a possible drift. According to these data, linearity was kept within 1.5% throughout the experiment including at the high velocity in the centerline of the jet. Therefore, the suspected drift of the hot wire calibration, either the shift of the origin or the onset of the nonlinearity, was concluded to be negligible. As for the assumption made on the dynamic calibration, Perry and Morrison (1971) tested the DISA 55A01 hot wire system without linearizer. They pointed out that the system sensitivity determined from static calibration is a strong function of the exponent in the King's law and that differed considerably from the result from the dynamic calibration in which the hot wire was mounted on the shaker with frequency 1-15 Hz. They reported the discrepancy over 10% in the velocity fluctuation profile behind a cylinder at different frequencies between the measurements based on the static calibration and on the dynamic calibration.

In the present experiment, the use of the linearizer and the limited range of the mean velocity variation in the wakes minimized the difficulty of fitting the proper exponent over a wide range of velocities and then reading a local slope from it. However, without the dynamic calibration data of the present hot wire system, we were not able to check the accuracy of the assumption on the dynamic calibration.

2b. Effect of Air Temperature Variation on Velocity Fluctuation Measurements

The variation in the ambient temperature during the run was less than ±0.5°C, but there was also the spatial variation up to 1°C in the fluid temperature due to the jet of slightly different temperature mixing into the ambient air. The effect of these temperature variations on the velocity fluctuation measurements made by the hot wire anemometer is estimated below.

The linearizer was compensated for temperature, therefore the discussion is limited to the response of the hot wire itself to the temperature. The velocity fluctuation is related to the bridge voltage fluctuation as

$$\frac{\overline{(u'^2)}^{\frac{1}{2}}}{U_\infty} = \frac{\left[\left(\frac{\partial \bar{u}}{\partial E}\right)_T^2 \overline{e'^2}\right]^{\frac{1}{2}}}{U_\infty} = \frac{\left(\frac{\partial u}{\partial E}\right)_T \overline{(e'^2)}^{\frac{1}{2}}}{U_\infty / E_\infty}$$

where u' and U are the fluctuation and mean velocity, e' and E are the AC and DC component of the bridge output respectively, and $E_o$ corresponds with the value in the free stream.

The coefficient $\left(\frac{\partial \bar{u}}{\partial E}\right)_T$ is calculated from King's law

$$\frac{E^2}{R(T_w - T_g)} = A + Bu^{1/n} \qquad (4)$$

where R is the resistance of the wire which is constant under the constant temperature operation, and $T_w$ and $T_g$ are the temperature of the wire and of the fluid respectively. From Eq. (4) it follows

$$u = \left[\frac{1}{B}\left(\frac{E^2}{R(T_w - T_g)} - A\right)\right]^n$$

and $$\therefore \quad \left(\frac{\partial u}{\partial E}\right)_T = \frac{n}{B}\frac{2E}{R(T_w - T_g)}\, u^{\frac{n-1}{n}} \quad .$$

Therefore, for a small change $\Delta T_g$,

$$\delta\left(\frac{\partial \bar{u}}{\partial E}\right)_T \Big/ \left(\frac{\partial \bar{u}}{\partial E}\right)_T = \frac{\Delta T_g}{T_w - T_g}$$

For $T_w - T_g = 0.5\, T_g \cong 150°C$ and $\Delta T_g = 1°C$, the contribution to the relative error of $\overline{(u'^2)}^{\frac{1}{2}}/U_\infty$ from the air temperature variation is

$$\frac{\delta\overline{(u'^2)}^{\frac{1}{2}}/U_\infty}{\overline{(u'^2)}^{\frac{1}{2}}/U_\infty} \sim 0.007 = 0.7\% \quad .$$

# APPENDIX C

## REYNOLDS STRESS MEASUREMENT WITH X-WIRE

X-wire used for the Reynolds stress measurement was 0.0129 mm in diameter and 1.5 mm in length. The probe was mounted on the probe holder which has a reflecting surface. A low intensity He-Ne laser beam was reflected in the mirror, and the probe orientation was read on the wall which stands a little over 10' away from the probe. Two sets of DISA 55A01 hot wire anemometers and the DISA 55D10 linearizers were used. Signals were amplified by an HP 4501 amplifier and a DISA 55D25 auxiliary unit. Output signals were digitized at the rate of 2000 per sec for 16K points, and the auto-correlation and the cross-correlation of the signals were computed. The calibration scheme is as follows:

If the linearizer is adjusted to produce a linear relationship between the output voltage $e_{1,2}$ and the velocity u and v, we can write

$$e_1 = a_1 u + b_1 v + C_1$$
$$e_2 = a_2 u + b_2 v + C_2 \quad .$$

In the free stream, we change the orientation of the probe $\alpha$ and we obtain

$$e_1 = S_1 U_\infty + C_1$$
$$e_2 = S_2 U_\infty + C_2$$

where

$$S_1 = a_1 \cos\alpha + b_1 \sin\alpha = \cos\alpha(a_1 + b_1 \tan\alpha)$$
$$S_2 = a_2 \cos\alpha + b_2 \sin\alpha = \cos\alpha(a_2 - b_2 \tan\alpha) \quad .$$

Coefficients $a_1$, $a_2$, $b_1$, $b_2$ are obtained from the plot between the quantities $S_{1,2}/\cos\alpha$ and $\tan\alpha$.

Orientation of the probe in the free stream is found as

$$\tan \alpha_o = \frac{\bar{v}_o}{\bar{u}_o} = \frac{a_2(\bar{e}_1 - C_1) - a_1(\bar{e}_2 - C_2)}{b_2(\bar{e}_1 - C_1) + b_1(\bar{e}_2 - C_2)} \quad .$$

The Reynolds stresses are computed from $\overline{e_1'^2}$, $\overline{e_2'^2}$ and $\overline{e_1' e_2'}$ as follows

$$\overline{u_*'^2} = \frac{b_2^2 \overline{e_1'^2} + 2b_1 b_2 \overline{e_1' e_2'} + b_1^2 \overline{e_2'^2}}{(a_1 b_2 + a_2 b_1)^2} \quad ,$$

$$\overline{v_*'^2} = \frac{a_2^2 \overline{e_1'^2} - 2a_1 a_2 \overline{e_1' e_2'} + a_1 \overline{e_2'^2}}{(a_1 b_2 + a_2 b_1)^2} \quad ,$$

and $$\overline{u_*' v_*'} = \frac{b_2 a_2 \overline{e_1'^2} - (a_1 b_2 - a_2 b_1)\overline{e_1' e_2'} - a_2 b_1 \overline{e_2'^2}}{(a_1 b_2 + a_2 b_1)^2} \quad .$$

The suffix * indicates that these are with respect to the probe coordinates system.

With respect to the free stream direction, these are rewritten as

$$\overline{u'^2} = \overline{u_*'^2} \cos^2 \alpha_o + 2\overline{u'v'_*} \cos\alpha_o \sin\alpha_o + \overline{v_*'^2} \sin^2 \alpha_o \quad ,$$

$$\overline{v'^2} = \overline{u_*'^2} \sin^2 \alpha_o - 2\overline{u'v'}_* \cos\alpha_o \sin\alpha_o + v_*'^2 \cos^2 \alpha_o \quad ,$$

and $$\overline{u'v'} = -\overline{u_*'^2} \cos\alpha_o \sin\alpha_o + \overline{u'v'_*}(\cos^2 \alpha_o - \sin^2 \alpha_o) + \overline{v_*'^2} \cos\alpha_o \sin\alpha_o \quad .$$

The probe is rotated $90^o$ on its axis, and similarly $\overline{w'^2}$ and $\overline{u'w'}$ are obtained.

According to the procedures above, the measurements in the pure wake and in the momentumless wake behind a smooth wall model

were conducted. However, during the calibration, the second channel of the hot wire system was found drifting and an accurate calibration of the coefficients $a_2$ and $b_2$ was not possible due to the scattering. Ambiguity due to this drift is indicated by the error bars in the figures. The results presented here are therefore to be taken as of a qualitative value. Due to the lack of the precise knowledge on the gain of the amplifier, the absolute magnitude was adjusted so that the result of axial turbulent intensity at X/D = 10 matches the result of a single wire measurement. Turbulent intensity profiles in the matched injection cases at X/D = 40 are given in Figs. 91 and 92. Axial decay of axial, radial and tangential turbulent intensities ($u'$, $v'$, $w'$) in the pure wake case and in the matched injection case are presented in Fig. 93. At X/D = 40, the magnitudes of $\overline{v'^2}$ and $\overline{w'^2}$ appear to be in balance both in the pure wake and in the momentumless wake. However, between $(\overline{u'^2})^{\frac{1}{2}}$ and $(\overline{v'^2})^{\frac{1}{2}}$, anisotropy remains stronger in the matched injection case than in the pure wake case. This seems to contradict the physical interpretation of the flow and to indicate the error in measurements. When the production of the turbulent energy is negligible, the tendency toward isotropy should be stronger. Therefore, the turbulence in the momentumless wake should become closer to isotropic than in the pure wake.

Profiles of $\overline{u'v'}$ in the matched injection case (Figs. 94 and 95) and in the pure wake case (Fig. 96) are in agreement with the result from the mean flow integral, but some discrepancy is noticed in the maximum shear stress decay as seen in Fig. 97. The quantity $\overline{u'w'}$ was found to be essentially zero within the range of scatter of the data, which is as expected from the axisymmetric nature of the flow.

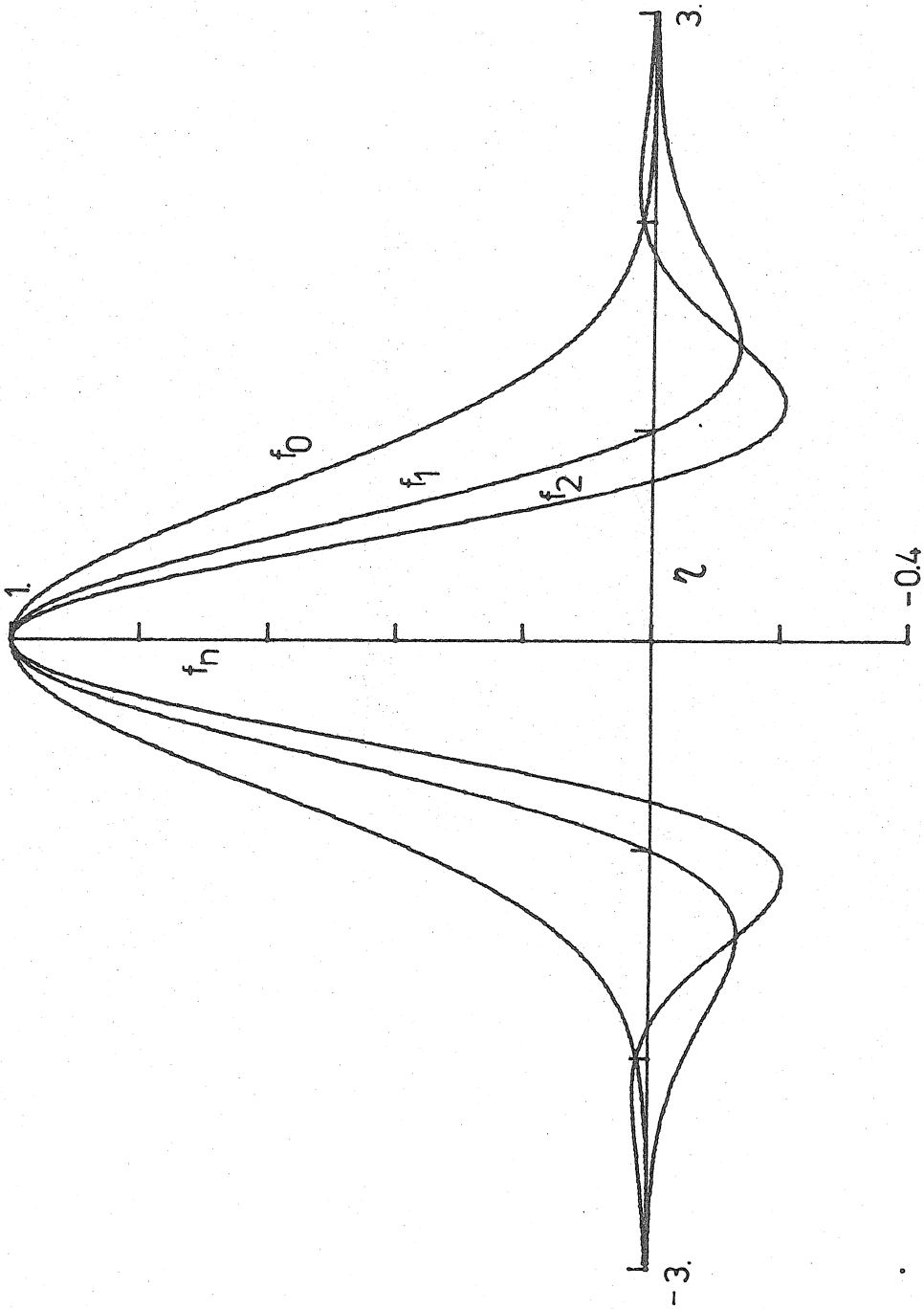


Fig. 88. Velocity Profile Functions with Constant Eddy Viscosity Model

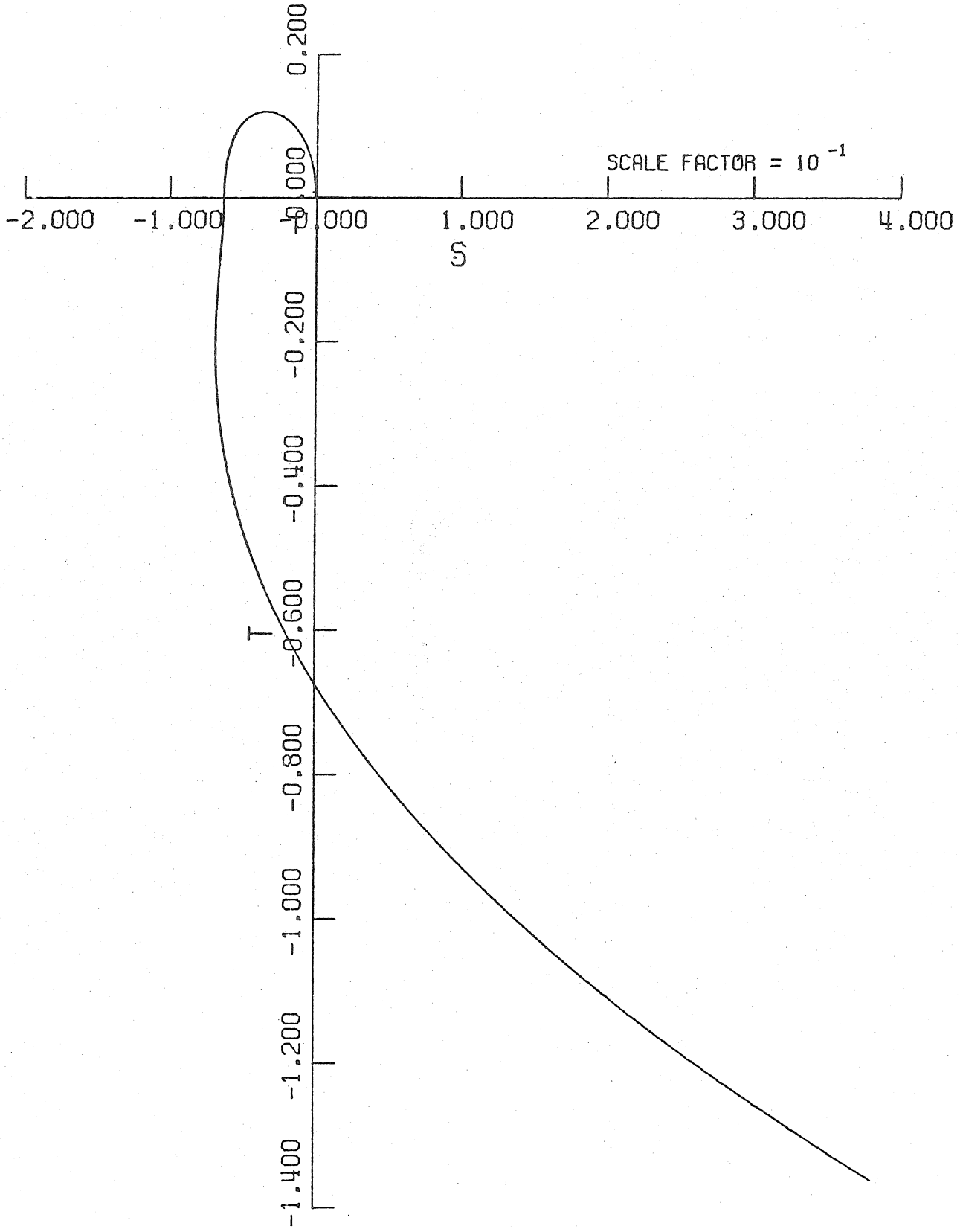


Fig. 89. Mixing-Length Model--Integral Curve in st-Plane

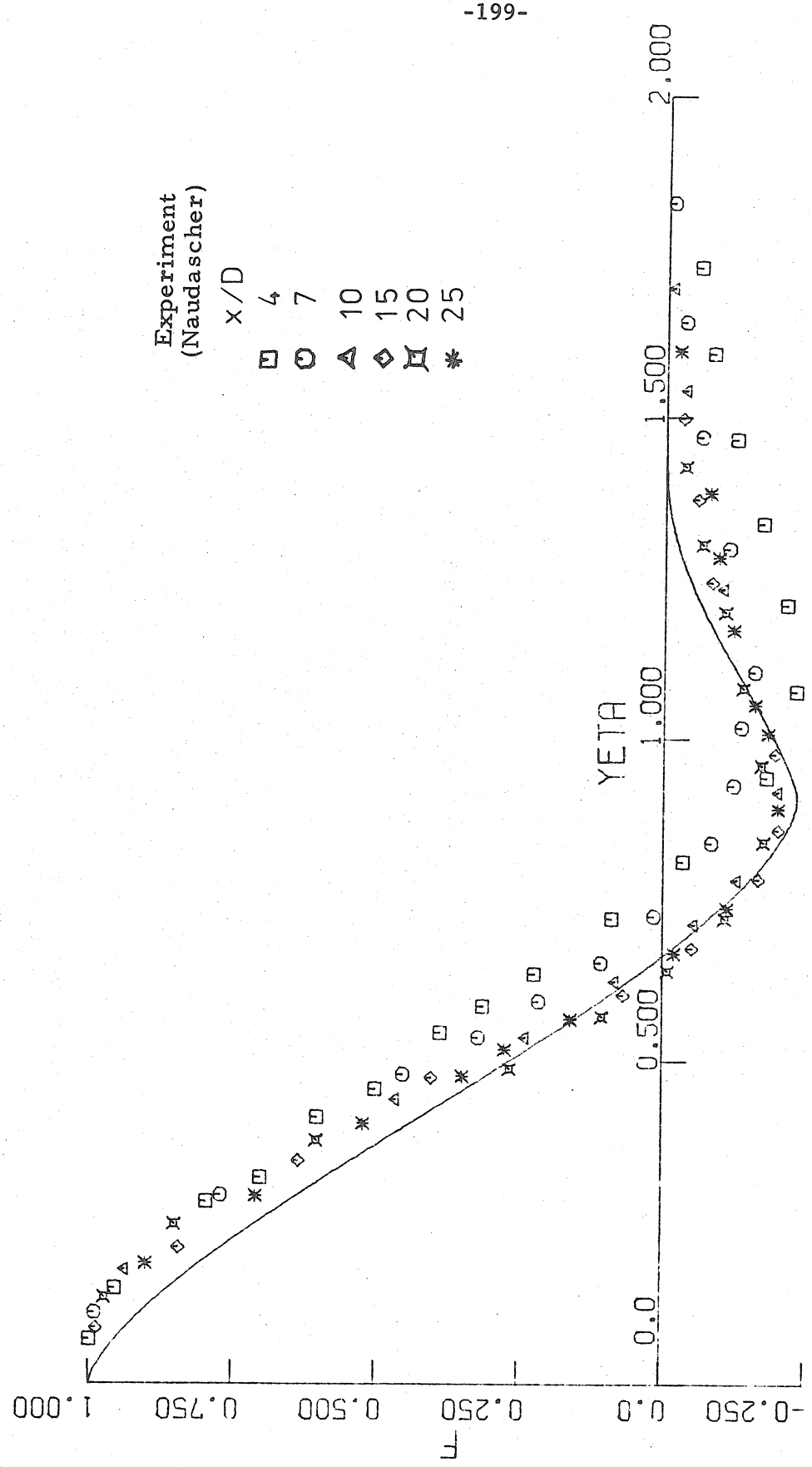


Fig. 90. Mixing-Length Model--Velocity Profile
($\eta$ at $u_{min}$ matched between experiment and theory)

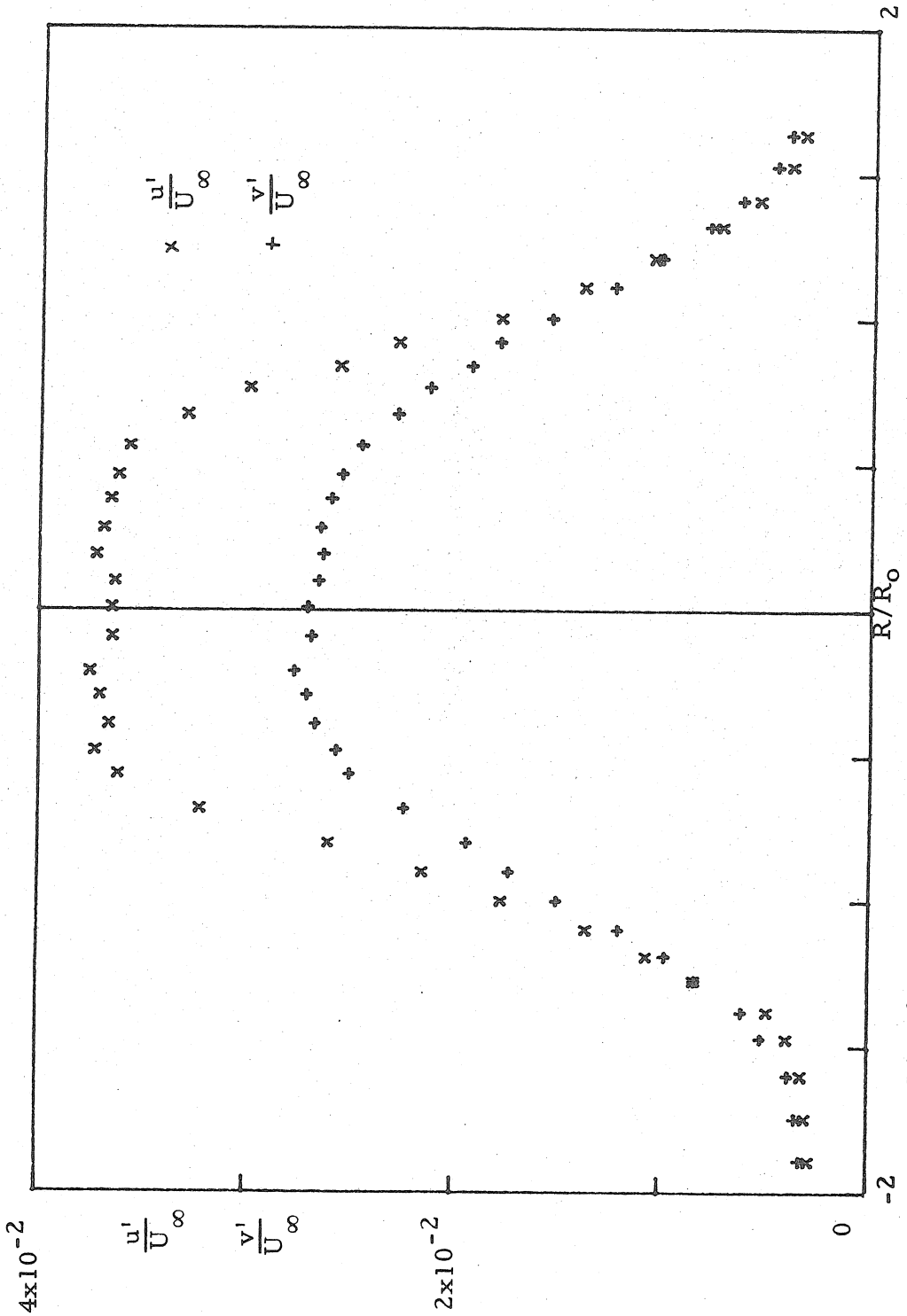


Fig. 91. Axial and Radial Turbulent Intensity Profiles from X-Wire Measurement Matched Injection X/D = 40

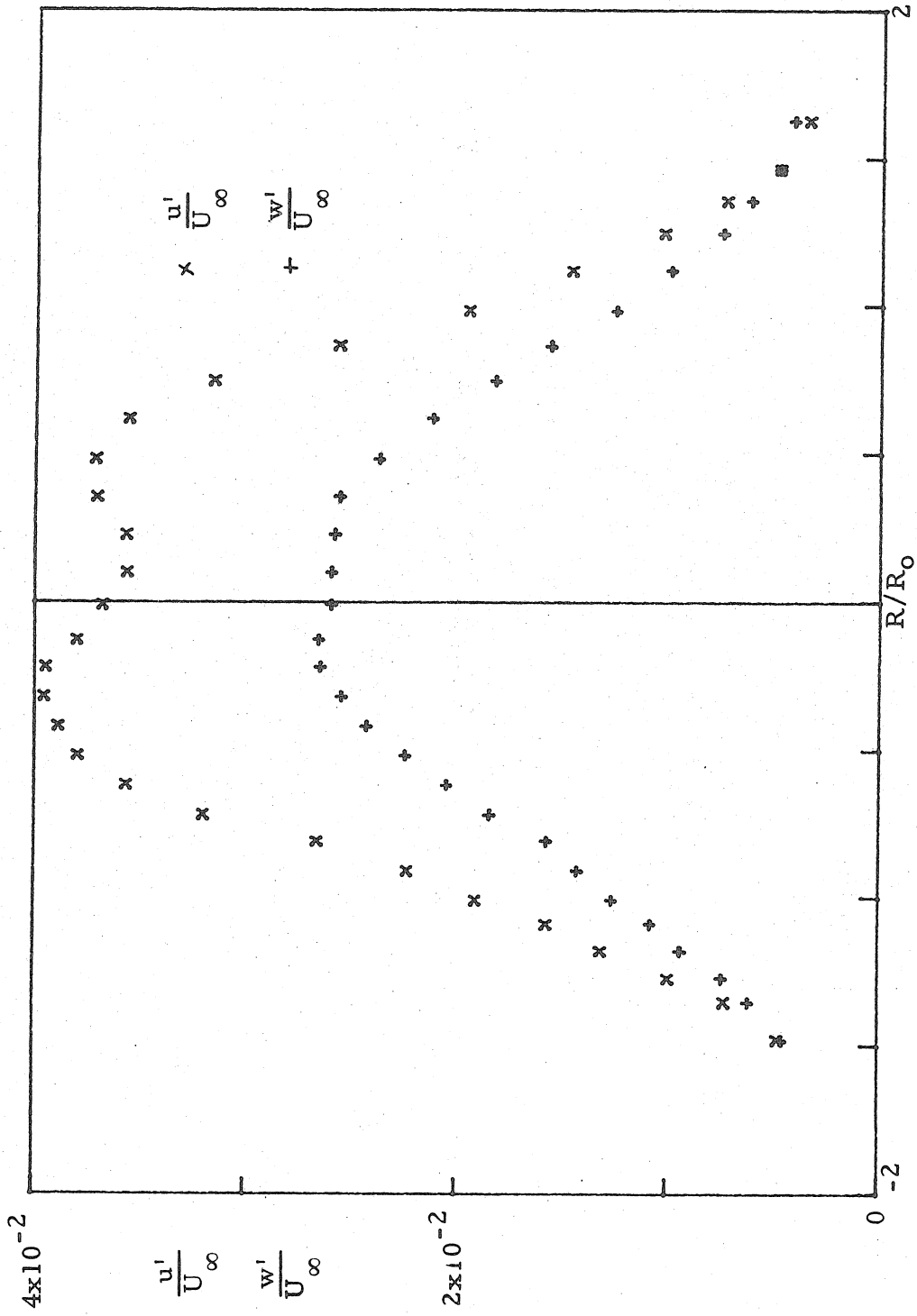


Fig. 92. Axial and Tangential Turbulent Intensity Profiles from X-Wire Measurement, Matched Injection X/D = 40

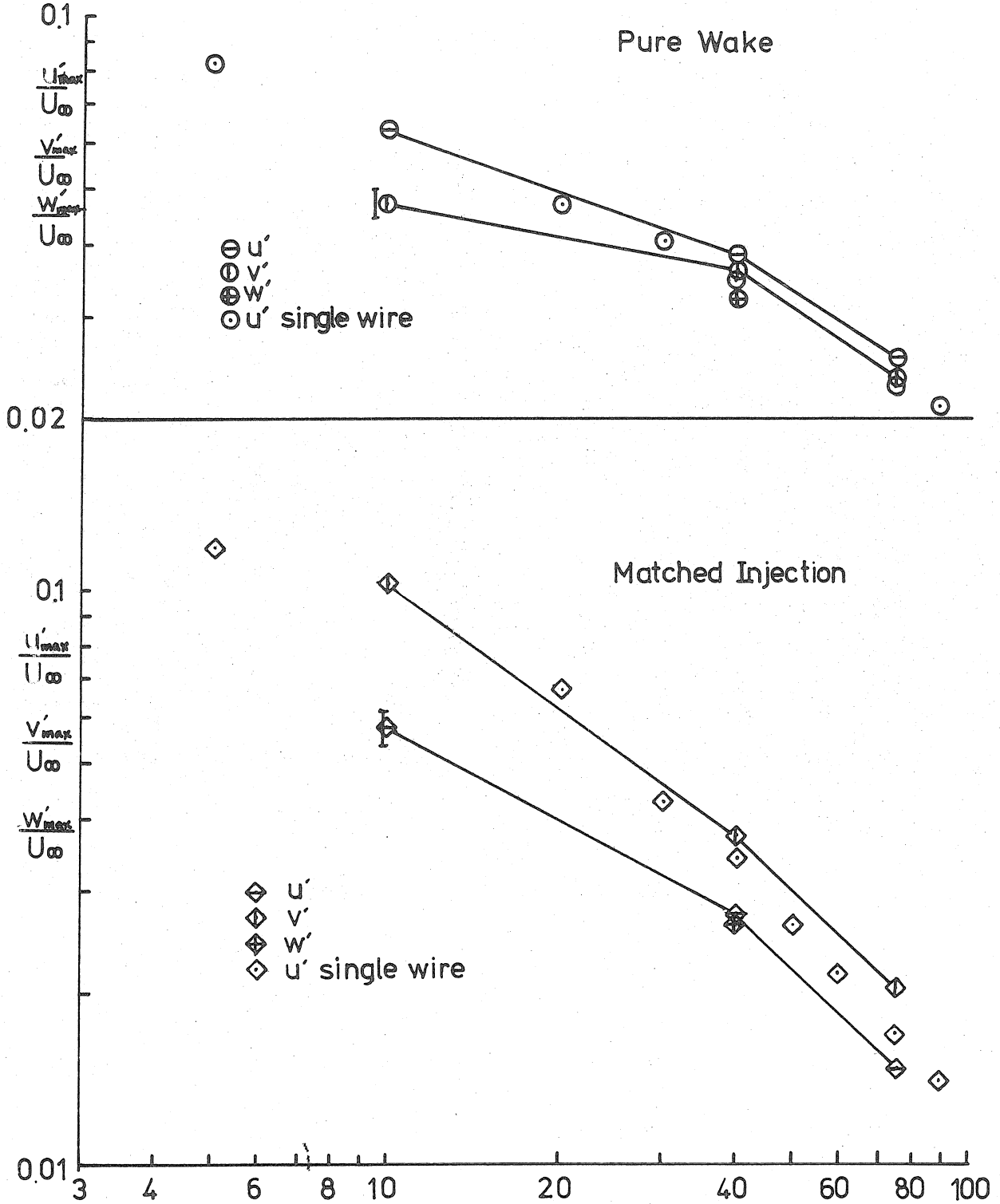


Fig. 93. Axial Decay of Reynolds Normal Stress from X-Wire Measurement

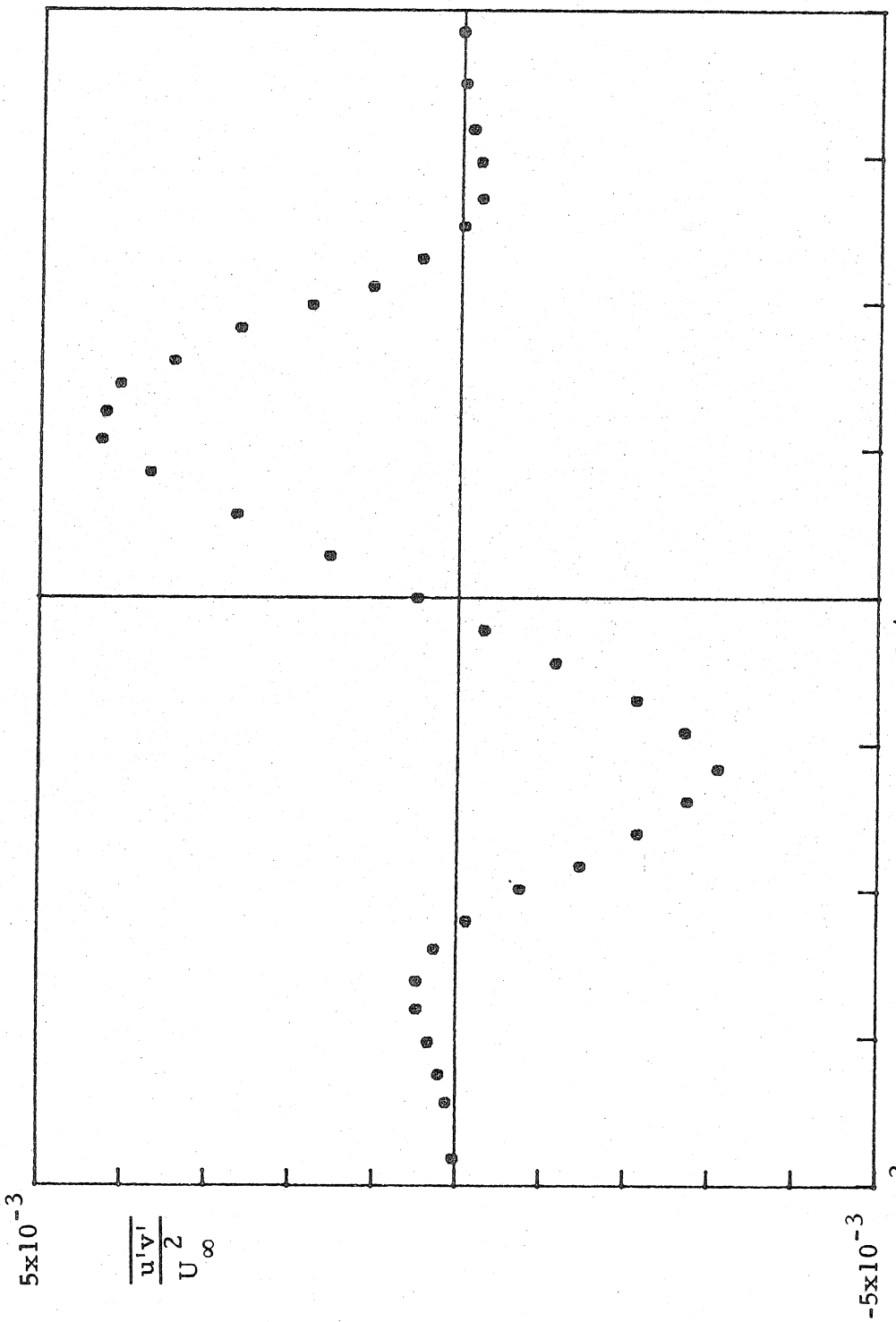


Fig. 94. Turbulent Shear Stress from X-Wire Measurement, Matched Injection X/D = 10

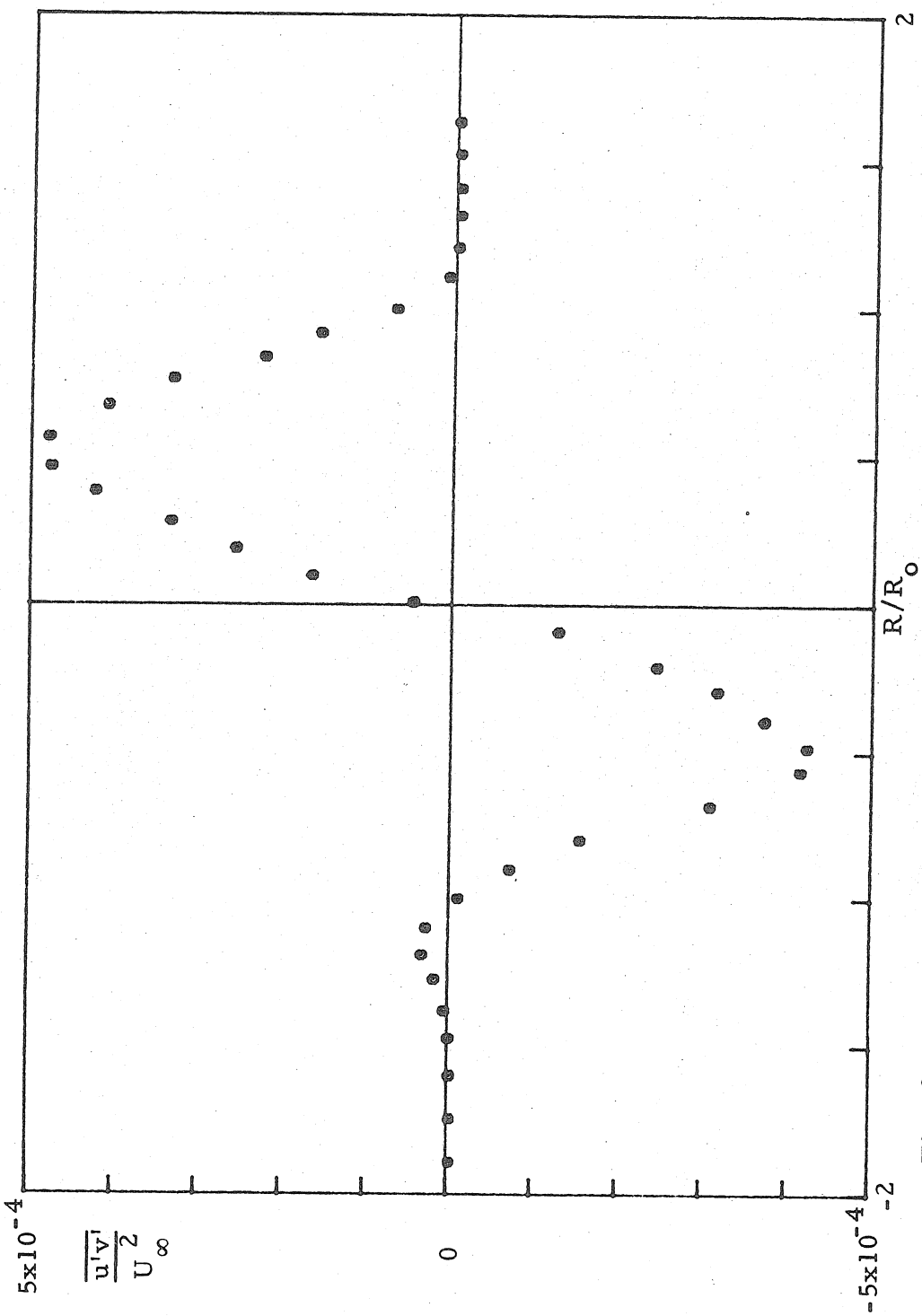


Fig. 95. Turbulent Shear Stress from X-Wire Measurement, Matched Injection X/D = 40

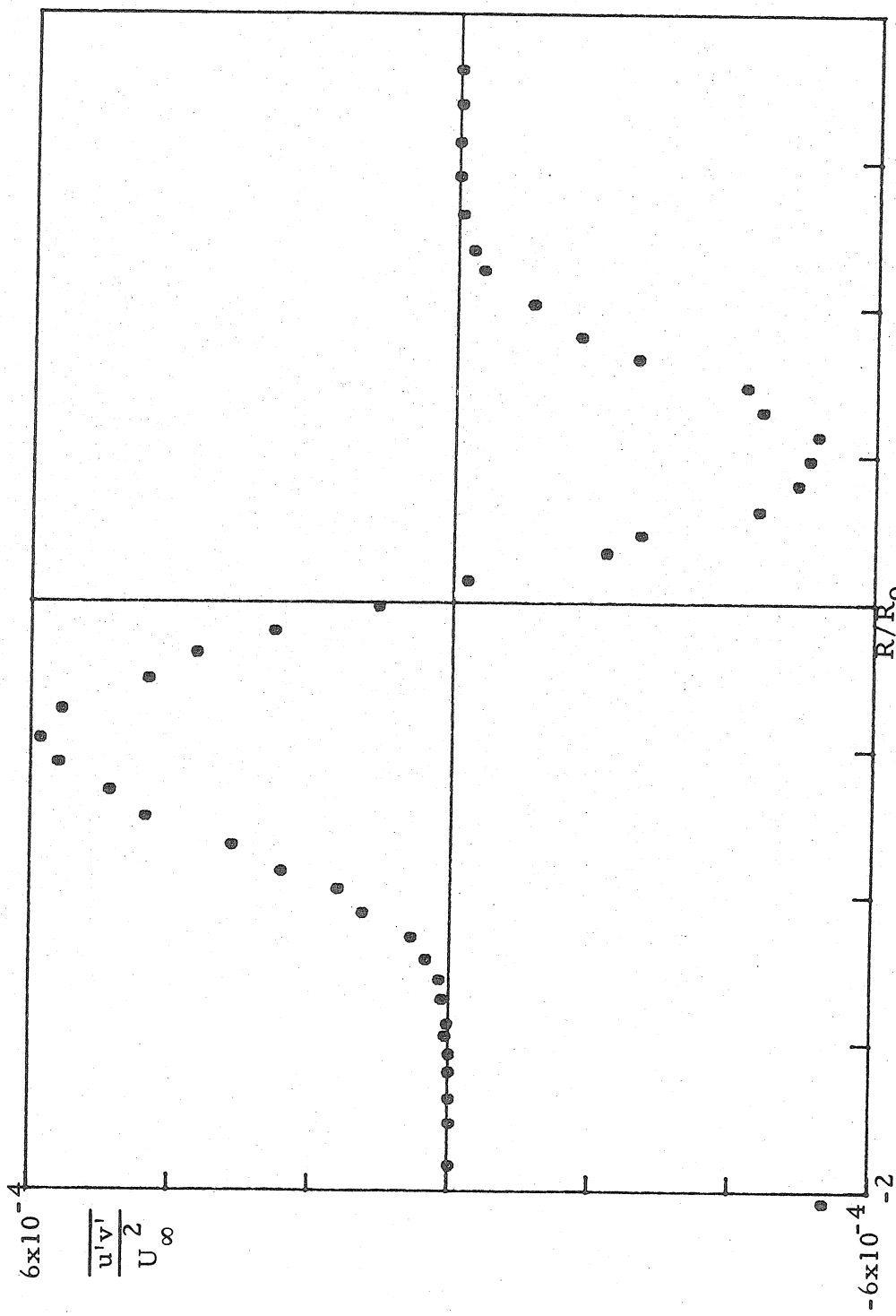


Fig. 96. Turbulent Shear Stress from X-Wire Measurement, Pure Wake
X/D = 40

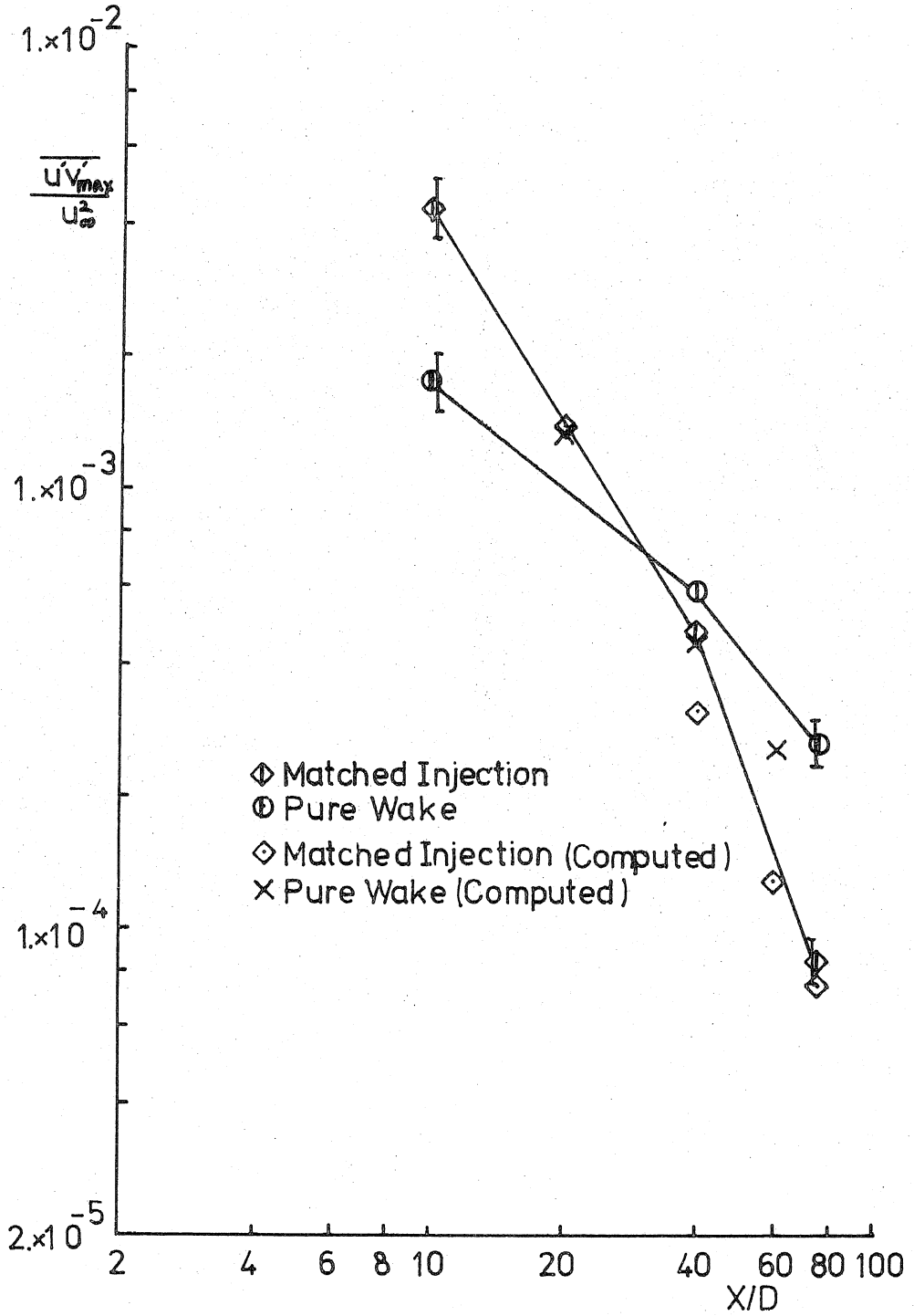


Fig. 97. Axial Variation of Maximum Turbulent Shear Stress Measured with X-Wire

REFERENCES

1. Antonia, R. A. and Bilger, R. W., "The prediction of the Axisymmetric Turbulent Jet Issuing into a Co-Flowing Stream," Aeronautical Quarterly, Vol. 25, Feb. 1974, pp. 69-80.

2. Becker, H. A. and Massaro, T. A., "Vortex Evolution in a Round Jet," Journal of Fluid Mechanics, Vol. 31, 1968, pp. 435-448.

3. Bevilaqua, P. M., "Intermittency, the Entrainment Problem," ARL TR 75-0095, 1975.

4. Birkhoff, G. and Zarantonello, E. H., "Jets, Wakes, and Cavities," Academic Press, 1957.

5. Bradshaw, P., Ferriss, D. H. and Atwell, N. P., "Calculation of Boundary-Layer Development using the Turbulent Energy Equation," Journal of Fluid Mechanics, Vol. 28, 1967, pp. 593-616.

6. Bradshaw, P. and Goodman, D. G., "The Effect on Static-Pressure Tubes," ARC R&M No. 3527, 1968.

7. Bukreev, V. I., Vasil'ev, O. F. and Lytkin, Yu. M., "On the Influence of Body Shape on the Characteristics of a Self-Similar Axisymmetric Wake," Doklady Akademiia Nauk, SSSR, Vol. 207, No. 4, 1972, pp. 804-807.

8. Carmody, T., "Establishment of the Wake Behind a Disk," Journal of Basic Engineering, Transaction of ASME, Series D, Vol. 86, 1964, pp. 869-882.

9. Chevray, R., "The Turbulent Wake of a Body of Revolution," Transactions of ASME, Series D, Vol. 90, 1968, pp. 275-284.

References (Cont'd)

10. Chieng, C. C., Jakubowski, A. K., and Schetz, J. A., "Investigation of the Turbulent Properties of the Wake Behind Self-Propelled, Axisymmetric Bodies," VPI Aero-025, Sept. 1974.

11. Coles, D., "The Young Person's Guide to the Data," A Survey Lecture Prepared for the 1968 AFOSR-IFP-Stanford Conference on Computation of Turbulent Boundary Layers.

12. Cooper, R. D. and Lutzky, M., "Exploratory Investigation of the Turbulent Wakes Behind Bluff Bodies," DTMB R&D Rept. No. 953, Oct. 1955, David Taylor Model Basin, Washington, D. C.

13. Demin, V. S., Morin, O. V., Polyakov, N. F. and Shcherbakov, V. A., "Measurement of Low Levels of Turbulence with a Hot-Wire Anemometer," Fluid Mechanics-Soviet Research, Vol. 2, No. 3, May-June 1973, pp. 59-63.

14. Dvorak, F. A., "Calculation of Turbulent Boundary Layers on Rough Surfaces in Pressure Gradient," AIAA Journal, Vol. 7, No. 9, 1969, pp. 1752-1759.

15. Eggers, J. M., "Turbulent Mixing of Coaxial Compressible Hydrogen-Air Jets," NASA TN D-6487, Sept. 1971.

16. Eggers, J. M. and Torrence, M. G., "An Experimental Investigation of the Mixing of Compressible-Air Jets in a Coaxial Configuration," NASA TN D-5315, July 1969.

17. Fage, A., "On the Static Pressure in Fully-Developed Turbulence," Proceedings of Royal Society of London, Series A, Vol. 155, 1936, pp. 576-596.

References (Cont'd)

18. Fejer, A. A., Torda, T. P., Boehman, L. I., Ghia, K. N. and Hermann, W. G., "Research on Mixing of Coaxial Streams," ARL 67-0058, Mar. 1967, Aerospace Research Laboratories, USAF.

19. Finson, M. L., "Similarity Behaviour of Momentumless Turbulent Wakes," Journal of Fluid Mechanics, Vol. 71, Part 3, 1975, pp. 465-479.

20. Gartshore, I. S., "Two-Dimensional Turbulent Wakes," Journal of Fluid Mechanics, Vol. 30, 1967, pp. 547-560.

21. Gibson, C. H., Chen, C. C. and Lin, S. C., "Measurements of Turbulent Velocity and Temperature Fluctuations in the Wake of a Sphere," AIAA Journal, Vol. 6, No. 4, Apr. 1968, pp. 642-649.

22. Ginevskii, A. S., Pochkina, K. A. and Ukahova, L. N., "Propagation of Turbulent Jet Flow with Zero Excess Impulse," IZV. AN SSSR Mekhanika Zhidkosti i Gaza, Vol. 1, No. 6, 1966, pp. 164-166, in Fluid Dynamics 1967, Faraday Press.

23. Ginevskii, A. S., Ukhanova, L. N. and Pochkina, K. A., "Turbulent Co-Flows with Zero Excess Momentum," Fluid Mechanics-Soviet Research, Vol. 1, No. 5, 1972, pp. 81-86.

24. Gold, H., "Stability of Laminar Wakes," Ph.D. Thesis, 1963, California Inst. of Technology.

25. Gran, R. L., "An Experiment on the Wake of a Slender Propeller-Driven Body," Report 20086-6006-RU-00, June 1973, TRW Systems.

References (Cont'd)

26. Griffin, O. M. and Votaw, C. W., "The Use of Aersols for the Visualization of Flow Phenomena," Int. Journal of Heat and Mass Transfer, Vol. 16, Jan. 1973, pp. 217-219.

27. Hall, A. A. and Hislop, G. S., "Velocity and Temperature Distributions in the Turbulent Wake Behind a Heated Body of Revolution," Proceedings of the Cambridge Philosophical Society, Vol. 34, 1938, pp. 345-350.

28. Harsha, P. T., "Free Turbulent Mixing: A Critical Evaluation of Theory and Experiment," AEDC-TR-71-36, Feb. 1971.

29. Harsha, P. T., "A General Analysis of Free Turbulent Mixing," AD-778 414, May 1974, Arnold Air Force Station, Tennessee.

30. Hinze, J. O., "Turbulence--An Introduction to its Mechanism and Theory," McGraw-Hill, 1959.

31. Kolpin, M. A., "Flow in the Mixing Region of a Jet," Mass. Inst. of Technology, Report ASRL TR 92-3, June 1962.

32. Kuethe, A. M., "Investigation of the Turbulent Mixing Regions Formed by Jets," Journal of Applied Mechanics, Vol. 2, No. 3, 1935, pp. 87-95.

33. Lewellen, W. S., Teske, M. and Donaldson, C. duP., "Application of Turbulence Model Equations to Axisymmetric Wakes," A.R.A.P. Report No. 191, Feb. 1973, Aeronautical Research Associates of Princeton, Inc.

34. Mazumder, M. K., Hoyle, B. D. and Kirsch, K. J., "Generation and Fluid Dynamics of Scattering Aerosols in Laser Doppler Velocimetry," Proceedings of the Second International Workshop

References (Cont'd)

34. (Continued)

on Laser Velocimetry, Vol. 2, March 1974, Purdue University, Thompson, H. D. and Stevenson, W. H. (Editors).

35. Mobbs, F. R., "Spreading and Contraction at the Boundaries of Free Turbulent Flows," Journal of Fluid Mechanics, Vol. 33, Part 2, 1968, pp. 227-239.

36. Narasimha, R. and Prabhu, A., "Equilibrium and Relaxation in Turbulent Wakes," Journal of Fluid Mechanics, Vol. 54, Part 1, 1972, pp. 1-17.

37. Naudascher, E., "Flow in the Wake of Self-Propelled Bodies and Related Sources of Turbulence," Journal of Fluid Mechanics, Vol. 22, Part 4, 1965, pp. 625-656.

38. Oswald, L. J. and Kibens, V., "Turbulent Flow in the Wake of a Disk," Report 002820, University of Michigan, 1971.

39. Perry, A. E. and Morrison, G. L., "Static and Dynamic Calibrations of Constant-Temperature Hot-Wire Systems," Journal of Fluid Mechanics, Vol. 47, Part 4, 1971, pp. 765-777.

40. Riddhagni, P.R., Bevilaqua, P. M., and Lykoudis, P. S., "Measurements in the Turbulent Wake of a Sphere," AIAA Journal, Vol. 9, No. 7, July 1971, pp. 1433-1434.

41. Ridjanovic, M., "Wake with Zero Change of Momentum Flux," Ph.D. Thesis, 1963, State University of Iowa.

42. Schetz, J. A. and Jakubowski, A. K., "Experimental Studies of the Turbulent Wake Behind Self-Propelled Slender Bodies," AIAA Journal, Vol. 13, No. 12, Dec. 1975, pp. 1568-1575.

References (Cont'd)

43. Schlichting, H., "Boundary-Layer Theory," McGraw-Hill 6th ed. 1968.

44. Sigal, A., "An Experimental Investigation of the Turbulent Boundary Layer Over a Wavy Wall," Ph.D. Thesis, 1971, California Institute of Technology.

45. Swanson, R. C., Schetz, J. A. and Jakubowski, A. K., "Turbulent Wake Behind Slender Bodies Including Self-Propelled Configurations," VPI-Aero-024, Sept. 1974, Virginia Polytechnic Institute and State University.

46. Tennekes, H. and Lumley, J. L., "A First Course in Turbulence," MIT Press, 1972.

47. Townsend, A. A., "Measurements in the Turbulent Wake of a Cylinder," Proc. Roy. Soc. London A190, 1947, pp. 551-561.

48. Townsend, A. A., "Entrainment and the Structure of Turbulent Flow," Journal of Fluid Mechanics, Vol. 41, 1970, pp. 13-46.

49. Townsend, A. A., "The Structures of Turbulent Shear Flow," 2nd Ed. Cambridge Univ. Press, 1976.

50. Uberoi, M. S. and Freymuth, P., "Turbulent Energy Balance and Spectra of the Axisymmetric Wake," The Physics of Fluids, Vol. 13, No. 9, Sept. 1970, pp. 2205-2210.

51. Viktorin, K., "Investigation of Turbulent Mixing Processes," Forschung auf dem Gebiete des Ingenieurwesens, Vol. 12, No. 1, 1941 (Also NASA TM 1096, 1946).

52. Wang, H., "Flow Behind a Point Source of Turbulence," Ph.D. Thesis, University of Iowa, 1965.

References (Cont'd)

53. Willmarth, W. W., Winkel, R. E., Bogar, T. J. and Sharma, L. K., "Axially Symmetric Turbulent Boundary Layers on Cylinders: Mean Velocity Profiles and Wall Pressure Fluctuations," Report 021490-3-T, University of Michigan, June 1975.

54. Wygnanski, I. and Fiedler, H., "Some Measurements in the Self-Preserving Jet," Journal of Fluid Mechanics, Vol. 38, Part 3, 1969, pp. 577-612.